U.PORTO

DOUTORAMENTO

CIÊNCIAS BIOMÉDICAS

Uncovering the mechanisms regulating the essential roles of dynein-2 in cilia function

Diogo Marques Rodrigues

D

2023

U.PORTO

Diogo Marques Rodrigues. Uncovering the mechanisms regulating the essential roles of dynein-2 in cilia function

Uncovering the mechanisms regulating the essential roles of dynein-2 in cilia function

Diogo Rafael Marques Rodrigues

D.ICBAS **2023**

SEDE ADMIISTRATIVA

INSTITUTO DE CIÊNCIAS BIOMÉDICAS ABEL SALAZAR

Diogo Rafael Marques Rodrigues

Uncovering the mechanisms regulating the essential roles of dynein-2 in cilia function

Tese de Candidatura ao grau de Doutor em Ciências Biomédicas;
Programa Doutoral da Universidade do Porto (Instituto de Ciências Biomédicas de Abel Salazar)

Trabalho desenvolvido no Instituto de Investigação e Inovação em Saúde (i3S) da Universidade do Porto

Orientador – Tiago Jorge Oliveira Gonçalves de Almeida Dantas

Categoria – Investigador Auxiliar

Afiliação - Instituto de Investigação e Inovação em Saúde, Instituto de Biologia Molecular e Celular, Universidade do Porto

Co-orientador – Carla Manuela de Castro Abreu

Categoria – Investigadora Auxiliar

Afiliação - Instituto de Investigação e Inovação em Saúde, Instituto de Biologia Molecular e Celular, Universidade do Porto

Co-orientador – Reto Gassmann

Categoria – Investigador Principal

Afiliação - Instituto de Investigação e Inovação em Saúde, Instituto de Biologia Molecular e Celular, Universidade do Porto

Declaração de honra

Declaro que a presente tese é de minha autoria e não foi utilizada previamente noutro curso ou unidade curricular, desta ou de outra instituição. As referências a outros autores (afirmações, ideias, pensamentos) respeitam escrupulosamente as regras da atribuição, e encontram-se devidamente indicadas no texto e nas referências bibliográficas, de acordo com as normas de referenciação. Tenho consciência de que a prática de plágio e auto-plágio constitui um ilícito académico.

Acknowledgements

First, I would like to thank my supervisor Tiago Dantas and co-supervisor Carla Abreu for the opportunity to develop my PhD project in their group. Thank you for believing in me and for being so patient during my learning process. I could not have asked for better supervisors. Also, I want to thank my co-supervisor Reto Gassmann for the scientific discussions, and for all the reagents and equipment provided.

I would also like to thank the scientific committee of the Biomedical Sciences PhD program, namely my professors Eduardo Rocha and Salomé Gomes for their guidance and support during these 4 years.

I am very grateful to all my friends, specially Hélio, Francisco, Vítor, and Ju. Life is not always about work, and it is good to have people to hang out with and have fun, to recharge batteries.

A very warm thank you to my girlfriend Márcia for all the support, care, and for bringing me peace when things start to become overwhelming.

Lastly, I am very grateful to my parents João and Cristina, and to my brother Daniel. They are my pillars, who always make me feel safe and supported. Making you feel proud has always been one of my primary goals.

Funding

This work was supported by Fundação para a Ciência e a Tecnologia (FCT) through the PhD fellowship that was granted to me (SFRH/BD/143985/2019), and the projects granted to my supervisor Dr. Tiago Dantas (2022.01955.PTDC), and my co-supervisor Dr. Carla Abreu (2022.01964.PTDC).

Fundação
para a Ciência
e a Tecnologia

This work was also supported by Fundo Europeu de Desenvolvimento Regional (FEDER) through the COMPETE 2020 Operacional Programme for Competitiveness and Internationalisation (POCI), Portugal 2020, and FCT, through the project POCI-01-0145-FEDER-029471 (PTDC/BIA-BID/29471/2017) granted to my supervisor Dr. Tiago Dantas.

COMPETE 2020

PORTUGAL 2020

UNIÃO EUROPEIA

Fundo Europeu
de Desenvolvimento Regional

Table of contents

List of publications

My PhD work included in this thesis has so far resulted in the publications listed below:

Article 1. "WDR60-mediated dynein-2 loading into cilia powers retrograde IFT and transition zone crossing"

Ana R. G. De-Castro*, **Diogo R. M. Rodrigues***, Maria J. G. De-Castro, Neide Vieira, Cármen Vieira, Ana X. Carvalho, Reto Gassmann, Carla M. C. Abreu, and Tiago J. Dantas

*these authors contributed equally to this work

J Cell Biol.; doi: 10.1083/jcb.202010178

This publication is in "Annex I" of this thesis, and the main text is integrated in "Chapter II". I generated the *wdr-60* knock-in and deletion mutants, and performed the biochemical analyses of their transcripts, and I actively contributed to the crossing of *C. elegans* strains, worm imaging, quantification analyses, and writing of the article.

Permission to use article content is granted according to Rockefeller University Press (https://rupress.org/pages/permissions-and-licensing), as cited:

"*In any of the following circumstances, you can use our content gratis (with appropriate attribution):*

- *If you are one of the original authors (in which case you retain copyright).*
  …
- *In your dissertation or doctoral thesis.*"

Article 2. "The IFT20 homolog in *Caenorhabditis elegans* is required for ciliogenesis and cilia-mediated behavior"

Ana R. G. De-Castro*, Joana Quintas-Gonçalves*, Tiago Silva-Ribeiro, **Diogo R. M. Rodrigues**, Maria J. G. De-Castro, Carla M. Abreu, and Tiago J. Dantas

*these authors contributed equally to this work

MicroPubl Biol.; doi: 10.17912/micropub.biology.000396

This publication is in “Annex II” of this thesis. I contributed to the crossing of *C. elegans* strains, and the genetic annotation of the *ift-20(ok3191)* mutation.

Abbreviation list

µM	Micromolar
µg	Microgram
µL	Microliter
µm	Micrometer
7d	7 days
18d	18 days
AAA+	ATPase associated with diverse cellular activities
AID	Auxin-inducible degradation
ANOVA	Analysis of variance
AU	Arbitrary unit
B9D2	B9 domain-containing protein 2
BBSome	Bardet-Biedl syndrome complex
BBS1/BBS-1	Bardet-Biedl syndrome protein 1
BBS2	Bardet-Biedl syndrome protein 2
BBS4	Bardet-Biedl syndrome protein 4
BBS5	Bardet-Biedl syndrome protein 5
BBS7	Bardet-Biedl syndrome protein 7
BBS8	Bardet-Biedl syndrome protein 8
BBS9	Bardet-Biedl syndrome protein 9
BBS18	Bardet-Biedl syndrome protein 18
BlastP	Basic local alignment search tool for proteins
bp	Base pair
Cas9	CRISPR associated protein 9
CEP-290	Centrosomal protein 290
CGC	Caenorhabditis genetics center
CHE-3	Chemotaxis abnormal protein 3
CHE-11	Chemotaxis abnormal protein 11
ChIP-seq	Chromatin immunoprecipitation sequencing
CRISPR	Clustered regularly interspaced short palindromic repeats
CT	C-terminus
DAF-19	Dauer formation abnormal protein 19
DHC-1	Dynein heavy chain 1
DHC-2	Dynein heavy chain 2

DIC	Differential interference contrast
DiI	1,1'-Dioctadecyl-3,3,3',3'-Tetramethylindocarbocyanine Perchlorate
DNA	Deoxyribonucleic acid
DPL-1	DP-like protein 1
DS	Distal segment
DTT	Dithiothreitol
DYCI-1	Dynein chain, intermediate 1
dyf-1	Dye filling abnormal 1
DYF-2	Dye filling abnormal 2
DYF-6	Dye filling abnormal 6
DYF-11	Dye filling abnormal 11
dync2h1	Dynein-2 heavy chain 1
ECL	Enhanced chemiluminescence
EFL-1	E2F-like protein 1
Fiji	Fiji is just imageJ
GFP	Green fluorescent protein
GPCR	G-protein-coupled receptor
gpd-2/*gpd-3*	Glyceraldehyde-3-phosphate dehydrogenase
gRNA	Guide ribonucleic acid
GST	Glutathione S-transferase
h	Hour
HC	Heavy chain
HEK293T	Human embryonic kidney 293T cell line
HRP	Horseradish peroxidase
HYLS-1	Hydrolethalus syndrome protein 1
IA	Isoamyl alcohol
IAA	Indole-3-acetic acid
IC	Intermediate chain
IFT	Intraflagellar transport
IFT22	Intraflagellar transport protein 22
IFT25	Intraflagellar transport protein 25
IFT27	Intraflagellar transport protein 27
IFT43	Intraflagellar transport protein 43
IFT46/IFT-46	Intraflagellar transport protein 46
IFT52/IFT-52	Intraflagellar transport protein 52
IFT56	Intraflagellar transport protein 56

IFT70	Intraflagellar transport protein 70
IFT74/IFT-74	Intraflagellar transport protein 74
IFT81	Intraflagellar transport protein 81
IFT88	Intraflagellar transport protein 88
IFT121/IFT-121	Intraflagellar transport protein 121
IFT122/IFT-122	Intraflagellar transport protein 122
IFT139/IFT-139	Intraflagellar transport protein 139
IFT140/IFT-140	Intraflagellar transport protein 140
IFT144/IFT-144	Intraflagellar transport protein 144
IFT-A	Intraflagellar transport complex A
IFT-B	Intraflagellar transport complex B
IFT-B1	Intraflagellar transport subcomplex B1
IFT-B2	Intraflagellar transport subcomplex B2
IFTA-1	Intraflagellar transport A protein 1
IMCD3	Inner medullary collecting duct 3 cell line
IP	Immunoprecipitation
KIF3A	Kinesin family member 3A
KIFAP3	Kinesin associated protein 3
KAP-1	Kinesin associated protein 1
kDa	Kilodalton
KIF17	Kinesin family member 17
KLP-20	Kinesin-like protein 20
KO	Knock-out
L1	Larval stage 1
L2	Larval stage 2
L3	Larval stage 3
L4	Larval stage 4
LC	Light chain
LC8	Light chain 8
LIC	Light-intermediate chain
LIC3	Light-intermediate chain 3
LSY-2	Laterally symmetric protein 2
MDa	Megadalton
mex-5	Muscle excess 5
min	Minutes
MKS	Meckel syndrome
MKS-5	Meckel syndrome protein 5

MKS-6	Meckel syndrome protein 6
MKSR-1	Meckel syndrome related protein 1
MKSR-2	Meckel syndrome related protein 2
mL	Milliliter
mM	Millimolar
MosSCI	Mos1-mediated single copy insertion
mRNA	Messenger ribonucleic acid
MS	Middle segment
ms	Milliseconds
myo-2	Myosin heavy chain 2
myo-3	Myosin heavy chain 3
N	Number of events
NA	Numerical aperture
NGM	Nematode growth medium
nm	Nanometer
NPHP	Nephronophthisis
NPHP-4	Nephronophthisis protein 4
ns	Non-significant
NT	N-terminus
NudE	Nuclear distribution E protein
NudEL	Nuclear distribution E-like protein
OSM-3	Osmotic avoidance abnormal 3
osm-6	Osmotic avoidance abnormal 6
PAGE	Polyacrylamide gel electrophoresis
PBS	Phosphate-buffered saline
PBS-T	Phosphate-buffered saline Tween-20
PCMC	Periciliary membrane compartment
PCR	Polymerase chain reaction
PHA	Phasmid neurons A
PHB	Phasmid neurons B
pN	Piconewton
rab-3	Ras-related 3
RB	Roadblock
RFP	Red fluorescent protein
RFX	Regulatory factor X
rol-6	Roller 6
RP2/RPI-2	Retinitis pigmentosa protein 2

RPE-1	Retinal pigment epithelial cell line
RPGRIP1L	Retinitis pigmentosa GTPase regulator interacting protein 1 like
s	Second
SCF	Skp, Cullin, F-box containing complex
SD	Standard deviation
SDS	Sodium dodecyl sulfate
SEM	Standard error of the mean
sGFP	Split green fluorescent protein
Shh	Sonic Hedgehog
SRPS	Short rib polydactyly syndrome
TIR1	Transport inhibitor response 1
TMEM-107	Transmembrane protein 107
TMEM67	Transmembrane protein 67
TULP3	Tubby-like protein 3
TZ	Transition zone
unc-119	Uncoordinated 119
vol	Volume
WDR34	WD repeat protein 34
WDR60/WDR-60	WD repeat protein 60
WT	Wild type
XBX-1	X-box promoter element regulated protein 1
YA	Young adult

Abstract

Cilia are microtubule-based structures that extend outwards from the surface of many cell types. The assembly and function of cilia rely on a specialized bidirectional transport system termed Intraflagellar transport (IFT). During this process, kinesin-2 and dynein-2 motors transport cargo into, and out of cilia, across the transition zone, a dense structure near the ciliary base that separates the cytoplasm from the intraciliary environment.

The dynein-2 motor is a multi-subunit complex built of heavy, intermediate, light-intermediate, and light chains. In this work, we identified the *C. elegans* ortholog of the intermediate chain WDR60, and studied its role in dynein-2 function. Loss of WDR-60 did not compromise axoneme extension, but resulted in a reduced incorporation of dynein-2 motors onto anterograde IFT trains. In turn, retrograde IFT kinetics became impaired, and dynein-2 motors could no longer generate enough force to efficiently push retrograde IFT trains through the transition zone to exit cilia. More recently, we observed that loss of WDR-60 may also result in partial uncoupling of some components from retrograde IFT trains. Strikingly, we found that removing the NPHP module from the transition zone was enough to restore the ciliary exit of IFT trains in the absence of WDR-60.

To test whether WDR-60 functions are interconnected during IFT, we generated N-terminal deletion mutants, including one lacking a highly conserved domain that binds IFT-54 during anterograde IFT. However, deletion of this domain did not reduce the loading of dynein-2 motors onto anterograde trains, reinforcing that other important interactions must still occur between the dynein-2 complex and the anterograde IFT train. During the process of generating the potential separation of function mutants, we also found an upstream region of the *wdr-60* coding sequence that appears to be important for its transcription.

We also searched for a *C. elegans* ortholog of the intermediate chain WDR34, and found that DYCI-1 (the intermediate chain of dynein-1) was the protein with the highest sequence homology. However, we were never able to detect DYCI-1 inside cilia of sensory neurons, suggesting that it is not part of the dynein-2 complex. Thus, it remains unclear whether there is another dynein-2-specific intermediate chain in *C. elegans*, or if WDR-60 forms a homodimer.

Together, our results contribute to understanding the molecular mechanisms underlying WDR60-related ciliopathies, while also shedding light on the interplay between the transition zone and the passage of IFT trains.

Resumo

Os cílios são estruturas baseadas em microtúbulos que se estendem a partir da superfície de diversos tipos de células. A construção e a função dos cílios dependem de um sistema de transporte bidirecional especializado denominado Transporte intraflagelar (IFT). Durante este processo, os motores cinesina-2 e dineína-2 transportam carga para dentro e para fora dos cílios, através da zona de transição, uma estrutura densa próxima da base do cílio que separa o citoplasma do ambiente intraciliar.

O motor dineína-2 é um complexo de múltiplas subunidades constituído por cadeias pesadas, intermédias, intermédias-leves e leves. Neste trabalho, identificámos o ortólogo da cadeia intermédia WDR60 em *C. elegans*, e analisámos o seu papel na função da dineína-2. A perda de WDR-60 não comprometeu a extensão do axonema, mas resultou numa incorporação reduzida de motores dineína-2 em comboios de IFT anterógrados. Por sua vez, a cinética retrógrada do IFT ficou prejudicada e os motores dineína-2 ficaram incapazes de gerar força suficiente para transportar eficientemente os comboios de IFT retrógrados através da zona de transição para sair dos cílios. Mais recentemente, observámos que a perda de WDR-60 também pode resultar no desacoplamento parcial de alguns componentes dos comboios de IFT retrógrados. Notavelmente, descobrimos que a remoção do módulo NPHP da zona de transição foi suficiente para restaurar a saída ciliar dos comboios de IFT na ausência de WDR-60.

Para testar se as funções do WDR-60 estão interconectadas durante o IFT, gerámos mutantes de deleção N-terminal, incluindo um que perde um domínio altamente conservado que se liga ao IFT-54 durante o IFT anterógrado. No entanto, a deleção deste domínio não reduziu o carregamento dos motores dineína-2 nos comboios anterógrados, reforçando a ideia de que outras interações importantes ainda devem ocorrer entre o complexo dineína-2 e o comboio anterógrado de IFT. Durante o processo de geração de mutantes para separação de função, também encontrámos uma região a montante da sequência codificante do *wdr-60* que aparenta ser importante para a sua transcrição.

Também procurámos por um ortólogo da cadeia intermédia WDR34 em *C. elegans* e descobrimos que a DYCI-1 (a cadeia intermédia da dineína-1) era a proteína com a maior homologia de sequência. No entanto, nunca conseguimos de detetar a DYCI-1 dentro dos cílios dos neurónios sensoriais, o que sugere que não faz parte do complexo dineína-2. Desta forma, ainda não é claro se existe outra cadeia intermédia específica da dineína-2 em *C. elegans*, ou se a WDR-60 forma um homodímero.

Os resultados obtidos neste trabalho contribuem para a compreensão dos mecanismos moleculares subjacentes às ciliopatias relacionadas com WDR60, e contribuem para elucidar a interação entre a zona de transição e a passagem dos comboios de IFT.

CHAPTER I – General Introduction

1.1. Cilia biology and function

Cilia are specialized microtubule-based organelles protruding from the surface of the plasma membrane in several organisms. These structures were first observed by Leeuwenhoek, in the seventeenth century, when looking at rainwater under a primitive homemade microscope. Back then, Leeuwenhoek referred to cilia as “little feet” at the surface of very small “animalcules” (Lane, 2015).

Since then, very diverse ciliary structures have been described across species, or even within the same organism **(Figure 1)**. These organelles can be motile or non-motile, depending on their function. Motile cilia are usually involved in fluid flow or cell locomotion, such as the airway cilia or the sperm flagellum, respectively. On the other hand, non-motile cilia (also known as primary cilia), possess sensory functions and participate in cell signaling pathways such as Wnt, Notch, or Shh (Choksi et al., 2014, Mitchison and Valente, 2017).

In humans, mutations in genes that encode ciliary components can lead to several pathologies that are collectively referred to as ciliopathies, which typically have an autosomal recessive transmission pattern (Mitchison and Valente, 2017, Braun and Hildebrandt, 2017). Ciliopathy symptoms manifest early during development or later in life, and include polycystic kidneys, brain developmental defects, retinal degeneration, skeletal malformations, or congenital heart disease (Braun and Hildebrandt, 2017, Mitchison and Valente, 2017).

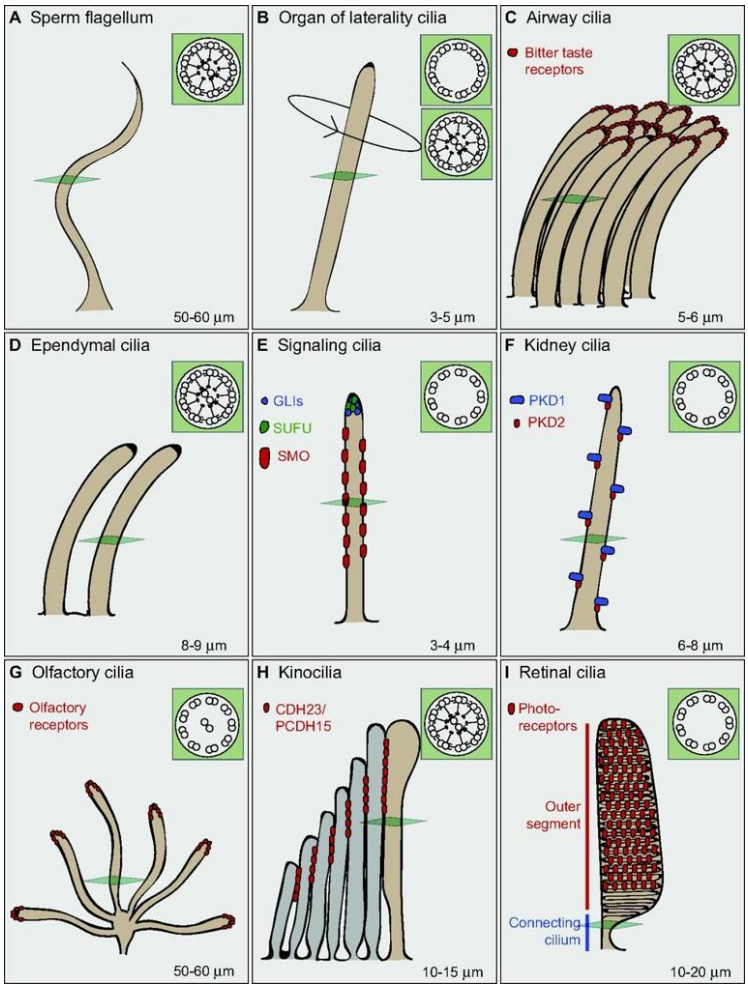

Figure 1 - Different types of cilia in vertebrates. **(A)** The sperm flagellum beats to power sperm movement. **(B)** Nodal cilia move to establish left-right asymmetry during development. **(C)** Airway cilia move to drive mucus flow. **(D)** Ependymal cilia move to circulate cerebrospinal fluid. **(E)** Signaling cilia detect extracellular messengers to activate signaling pathways. **(F)** Cilia in the kidneys sense urine flow. **(G)** Olfactory cilia detect odorant molecules. **(H)** Kinocilia participate in hair cell morphogenesis during development. **(I)** The connecting cilium supports a photoreceptor-rich protrusion in retinal cells. Adapted from (Choksi et al., 2014).

1.2. Intraflagellar transport (IFT)

The scaffold of every type of cilia is a microtubule-based axoneme that extends from the basal body. Molecular motors bind this axoneme to transport cargo into, and out of cilia, in a dynamic process termed Intraflagellar Transport (IFT) **(Figure 2)**. This bidirectional transport system was first discovered in *Chlamydomonas*, when the Rosenbaum lab

observed small granular particles moving along the length of flagella (Kozminski et al., 1993). Distal to the basal body, the transition zone (TZ) acts as a dense gate that controls what enters and exits cilia, and only allows passive diffusion of small particles, to maintain a specialized environment inside cilia. (Garcia-Gonzalo and Reiter, 2017).

During intraflagellar transport, large protein complexes, commonly called IFT trains, are assembled at the ciliary base and are transported in the anterograde direction by kinesin-2 motors through the transition zone and into the cilium. These travel along the length of the axoneme, until they reach the ciliary tip for the delivery of ciliary components, such as tubulin or membrane receptors. Once at the tip, anterograde IFT trains are remodeled into retrograde IFT trains which are then transported by dynein-2 motors along the axoneme track in the opposite direction, until they cross the transition zone, and reach the ciliary base. This, in turn, serves to deliver signaling molecules, as well as ciliary turnover products, back to the cytoplasm (Ishikawa and Marshall, 2011). IFT is required for the building and maintenance of nearly all types of cilia. Known exceptions are the cilia of *P. falciparum* and the *Drosophila* sperm flagellum, where the axoneme is built in the cytoplasm in an IFT-independent manner, and then expelled to a membrane bulge (Sinden et al., 1976, Han et al., 2003, Sarpal et al., 2003).

IFT trains are built of large multiprotein complexes that associate with kinesin-2 and dynein-2 motors to transport cargo between the cilium and the cytoplasm. These large complexes can be divided into the IFT-A, IFT-B, and the BBSome.

The IFT-A complex contains 6 proteins and is typically divided into the core IFT-A1 complex (IFT144, IFT140, and IFT122), and the peripheral IFT-A2 complex (IFT43, IFT121, and IFT139), which are bridged by IFT122 (Lacey et al., 2023, Hesketh et al., 2022). IFT-A has traditionally been associated with retrograde IFT, as mutants of this complex across species display distal ciliary accumulations of IFT material, typical of defective retrograde transport (Iomini et al., 2001, Piperno et al., 1998, Quidwai et al., 2021). Recent work by our lab has uncovered that the IFT-A complex is required for the assembly of the retrograde IFT train, and the efficient activation of the dynein-2 motor (Goncalves-Santos et al., 2023). Interestingly, other studies have shown that the IFT-A complex is also involved in the import of ciliary membrane receptors through the concerted action with the TULP3 adaptor (Hesketh et al., 2022, Mukhopadhyay et al., 2010, Loktev and Jackson, 2013, Sun et al., 2012, Mukhopadhyay et al., 2013, Badgandi et al., 2017).

The IFT-B complex contains 16 proteins which are comprised into 2 subcomplexes (Nakayama and Katoh, 2018): the core IFT-B1 subcomplex, composed of 10 proteins (IFT22, IFT25, IFT27, IFT46, IFT52, IFT56, IFT70, IFT74, IFT81, and IFT88); and the

peripheral IFT-B2 subcomplex, composed by 6 proteins (IFT20, IFT38, IFT54, IFT57, IFT80, IFT172). IFT-B1 is known to bind and activate kinesin-2 motors (Mohamed et al., 2018, Funabashi et al., 2018), and to transport tubulin into the cilium (Kubo et al., 2016, Bhogaraju et al., 2013). IFT-B2 is thought to be involved in the anterograde transport of dynein-2 to the tip of cilia (Jordan et al., 2018, Lacey et al., 2023, Zhu et al., 2021, Hiyamizu et al., 2023). Overall, the IFT-B complex has a strong connection with anterograde IFT, and mutations in this complex can lead to severe ciliary phenotypes, or even absence of cilia (Berbari et al., 2011, Katoh et al., 2017, Katoh et al., 2016, Houde et al., 2006).

Lastly, the BBSome (Bardet-Biedl syndrome complex) is a specialized complex made of 8 proteins (BBS1, BBS2, BBS4, BBS5, BBS7, BBS8, BBS9, and BBS18) that is involved in the removal of activated GPCRs (G-protein-coupled receptors) from cilia via retrograde IFT (Ye et al., 2018).

However, these complexes and IFT subunits have many other functions apart from the abovementioned, reviewed in (Nakayama and Katoh, 2020). IFT is a tightly controlled system, and many regulatory processes are yet to be elucidated. In fact, many basic questions remain unanswered, such as how anterograde IFT trains disassemble at the ciliary tip and are reassembled into retrograde trains, or how dynein-2 is activated to power retrograde IFT.

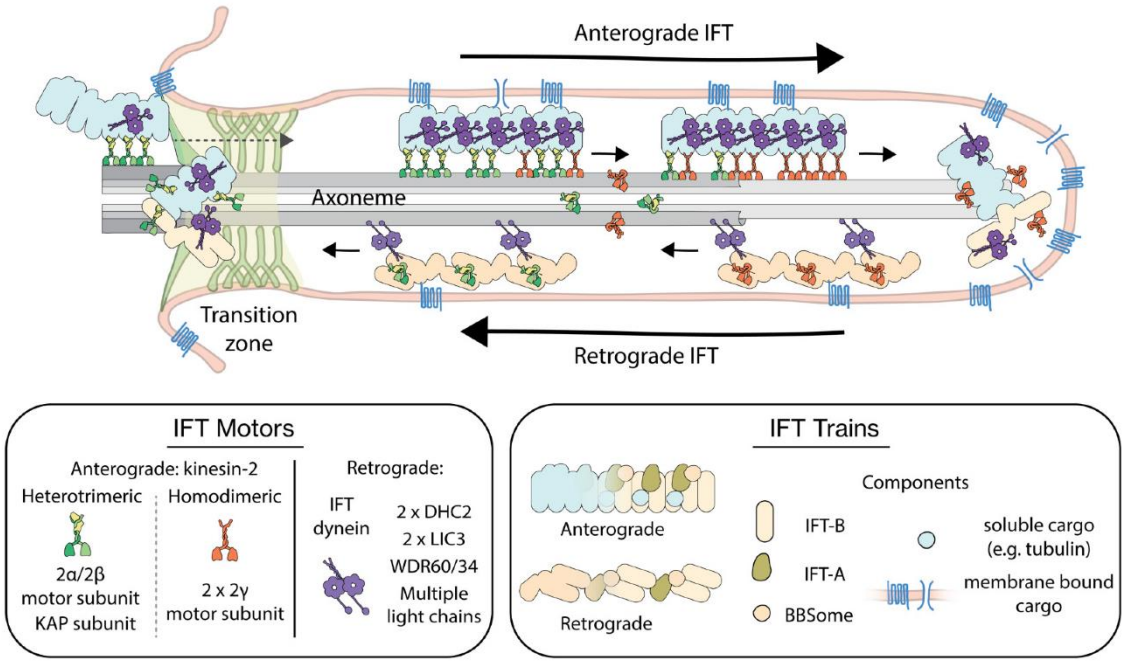

Figure 2 – Intraflagellar Transport. Anterograde IFT trains are built in the ciliary base, and are transported by kinesin-2 motors across the transition zone and into the cilium, along the microtubule track, until they reach the tip. Once at the tip, anterograde trains are rearranged into retrograde IFT

trains which are transported by dynein-2 motors, along the microtubule track and across the transition zone, back to the ciliary base. Adapted from (Mul et al., 2022).

1.3. The ciliary transition zone

The transition zone (TZ) is a dense structure near the base of cilia that assembles early during ciliogenesis, soon after basal body docking to the membrane (Li et al., 2017, Williams et al., 2011). Although the ultrastructure of the TZ varies between species and tissues (Jana et al., 2018, Akella et al., 2019), typical structures can be easily identified by electron microscopy, such as a central cylinder on the inside of the axoneme, and Y-shaped structures attaching the microtubule doublets to the ciliary membrane **(Figure 3)** (Park and Leroux, 2022).

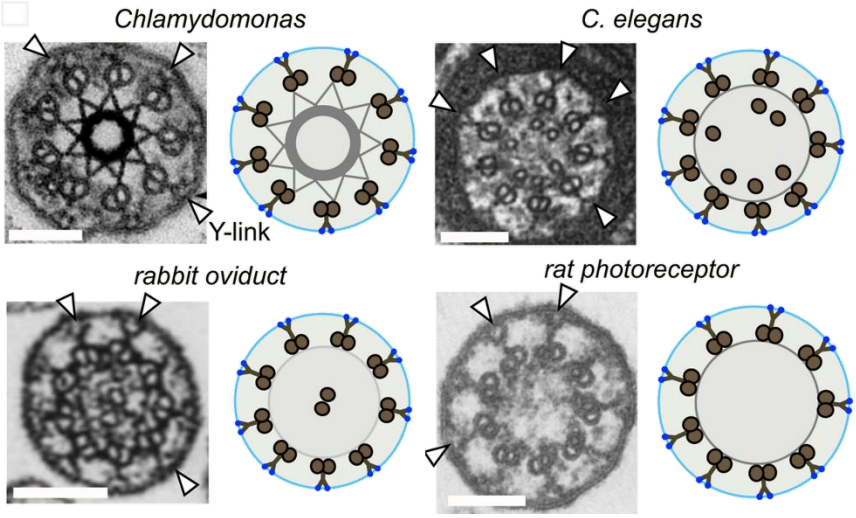

Figure 3 – Diverse TZ ultrastructure among species. Arrow heads point to "Y-link" structures. Scale bars: 0.5 µm. Adapted from (Park and Leroux, 2022).

The TZ is usually referred to as a "ciliary gate" that restricts diffusion into and out of cilia, to maintain a specialized ciliary environment, separated from the cytoplasm. This structure acts as a size-dependent sieve that restricts diffusion of large soluble molecules (Breslow et al., 2013), while also maintaining a specialized ciliary membrane receptor composition (Li et al., 2016). In this sense, the ciliary entry and exit of IFT components is assured by their coupling to kinesin-II and dynein-2 motors, respectively.

Many components of the TZ have been identified, and are typically grouped as part of the MKS or the NPHP modules **(Figure 4)** (Garcia-Gonzalo and Reiter, 2017, Park and Leroux, 2022, Goncalves and Pelletier, 2017). Proteins within these modules have been shown to interact hierarchically during TZ assembly, meaning that the localization of the most downstream components is dependent on the recruitment of the most upstream components to the TZ region (Goncalves and Pelletier, 2017, Park and Leroux, 2022).

Given the importance of the TZ for correct cilia assembly and function, it is not surprising that mutations in TZ components are also a cause of ciliopathies (Park and Leroux, 2022, Goncalves and Pelletier, 2017). In fact, several aberrant phenotypes have been observed in TZ mutant model systems, such as leakage of cytoplasmic proteins into the cilium, microtubule destabilization, or defective TZ ultrastructure (Awata et al., 2014, Li et al., 2016, Jensen et al., 2015, Williams et al., 2011, Schouteden et al., 2015).

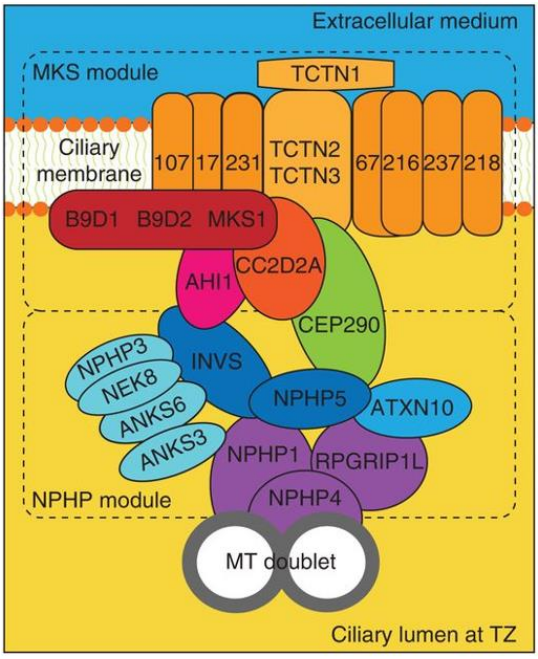

Figure 4 – Model depicting protein interactions in MKS and NPHP modules. TMEM proteins are represented only by their number. Adapted from (Garcia-Gonzalo and Reiter, 2017).

1.4. The dynein-2 complex

The dynein-2 heavy chain was discovered by the Gibbons lab, when searching for novel dynein heavy chain genes in sea urchin embryos (Gibbons et al., 1994), one year after the first observation of IFT (Kozminski et al., 1993). The dynein-2 light intermediate chain (LIC3) was later identified in vertebrates (Mikami et al., 2002), and only much later the dynein-2-specific intermediate chains WDR34 and WDR60 were found in *Chlamydomonas* (Rompolas et al., 2007, Patel-King et al., 2013).

Even so, the structure of the full human dynein-2 complex was only recently solved in vitro **(Figure 5)** (Toropova et al., 2019). Briefly, the two heavy chains (DHC2, encoded by *DYNC2H1*) that comprise the AAA+ motor domains are stabilized by two light-intermediate chains (LIC3, encoded by *DYNC2LI1*). Then, a heterodimer of intermediate chains (WDR60 and WDR34, encoded by *DYNC2I1* and *DYNC2I2*, respectively) along with an array of light chains (two RB, six LC8, and two TCTEX type light chains, encoded by *DYNLRB*, *DYNLL*, and *DYNLT* genes, respectively) bind the heavy chains to dimerize the complex. Mutations in genes encoding these dynein-2 subunits are more commonly associated with skeletal ciliopathies (Braun and Hildebrandt, 2017). However, the contribution of each specific subunit to the regulation of dynein-2 activity still remains unclear.

Akin to dynein-1 (Zhang et al., 2017), the dynein-2 complex by itself is also rendered to an autoinhibitory conformation in vitro (Toropova et al., 2019), exhibiting slow microtubule gliding when compared with the isolated motor domain, or the velocity of retrograde IFT in mammalian cells (Toropova et al., 2017, Ye et al., 2018). The fact that dynein-2 adopts this autoinhibitory conformation together with being loaded onto anterograde trains with its motor domains facing toward the ciliary membrane has been proposed to be important for dynein-2 to not offer resistance when it is being transported itself as a cargo on anterograde IFT trains by kinesin-2 motors (Toropova et al., 2019, Jordan et al., 2018, Lacey et al., 2023, Goncalves-Santos et al., 2023). However, the mechanisms controlling the activation of dynein-2 at the ciliary tip to power retrograde IFT are still unclear.

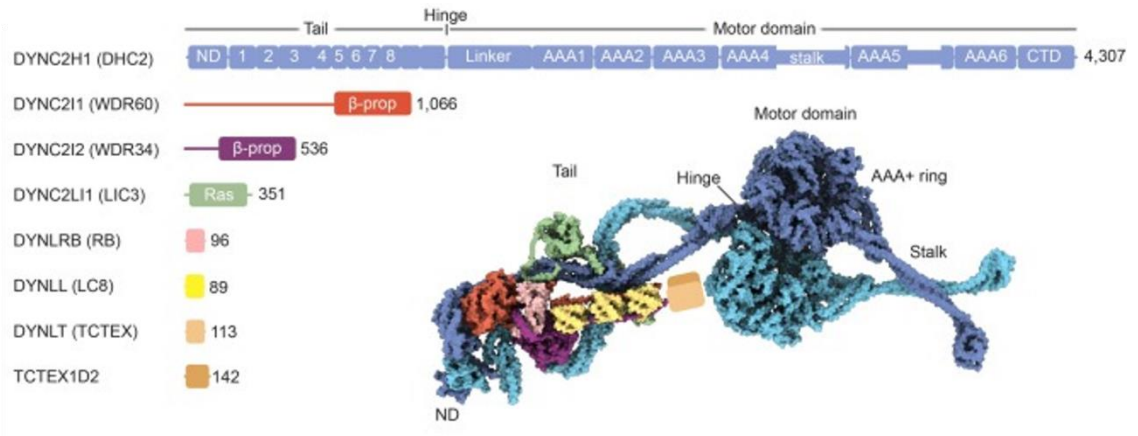

Figure 5 – Structure of the human dynein-2. The human dynein-2 is a multisubunit ~1.4 MDa complex. A homodimer of the heavy chains (DHC2) is stabilized by two light-intermediate chains (LIC3). A heterodimer of intermediate chains (WDR60 and WDR34) bind the N-terminal of the heavy chains through their C-terminal β-propeller. An array of light chains (two RB, six LC8, and two TCTEX type light chains) bind the N-terminal of the intermediate chains to dimerize the complex. Adapted from (Webb et al., 2020).

1.5. *C. elegans* as a model to study IFT and dynein-2

Caenorhabditis elegans is a small nematode that has been leveraged for the last two decades to dissect the mechanisms of IFT (Snow et al., 2004, Ou et al., 2005, Wei et al., 2012, Mijalkovic et al., 2017, Yi et al., 2017, De-Castro et al., 2022, Blacque and Sanders, 2014).

Unlike vertebrate animals, *C. elegans* do not require cilia for development or survival (Swoboda et al., 2000), which has allowed the study of IFT in mutant backgrounds, without compromising viability. Also, ciliary defects do not compromise the fertility of hermaphrodites given that *C. elegans* sperm cells do not possess flagella, and instead rely on the extension of pseudopods for their locomotion (Nelson et al., 1982).

Among other advantages, this animal has a short life cycle (~3.5 days) **(Figure 6)**, and is easily maintained in the lab, dwelling in small plates while feeding on bacteria (Brenner, 1974). The propagation of animals with the same genetic background is also made easy given that the majority of a *C. elegans* population consists of self-fertilizing hermaphrodites,

with only occasional occurrence of males (~1%) (Chasnov and Chow, 2002). These males, however, are useful when crossing animals carrying different mutant alleles to generate new strains with genetic traits of interest.

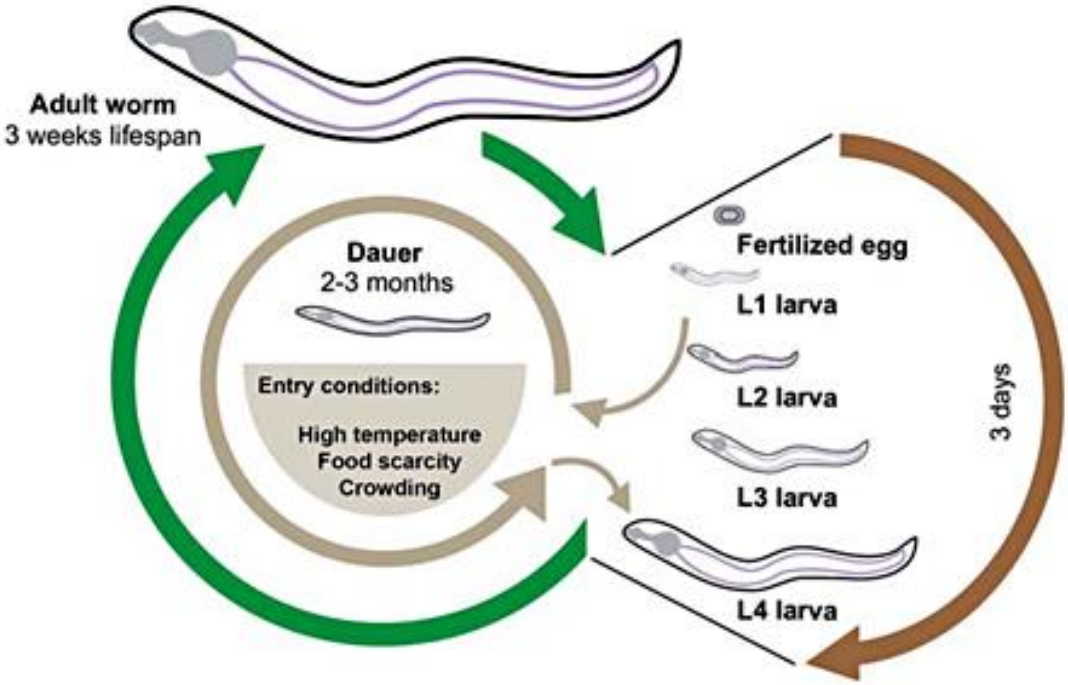

Figure 6 – *C. elegans* life cycle. *C. elegans* life cycle takes approximately 3.5 days at 20°C. A fertilized egg develops through 4 larval stages (each separated by a molt) until reaching the young adult stage. Under stressful conditions (such as high temperature, food scarcity, crowding), L1 and L2 worms can enter a latent developmental state called “Dauer” that provides higher resistance to environmental insults. When more favorable conditions are met, Dauer animals can reenter their larval development at the L4 stage. Adult worms have an average lifespan of 3 weeks. Adapted from (Ewald et al., 2018).

An adult hermaphrodite has 302 neurons, all of which have been mapped (White et al., 1986). Sixty of these neurons have sensory functions and possess cilia at their dendritic ends, which are typically exposed to the environment (Inglis et al., 2007). These neurons function as the animals’ sensory system, perceiving chemical and mechanical stimuli from the surrounding environment, and triggering behavioral responses.

Live imaging of IFT in *C. elegans* is typically carried out on the cilia of the phasmid sensory neurons A and B (PHA and PHB, respectively) in the tail of the animal **(Figure 7)**. These neurons detect both chemical and mechanical cues and are involved in triggering forward motion (Zou et al., 2017, Hall and Russell, 1991). The fact that *C. elegans* are small and

transparent allows phasmid cilia to be easily imaged when these animals are immobilized with 5-10 mM levamisole.

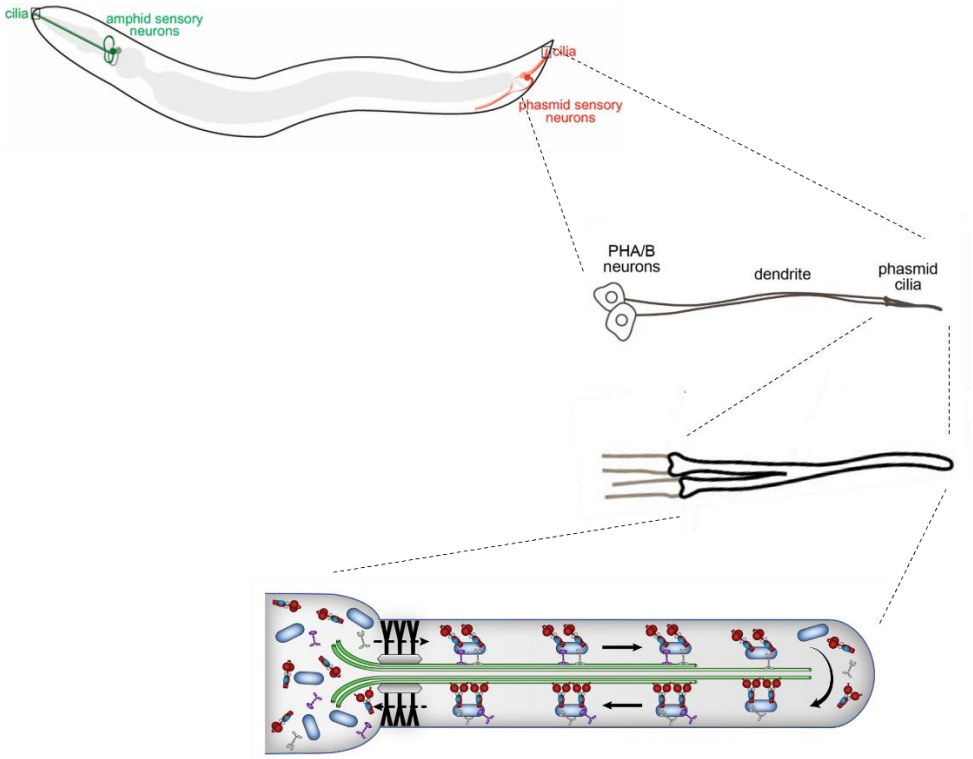

Figure 7 – *C. elegans* as a model organism to study IFT. The *C. elegans* nematode possesses cilia at the dendritic ends of sensory neurons. Live imaging of IFT is well optimized for cilia of the two pairs of PHA and PHB neurons at the tail of these animals.

1.6. Objectives and main findings

In this work, we aimed to gain further insights into the mechanisms regulating dynein-2 and retrograde IFT, using the nematode *C. elegans* as an animal model. Our main objectives were:

1- To identify the orthologs of the dynein-2 intermediate chains WDR60 and WDR34 in *C. elegans*.

We identified the WDR60 ortholog in *C. elegans*, which we named WDR-60. When searching for an ortholog of WDR34, we found that the protein with the highest sequence homology was DYCI-1 (the intermediate chain of dynein-1). However, when probing for

DYCI-1 specifically in sensory neurons, we did not observe this protein inside cilia, suggesting it does not integrate the dynein-2 complex. Thus, it remains elusive whether there is another intermediate chain within the dynein-2 complex in *C. elegans*, or if WDR-60 can form homodimers.

2- To dissect how WDR-60 regulates dynein-2-driven retrograde IFT.

We observed that the absence of WDR-60 in *C. elegans* resulted in a reduced loading of dynein-2 motors onto anterograde IFT trains, and overall reduced ciliary levels of dynein-2. In turn, retrograde IFT trains became underpowered as they had fewer dynein-2 motors carrying them. As a result, retrograde IFT trains accumulated specifically at the distal side of the TZ, unable to efficiently push through this dense barrier to reach the ciliary base.

3- To dissect which TZ components control the exit of retrograde IFT trains.

We hypothesized that disrupting the TZ could facilitate the exit of retrograde IFT trains in the absence of WDR-60. On that notion, we generated several *C. elegans* strains combining different TZ mutations, and observed that the removal of the NPHP module from the TZ restored the ciliary exit of WDR-60-deficient dynein-2, preventing its accumulation at the distal side of the TZ.

4- To assess if WDR-60 is required for the coupling between dynein-2 and cargo during retrograde IFT

We show that, in the absence of WDR-60, most of the IFT machinery also accumulated at the distal side of the TZ, suggesting that it is still coupled to dynein-2 during retrograde IFT (exceptions may be IFT-74, IFT-121, and BBS-1). Notably, disruption of the NPHP module also prevented the accumulation of IFT components at the distal side of the TZ upon loss of WDR-60, indicating that dynein-2 retains its capacity to retrieve cargo back to the ciliary base.

5- To dissect how WDR-60 mediates dynein-2 loading onto anterograde trains

We uncovered that a very conserved region in the N-terminus of WDR-60 interacts with the anterograde IFT train. However, the deletion of this conserved region only slightly reduced the loading of dynein-2 motors into cilia. This observation reinforces that other important interactions must still occur between the dynein-2 complex and the anterograde IFT train.

1.6. References

AKELLA, J. S., SILVA, M., MORSCI, N. S., NGUYEN, K. C., RICE, W. J., HALL, D. H. & BARR, M. M. 2019. Cell type-specific structural plasticity of the ciliary transition zone in C. elegans. *Biol Cell,* 111**,** 95-107.

AWATA, J., TAKADA, S., STANDLEY, C., LECHTRECK, K. F., BELLVE, K. D., PAZOUR, G. J., FOGARTY, K. E. & WITMAN, G. B. 2014. NPHP4 controls ciliary trafficking of membrane proteins and large soluble proteins at the transition zone. *J Cell Sci,* 127**,** 4714-27.

BADGANDI, H. B., HWANG, S. H., SHIMADA, I. S., LORIOT, E. & MUKHOPADHYAY, S. 2017. Tubby family proteins are adapters for ciliary trafficking of integral membrane proteins. *J Cell Biol,* 216**,** 743-760.

BERBARI, N. F., KIN, N. W., SHARMA, N., MICHAUD, E. J., KESTERSON, R. A. & YODER, B. K. 2011. Mutations in Traf3ip1 reveal defects in ciliogenesis, embryonic development, and altered cell size regulation. *Dev Biol,* 360**,** 66-76.

BHOGARAJU, S., CAJANEK, L., FORT, C., BLISNICK, T., WEBER, K., TASCHNER, M., MIZUNO, N., LAMLA, S., BASTIN, P., NIGG, E. A. & LORENTZEN, E. 2013. Molecular basis of tubulin transport within the cilium by IFT74 and IFT81. *Science,* 341**,** 1009-12.

BLACQUE, O. E. & SANDERS, A. A. 2014. Compartments within a compartment: what C. elegans can tell us about ciliary subdomain composition, biogenesis, function, and disease. *Organogenesis,* 10**,** 126-37.

BRAUN, D. A. & HILDEBRANDT, F. 2017. Ciliopathies. *Cold Spring Harb Perspect Biol,* 9.

BRENNER, S. 1974. The genetics of Caenorhabditis elegans. *Genetics,* 77**,** 71-94.

BRESLOW, D. K., KOSLOVER, E. F., SEYDEL, F., SPAKOWITZ, A. J. & NACHURY, M. V. 2013. An in vitro assay for entry into cilia reveals unique properties of the soluble diffusion barrier. *J Cell Biol,* 203**,** 129-47.

CHASNOV, J. R. & CHOW, K. L. 2002. Why are there males in the hermaphroditic species Caenorhabditis elegans? *Genetics,* 160**,** 983-94.

CHOKSI, S. P., LAUTER, G., SWOBODA, P. & ROY, S. 2014. Switching on cilia: transcriptional networks regulating ciliogenesis. *Development,* 141**,** 1427-41.

DE-CASTRO, A. R. G., RODRIGUES, D. R. M., DE-CASTRO, M. J. G., VIEIRA, N., VIEIRA, C., CARVALHO, A. X., GASSMANN, R., ABREU, C. M. C. & DANTAS, T. J. 2022. WDR60-mediated dynein-2 loading into cilia powers retrograde IFT and transition zone crossing. *J Cell Biol,* 221.

EWALD, C. Y., CASTILLO-QUAN, J. I. & BLACKWELL, T. K. 2018. Untangling Longevity, Dauer, and Healthspan in Caenorhabditis elegans Insulin/IGF-1-Signalling. *Gerontology,* 64**,** 96-104.

FUNABASHI, T., KATOH, Y., OKAZAKI, M., SUGAWA, M. & NAKAYAMA, K. 2018. Interaction of heterotrimeric kinesin-II with IFT-B-connecting tetramer is crucial for ciliogenesis. *J Cell Biol,* 217**,** 2867-2876.

GARCIA-GONZALO, F. R. & REITER, J. F. 2017. Open Sesame: How Transition Fibers and the Transition Zone Control Ciliary Composition. *Cold Spring Harb Perspect Biol,* 9.

GIBBONS, B. H., ASAI, D. J., TANG, W. J., HAYS, T. S. & GIBBONS, I. R. 1994. Phylogeny and expression of axonemal and cytoplasmic dynein genes in sea urchins. *Mol Biol Cell,* 5**,** 57-70.

GONCALVES-SANTOS, F., DE-CASTRO, A. R. G., RODRIGUES, D. R. M., DE-CASTRO, M. J. G., GASSMANN, R., ABREU, C. M. C. & DANTAS, T. J. 2023. Hot-wiring dynein-2 establishes roles for IFT-A in retrograde train assembly and motility. *Cell Rep,* 42**,** 113337.

GONCALVES, J. & PELLETIER, L. 2017. The Ciliary Transition Zone: Finding the Pieces and Assembling the Gate. *Mol Cells,* 40**,** 243-253.

HALL, D. H. & RUSSELL, R. L. 1991. The posterior nervous system of the nematode Caenorhabditis elegans: serial reconstruction of identified neurons and complete pattern of synaptic interactions. *J Neurosci,* 11**,** 1-22.

HAN, Y. G., KWOK, B. H. & KERNAN, M. J. 2003. Intraflagellar transport is required in Drosophila to differentiate sensory cilia but not sperm. *Curr Biol,* 13**,** 1679-86.

HESKETH, S. J., MUKHOPADHYAY, A. G., NAKAMURA, D., TOROPOVA, K. & ROBERTS, A. J. 2022. IFT-A structure reveals carriages for membrane protein transport into cilia. *Cell,* 185**,** 4971-4985 e16.

HIYAMIZU, S., QIU, H., VUOLO, L., STEVENSON, N. L., SHAK, C., HEESOM, K. J., HAMADA, Y., TSURUMI, Y., CHIBA, S., KATOH, Y., STEPHENS, D. J. & NAKAYAMA, K. 2023. Multiple interactions of the dynein-2 complex with the IFT-B complex are required for effective intraflagellar transport. *J Cell Sci,* 136.

HOUDE, C., DICKINSON, R. J., HOUTZAGER, V. M., CULLUM, R., MONTPETIT, R., METZLER, M., SIMPSON, E. M., ROY, S., HAYDEN, M. R., HOODLESS, P. A. & NICHOLSON, D. W. 2006. Hippi is essential for node cilia assembly and Sonic hedgehog signaling. *Dev Biol,* 300**,** 523-33.

INGLIS, P. N., OU, G., LEROUX, M. R. & SCHOLEY, J. M. 2007. The sensory cilia of Caenorhabditis elegans. *WormBook***,** 1-22.

IOMINI, C., BABAEV-KHAIMOV, V., SASSAROLI, M. & PIPERNO, G. 2001. Protein particles in Chlamydomonas flagella undergo a transport cycle consisting of four phases. *J Cell Biol,* 153**,** 13-24.

ISHIKAWA, H. & MARSHALL, W. F. 2011. Ciliogenesis: building the cell's antenna. *Nat Rev Mol Cell Biol,* 12**,** 222-34.

JANA, S. C., MENDONCA, S., MACHADO, P., WERNER, S., ROCHA, J., PEREIRA, A., MAIATO, H. & BETTENCOURT-DIAS, M. 2018. Differential regulation of transition zone and centriole proteins contributes to ciliary base diversity. *Nat Cell Biol,* 20**,** 928-941.

JENSEN, V. L., LI, C., BOWIE, R. V., CLARKE, L., MOHAN, S., BLACQUE, O. E. & LEROUX, M. R. 2015. Formation of the transition zone by Mks5/Rpgrip1L establishes a ciliary zone of exclusion (CIZE) that compartmentalises ciliary signalling proteins and controls PIP2 ciliary abundance. *EMBO J,* 34**,** 2537-56.

JORDAN, M. A., DIENER, D. R., STEPANEK, L. & PIGINO, G. 2018. The cryo-EM structure of intraflagellar transport trains reveals how dynein is inactivated to ensure unidirectional anterograde movement in cilia. *Nat Cell Biol,* 20**,** 1250-1255.

KATOH, Y., MICHISAKA, S., NOZAKI, S., FUNABASHI, T., HIRANO, T., TAKEI, R. & NAKAYAMA, K. 2017. Practical method for targeted disruption of cilia-related genes by using CRISPR/Cas9-mediated, homology-independent knock-in system. *Mol Biol Cell,* 28**,** 898-906.

KATOH, Y., TERADA, M., NISHIJIMA, Y., TAKEI, R., NOZAKI, S., HAMADA, H. & NAKAYAMA, K. 2016. Overall Architecture of the Intraflagellar Transport (IFT)-B Complex Containing Cluap1/IFT38 as an Essential Component of the IFT-B Peripheral Subcomplex. *J Biol Chem,* 291**,** 10962-75.

KOZMINSKI, K. G., JOHNSON, K. A., FORSCHER, P. & ROSENBAUM, J. L. 1993. A motility in the eukaryotic flagellum unrelated to flagellar beating. *Proc Natl Acad Sci U S A,* 90**,** 5519-23.

KUBO, T., BROWN, J. M., BELLVE, K., CRAIGE, B., CRAFT, J. M., FOGARTY, K., LECHTRECK, K. F. & WITMAN, G. B. 2016. Together, the IFT81 and IFT74 N-termini form the main module for intraflagellar transport of tubulin. *J Cell Sci,* 129**,** 2106-19.

LACEY, S. E., FOSTER, H. E. & PIGINO, G. 2023. The molecular structure of IFT-A and IFT-B in anterograde intraflagellar transport trains. *Nat Struct Mol Biol,* 30**,** 584-593.

LANE, N. 2015. The unseen world: reflections on Leeuwenhoek (1677) 'Concerning little animals'. *Philos Trans R Soc Lond B Biol Sci,* 370.

LI, C., JENSEN, V. L., PARK, K., KENNEDY, J., GARCIA-GONZALO, F. R., ROMANI, M., DE MORI, R., BRUEL, A. L., GAILLARD, D., DORAY, B., LOPEZ, E., RIVIERE, J.

B., FAIVRE, L., THAUVIN-ROBINET, C., REITER, J. F., BLACQUE, O. E., VALENTE, E. M. & LEROUX, M. R. 2016. MKS5 and CEP290 Dependent Assembly Pathway of the Ciliary Transition Zone. *PLoS Biol,* 14**,** e1002416.

LI, W., YI, P., ZHU, Z., ZHANG, X., LI, W. & OU, G. 2017. Centriole translocation and degeneration during ciliogenesis in Caenorhabditis elegans neurons. *EMBO J,* 36**,** 2553-2566.

LOKTEV, A. V. & JACKSON, P. K. 2013. Neuropeptide Y family receptors traffic via the Bardet-Biedl syndrome pathway to signal in neuronal primary cilia. *Cell Rep,* 5**,** 1316-29.

MIJALKOVIC, J., PREVO, B., OSWALD, F., MANGEOL, P. & PETERMAN, E. J. 2017. Ensemble and single-molecule dynamics of IFT dynein in Caenorhabditis elegans cilia. *Nat Commun,* 8**,** 14591.

MIKAMI, A., TYNAN, S. H., HAMA, T., LUBY-PHELPS, K., SAITO, T., CRANDALL, J. E., BESHARSE, J. C. & VALLEE, R. B. 2002. Molecular structure of cytoplasmic dynein 2 and its distribution in neuronal and ciliated cells. *J Cell Sci,* 115**,** 4801-8.

MITCHISON, H. M. & VALENTE, E. M. 2017. Motile and non-motile cilia in human pathology: from function to phenotypes. *J Pathol,* 241**,** 294-309.

MOHAMED, M. A. A., STEPP, W. L. & OKTEN, Z. 2018. Reconstitution reveals motor activation for intraflagellar transport. *Nature,* 557**,** 387-391.

MUKHOPADHYAY, S., WEN, X., CHIH, B., NELSON, C. D., LANE, W. S., SCALES, S. J. & JACKSON, P. K. 2010. TULP3 bridges the IFT-A complex and membrane phosphoinositides to promote trafficking of G protein-coupled receptors into primary cilia. *Genes Dev,* 24**,** 2180-93.

MUKHOPADHYAY, S., WEN, X., RATTI, N., LOKTEV, A., RANGELL, L., SCALES, S. J. & JACKSON, P. K. 2013. The ciliary G-protein-coupled receptor Gpr161 negatively regulates the Sonic hedgehog pathway via cAMP signaling. *Cell,* 152**,** 210-23.

MUL, W., MITRA, A. & PETERMAN, E. J. G. 2022. Mechanisms of Regulation in Intraflagellar Transport. *Cells,* 11.

NAKAYAMA, K. & KATOH, Y. 2018. Ciliary protein trafficking mediated by IFT and BBSome complexes with the aid of kinesin-2 and dynein-2 motors. *J Biochem,* 163**,** 155-164.

NAKAYAMA, K. & KATOH, Y. 2020. Architecture of the IFT ciliary trafficking machinery and interplay between its components. *Crit Rev Biochem Mol Biol,* 55**,** 179-196.

NELSON, G. A., ROBERTS, T. M. & WARD, S. 1982. Caenorhabditis elegans spermatozoan locomotion: amoeboid movement with almost no actin. *J Cell Biol,* 92**,** 121-31.

OU, G., BLACQUE, O. E., SNOW, J. J., LEROUX, M. R. & SCHOLEY, J. M. 2005. Functional coordination of intraflagellar transport motors. *Nature,* 436**,** 583-7.

PARK, K. & LEROUX, M. R. 2022. Composition, organization and mechanisms of the transition zone, a gate for the cilium. *EMBO Rep,* 23**,** e55420.

PATEL-KING, R. S., GILBERTI, R. M., HOM, E. F. & KING, S. M. 2013. WD60/FAP163 is a dynein intermediate chain required for retrograde intraflagellar transport in cilia. *Mol Biol Cell,* 24**,** 2668-77.

PIPERNO, G., SIUDA, E., HENDERSON, S., SEGIL, M., VAANANEN, H. & SASSAROLI, M. 1998. Distinct mutants of retrograde intraflagellar transport (IFT) share similar morphological and molecular defects. *J Cell Biol,* 143**,** 1591-601.

QUIDWAI, T., WANG, J., HALL, E. A., PETRIMAN, N. A., LENG, W., KIESEL, P., WELLS, J. N., MURPHY, L. C., KEIGHREN, M. A., MARSH, J. A., LORENTZEN, E., PIGINO, G. & MILL, P. 2021. A WDR35-dependent coat protein complex transports ciliary membrane cargo vesicles to cilia. *Elife,* 10.

ROMPOLAS, P., PEDERSEN, L. B., PATEL-KING, R. S. & KING, S. M. 2007. Chlamydomonas FAP133 is a dynein intermediate chain associated with the retrograde intraflagellar transport motor. *J Cell Sci,* 120**,** 3653-65.

SARPAL, R., TODI, S. V., SIVAN-LOUKIANOVA, E., SHIROLIKAR, S., SUBRAMANIAN, N., RAFF, E. C., ERICKSON, J. W., RAY, K. & EBERL, D. F. 2003. Drosophila KAP interacts with the kinesin II motor subunit KLP64D to assemble chordotonal sensory cilia, but not sperm tails. *Curr Biol,* 13**,** 1687-96.

SCHOUTEDEN, C., SERWAS, D., PALFY, M. & DAMMERMANN, A. 2015. The ciliary transition zone functions in cell adhesion but is dispensable for axoneme assembly in C. elegans. *J Cell Biol,* 210**,** 35-44.

SINDEN, R. E., CANNING, E. U. & SPAIN, B. 1976. Gametogenesis and fertilization in Plasmodium yoelii nigeriensis: a transmission electron microscope study. *Proc R Soc Lond B Biol Sci,* 193**,** 55-76.

SNOW, J. J., OU, G., GUNNARSON, A. L., WALKER, M. R., ZHOU, H. M., BRUST-MASCHER, I. & SCHOLEY, J. M. 2004. Two anterograde intraflagellar transport motors cooperate to build sensory cilia on C. elegans neurons. *Nat Cell Biol,* 6**,** 1109-13.

SUN, X., HALEY, J., BULGAKOV, O. V., CAI, X., MCGINNIS, J. & LI, T. 2012. Tubby is required for trafficking G protein-coupled receptors to neuronal cilia. *Cilia,* 1**,** 21.

SWOBODA, P., ADLER, H. T. & THOMAS, J. H. 2000. The RFX-type transcription factor DAF-19 regulates sensory neuron cilium formation in C. elegans. *Mol Cell,* 5**,** 411-21.

TOROPOVA, K., MLADENOV, M. & ROBERTS, A. J. 2017. Intraflagellar transport dynein is autoinhibited by trapping of its mechanical and track-binding elements. *Nat Struct Mol Biol,* 24**,** 461-468.

TOROPOVA, K., ZALYTE, R., MUKHOPADHYAY, A. G., MLADENOV, M., CARTER, A. P. & ROBERTS, A. J. 2019. Structure of the dynein-2 complex and its assembly with intraflagellar transport trains. *Nat Struct Mol Biol,* 26**,** 823-829.

WEBB, S., MUKHOPADHYAY, A. G. & ROBERTS, A. J. 2020. Intraflagellar transport trains and motors: Insights from structure. *Semin Cell Dev Biol,* 107**,** 82-90.

WEI, Q., ZHANG, Y., LI, Y., ZHANG, Q., LING, K. & HU, J. 2012. The BBSome controls IFT assembly and turnaround in cilia. *Nat Cell Biol,* 14**,** 950-7.

WHITE, J. G., SOUTHGATE, E., THOMSON, J. N. & BRENNER, S. 1986. The structure of the nervous system of the nematode Caenorhabditis elegans. *Philos Trans R Soc Lond B Biol Sci,* 314**,** 1-340.

WILLIAMS, C. L., LI, C., KIDA, K., INGLIS, P. N., MOHAN, S., SEMENEC, L., BIALAS, N. J., STUPAY, R. M., CHEN, N., BLACQUE, O. E., YODER, B. K. & LEROUX, M. R. 2011. MKS and NPHP modules cooperate to establish basal body/transition zone membrane associations and ciliary gate function during ciliogenesis. *J Cell Biol,* 192**,** 1023-41.

YE, F., NAGER, A. R. & NACHURY, M. V. 2018. BBSome trains remove activated GPCRs from cilia by enabling passage through the transition zone. *J Cell Biol,* 217**,** 1847-1868.

YI, P., LI, W. J., DONG, M. Q. & OU, G. 2017. Dynein-Driven Retrograde Intraflagellar Transport Is Triphasic in C. elegans Sensory Cilia. *Curr Biol,* 27**,** 1448-1461 e7.

ZHANG, K., FOSTER, H. E., RONDELET, A., LACEY, S. E., BAHI-BUISSON, N., BIRD, A. W. & CARTER, A. P. 2017. Cryo-EM Reveals How Human Cytoplasmic Dynein Is Auto-inhibited and Activated. *Cell,* 169**,** 1303-1314 e18.

ZHU, X., WANG, J., LI, S., LECHTRECK, K. & PAN, J. 2021. IFT54 directly interacts with kinesin-II and IFT dynein to regulate anterograde intraflagellar transport. *EMBO J,* 40**,** e105781.

ZOU, W., CHENG, H., LI, S., YUE, X., XUE, Y., CHEN, S. & KANG, L. 2017. Polymodal Responses in C. elegans Phasmid Neurons Rely on Multiple Intracellular and Intercellular Signaling Pathways. *Sci Rep,* 7**,** 42295.

CHAPTER II – WDR60-mediated dynein-2 loading into cilia powers retrograde IFT and transition zone crossing

This chapter was adapted from **Article 1** ("WDR60-mediated dynein-2 loading into cilia powers retrograde IFT and transition zone crossing"). The integral publication is in "Annex I". I generated the *wdr-60* knock-in and deletion mutants, and performed the biochemical analyses of their transcripts, and I actively contributed to the crossing of *C. elegans* strains, worm imaging, quantification analyses, and writing of the article.

2.1. Introduction

Dynein-2 is a giant (>1 MDa) motor protein complex composed of heavy chains (HCs), intermediate chains (ICs), light intermediate chains (LICs), and light chains (LCs) (Toropova et al., 2019). Recent work analyzing the effects of depleting or disrupting the WDR60/WDR34 ICs in human cells has yielded inconsistent results, particularly regarding the requirement of WDR60 for ciliogenesis and cilia axoneme length control (Asante et al., 2014, Hamada et al., 2018, McInerney-Leo et al., 2013, Vuolo et al., 2018). Importantly, the impact of WDR60 loss on dynein-2 activity and dynamics during IFT has not been determined. This in part is due to the difficulty in visualizing and quantifying IFT kinetics of dynein-2 subunits (especially of DHC2) inside cilia of cultured cells (Hamada et al., 2018, Vuolo et al., 2018, Taylor et al., 2015).

Although most dynein-2 core subunits have been identified in *C. elegans*, clear homologues of WDR34 and WDR60 have remained unknown (Vuolo et al., 2020, Hou and Witman, 2015). Here, we identify the *C. elegans* WDR60 homologue, WDR-60, and dissect its contribution to ciliary recruitment of dynein-2 subunits, retrograde IFT, and cilia-mediated behavior. Using CRISPR/Cas9-mediated genome editing, we tagged endogenous WDR-60 with GFP and tracked its dynamics during IFT in cilia of sensory neurons. In addition, we generated a strain expressing an SRPS (short rib polydactyly syndrome) patient-equivalent WDR-60 truncation (McInerney-Leo et al., 2013) that lacks the DHC2-binding β-propeller domain (Toropova et al., 2019), and compared this mutant with a *wdr-60(null)* mutant. We show that WDR-60 is mostly dispensable for axoneme extension but is required for efficient loading of dynein-2 onto anterograde IFT trains, for reaching maximum retrograde IFT velocity, and for dynein-2 crossing of the TZ to exit cilia. By targeting specific TZ components, we were able to facilitate dynein-2 exit from WDR-60–deficient cilia, showing that dynein-2 is unable to overcome the resistance offered by the TZ barrier in the absence of WDR-60.

2.2. Results

2.2.1. WDR-60 is recruited to cilia in *C. elegans* sensory neurons and undergoes IFT with kinetics similar to those of dynein-2 HC

We set out to identify the gene encoding the so-far uncharacterized homologue of WDR60 in *C. elegans* (Hou and Witman, 2015, Vuolo et al., 2020). Through protein sequence alignments, we found that the *C27F2.1* gene in *C. elegans* encodes the protein with the highest sequence homology to human WDR60. Interestingly, *C27F2.1* (hereafter referred to as *wdr-60*) was one of the early candidate genes identified in a screen for transcripts specific for ciliated sensory neurons (Blacque et al., 2005). Like genes encoding for other dynein-2 subunits (Swoboda et al., 2000), *wdr-60* contains a predicted X-box sequence **(Figure 1)**, which is a target of the regulatory factor X (RFX)-like transcription factor DAF-19 (Blacque et al., 2005).

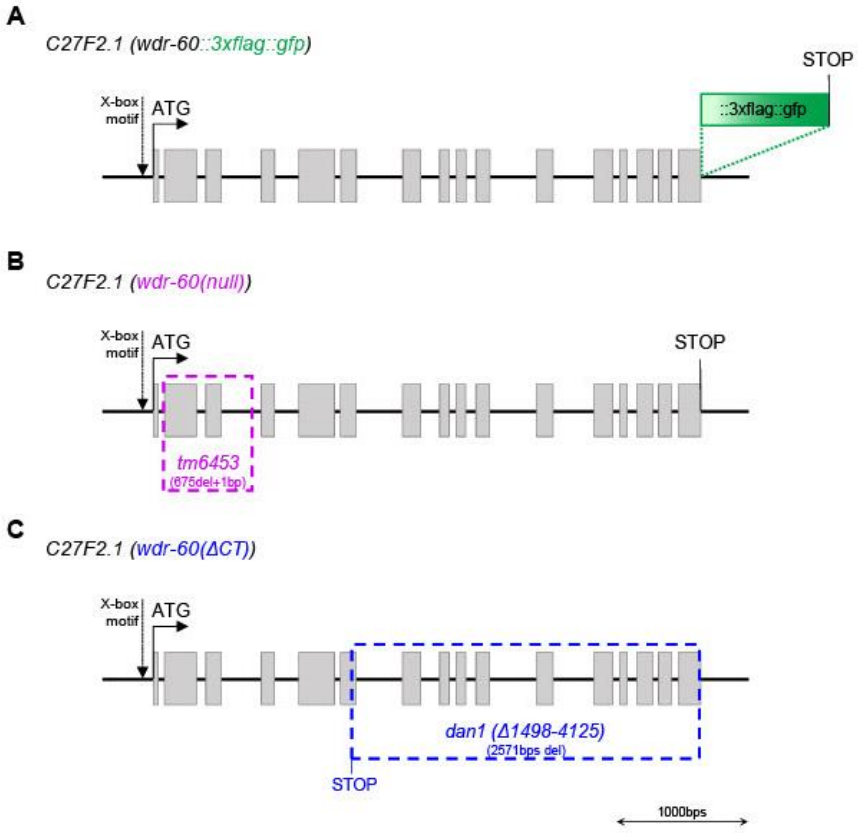

Figure 1 - Schematic of the *C27F2.1* locus organization in the *C. elegans* genome. Predicted *wdr-60* exons (in gray boxes), including the start and stop codons, and the X-box motif according to (Blacque et al., 2005). **(A)** Knock-in insertion of the *::3xflag::gfp* sequence at the 3′ end of the *wdr-60* genomic sequence (in-frame with the WDR-60 coding sequence). **(B)** Representation of the *wdr-60(tm6453)* null allele. **(C)** Representation of the *wdr-60(ΔCT)* allele (also named *dan1(Δ1498-4125)*) corresponding to a WDR-60 truncation of the C-terminal β-propeller domain (Δ288–668 aa).

To directly visualize and analyze the dynamics of the protein encoded by *wdr-60*, we used genome editing to introduce the coding sequence for a 3xFLAG::GFP tag at the endogenous *wdr-60* locus **(Figure 1A)**. Similar to what has been described for dynein-2 LIC and HC (Wicks et al., 2000, Schafer et al., 2003), we found that WDR-60 expression is restricted to ciliated sensory neurons. To better define the tissue-specific expression of WDR-60, we performed the classic dye filling assay that takes advantage of a lipophilic fluorescent dye (DiI) that is specifically incorporated into ciliated sensory neurons that have their cilia in contact with the environment. As a control, we used a GFP knock-in strain of dynein-2 HC, GFP::CHE-3 (Yi et al., 2017). We found that the expression pattern of WDR-60::3xFLAG::GFP is identical to that of GFP::CHE-3 and perfectly matches the neurons that take up dye **(Figure 2A)**. While a large part of the signal is detected in the soma and dendrites of these neurons, WDR-60 is also found inside cilia, similar to what has been observed for GFP::CHE-3 (Yi et al., 2017).

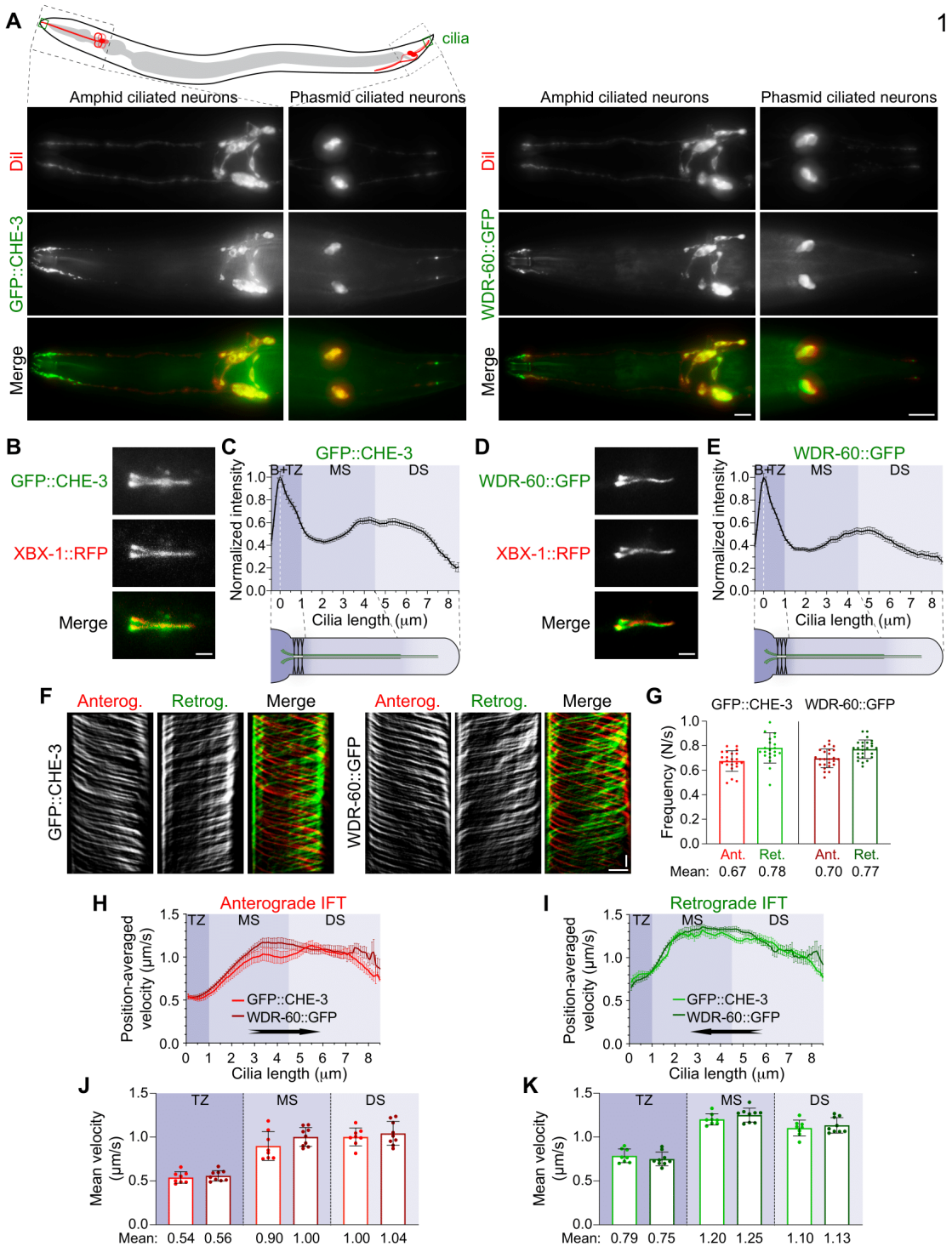

Figure 2 - WDR-60 expression is restricted to ciliated sensory neurons, where it has distribution and IFT kinetics similar to those of dynein-2 HC. (A) Endogenously tagged WDR-60::3xFLAG::GFP is expressed in the same ciliated neurons that express dynein-2 HC (GFP::CHE-3). These are the same neurons that incorporate the DiI lipophilic dye. The top illustration shows the relative localization of amphid and phasmid ciliated neurons in *C. elegans*. **(B)** Phasmid cilia coexpressing GFP::CHE-3 and XBX-1::RFP. **(C)** Quantification of GFP::CHE-3 signal intensity along cilia (n = 109 cilia). **(D)** Phasmid cilia coexpressing WDR-60::3xFLAG::GFP and XBX-1::RFP. **(E)** Quantification of WDR-60::3xFLAG::GFP signal intensity along cilia (n = 101 cilia). **(F)** Cilium

kymographs of GFP::CHE-3 and WDR-60::3xFLAG::GFP. Single and merge channels for particles moving anterogradely and retrogradely are shown. **(G)** Mean IFT frequency of anterogradely and retrogradely moving GFP::CHE-3 and WDR-60::3xFLAG::GFP particles per second (n ≥ 22 cilia). **(H and I)** Anterograde and retrograde velocities of GFP::CHE-3 and WDR-60::3xFLAG::GFP particles along cilia. **(J and K)** Mean velocities for each cilium subcompartment (n ≥ 430 particle traces were analyzed in ≥ 8 cilia). B, cilium base; TZ, transition zone; MS, middle segment; DS, distal segment. XY velocity and intensity distribution graphs are shown as mean ± SEM, and graphs in columns are shown as mean ± SD. Student' t test was used to analyze the datasets in **G**, **J**, and **K**. Scale bars: 10 μm (**A**); 2 μm (**B** and **D**); vertical 5 s, horizontal 2 μm (**F**).

When analyzing WDR-60::GFP ciliary distribution in more detail, we found that WDR-60 is particularly enriched at the ciliary base, as is the case for GFP::CHE-3 **(Figure 2B–E)**. Furthermore, both subunits colocalize with dynein-2 LIC, XBX-1::RFP (Yi et al., 2017). Next, we performed time-lapse imaging to gain insight into WDR-60 dynamics (Video 1 in (De-Castro et al., 2022)). We found that both anterograde and retrograde frequencies **(Figure 2F and 2G)** and velocities **(Figure 2H–K)** of WDR-60::GFP particles match those of GFP::CHE-3. Furthermore, retrograde WDR-60::GFP motility follows a triphasic model **(Figure 2I and 2K)**, as previously reported for GFP::CHE-3 (Yi et al., 2017). Together, these data strongly support that *C27F2.1*/*wdr-60* encodes for the *C. elegans* WDR60 homologue, which undergoes IFT with kinetics that resemble those of dynein-2 HC.

2.2.2. The β-propeller domain is important but not essential for WDR-60 incorporation into cilia

To determine the importance of WDR-60 for dynein-2–mediated IFT and cilia assembly, we first characterized WDR-60 levels and distribution in two distinct *wdr-60* mutants. We took advantage of the available *wdr-60* deletion allele *tm6453* **(Figure 1B)**, a null mutation, and we engineered a *wdr-60* allele that produces a truncated form of WDR-60 specifically lacking the CT β-propeller domain (ΔCT) **(Figures 1C and 3A)**, required for dynein-2 HC binding (Toropova et al., 2019). The *wdr-60(ΔCT)* mutant mimics a truncating mutation found in a short rib polydactyly syndrome (SRPS) patient (WDR60: c.1891C>T; p.Q631*) (McInerney-Leo et al., 2013).

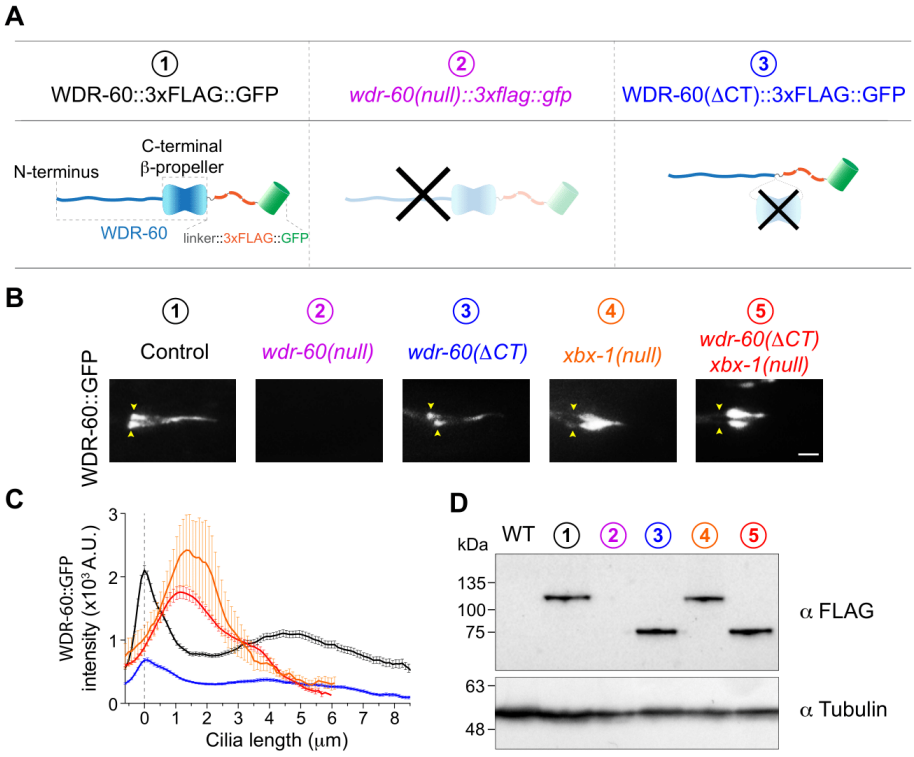

Figure 3 - Truncation of the β-propeller domain reduces, but does not abolish, entry of WDR-60 into cilia. (A) Schematic representation of WDR-60 tagging with 3xFLAG::GFP in control, *wdr-60(tm6453)* null, and truncated *wdr-60* knock-in strains: (1) full-length WDR-60, composed of an NT disordered region and a CT β-propeller domain; (2) *wdr-60(tm6453)*, predicted to be a null mutant; (3) *wdr-60(ΔCT)*, expected to produce a protein composed of the WDR-60 NT fused to the 3xFLAG::GFP tag (lacking the β-propeller). **(B)** Phasmid cilia of each *wdr-60* knock-in strain as indicated. Yellow arrowheads indicate the ciliary base. Note that no GFP signal is detected in the *wdr-60(tm6453)::3xflag::gfp* strain. Scale bar: 2 μm. **(C)** Quantification of GFP signal intensity distribution along the cilium in *wdr-60* mutants shown in B (n ≥ 55 cilia). Graph is shown as mean ± SEM. **(D)** Western blot of extracts from wild-type and *wdr-60* knock-in strains using an anti-FLAG antibody. The predicted sizes are 105.6 kDa for WDR-60::3xFLAG::GFP and 63.2 kDa for WDR-60(ΔCT)::3xFLAG::GFP truncation. No signal is detected in *wdr-60(tm6453)::3xflag::gfp* extracts, demonstrating that this is indeed a null strain. α-Tubulin was used as a loading control.

As endogenous labeling of WDR-60 did not alter IFT kinetics **(Figure 2G–K)**, we inserted the same 3xFLAG::GFP tag sequence in-frame with the 3′ end of both *wdr-60* mutants **(Figures 1A and 3A)**. Together with the dye-filling assay, this allowed us to analyze the overall integrity of cilia while comparing the neuronal localization and relative levels of WDR-60 in wild-type and in each mutant **(Figure 4A and 4B)**. Interestingly, and in contrast to the null *xbx-1(ok279)* LIC mutant, both *wdr-60* mutants had all ciliated sensory neurons stained with DiI, suggesting that sensory cilia can form and take up dye. No GFP signal was

detectable in sensory neurons or in cilia of the *wdr-60(tm6453)* mutant, indicating that no WDR-60 is produced in this strain. In contrast, the GFP signal in neurons of the *wdr-60(ΔCT)* mutant was readily visible and overlapped with the neuronal pattern of the dye **(Figures 4A, 4B and 3B)**. Interestingly, the ciliary signal of WDR-60(ΔCT)::GFP was overall weaker than in controls (approximately threefold reduction) **(Figure 3C)** but showed a similar distribution profile along the axoneme, suggesting that a fraction of WDR-60(ΔCT) is able to enter cilia and undergo IFT. Strikingly, although dynein-2 LIC stabilizes the HC (Blisnick et al., 2014, Hou et al., 2004, Taylor et al., 2015, Reck et al., 2016) and contributes to ciliary entry of dynein-2 by directly interacting with IFT-B (Zhu et al., 2021), XBX-1 loss did not significantly affect the ciliary recruitment of WDR-60::GFP or WDR-60(ΔCT)::GFP **(Figure 3B and 3C)**. However, it did lead to the accumulation of both forms of WDR-60 inside cilia, likely due to the complete block of retrograde IFT that occurs in the *xbx-1(null)* mutant (Yi et al., 2017, Schafer et al., 2003). We conclude that WDR-60 can be recruited to cilia independently of dynein-2 LIC and HC subunits.

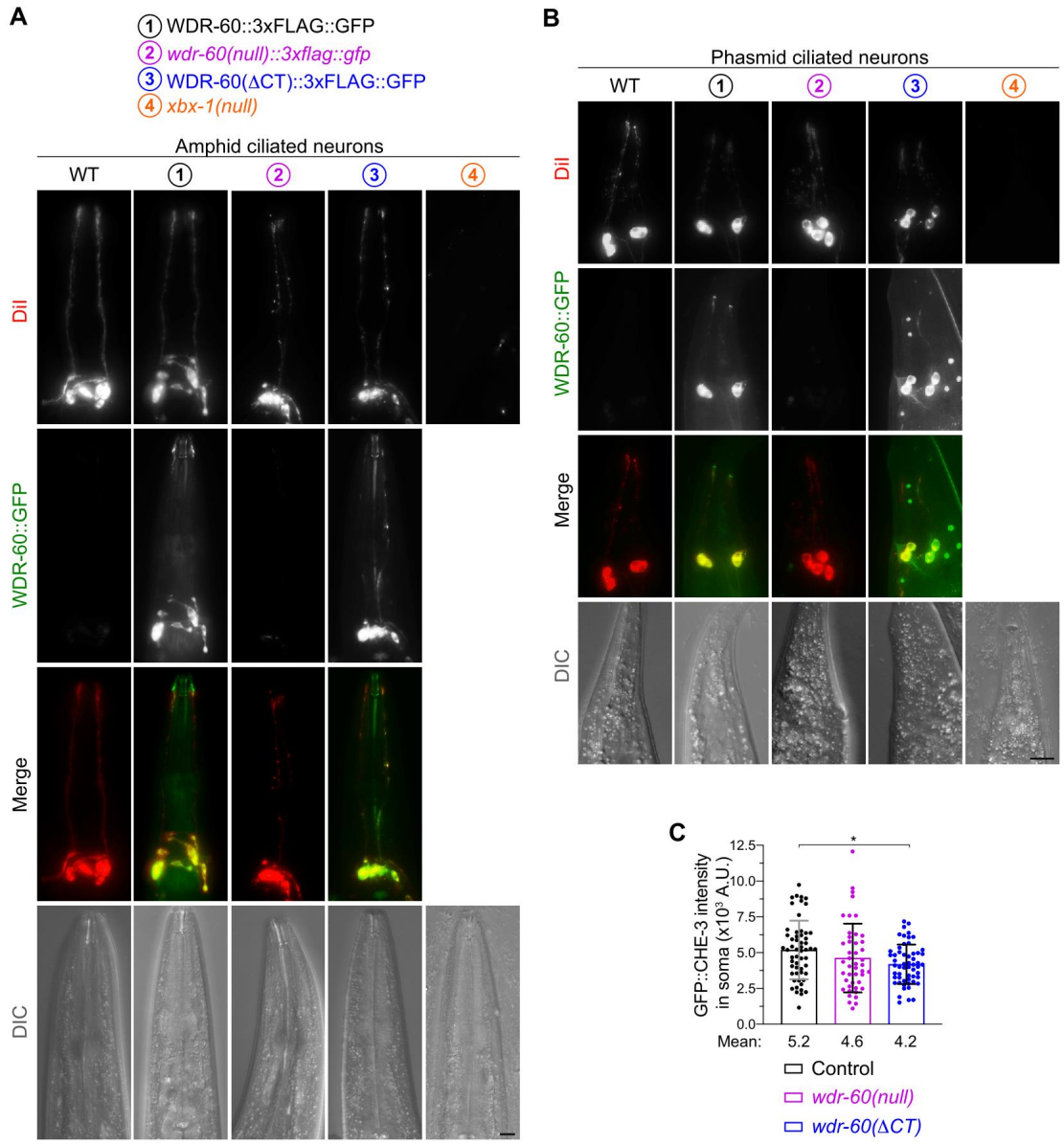

Figure 4 - WDR-60::3xFLAG::GFP expression is restricted to ciliated sensory neurons. (A and B) Endogenously tagged WDR-60::3xFLAG::GFP and WDR-60(ΔCT)::3xFLAG::GFP are expressed in the same amphid (**A**) and phasmid (**B**) ciliated neurons that incorporate the DiI lipophilic dye (in red). The *wdr-60(null)::3xflag::gfp* strain has no detectable GFP signal in its neurons; however, they are still able to take up the DiI dye. Scale bars: 10 µm. DIC, differential interference contrast. **(C)** GFP::CHE-3 intensity in soma of phasmid sensory neurons of untagged *wdr-60* mutants (n ≥ 45 somas). Graph is shown as mean ± SD. Kruskal–Wallis test followed by the Dunn's multiple comparison were used to analyze these datasets. *, P ≤ 0.05.

Taking advantage of the 3xFLAG epitope in our tag, we performed immunoblotting to determine whether the reduction in ciliary levels of mutant WDR-60 reflected differences in overall protein levels **(Figure 3D)**. Given that no protein bands were detectable in *wdr-*

60(tm6453) worm extracts, we conclude that this mutant strain is indeed a *wdr-60* null. In contrast, the levels of WDR-60(ΔCT)::GFP were comparable to those of full-length WDR-60::GFP, indicating that the reduced ciliary recruitment of WDR-60(ΔCT)::GFP is due to loss of the β-propeller rather than a down-regulation of protein levels.

2.2.3. Disruption of WDR-60 reduces dynein-2 loading into cilia and the kinetics of retrograde IFT

Loss of the dynein-2 LIC XBX-1 destabilizes the dynein-2 HC CHE-3, completely abolishing its recruitment to cilia, blocking retrograde IFT and, consequently, axoneme extension. The resulting cilia are severely truncated and bulged (Yi et al., 2017, Schafer et al., 2003). To directly assess the impact of WDR-60 disruption on cilia and other dynein-2 subunits, we crossed the *wdr-60* mutants with knock-in strains of GFP::CHE-3/XBX-1::RFP (Yi et al., 2017) and analyzed their ciliary recruitment and distribution. While both *wdr-60* mutants were capable of assembling seemingly normal cilia (with only a minor reduction in length in the *wdr-60(null)* mutant), we observed a strong reduction in the total levels of ciliary GFP::CHE-3 (~40%) **(Figure 5A–C)**. Interestingly, we also found that the remaining pool of WDR-60–deficient dynein-2 accumulated particularly near the ciliary base **(Figure 5D)**. Considering that GFP::CHE-3 levels were not greatly altered in the soma of the ciliated phasmid neurons of *wdr-60* mutants **(Figure 4C)**, these observations suggest that WDR-60 contributes to both recruitment and ciliary distribution of dynein-2.

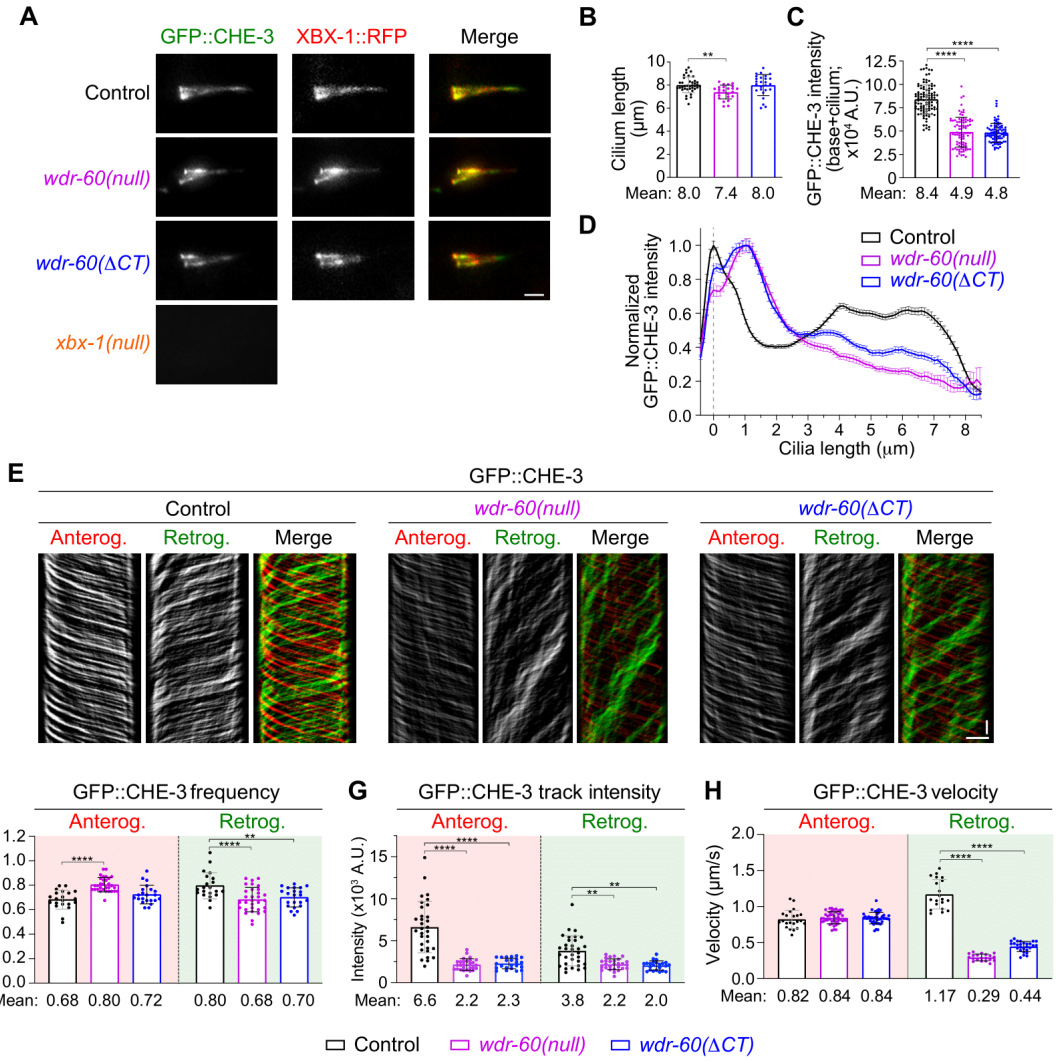

Figure 5 - *wdr-60* mutants have reduced dynein-2 recruitment and incorporation into cilia, accompanied by impaired retrograde IFT. (A) Phasmid cilia coexpressing GFP::CHE-3 and XBX-1::RFP. **(B)** Cilia length in *wdr-60* mutants (n ≥ 24 cilia). **(C and D)** Total signal intensity of GFP::CHE-3 from the base to the tip of cilia (**C**) and relative distribution of GFP::CHE-3 along cilia (**D**; n ≥ 88 cilia). **(E)** GFP::CHE-3 kymographs of phasmid cilia of the indicated strains. Single and merge channels for particles moving anterogradely and retrogradely are shown. **(F)** Frequency of IFT particles detected at the distal segment of cilia (n ≥ 20 cilia). **(G)** Quantification of the average intensity of GFP::CHE-3 particles moving on anterograde and retrograde tracks (n ≥ 345 particle traces were analyzed in ≥ 23 cilia). **(H)** Velocity of anterograde and retrograde GFP::CHE-3 particles in control and *wdr-60* mutants (n ≥ 300 particle traces were analyzed in ≥20 cilia). XY intensity distribution graph is shown as mean ± SEM, and graphs in columns are shown as mean ± SD. One-way ANOVA followed by Dunnett's, Holm–Sidak, and Games–Howell multiple comparison were used to analyze the datasets in **B**, **F**, and **G**, respectively. Kruskal–Wallis test followed by Dunn's multiple comparison were used to analyze the datasets in **C** and **H**. **, P ≤ 0.01; ****, P ≤ 0.0001. Scale bars: 2 μm (**A**); vertical 5 s, horizontal 2 μm (**E**).

To determine when these WDR-60–associated phenotypes start manifesting and whether they vary with aging, we repeated our analysis of GFP::CHE-3 recruitment and distribution in developing and post-adulthood animals. We found that, as early as larval stage 2 in the *wdr-60(null)* mutant, ciliary levels of GFP::CHE-3 were already reduced and its distribution altered, albeit to a lesser degree than in young adults. This suggests that WDR-60–associated dynein-2 phenotypes arise early on and become progressively worse as the mutant animals develop **(Figure 6)**. In addition, we found that the abnormal distribution of GFP::CHE-3 does not significantly change with age in *wdr-60(null)* animals (7 and 18 days after adulthood) **(Figure 6C–H)**, suggesting that there is no age-dependent suppression of these WDR-60–associated phenotypes, in contrast to what has been observed for some IFT mutants (Cornils et al., 2016).

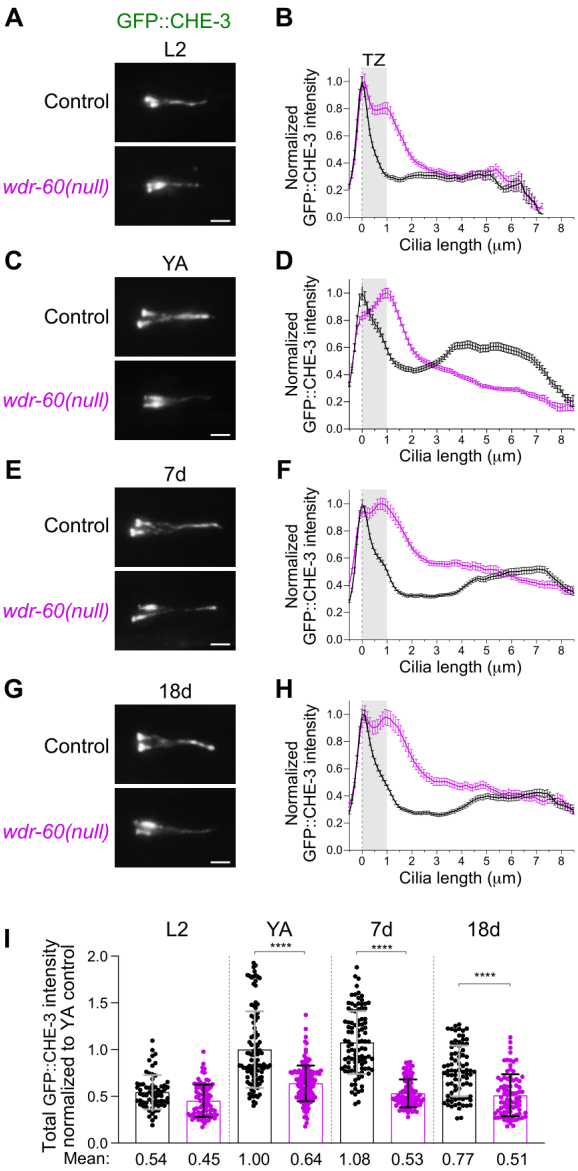

Figure 6 - WDR-60–associated phenotypes become worse as the animals develop to adulthood and do not improve with aging. (A, C, E, and G) GFP::CHE-3-expressing phasmid cilia of wild-type and *wdr-60(null)* mutants at several stages of development and aging. L2, larval stage 2 worms; YA: young adult worms; 7d, worms 7 days after reaching adulthood; 18d, worms 18 days after reaching adulthood. Scale bars: 2 μm. **(B, D, F, and H)** Corresponding distribution of GFP::CHE-3 signal intensity along cilia. Gray rectangles highlight the TZ, as previously defined. n = 77 cilia for **B**, n ≥ 95 cilia for **D**, n ≥ 113 cilia for **F**, and n ≥ 110 cilia for **H**. XY intensity distribution graphs are shown as mean ± SEM. **(I)** Column graph showing GFP::CHE-3 total intensity from the base to the tip of cilia from wild-type and *wdr-60(null)* mutants analyzed in **B**, **C**, **F**, and **H**. Graph is shown as mean ± SD. Mann–Whitney U test was used to analyze these datasets. **, P ≤ 0.01; ****, P ≤ 0.0001.

To gain further insight into the importance of WDR-60 for dynein-2 loading and dynamics inside cilia, we analyzed the IFT kinetics of GFP::CHE-3 by time-lapse imaging **(Figure 5E–H)**. While we found a small increase in the frequency of GFP::CHE-3 particles moving in the anterograde direction in the *wdr-60(null)* mutant, the number of particles in the retrograde direction was significantly reduced in both mutants (∼15%) **(Figure 5F)**. Importantly, we found that both the loss of WDR-60 and the truncation of its β-propeller led to a strong reduction in the average amount of GFP::CHE-3 transported on anterograde tracks (∼67%) **(Figure 5G)**. This establishes a role for WDR-60 in the loading of dynein-2 onto anterograde IFT trains. Consistent with this, we found that the intensity of GFP::CHE-3 moving on retrograde tracks was significantly reduced in both *wdr-60* mutants, suggesting that each retrograde IFT train is being powered by fewer dynein-2 motors. In addition, while the velocity of anterograde trains carrying GFP::CHE-3 remained similar to that of controls, we observed a strong reduction in the velocity of GFP::CHE-3-driven retrograde trains in both *wdr-60* mutants (three- to fourfold) **(Figure 5H)**.

Taken together, these results show that loss of WDR-60 or truncation of its β-propeller reduces the loading of dynein-2 HC onto anterograde IFT trains, and consequently the pool of dynein-2 available at the tip of cilia to power retrograde IFT. In agreement, fewer dynein-2 motors were present in particles moving retrogradely, which may explain the reduced kinetics of retrograde IFT in *wdr-60* mutants and the inability of dynein-2 to fully return to the ciliary base.

2.2.4. WDR-60 is required for efficient recycling of IFT components and contributes to cilia-mediated behavior

To better understand the importance of WDR-60 in IFT, we analyzed fluorescently labeled subunits of the IFT-A/B complexes **(Figure 7)** and anterograde kinesins **(Figure 8A and 8B)**. Measurements of cilia expressing CHE-11::mCherry (*C. elegans* ortholog of IFT140) or IFT-74::GFP confirmed the small but significant decrease in cilium length in the *wdr-60(null)* mutant **(Figure 7A, 7B, 7D, and 7E)**. We note, however, that this minor defect in axoneme extension is distinct from the severely shortened and bulged cilia phenotype caused by XBX-1 loss **(Figure 7A and 7D)**.

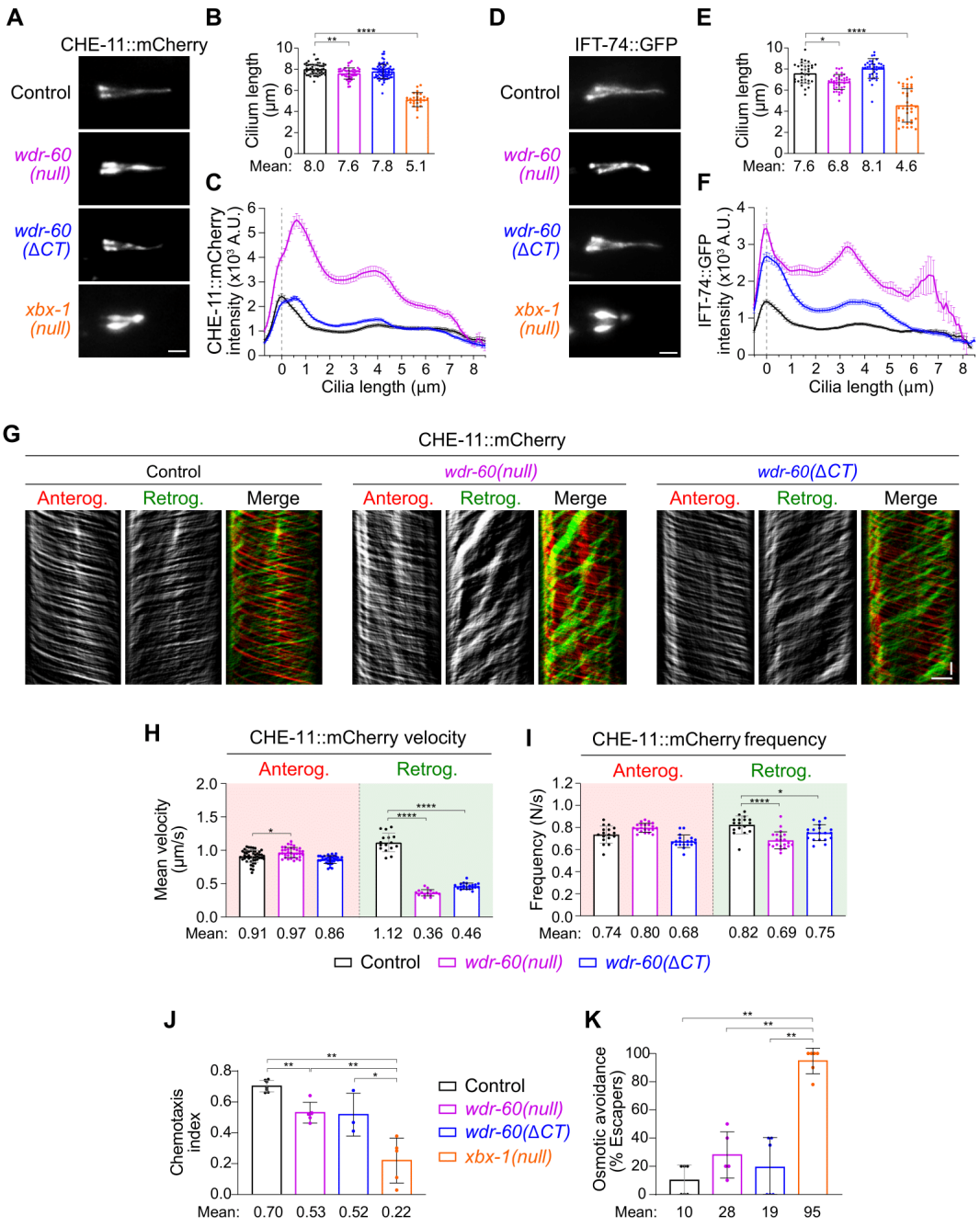

Figure 7 - *wdr-60* mutants have reduced retrograde transport of IFT-A and IFT-B complexes and lower efficiency of cilia-mediated signaling. (A and D) Phasmid cilia from control, *wdr-60(null)*, *wdr-60(ΔCT)*, and *xbx-1(null)* animals expressing CHE-11::mCherry (**A**) or IFT-74::GFP (**D**). **(B and E)** Cilia length measured with CHE-11::mCherry (**B**) or IFT-74::GFP (**E**; n ≥ 26 and n ≥ 34 cilia, respectively). **(C and F)** Quantification of the average intensity of CHE-11::mCherry (**C**) and IFT-74::GFP (**F**) along cilia (n ≥ 42 and n ≥ 66 cilia, respectively). **(G)** CHE-11::mCherry kymographs of phasmid cilia from the indicated strains. **(H)** Mean velocity of CHE-11::mCherry particles moving on anterograde and retrograde tracks (n ≥ 225 particle traces were analyzed in ≥15 cilia). **(I)** Frequency of IFT particles detected at the distal segment of cilia (n ≥ 17 cilia). **(J)** Chemotaxis index for the attractant IA (n ≥ 450 animals tracked over ≥ 3 assays). **(K)** Osmotic avoidance assay to test

whether sensory cilia detect a hypertonic glycerol barrier (n ≥ 20 animals tracked over ≥ 4 assays). The dynein-2 LIC *xbx-1(null)* strain was used for comparison. XY intensity distribution graph is shown as mean ± SEM, and graphs in columns are shown as mean ± SD. One-way ANOVA followed by Tukey's multiple comparison were used to analyze the datasets in **B**, **H**, and **I**. Kruskal–Wallis test followed by Dunn's multiple comparison were used to analyze the datasets in **E**. *, P ≤ 0.05; **, P ≤ 0.01; ****, P ≤ 0.0001. Scale bars: 2 µm (**A** and **D**); vertical 5 s, horizontal 2 µm (**G**).

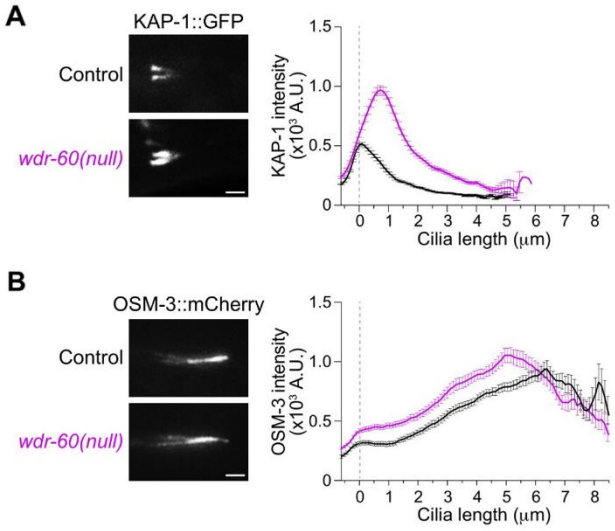

Figure 8 - Loss of WDR-60 results in a severe accumulation of KAP-1 near the base of cilia but only has a modest effect on the distribution of OSM-3. (A) Examples of phasmid cilia from control and *wdr-60(null)* worms expressing KAP-1::GFP and quantification of the signal intensity along cilia (n ≥ 60 cilia for each strain). The intensity of KAP-1::GFP in cilia is significantly increased in the *wdr-60(null)* mutant with particles accumulating near the TZ. **(B)** Examples of phasmid cilia from control and *wdr-60(null)* worms expressing OSM-3::mCherry and quantification of the signal intensity along cilia (n ≥ 88 cilia for each strain). OSM-3::mCherry distribution and intensity along the cilium is only slightly altered in the *wdr-60(null)* mutant. XY intensity distribution graphs are shown as mean ± SEM. Scale bars: 2 µm (**A** and **B**).

When analyzing the ciliary distribution of CHE-11::mCherry, we found that this IFT-A component accumulated predominantly near the ciliary base in both *wdr-60* mutants **(Figure 7A and 7C)**, similar to our observations with GFP::CHE-3. Interestingly, the total levels of CHE-11::mCherry retained inside cilia were substantially higher in the *wdr-60(null)* mutant when compared with the *wdr-60(ΔCT)* mutant.

Consistent with defects in dynein-2 function, we found that the retrograde velocity of CHE-11::mCherry was strongly reduced in both *wdr-60* mutants (approximately threefold) **(Figure**

7G and 7H). In addition, the frequency of CHE-11::mCherry tracks was also significantly reduced in the retrograde direction (~16% lower in *wdr-60(null*) cilia) **(Figure 7I)**.

The IFT-B subunit IFT-74::GFP accumulated at multiple places along cilia in both *wdr-60* mutants **(Figures 7D, 7F, and 8A)**, underscoring the importance of WDR-60 in dynein-2–mediated transport of the IFT-B machinery to the ciliary base. When analyzing the distribution of kinesins, we also observed ciliary accumulations for the kinesin-2-associated protein KAP-1 (KIFAP3) and, to a lesser extent, for the distal segment kinesin OSM-3 (KIF17) **(Figure 8A and 8B)**. Altogether, these results show that loss of WDR-60 greatly impairs removal of IFT components from cilia.

To determine the impact of *wdr-60*–associated IFT defects on ciliary functions, we analyzed cilia-dependent behavior in our mutant strains. We tested chemotaxis attraction to isoamyl alcohol (AI) and osmotic tolerance to high concentrations of glycerol **(Figure 7J and 7K)**. Both *wdr-60* mutants showed modest defects in these assays, contrasting with the *xbx-1(null)* mutant, in which chemotaxis attraction and osmotic tolerance is severely compromised. These results suggest that although WDR-60 plays critical roles in dynein-2–mediated IFT, WDR-60–deficient sensory cilia remain partially functional.

2.2.5. TZ integrity and gating function are maintained in *wdr-60* mutants but not in the *xbx-1* mutant

Given that dynein-2 and IFT-A components were recently shown to be required for maintaining the TZ barrier (Jensen et al., 2018, Scheidel and Blacque, 2018, Vuolo et al., 2018), we investigated whether the integrity and gating capacity of the TZ are affected in *wdr-60* and *xbx-1* mutants. We analyzed the localization of four TZ components: TMEM-107, NPHP-4, MKS-6, and MKSR-1 (Jensen et al., 2018, Lambacher et al., 2016, Prevo et al., 2015, Schouteden et al., 2015, Williams et al., 2011). In agreement with what has been reported for CHE-3 and IFT-A mutants (Scheidel and Blacque, 2018, Jensen et al., 2018), we found that loss of XBX-1 results in ectopic localization of these TZ components along the ciliary axoneme **(Figure 9)**. In contrast, the localization of TZ components in *wdr-60* mutants was indistinguishable from controls **(Figure 9)**, suggesting that loss of WDR-60 does not affect the integrity of the TZ. To directly test the integrity and gating capacity of the TZ in *wdr-60* mutants, we analyzed its ability to block the entry of RPI-2::GFP (RP2), a component of the periciliary membrane compartment (PCMC) restricted to the base of cilia (Jensen et al., 2018). While loss of XBX-1 resulted in abnormal entry of RPI-2::GFP into cilia, no RPI-2::GFP signal was detectable inside cilia in *wdr-60* mutants **(Figure 9C and**

9D). These results show that the loss of WDR-60 does not compromise TZ integrity or its gating function in *C. elegans*. In addition, our results uncover an important role for the dynein-2 LIC XBX-1 in maintaining the TZ barrier, likely by stabilizing CHE-3.

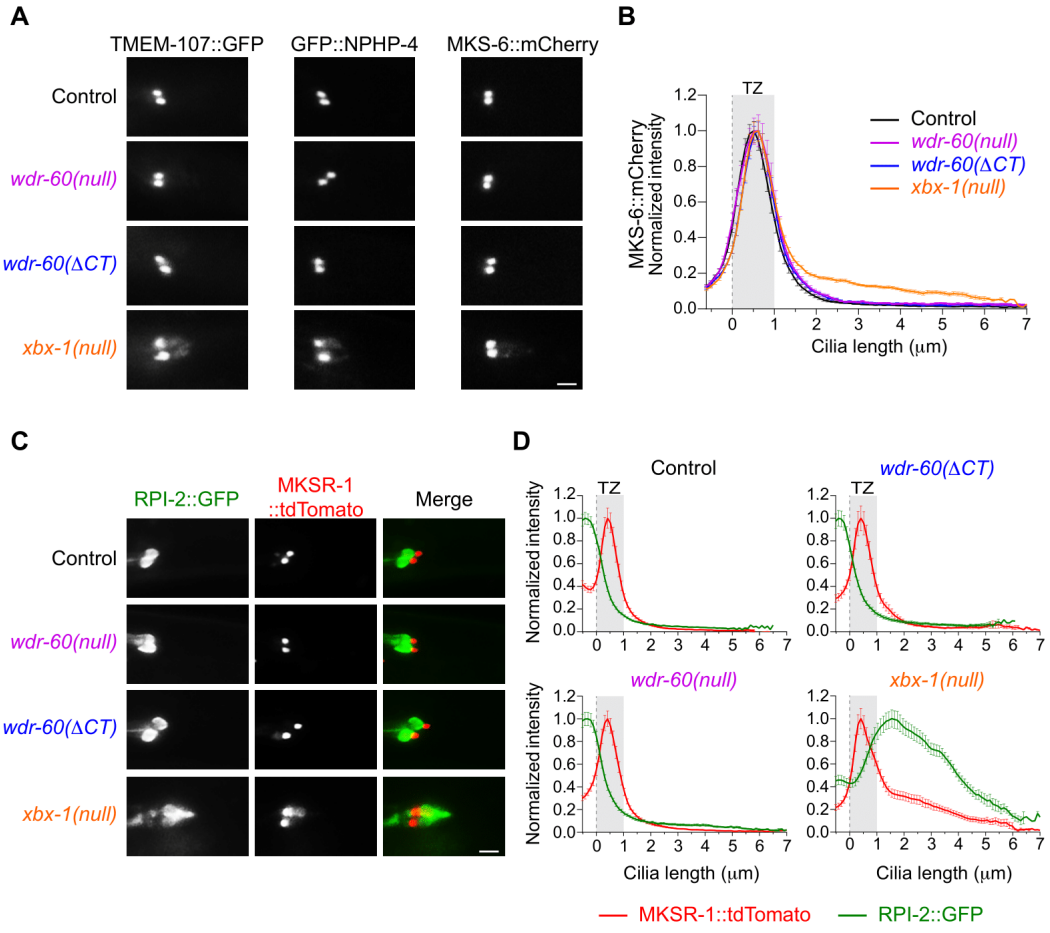

Figure 9 - The integrity and gating function of the TZ are maintained in *wdr-60* mutants but compromised in the *xbx-1* mutant. (A) Analysis of the localization of several components of the MKS (TMEM-107::GFP and MKS-6::mCherry) and NPHP (GFP::NPHP-4) modules of the TZ in phasmid cilia of the indicated strains. **(B)** Quantification of MKS-6::mCherry signal intensity confined at the TZ and dispersed along cilia (n ≥ 38 cilia). **(C)** Relative localization of the nonciliary membrane protein RPI-2::GFP to the TZ (labeled with MKSR-1::tdTomato) in phasmid cilia of the indicated strains. **(D)** Signal overlap between these components and quantification of the amount of RPI-2::GFP leaking into cilia (n ≥ 33 cilia). Gray rectangles highlight the TZ region, defined by MKS-6 and MKSR-1 localization. XY intensity distribution graphs are shown as mean ± SEM. Scale bars: 2 μm.

2.2.6. WDR-60 is required for dynein-2 passage through the TZ to exit cilia

To more precisely determine where the ciliary pool of dynein-2 accumulates in *wdr-60* mutants, we colabeled GFP::CHE-3 with markers specific for the ciliary base (mCherry::HYLS-1) (Schouteden et al., 2015) and for the TZ (MKS-6::mCherry) (Williams et al., 2011). In controls, GFP::CHE-3 mainly accumulates at the ciliary base **(Figure 10A)** before entering cilia through the TZ. In contrast, we found that GFP::CHE-3 accumulates mostly at the distal side of the TZ in both *wdr-60* mutants **(Figure 10B and 10C)**.

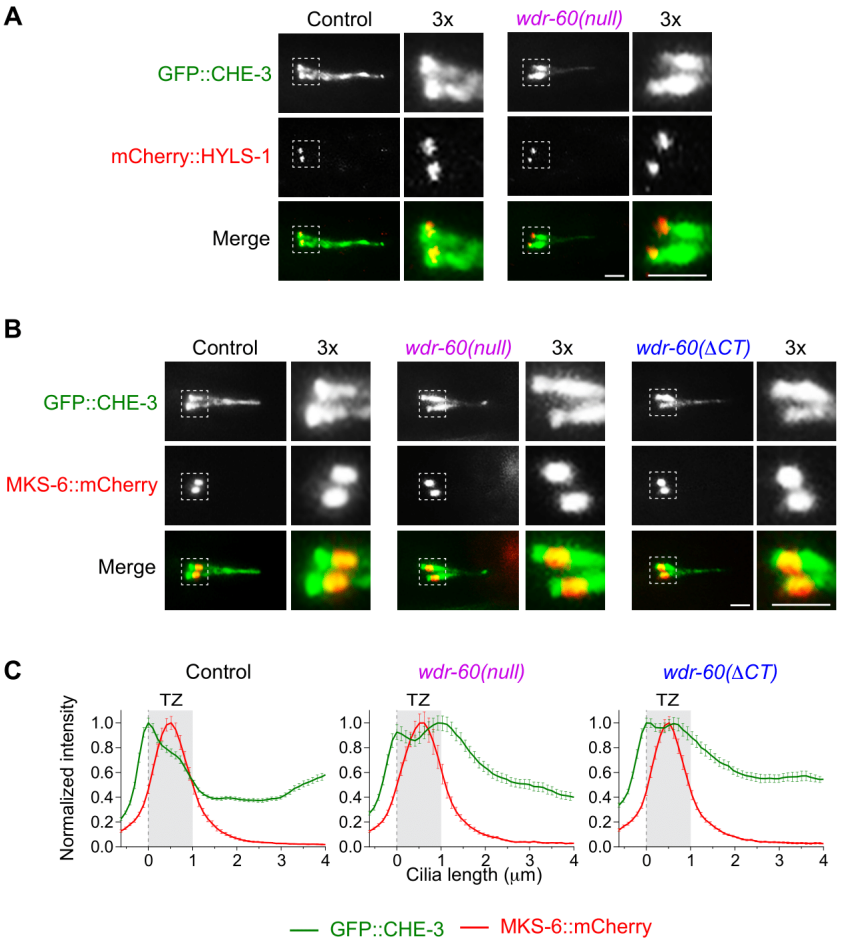

Figure 10 - Dynein-2 accumulates on the distal side of the TZ, unable to complete retrograde IFT in *wdr-60* mutants. (A) GFP::CHE-3 localization relative to the centriolar wall component mCherry::HYLS-1 at the base of phasmid cilia of the indicated strains. **(B)** GFP::CHE-3 localization relative to the MKS-6::mCherry TZ component in phasmid cilia of the indicated strains. **(C)** Quantification GFP::CHE-3 signal distribution in relation to the TZ, as determined by MKS-6 localization (n ≥ 38 cilia). Gray rectangles define the TZ region. 3× magnifications of the square

section in each micrograph were included to better visualize the distribution of the dynein-2 HC relative to the base and TZ of *wdr-60* mutant cilia. Graphs are shown as mean ± SEM. Scale bars: 2 µm.

Recent studies have shown that retrograde trains slow down as they cross the TZ, suggesting that this ciliary gate offers resistance to the passage of retrograde IFT trains (Jensen et al., 2015, Prevo et al., 2015, Oswald et al., 2018). Given that loss of WDR-60 reduces the amount of dynein-2 driving retrograde trains and impairs retrograde IFT velocity **(Figure 5)**, we hypothesized that WDR-60–deficient retrograde trains may not be able to generate enough force to push through the TZ barrier, and are consequently unable to exit cilia. As removal of MKS-5 (RPGRIP1L), a key component for the assembly of all TZ structures, significantly increases the velocity of IFT trains moving in the TZ region (Jensen et al., 2015), we reasoned that the exit of WDR-60–deficient dynein-2 from cilia might be facilitated by disrupting MKS-5. In agreement, we found that GFP::CHE-3 no longer accumulated on the distal side of the TZ in the *mks-5(tm3100)*;*wdr-60(null)* double mutant **(Figure 11A-D)**. Instead, the GFP::CHE-3 distribution profile in this mutant was similar to that observed in controls. This result further supports that retrograde trains driven by dynein-2 are unable to efficiently cross the TZ in *wdr-60* mutants.

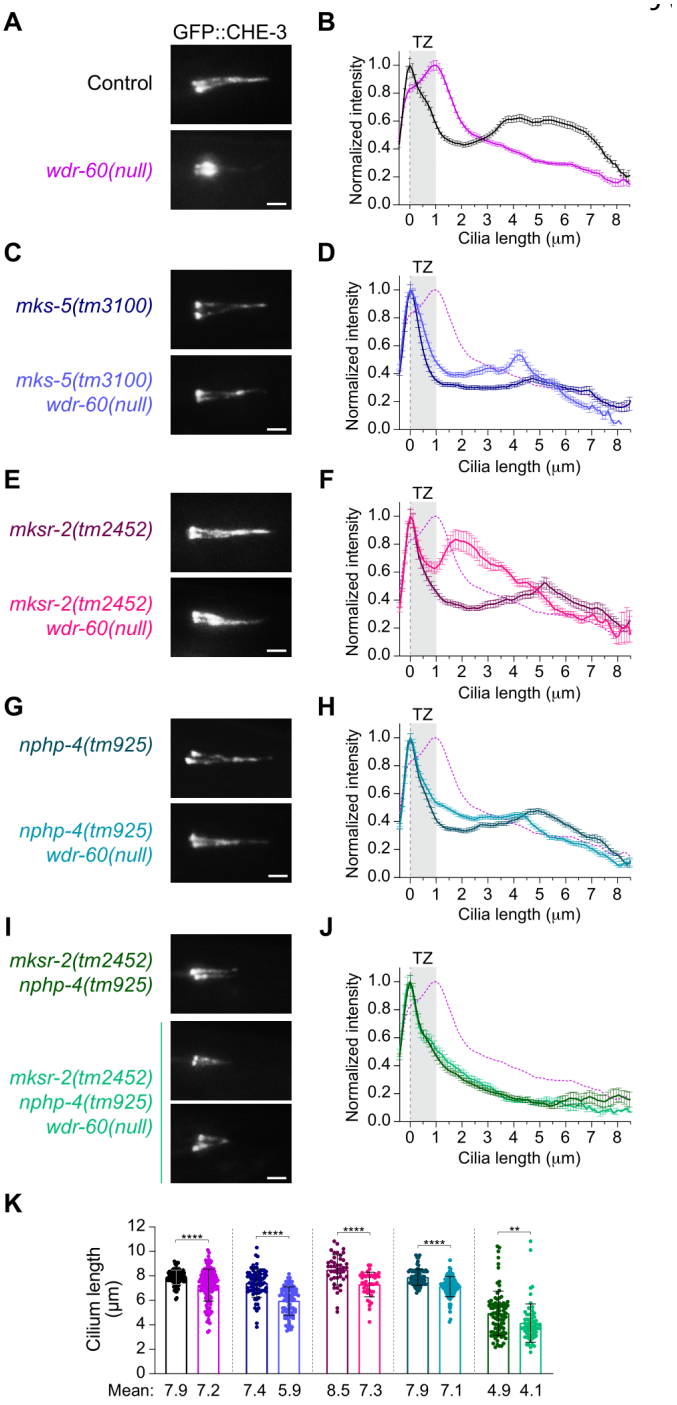

Figure 11 - Disruption of specific TZ components rescues dynein-2 accumulation inside cilia of *wdr-60* mutants. (A, C, E, G, and I) Representative examples of phasmid cilia of the indicated *wdr-60* and TZ mutant genotypes, expressing GFP::CHE-3. **(B, D, F, H, and J)** Relative distribution of GFP::CHE-3 signal intensity along cilia. The purple dashed line represents the data from the *wdr-60(null)* in **B**. Gray rectangles highlight the TZ, as previously defined. n ≥ 108 cilia for **B**, n ≥ 74 cilia for **D**, n ≥ 42 cilia for **F**, n ≥ 80 cilia for **H**, and n ≥ 64 cilia for **J**. XY intensity distribution graphs are shown as mean ± SEM. **(K)** Length of the cilia analyzed in **B**, **D**, **F**, **H**, and **J** from the same color-coded genotypes indicated in **A**, **C**, **E**, **G**, and **I**. Loss of WDR-60 combined with TZ mutations always

resulted in a slight decrease of cilia length relative to the respective TZ mutant control. Graph is shown as mean ± SD. Mann–Whitney U test was used to analyze each pair of datasets. **, P ≤ 0.01; ****, P ≤ 0.0001. Scale bars: 2 μm.

To better dissect which TZ modules restrict dynein-2 passage, we next examined GFP::CHE-3 distribution in *wdr-60(null)* cilia after disrupting key components required for the assembly of each TZ module. Removal of the MKS module by inhibiting MKSR-2 (B9D2) or CEP-290 with the *mksr-2(tm2452)* or *cep-290(tm4927)* mutations did not prevent the accumulation of GFP::CHE-3 near the TZ region of *wdr-60(null)* cilia **(Figures 11E, 11F, 12A, and 12B)**. In contrast, disrupting the NPHP module with the *nphp-4(tm925)* mutation in the *wdr-60(null)* background almost completely rescued GFP::CHE-3 accumulation at the distal side of the TZ **(Figure 11G and 11H)**. Joint disruption of NPHP-4 and MKSR-2 further enhanced this rescue effect **(Figure 11I and 11J)**, although we note that both cilia size and GFP::CHE-3 levels along cilia were strongly reduced in the *mksr-2(tm2452)*;*nphp-4(tm925)* double mutant **(Figures 11K, 12C, and 12D)**. We conclude that NPHP is the main module restricting the passage of underpowered retrograde trains through the TZ in *wdr-60(null)* cilia.

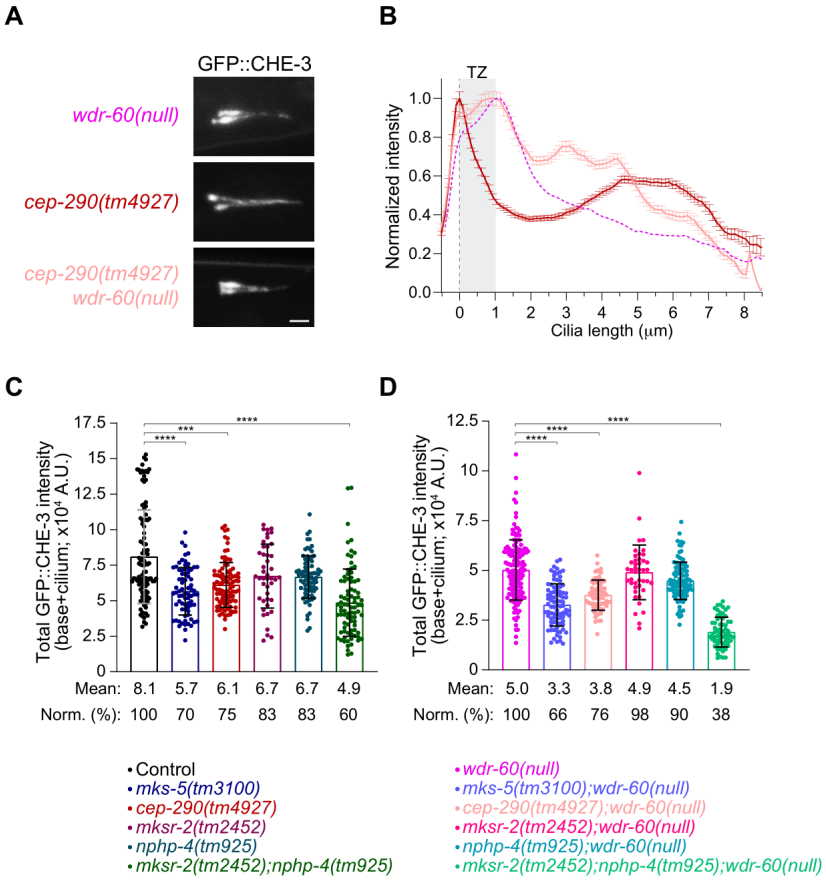

Figure 12 - Disruption of some TZ components changes the average levels of ciliary dynein-2. (A) Phasmid cilia of the indicated *wdr-60* and *cep-290* mutant genotypes, expressing GFP::CHE-3. Scale bar: 2 µm. **(B)** Distribution of GFP::CHE-3 signal intensity along cilia from the strains in **A** (n ≥ 74 cilia). The gray rectangle highlights the TZ, as previously defined. XY intensity distribution graph is shown as mean ± SEM. **(C and D)** Total GFP::CHE-3 intensity from the base to the tip of cilia from TZ mutants of the indicated genotypes, in wild-type *wdr-60* (**C**) and *wdr-60(null)* mutant (**D**) backgrounds. The cilia quantified here correspond to the same that were used to quantify the GFP::CHE-3 distribution profiles depicted in Figure 11. Column graphs are shown as mean ± SD. Kruskal–Wallis test followed by Dunn's multiple comparison were used to analyze these datasets. ***, P ≤ 0.001; ****, P ≤ 0.0001.

Next, we tested whether disrupting the TZ could compensate for more severe retrograde IFT defects, such as those caused by a mutation in the microtubule-binding domain of CHE-3(K2935Q), which completely blocks dynein-2 motility and leads to severely truncated cilia (Yi et al., 2017). In contrast to the rescue that we observed earlier in the *wdr-60(null)* mutant background, disrupting MKS-5, NPHP-4, or both MKSR-2/NPHP-4, failed to prevent GFP::CHE-3(K2935Q) accumulation inside cilia **(Figure 13A–H)**. These results show that even the complete removal of the TZ barrier is not sufficient to rescue the accumulation of

nonmotile dynein-2 inside cilia. Although cilia size slightly increased in the absence of MKS-5 or NPHP-4 **(Figure 13I)**, none of the TZ mutants were able to restore anterograde IFT in animals expressing GFP::CHE-3(K2935Q) **(Figure 13J)**. Thus, IFT requires a minimum amount of functional dynein-2 regardless of the state of the TZ barrier.

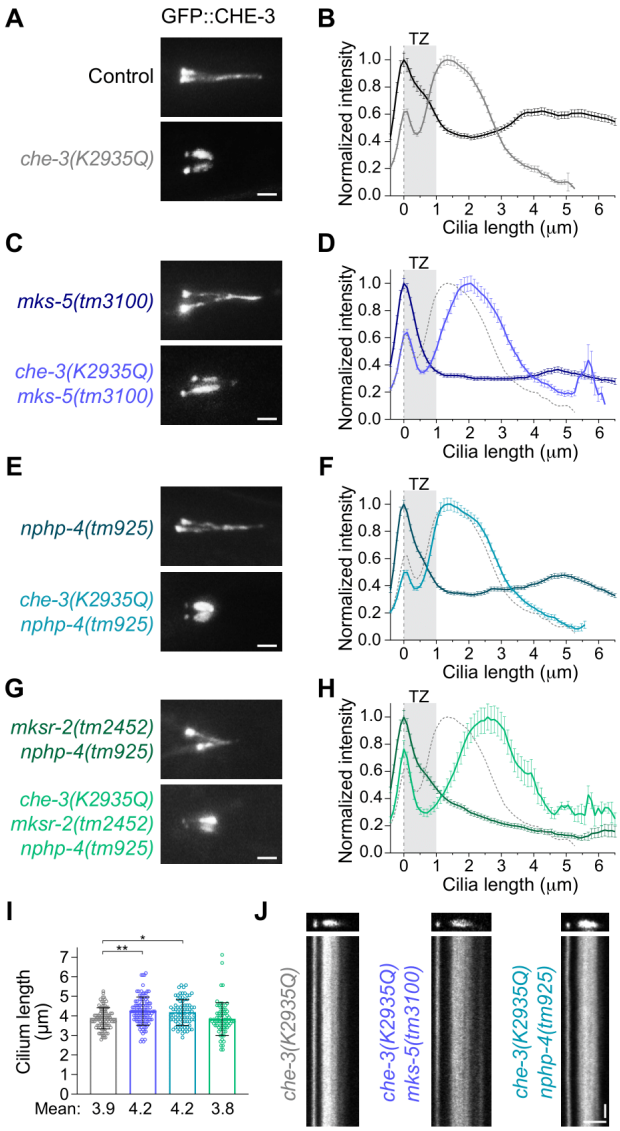

Figure 13 - Complete loss of dynein-2 motility results in ciliary accumulations even when the TZ barrier is completely disrupted. (A, C, E, and G) Representative examples of phasmid cilia of the indicated TZ mutant genotypes, expressing wild-type GFP::CHE-3 or the nonmotile GFP::CHE-3(K2935Q). **(B, D, F, and H)** Relative distribution of GFP::CHE-3(K2935Q) signal intensity along cilia, in control and TZ mutant backgrounds. The gray dashed line represents the data from the GFP::CHE-3(K2935Q) mutant in **B**. Gray rectangles highlight the TZ, as previously defined. n ≥ 105 cilia for **B**, n ≥ 104 cilia for **D**, n ≥ 80 cilia for **F**, and n ≥ 86 cilia for **H**. XY intensity distribution graphs are shown as mean ± SEM. **(I)** Length of GFP::CHE-3(K2935Q) mutant cilia analyzed in **B**, **D**, **F**, and **H**, with

the same color-coded genotypes as indicated. Graph is shown as mean ± SD. Kruskal–Wallis test followed by Dunn's multiple comparison were used to analyze these datasets. *, P ≤ 0.05; **, P ≤ 0.01. **(J)** Cilia and the respective kymographs from the specified strain genotypes. No anterograde or retrograde IFT was detectable in the GFP::CHE-3(K2935Q) mutant, not even in combination with the disruption of MKS-5 or NPHP-4. Scale bars: 2 μm (**A**, **C**, **E**, and **G**); vertical 5 s, horizontal 2 μm (**J**).

2.2.7. The NPHP module restricts dynein-2 movement through the TZ

Next, we investigated whether the kinetics of WDR-60–deficient dynein-2 were altered by the complete removal of the TZ barrier or by the loss of the NPHP module. Consistent with a previous study (Jensen et al., 2015), we observed that loss of MKS-5 increases both the anterograde and retrograde velocities of GFP::CHE-3 particles in the TZ region **(Figure 14A, 14C, and 14D)**. We also observed a similar, albeit more modest, increase in IFT velocities at the TZ region in the *nphp-4* mutant background. Importantly, we found that loss of either MKS-5 or NPHP-4 increased the retrograde velocity of GFP::CHE-3 in the TZ region of WDR-60–deficient cilia **(Figure 14A, 14C, and 14D)**. Interestingly, retrograde IFT velocity in the middle segment of *wdr-60(null)* cilia also increased upon the removal of MKS-5 or NPHP-4 **(Figure 14C)**, suggesting that clearing the accumulated IFT trains near the TZ allows for more steady buildup of retrograde IFT velocities in these mutants. We note that IFT frequency was not greatly affected by disruption of MKS-5 or NPHP-4 **(Figure 14B)**, suggesting that loss of the TZ barrier does not compromise the poorly understood mechanisms regulating the rate of IFT injection into cilia. Altogether, these results further support that WDR-60 loss impairs dynein-2 passage through the TZ, and that the NPHP module restricts dynein-2 exit from WDR-60–deficient cilia.

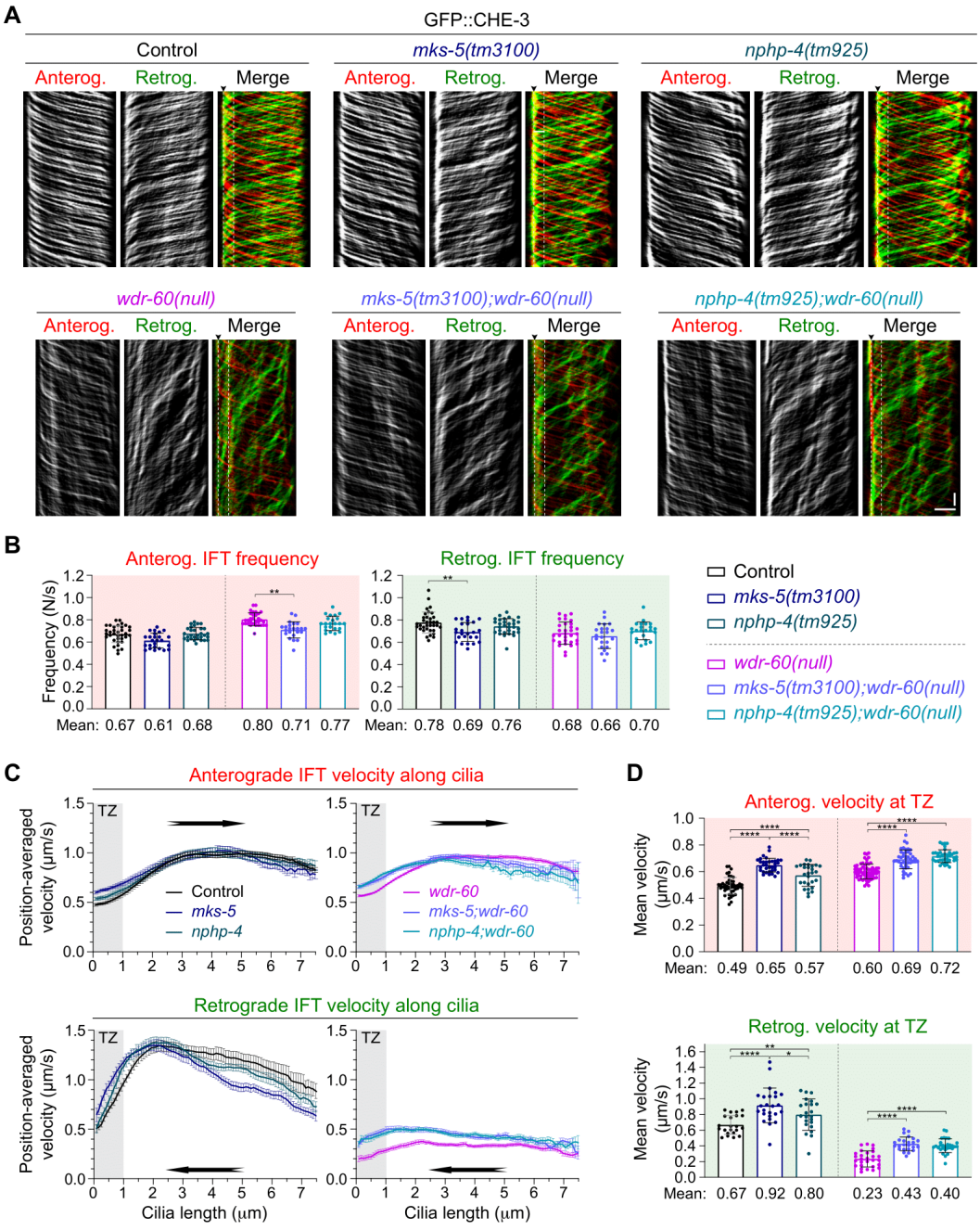

Figure 14 - Disruption of NPHP-4 is sufficient to increase the velocity of WDR-60–deficient dynein-2 through the TZ region. (A) GFP::CHE-3 kymographs of phasmid cilia from the indicated strains. Single and merge channels for particles moving anterogradely and retrogradely are shown. Arrowhead labels the base, and white dashed line marks the limit of the TZ region (1 µm). Scale bars: vertical 5 s, horizontal 2 µm. **(B)** Frequency of IFT particles detected at the distal segment of cilia for each represented strain (n ≥ 23 cilia). **(C)** GFP::CHE-3 velocity moving in the anterograde and retrograde direction along the cilia of the indicated genotypes (n ≥ 345 particle traces were analyzed in ≥ 23 cilia for each strain). Gray rectangles highlight the TZ, as previously defined. **(D)** Average velocity of GFP::CHE-3 crossing the TZ region of the same cilia analyzed in **C**, for each indicated genotype. XY velocity graphs are shown as mean ± SEM, and graphs in columns are shown

as mean ± SD. One-way ANOVA followed by Sidak and the Holm–Sidak multiple comparisons were used to analyze the datasets in **B** and **D**, respectively. *, P ≤ 0.05; **, P ≤ 0.01; ****, P ≤ 0.0001.

2.3. Discussion

2.3.1. WDR-60 is incorporated into cilia even in the absence of dynein-2

Our data reveal that WDR-60 is specifically expressed in ciliated sensory neurons in *C. elegans* and undergoes IFT with kinetics similar to those reported for the dynein-2 HC (Yi et al., 2017). Moreover, our findings indicate that WDR-60(ΔCT) is robustly expressed, showing that the β-propeller is not required for WDR-60 stability. Interestingly, we find that the WDR-60 NT on its own can be recruited to the ciliary base and incorporated into IFT trains, albeit less efficiently than full-length WDR-60. Furthermore, dynein-2 HC destabilization through XBX-1 loss resulted in WDR-60 and WDR-60(ΔCT) sequestration inside cilia, indicating that WDR-60 can enter cilia without dynein-2 but requires its activity in retrograde IFT to exit. Thus, we conclude that the NT of WDR-60 can establish links with other components of the IFT machinery to be incorporated into cilia in the absence of dynein-2. This is in agreement with the weaker but persistent interaction between IFT-B components and the human WDR60[Q631*] truncation lacking the DHC2-binding β-propeller domain (Vuolo et al., 2018).

2.3.2. WDR-60 is required for efficient IFT recycling and contributes to cilia-mediated behavior

Two recent studies in human cells showed that WDR60 loss leads to the misplacement of IFT and signaling particles in cilia without greatly affecting axoneme extension (Hamada et al., 2018, Vuolo et al., 2018). Remarkably, in spite of the strong defect in retrograde IFT, we show that the *wdr-60(null)* mutant is still capable of building nearly full-length cilia in *C. elegans*, similar to what was observed in WDR60 knockout (KO) human cells (Vuolo et al., 2018). We also show that WDR-60–deficient cilia are at least partially functional in

chemotaxis and osmotic tolerance assays, contrasting with the strong behavioral defects exhibited by the *xbx-1(null)* mutant, which assembles severely shortened cilia. The mild chemotaxis and osmotic defects that we observe in *wdr-60* mutants likely mirror the signaling defects underlying WDR60-associated SRPS (Cossu et al., 2016, McInerney-Leo et al., 2013, Kakar et al., 2018).

We find that WDR-60 disruption results in accumulation of IFT-74, CHE-11 (IFT140), and the kinesin-2 subunit KAP-1 inside cilia. However, we also show that WDR-60 disruption has different effects on the distribution profile of these IFT components along cilia: IFT-74 (IFT-B) levels peak at the tip and in the middle-to-distal-segment transition (both regions containing microtubule plus ends), while CHE-11 (IFT-A) and KAP-1 levels peak closer to the ciliary base and the TZ region, which is similar to the distribution profile of the dynein-2 motor itself. This suggests that some IFT subunits might be less efficiently incorporated into retrograde IFT trains in WDR-60–deficient cilia. In agreement with this, similar differences in IFT component distribution can be discerned in prior studies using WDR60 KO human cells: IFT88 (IFT-B) accumulates inside their cilia, peaking mostly at the tip, while the peak levels of accumulated IFT140 and IFT43 (both IFT-A) are found closer to the ciliary base (Hamada et al., 2018, Vuolo et al., 2018, Tsurumi et al., 2019).

Interestingly, our results suggest that the WDR-60 NT retains residual activity in IFT, as the accumulation of IFT-A/B particles inside cilia is less pronounced for the *wdr-60(ΔCT)* mutant than for the *wdr-60(null)* mutant. This is consistent with what was observed in WDR60 KO rescue experiments with an equivalent WDR60 β-propeller truncation construct (WDR60[Q631*]) (Vuolo et al., 2018). Apart from the less pronounced IFT accumulations, the loss of the WDR-60 β-propeller leads to defects in dynein-2 incorporation, retrograde IFT kinetics, and cilia-mediated behavior that are similar to those observed upon the complete loss of WDR-60. Thus, our results show that the WDR-60 β-propeller is critical for dynein-2 function.

2.3.3. Normal TZ integrity and gating function in the absence of WDR-60

A recent study uncovered that the dynein-2 HC CHE-3 is necessary for the stability and gating functions of the TZ (Jensen et al., 2018). Consistent with this, we show that loss of the dynein-2 LIC XBX-1 also impairs the integrity and gating functions of the TZ barrier. In a recent study, Vuolo et al. (2018) observed mislocalization of the TZ components TMEM67 and RPGRIP1L (MKS-5 orthologue) in a subset of human RPE1 WDR60 KO cells. In

contrast, we do not observe any defects in TZ integrity and gating function in *wdr-60* mutants, as judged by the correct localization of multiple TZ components and the complete RPI-2 exclusion from their sensory cilia. We therefore conclude that the integrity and function of the TZ barrier are maintained in the absence of WDR-60 in *C. elegans*. The difference in TZ susceptibility to WDR60 loss may arise from the variations in TZ structure observed between different types of cilia (Jana et al., 2018, Akella et al., 2019) or from potential differences in the minimal threshold of dynein-2 function required for maintaining TZ integrity in each model system.

2.3.4. Disruption of WDR-60 reduces dynein-2 loading into cilia and the kinetics of retrograde IFT

Prior studies reported that WDR60 loss resulted in the complete disappearance of dynein-2 LIC from the base and axoneme of cilia (Hamada et al., 2018, Vuolo et al., 2018), but no detectable difference was observed in the recruitment of the dynein-2 HC to the ciliary base (Vuolo et al., 2018). Our analyses of endogenously labeled dynein-2 HC and LIC in *C. elegans* reveals that both subunits still colocalize inside WDR-60–deficient cilia. Importantly, the efficiency of dynein-2 HC recruitment to cilia is substantially decreased in the absence of WDR-60 or its dynein-2–binding β-propeller domain. Given that dynein-2 HC levels in the soma of ciliated sensory neurons are not greatly altered by the loss of WDR-60, our results argue that WDR-60 directly contributes to dynein-2 recruitment to cilia rather than having a significant role in dynein-2 HC stabilization, as is the case for dynein-2 LIC (Taylor et al., 2015, Toropova et al., 2019).

A recent structural study revealed that binding of the WDR60-WDR34 heterodimer contributes to the asymmetric conformation of the autoinhibited dynein-2 complex, and this was proposed to facilitate dynein-2 incorporation onto anterograde IFT trains (Toropova et al., 2019). Our quantifications of dynein-2 HC (GFP::CHE-3) signal on anterograde tracks inside *wdr-60* mutant cilia provide the first direct evidence for this model in vivo. This conclusion is supported by the observation that the reduction in dynein-2 loading onto anterograde trains (approximately threefold) is even greater than the reduction in dynein-2 recruitment to cilia (approximately twofold) in *wdr-60* mutants.

Intriguingly, the observation that a fraction of dynein-2 motors still become incorporated onto anterograde IFT trains indicates that WDR-60 is not the only link that dynein-2 can establish with anterograde trains. This conclusion is further supported by the recent report of a direct interaction between dynein-2 LIC and IFT54 of the IFT-B complex (Zhu et al., 2021) and by

cryo-EM data suggesting that the main contacts between anterograde IFT trains and dynein-2 motors may also involve the HC (Toropova et al., 2019).

Although less dynein-2 reaches the cilium tip to then power retrograde IFT, we find that the frequency of retrograde IFT is only mildly affected in the absence of WDR-60. Taken together with the observation that dynein-2 does not accumulate at the ciliary tip, this result argues that WDR-60 is dispensable for dynein-2 activation and the start of retrograde IFT.

2.3.5. Underpowered retrograde IFT trains fail to push through the TZ barrier to exit cilia in *wdr-60* mutants

Emerging evidence points to an important interplay between IFT-A and the BBSome in regulating the traffic of G protein–coupled receptors in and out of cilia across the TZ, in part by coupling the receptors to IFT trains (Nachury and Mick, 2019). As a dense gating structure, the TZ has been shown to slow down the passage of motor-powered IFT trains, supporting the notion that this physical barrier offers substantial resistance to the passage of IFT trains (Jensen et al., 2015, Oswald et al., 2018, Prevo et al., 2015). However, little is known about the mechanisms that enable the IFT machinery to pass through the TZ barrier.

Our live imaging analysis shows that WDR-60–deficient retrograde IFT trains are driven by fewer dynein-2 motors, at severely reduced velocity, and accumulate at the distal side of the TZ. We propose that the accumulation of these underpowered IFT trains reflects their inability to push through the TZ barrier **(Figure 15)**. Additional lines of evidence support a model in which a force production threshold needs to be met for retrograde IFT to cross the TZ barrier: (a) in experiments using purified “untrapped” dimers of GST-dynein-2 motor domains, maximum microtubule gliding velocity can be achieved only after a certain dynein-2 concentration is reached (Toropova et al., 2017); (b) the same study showed that DNA origamis mimicking IFT trains were transported less efficiently (less processive runs) when attached to three untrapped dynein-2 motor dimers than when attached to seven dimers (Toropova et al., 2017); (c) the cooperative action of multiple dynein-2 motors in retrograde IFT has been shown to be capable of generating considerable forces (≥25 pN) to move against resisting loads (Roberts, 2018, Shih et al., 2013); and (d) we show in this study that removing the resistance offered by the TZ rescues the exit of the underpowered retrograde IFT trains driven by fewer dynein-2 motors in *wdr-60* mutants.

Our findings are also consistent with the “motorized plough” model, which posits that dynein-2 motors remove IFT trains and their cargoes out of the cilium by dragging them

while pushing through the TZ barrier (Nachury and Mick, 2019). We note, nonetheless, that we cannot fully exclude the possibility that WDR-60 might also contribute in other ways to retrograde IFT or ciliary exit.

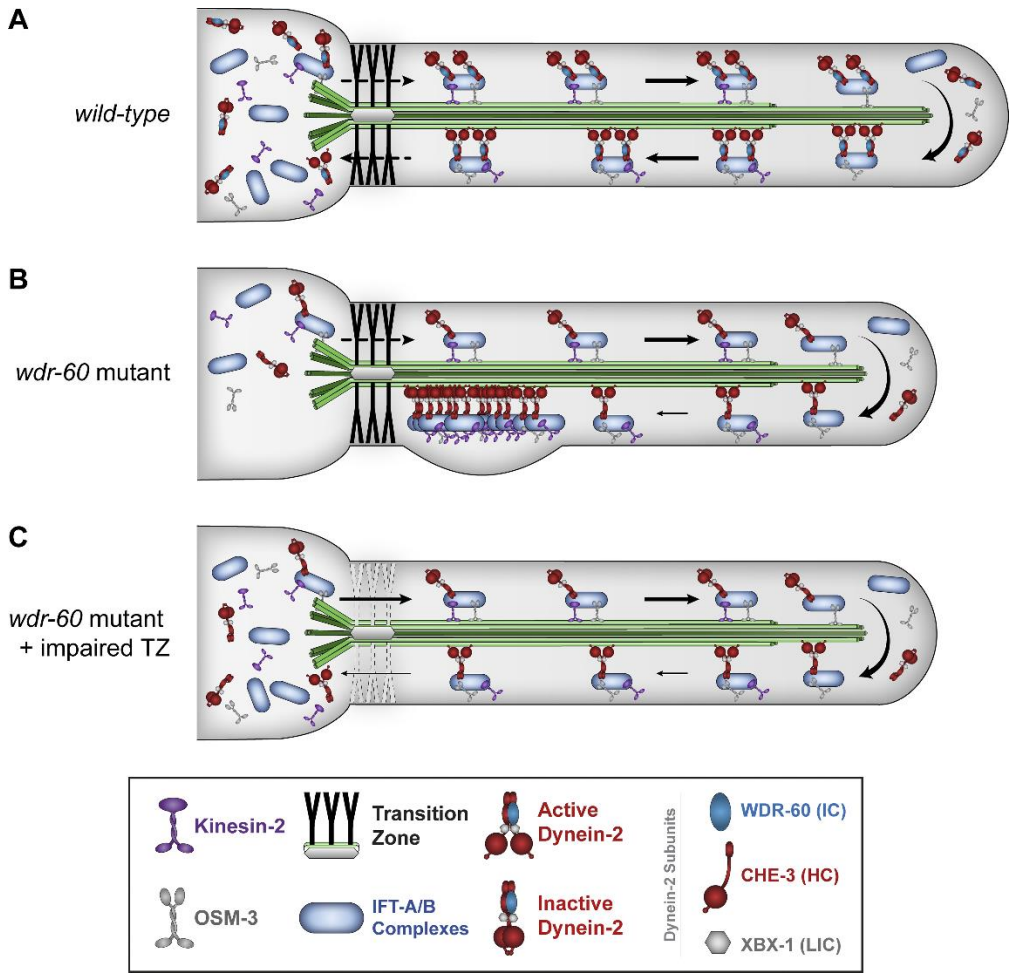

Figure 15 - Model for how WDR-60 contributes to efficient dynein-2–mediated retrograde IFT, and the crossing of the TZ to recycle the IFT machinery. (A) In wild-type *C. elegans* cilia, kinesin motors carry dynein-2 as a cargo on anterograde IFT trains across the TZ to enter the cilium compartment and reach the ciliary tip. After rearrangement, dynein-2 transports trains in the retrograde direction, crossing the TZ barrier to return them to the base of the cilium, so they can be recycled. **(B)** In the absence of WDR-60, less dynein-2 is recruited and loaded onto anterograde IFT trains to be incorporated into cilia. Consequently, fewer dynein-2 motors are available at the ciliary tip to power the newly rearranged retrograde trains. These underpowered dynein-2–driven trains move at slower velocities and tend to accumulate at the distal side of the TZ, unable to generate enough force to cross this barrier. **(C)** Disrupting the NPHP module reduces the resistance offered by the TZ to the passage of IFT trains, facilitating the exit of retrograde IFT to the cilium base and compensating for the less efficient WDR-60–deficient dynein-2 trains.

2.3.6. The NPHP module offers resistance to dynein-2 passage through the TZ

Our results reveal that disrupting MKS-5, the most upstream TZ assembly factor, can rescue the exit of underpowered retrograde IFT trains from *wdr-60(null)* cilia. We then dissected which TZ modules offer resistance to dynein-2 exit by targeting their respective upstream components. We find that removal of the NPHP module by disrupting NPHP-4 almost completely rescues the exit of WDR-60–deficient dynein-2 from cilia, while the loss of the MKS module by disrupting MKSR-2 or CEP-290 did not. Given that previous studies showed that the recruitment of NPHP-4 and the assembly of the NPHP module are unaffected by the loss of either CEP-290 or MKSR-2 (Blacque and Sanders, 2014, Schouteden et al., 2015, Li et al., 2016), our findings support a pivotal role for the NPHP module in restricting dynein-2 passage through the TZ. Interestingly, in addition to disrupting the assembly of the NPHP module, NPHP-4 loss has also been shown to reduce the number of Y-links and their densities (Jensen et al., 2015, Lambacher et al., 2016). However, additional experimental work will be required to directly determine whether Y-links themselves influence the passage of IFT trains through the TZ.

Consistent with an important role for NPHP-4 and the NPHP module in restricting dynein-2 crossing of the TZ, studies in *C. elegans* and *Chlamydomonas* have shown that NPHP4 loss weakens and permeabilizes the TZ barrier, allowing entry of normally excluded cytoplasmic proteins and reducing the retention of ciliary proteins (Awata et al., 2014, Williams et al., 2011, Jauregui et al., 2008). In agreement with this, we find that removal of NPHP-4 increases the velocity of both anterograde and retrograde IFT trains crossing the TZ roadblock, particularly improving the retrograde velocity of underpowered WDR-60–deficient trains exiting cilia. This effect was even comparable with the increased IFT velocity in the TZ region that results from the disruption of MKS-5 in *wdr-60(null)* cilia. This supports the idea that even though NPHP-4 loss does not impair the TZ to the same extent as MKS-5 inhibition, it considerably reduces the resistance offered to IFT trains crossing the TZ barrier.

Interestingly, our results also indicate that even the complete removal of the TZ barrier is not sufficient for clearing out nonmotile CHE-3(K2935Q) dynein-2 from cilia. This finding implies that, although reduced, dynein-2 motors powering WDR-60–deficient retrograde IFT trains make an important contribution to the rescue observed upon disruption of the TZ barrier.

Taken together, our results provide direct evidence that the NPHP module of the TZ offers resistance to the passage of dynein-2–driven IFT trains and strongly support that dynein-2 motors need to reach a minimal force-generating threshold to power passage of retrograde trains through the TZ barrier to exit cilia.

2.4. References

AKELLA, J. S., SILVA, M., MORSCI, N. S., NGUYEN, K. C., RICE, W. J., HALL, D. H. & BARR, M. M. 2019. Cell type-specific structural plasticity of the ciliary transition zone in C. elegans. *Biol Cell,* 111**,** 95-107.

ASANTE, D., STEVENSON, N. L. & STEPHENS, D. J. 2014. Subunit composition of the human cytoplasmic dynein-2 complex. *J Cell Sci,* 127**,** 4774-87.

AWATA, J., TAKADA, S., STANDLEY, C., LECHTRECK, K. F., BELLVE, K. D., PAZOUR, G. J., FOGARTY, K. E. & WITMAN, G. B. 2014. NPHP4 controls ciliary trafficking of membrane proteins and large soluble proteins at the transition zone. *J Cell Sci,* 127**,** 4714-27.

BLACQUE, O. E., PERENS, E. A., BOROEVICH, K. A., INGLIS, P. N., LI, C., WARNER, A., KHATTRA, J., HOLT, R. A., OU, G., MAH, A. K., MCKAY, S. J., HUANG, P., SWOBODA, P., JONES, S. J., MARRA, M. A., BAILLIE, D. L., MOERMAN, D. G., SHAHAM, S. & LEROUX, M. R. 2005. Functional genomics of the cilium, a sensory organelle. *Curr Biol,* 15**,** 935-41.

BLACQUE, O. E. & SANDERS, A. A. 2014. Compartments within a compartment: what C. elegans can tell us about ciliary subdomain composition, biogenesis, function, and disease. *Organogenesis,* 10**,** 126-37.

BLISNICK, T., BUISSON, J., ABSALON, S., MARIE, A., CAYET, N. & BASTIN, P. 2014. The intraflagellar transport dynein complex of trypanosomes is made of a heterodimer of dynein heavy chains and of light and intermediate chains of distinct functions. *Mol Biol Cell,* 25**,** 2620-33.

CORNILS, A., MAURYA, A. K., TERESHKO, L., KENNEDY, J., BREAR, A. G., PRAHLAD, V., BLACQUE, O. E. & SENGUPTA, P. 2016. Structural and Functional Recovery of Sensory Cilia in C. elegans IFT Mutants upon Aging. *PLoS Genet,* 12**,** e1006325.

COSSU, C., INCANI, F., SERRA, M. L., COIANA, A., CRISPONI, G., BOCCONE, L. & ROSATELLI, M. C. 2016. New mutations in DYNC2H1 and WDR60 genes revealed

by whole-exome sequencing in two unrelated Sardinian families with Jeune asphyxiating thoracic dystrophy. *Clin Chim Acta,* 455**,** 172-80.

DE-CASTRO, A. R. G., RODRIGUES, D. R. M., DE-CASTRO, M. J. G., VIEIRA, N., VIEIRA, C., CARVALHO, A. X., GASSMANN, R., ABREU, C. M. C. & DANTAS, T. J. 2022. WDR60-mediated dynein-2 loading into cilia powers retrograde IFT and transition zone crossing. *J Cell Biol,* 221.

HAMADA, Y., TSURUMI, Y., NOZAKI, S., KATOH, Y. & NAKAYAMA, K. 2018. Interaction of WDR60 intermediate chain with TCTEX1D2 light chain of the dynein-2 complex is crucial for ciliary protein trafficking. *Mol Biol Cell,* 29**,** 1628-1639.

HOU, Y., PAZOUR, G. J. & WITMAN, G. B. 2004. A dynein light intermediate chain, D1bLIC, is required for retrograde intraflagellar transport. *Mol Biol Cell,* 15**,** 4382-94.

HOU, Y. & WITMAN, G. B. 2015. Dynein and intraflagellar transport. *Exp Cell Res,* 334**,** 26-34.

JANA, S. C., MENDONCA, S., MACHADO, P., WERNER, S., ROCHA, J., PEREIRA, A., MAIATO, H. & BETTENCOURT-DIAS, M. 2018. Differential regulation of transition zone and centriole proteins contributes to ciliary base diversity. *Nat Cell Biol,* 20**,** 928-941.

JAUREGUI, A. R., NGUYEN, K. C., HALL, D. H. & BARR, M. M. 2008. The Caenorhabditis elegans nephrocystins act as global modifiers of cilium structure. *J Cell Biol,* 180**,** 973-88.

JENSEN, V. L., LAMBACHER, N. J., LI, C., MOHAN, S., WILLIAMS, C. L., INGLIS, P. N., YODER, B. K., BLACQUE, O. E. & LEROUX, M. R. 2018. Role for intraflagellar transport in building a functional transition zone. *EMBO Rep,* 19.

JENSEN, V. L., LI, C., BOWIE, R. V., CLARKE, L., MOHAN, S., BLACQUE, O. E. & LEROUX, M. R. 2015. Formation of the transition zone by Mks5/Rpgrip1L establishes a ciliary zone of exclusion (CIZE) that compartmentalises ciliary signalling proteins and controls PIP2 ciliary abundance. *EMBO J,* 34**,** 2537-56.

KAKAR, N., HORN, D., DECKER, E., SOWADA, N., KUBISCH, C., AHMAD, J., BORCK, G. & BERGMANN, C. 2018. Expanding the phenotype associated with biallelic WDR60 mutations: Siblings with retinal degeneration and polydactyly lacking other features of short rib thoracic dystrophies. *Am J Med Genet A,* 176**,** 438-442.

LAMBACHER, N. J., BRUEL, A. L., VAN DAM, T. J., SZYMANSKA, K., SLAATS, G. G., KUHNS, S., MCMANUS, G. J., KENNEDY, J. E., GAFF, K., WU, K. M., VAN DER LEE, R., BURGLEN, L., DOUMMAR, D., RIVIERE, J. B., FAIVRE, L., ATTIE-BITACH, T., SAUNIER, S., CURD, A., PECKHAM, M., GILES, R. H., JOHNSON, C. A., HUYNEN, M. A., THAUVIN-ROBINET, C. & BLACQUE, O. E. 2016. TMEM107

recruits ciliopathy proteins to subdomains of the ciliary transition zone and causes Joubert syndrome. *Nat Cell Biol,* 18**,** 122-31.

LI, C., JENSEN, V. L., PARK, K., KENNEDY, J., GARCIA-GONZALO, F. R., ROMANI, M., DE MORI, R., BRUEL, A. L., GAILLARD, D., DORAY, B., LOPEZ, E., RIVIERE, J. B., FAIVRE, L., THAUVIN-ROBINET, C., REITER, J. F., BLACQUE, O. E., VALENTE, E. M. & LEROUX, M. R. 2016. MKS5 and CEP290 Dependent Assembly Pathway of the Ciliary Transition Zone. *PLoS Biol,* 14**,** e1002416.

MCINERNEY-LEO, A. M., SCHMIDTS, M., CORTES, C. R., LEO, P. J., GENER, B., COURTNEY, A. D., GARDINER, B., HARRIS, J. A., LU, Y., MARSHALL, M., CONSORTIUM, U. K., SCAMBLER, P. J., BEALES, P. L., BROWN, M. A., ZANKL, A., MITCHISON, H. M., DUNCAN, E. L. & WICKING, C. 2013. Short-rib polydactyly and Jeune syndromes are caused by mutations in WDR60. *Am J Hum Genet,* 93**,** 515-23.

NACHURY, M. V. & MICK, D. U. 2019. Establishing and regulating the composition of cilia for signal transduction. *Nat Rev Mol Cell Biol,* 20**,** 389-405.

OSWALD, F., PREVO, B., ACAR, S. & PETERMAN, E. J. G. 2018. Interplay between Ciliary Ultrastructure and IFT-Train Dynamics Revealed by Single-Molecule Super-resolution Imaging. *Cell Rep,* 25**,** 224-235.

PREVO, B., MANGEOL, P., OSWALD, F., SCHOLEY, J. M. & PETERMAN, E. J. 2015. Functional differentiation of cooperating kinesin-2 motors orchestrates cargo import and transport in C. elegans cilia. *Nat Cell Biol,* 17**,** 1536-45.

RECK, J., SCHAUER, A. M., VANDERWAAL MILLS, K., BOWER, R., TRITSCHLER, D., PERRONE, C. A. & PORTER, M. E. 2016. The role of the dynein light intermediate chain in retrograde IFT and flagellar function in Chlamydomonas. *Mol Biol Cell,* 27**,** 2404-22.

ROBERTS, A. J. 2018. Emerging mechanisms of dynein transport in the cytoplasm versus the cilium. *Biochem Soc Trans,* 46**,** 967-982.

SCHAFER, J. C., HAYCRAFT, C. J., THOMAS, J. H., YODER, B. K. & SWOBODA, P. 2003. XBX-1 encodes a dynein light intermediate chain required for retrograde intraflagellar transport and cilia assembly in Caenorhabditis elegans. *Mol Biol Cell,* 14**,** 2057-70.

SCHEIDEL, N. & BLACQUE, O. E. 2018. Intraflagellar Transport Complex A Genes Differentially Regulate Cilium Formation and Transition Zone Gating. *Curr Biol,* 28**,** 3279-3287 e2.

SCHOUTEDEN, C., SERWAS, D., PALFY, M. & DAMMERMANN, A. 2015. The ciliary transition zone functions in cell adhesion but is dispensable for axoneme assembly in C. elegans. *J Cell Biol,* 210**,** 35-44.

SHIH, S. M., ENGEL, B. D., KOCABAS, F., BILYARD, T., GENNERICH, A., MARSHALL, W. F. & YILDIZ, A. 2013. Intraflagellar transport drives flagellar surface motility. *Elife,* 2**,** e00744.

SWOBODA, P., ADLER, H. T. & THOMAS, J. H. 2000. The RFX-type transcription factor DAF-19 regulates sensory neuron cilium formation in C. elegans. *Mol Cell,* 5**,** 411-21.

TAYLOR, S. P., DANTAS, T. J., DURAN, I., WU, S., LACHMAN, R. S., UNIVERSITY OF WASHINGTON CENTER FOR MENDELIAN GENOMICS, C., NELSON, S. F., COHN, D. H., VALLEE, R. B. & KRAKOW, D. 2015. Mutations in DYNC2LI1 disrupt cilia function and cause short rib polydactyly syndrome. *Nat Commun,* 6**,** 7092.

TOROPOVA, K., MLADENOV, M. & ROBERTS, A. J. 2017. Intraflagellar transport dynein is autoinhibited by trapping of its mechanical and track-binding elements. *Nat Struct Mol Biol,* 24**,** 461-468.

TOROPOVA, K., ZALYTE, R., MUKHOPADHYAY, A. G., MLADENOV, M., CARTER, A. P. & ROBERTS, A. J. 2019. Structure of the dynein-2 complex and its assembly with intraflagellar transport trains. *Nat Struct Mol Biol,* 26**,** 823-829.

TSURUMI, Y., HAMADA, Y., KATOH, Y. & NAKAYAMA, K. 2019. Interactions of the dynein-2 intermediate chain WDR34 with the light chains are required for ciliary retrograde protein trafficking. *Mol Biol Cell,* 30**,** 658-670.

VUOLO, L., STEVENSON, N. L., HEESOM, K. J. & STEPHENS, D. J. 2018. Dynein-2 intermediate chains play crucial but distinct roles in primary cilia formation and function. *Elife,* 7.

VUOLO, L., STEVENSON, N. L., MUKHOPADHYAY, A. G., ROBERTS, A. J. & STEPHENS, D. J. 2020. Cytoplasmic dynein-2 at a glance. *J Cell Sci,* 133.

WICKS, S. R., DE VRIES, C. J., VAN LUENEN, H. G. & PLASTERK, R. H. 2000. CHE-3, a cytosolic dynein heavy chain, is required for sensory cilia structure and function in Caenorhabditis elegans. *Dev Biol,* 221**,** 295-307.

WILLIAMS, C. L., LI, C., KIDA, K., INGLIS, P. N., MOHAN, S., SEMENEC, L., BIALAS, N. J., STUPAY, R. M., CHEN, N., BLACQUE, O. E., YODER, B. K. & LEROUX, M. R. 2011. MKS and NPHP modules cooperate to establish basal body/transition zone membrane associations and ciliary gate function during ciliogenesis. *J Cell Biol,* 192**,** 1023-41.

YI, P., LI, W. J., DONG, M. Q. & OU, G. 2017. Dynein-Driven Retrograde Intraflagellar Transport Is Triphasic in C. elegans Sensory Cilia. *Curr Biol,* 27**,** 1448-1461 e7.

ZHU, X., WANG, J., LI, S., LECHTRECK, K. & PAN, J. 2021. IFT54 directly interacts with kinesin-II and IFT dynein to regulate anterograde intraflagellar transport. *EMBO J,* 40**,** e105781.

CHAPTER III – IFT subunits are mostly coupled to WDR-60-deficient dynein-2 motors during retrograde transport

3.1. Introduction

In the previous chapter, we showed that, in the absence of WDR-60, dynein-2-driven retrograde IFT trains become underpowered and fail to exit cilia efficiently, as they accumulate on the distal side of the TZ (De-Castro et al., 2022). Moreover, we found that the removal of the NPHP module from the TZ of *wdr-60* KO worms facilitated the ciliary exit of dynein-2, preventing these accumulations. Interestingly, we observed different patterns for the ciliary distribution of IFT-140 (IFT-A), IFT-74 (IFT-B), KAP-1 (heterotrimeric kinesin-2), and OSM-3 (homodimeric kinesin-2) in the absence of WDR-60. While IFT-140 distribution closely resembled the one of dynein-2, accumulating predominantly at the distal side of the TZ, IFT-74 was found to accumulate along the whole cilium. On the other hand, KAP-1 was also strongly accumulated near the TZ and the base upon loss of WDR-60, while the ciliary distribution of OSM-3 was only mildly altered. Based on these observations, we hypothesized that IFT-140 and KAP-1 were still coupled to retrograde IFT trains in the absence of WDR-60, while IFT-74 became, at least partially, uncoupled.

To further dissect whether some IFT machinery become at least partially uncoupled from retrograde IFT trains in the absence of WDR-60, we extended these experiments to several other components, while also assessing the effects of removing the NPHP module. To our advantage, many studies have been recently published on the structure of the IFT-A/B complexes **(Figure 1)** (Hesketh et al., 2022, Jiang et al., 2023, Lacey et al., 2023, Ma et al., 2023, McCafferty et al., 2022, Meleppattu et al., 2022, Nakayama and Katoh, 2020, Petriman et al., 2022), which helped us select which IFT subunits to analyze in the absence of WDR-60 and/or the NPHP module. Since the IFT-A and IFT-B complexes are composed of 6 and 16 subunits, respectively, we preferentially analyzed subunits from opposite regions, to have a more representative analysis of each complex. Interestingly, the IFT-A complex has been found to be structurally similar across species, namely, in human (Hesketh et al., 2022, Jiang et al., 2023), *C. reinhardtii* (Lacey et al., 2023), *Tetrahymena* (Ma et al., 2023, McCafferty et al., 2022), and *Leishmania* (Meleppattu et al., 2022). On the other hand, the structure of the IFT-B complex has, so far, only been solved in *C. reinhardtii* (Lacey et al., 2023, Petriman et al., 2022). Nevertheless, we expect it should also be highly conserved between species, as the already reported interaction between IFT-B subunits in human cells (Nakayama and Katoh, 2020) are consistent with the structures obtained of the *C. reinhardtii* IFT-B complex.

Here, we observed that most of the IFT subunits analyzed accumulated at the distal side of the TZ in the absence of WDR-60, as was the case for dynein-2. Also, disrupting the NPHP module prevented the accumulation of these IFT components at the distal side of the TZ upon loss of WDR-60. Together, these data suggest that, in the absence of WDR-60, most of the IFT train machinery remains coupled to dynein-2 during retrograde IFT.

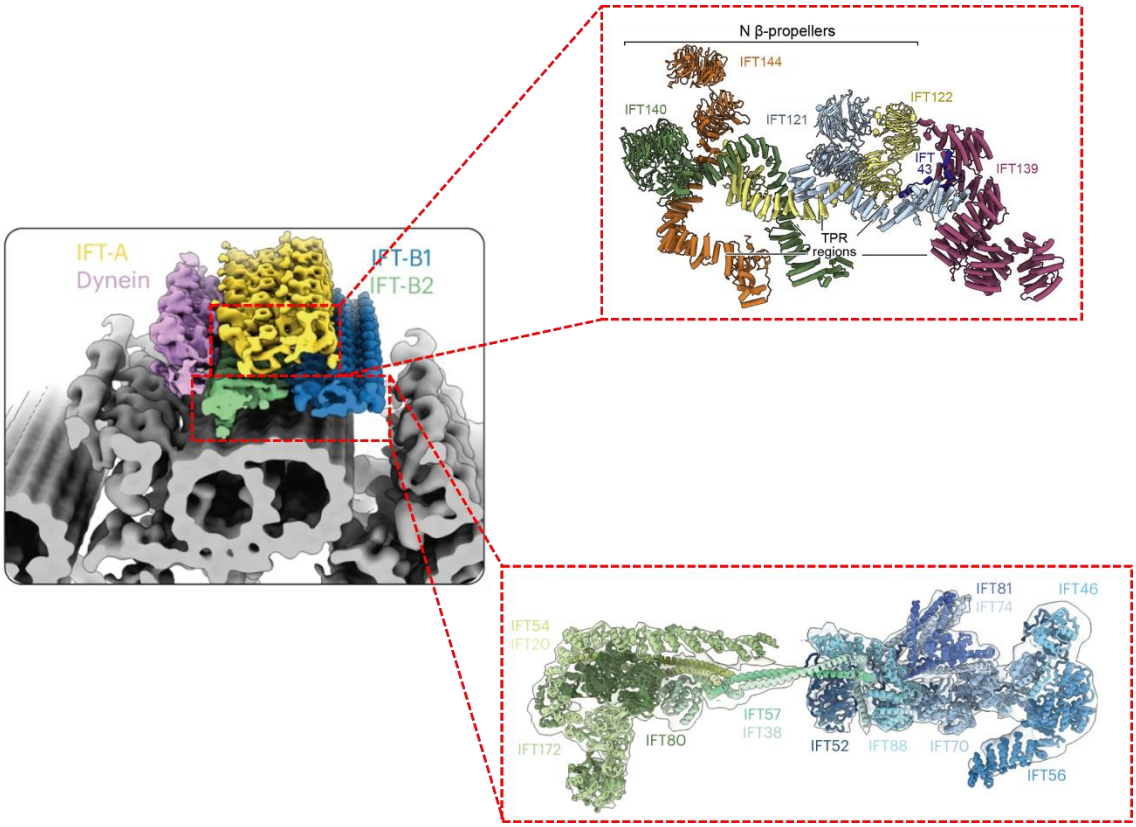

Figure 1 – Structure of the IFT-A and IFT-B complexes in the anterograde IFT train. The IFT-A complex is interconnected. IFT122 bridges the IFT-A core (IFT144, IFT140, and IFT122), and the IFT-A peripheral (IFT121 and IFT139). IFT-B is divided into the IFT-B1 (right) and IFT-B2 (left) subcomplexes bridged by the connecting tetramer (IFT57, IFT38, IFT52, and IFT88) (Nakayama and Katoh, 2020). Image adapted from (Lacey et al., 2023) and (Hesketh et al., 2022).

3.2. Results

3.2.1. IFT-A complex remains mostly coupled to dynein-2 in the absence of WDR-60

In our previous work, we observed that the ciliary distribution of IFT-140 in the absence of WDR-60 closely resembles the one of dynein-2 (De-Castro et al., 2022), suggesting that IFT-140 remains directly, or indirectly, coupled to dynein-2 during retrograde IFT. To assess if the IFT-A complex is entirely coupled to dynein-2 in the absence of WDR-60, we analyzed the ciliary distribution of IFT-144 and IFT-121 (DYF-2 and IFTA-1 in *C. elegans*, respectively), two components which localize at opposite ends of the IFT-A complex (Hesketh et al., 2022, Jiang et al., 2023, Lacey et al., 2023, Ma et al., 2023, McCafferty et al., 2022, Meleppattu et al., 2022). Although IFT-139 is more peripheral than IFT-121 in the IFT-A complex, it is coded in chromosome III of *C. elegans* (very near to the *wdr-60 locus*), which impeded the crossing of *ift-139* and *wdr-60* alleles.

The absence of WDR-60 led to a significant increase of the ciliary levels of both IFT-144 and IFT-121 **(Figure 2C and 2F)**, in contrast to dynein-2, whose ciliary levels were reduced (De-Castro et al., 2022). Regarding ciliary distribution, IFT-144 behaved very similar to dynein-2 in the absence of WDR-60, as we observed a strong accumulation of this component at the distal side of the TZ barrier, that was fully prevented when we removed the NPHP module from the TZ **(Figure 2A and 2B)**. On the other hand, loss of WDR-60 caused IFT-121 to accumulate not only at the distal side of the TZ, but also around the end of the middle segment of cilia **(Figure 2D and 2E)**. This observation suggests that IFT-121 might be more weakly bound or only partially coupled to dynein-2 in the absence of WDR-60. However, removal of the NPHP module from the TZ prevented the proximal ciliary accumulation of IFT-121, which is in agreement with our proposed model that the TZ offers resistance to the exit of retrograde IFT trains. Interestingly, we also noticed that the sole removal of the NPHP module from the TZ also slightly reduced the ciliary recruitment of these IFT-A components **(Figure 2C and 2F)**, as was the case for dynein-2 (De-Castro et al., 2022).

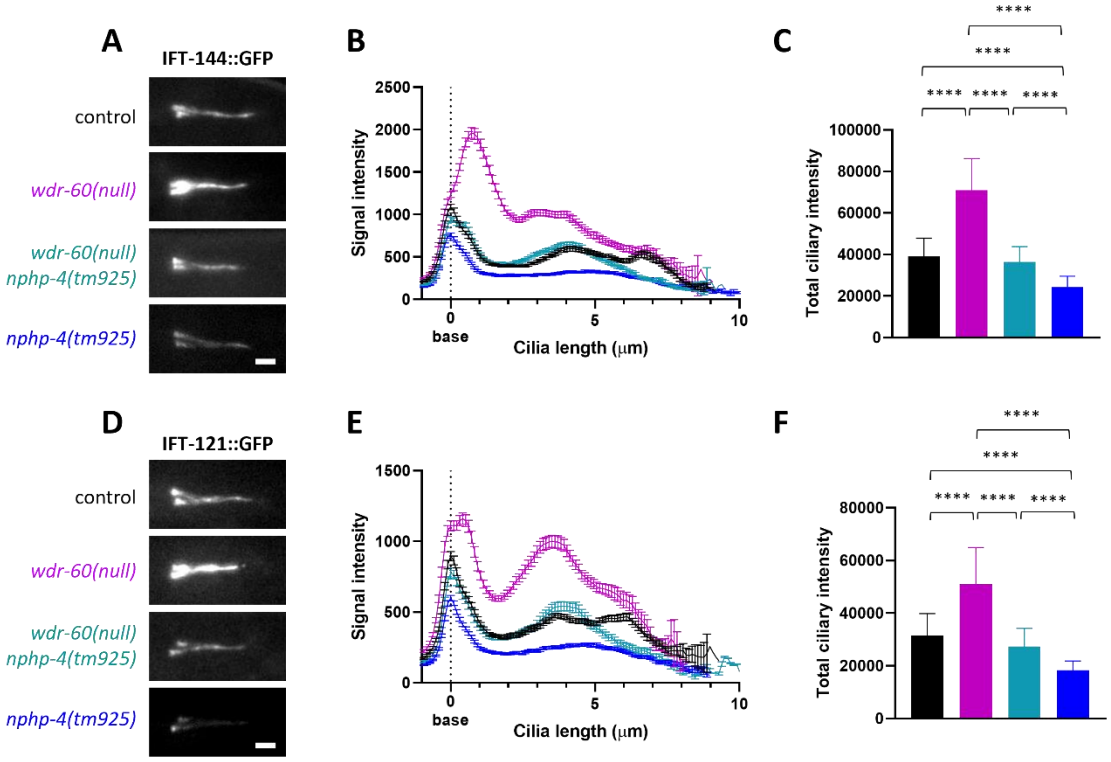

Figure 2 – IFT-A behavior in *wdr-60* and *nphp-4* mutant cilia. (A and D) Representative examples of phasmid cilia expressing IFT-144::GFP and IFT-121::GFP (controls), respectively, and in combination with the *wdr-60* and/or *nphp-4* mutant backgrounds. Scale bars: 2 μm. **(B and E)** Ciliary distribution of IFT-144 and IFT-121, respectively, in the aforementioned genetic conditions. For each condition, n ≥ 58 cilia for IFT-144::GFP, and n ≥ 48 cilia for IFT-121::GFP. **(C and F)** Total intensity of IFT-144::GFP and IFT-121::GFP, respectively, inside cilia of controls and *wdr-60*/*nphp-4* mutants. The Kruskal-Wallis test followed by Dunn's multiple comparisons were used to analyze the datasets. ****, P ≤ 0.0001.

3.2.2. Most of the IFT-B complex remains connected to dynein-2 in the absence of WDR-60

Previously, we observed that IFT-74 accumulated along the whole length of cilia in the absence of WDR-60, in contrast to IFT-140 and the dynein-2 HC, which accumulated predominantly at the distal side of the TZ (De-Castro et al., 2022). This led us to believe that, in the absence of WDR-60, IFT-74 was uncoupled from dynein-2 during retrograde IFT. To further clarify how the IFT-B complex behaves in the absence of WDR-60, we analyzed the ciliary distribution of three additional IFT-B subunits: IFT-54 (DYF-11 in *C. elegans*), from the IFT-B2 subcomplex, and IFT-52 and IFT-46 (OSM-6 and DYF-6 in *C.*

elegans, respectively), from the IFT-B1 subcomplex. Also, we analyzed the effects of removing the NPHP module from the TZ in these mutants.

Akin to IFT-A subunits, the loss of WDR-60 also led to a significant increase of the ciliary levels of IFT-B subunits **(Figure 3C, 3F, 3I, and 3L)**. Also, we observed that IFT-54, IFT-52, and IFT-46 were found to accumulate predominantly at the distal side of the TZ, in the absence of WDR-60 **(Figure 3B, 3H, and 3K)**, as was the case for the dynein-2 HC. This result suggests that these IFT components also remain coupled to dynein-2 during retrograde IFT, in the absence of WDR-60. In contrast, loss of WDR-60 caused IFT-74 to accumulate along the whole length of cilia **(Figure 3E)**, as previously observed (De-Castro et al., 2022). This observation indicates that loss of WDR-60 may lead to uncoupling between IFT-74 and dynein-2 during retrograde IFT. Interestingly, however, removal of the NPHP module prevented the ciliary accumulations at the distal side of the TZ of all the IFT-B components analyzed, including a large portion of IFT-74 **(Figure 3B, 3H, and 3K)**. The latter result suggests that even if more weakly bound to the IFT train in the absence of WDR-60, IFT-74 can remain associated as long as IFT traffic jams are avoided. Finally, as we observed when tracking IFT-A subunits, we also noted that the sole removal of the NPHP module from the TZ also slightly reduced the ciliary levels of all IFT-B subunits analyzed **(Figure 3C, 3F, 3I, and 3L)**.

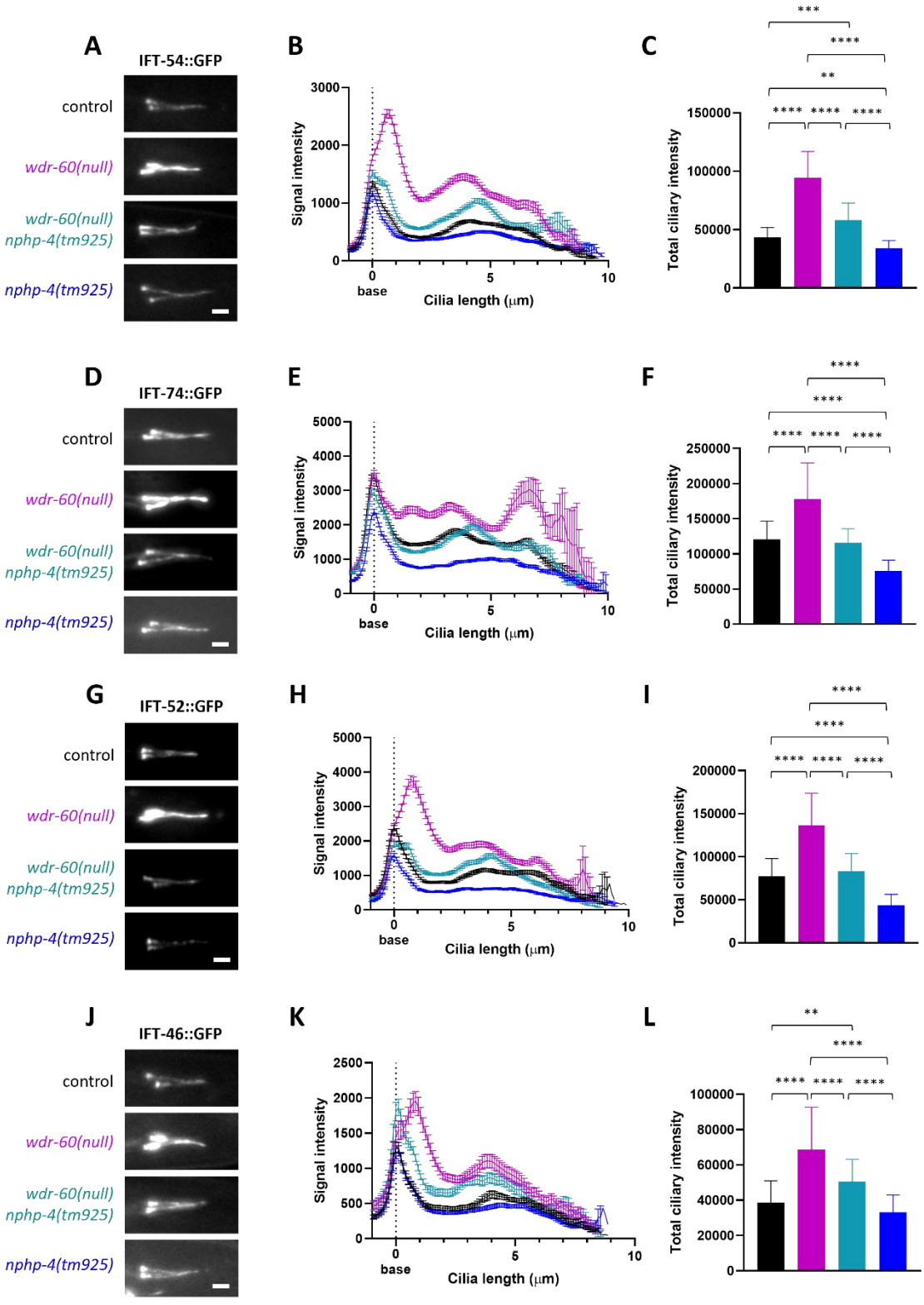

Figure 3 – IFT-B behavior in *wdr-60* and *nphp-4* mutant cilia. (A, D, G, and J) Representative examples of phasmid cilia expressing IFT-54::GFP, IFT-74::GFP, IFT-52::GFP, and IFT-46::GFP (controls), respectively, and in combination with the *wdr-60* and/or *nphp-4* mutant backgrounds. Scale bars: 2 μm. **(B, E, H, and K)** Ciliary distribution of IFT-54, IFT-74, IFT-52, and IFT-46, respectively, in the aforementioned genetic conditions. For each condition, n ≥ 52 cilia for IFT-54::GFP, n ≥ 62 cilia for IFT-74::GFP, n ≥ 50 for IFT-52::GFP, and n ≥ 30 cilia for IFT-46::GFP. **(C, F,**

I, and L) Total intensity of IFT-54::GFP, IFT-74::GFP, IFT-52::GFP, and IFT-46::GFP, respectively, inside cilia of controls and *wdr-60*/*nphp-4* mutants. The Kruskal-Wallis test followed by Dunn's multiple comparisons were used to analyze the datasets in **C** and **F**. The one-way ANOVA test followed by Tukey's multiple comparisons were used to analyze the datasets in **I** and **L**. **, P ≤ 0.01; ***, P ≤ 0.001; ****, P ≤ 0.0001.

3.2.3. Heterotrimeric kinesin-2 remains coupled to dynein-2 in the absence of WDR-60

We already showed that loss of WDR-60 results in a strong accumulation of heterotrimeric kinesin-2 at the distal side of the TZ, while only having a modest effect on the ciliary distribution of the homodimeric kinesin-2 (De-Castro et al., 2022). This may be explained by the fact that homodimeric kinesin-2 is mostly present at the distal segment of the cilium (Prevo et al., 2015), while the major phenotype resulting from the loss of WDR-60 is the accumulation of IFT material near its base.

Here, we sought to further dissect how the heterotrimeric kinesin-2 behaves upon loss of WDR-60 and the NPHP module, by re-analyzing the ciliary distribution of the associated protein KAP-1, and expanding these analyses to the motor subunit KLP-20 (*C. elegans* homolog of KIF3A). Loss of WDR-60 also led to an increase of the ciliary levels of both subunits, and their accumulation near the base of cilia **(Figure 4)**. In turn, this accumulation was extensively rescued upon removal of the NPHP module from the TZ **(Figure 4B and 4E)**, indicating that the heterotrimeric kinesin-2 remains coupled to dynein-2 in the absence of WDR-60. Interestingly, the removal of the NPHP module from the TZ did not alter heterotrimeric kinesin-2 levels at the base, and only slightly reduced its levels inside cilia **(Figure 4B, 4C, 4E, and 4F)**.

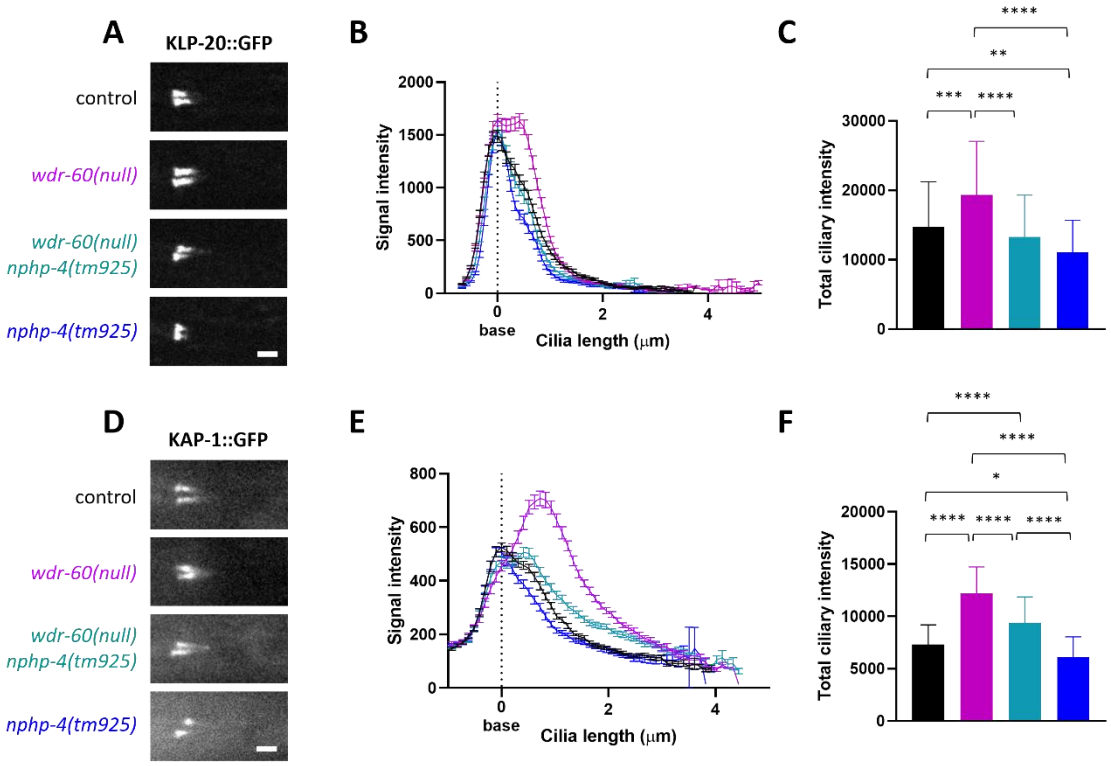

Figure 4 – Heterotrimeric kinesin-2 accumulates near the ciliary base in the absence of WDR-60. (A and D) Representative examples of phasmid cilia expressing KLP-20::GFP and KAP-1::GFP (controls), respectively, and in combination with the *wdr-60* and/or *nphp-4* mutant backgrounds. Scale bars: 2 μm. **(B and E)** Ciliary distribution of KLP-20 and KAP-1, respectively, in the aforementioned genetic conditions. For each condition, n ≥ 64 cilia for KLP-20::GFP, and n ≥ 44 cilia for KAP-1::GFP. **(C and F)** Total intensity of KLP-20::GFP and KAP-1::GFP, respectively, inside cilia of controls and *wdr-60*/*nphp-4* mutants. The Kruskal-Wallis test followed by Dunn's multiple comparisons were used to analyze the datasets in **C**. The one-way ANOVA test followed by Tukey's multiple comparisons were used to analyze the datasets in **F**. *, P ≤ 0.05; **, P ≤ 0.01; ***, P ≤ 0.001; ****, P ≤ 0.0001.

3.2.4. BBS-1 accumulates inside cilia in the absence of WDR-60

The BBSome is a complex of 8 different Bardet-Biedl Syndrome proteins that is involved in the removal of activated GPCRs from cilia (Ye et al., 2018). In *C. elegans*, it is also believed to participate in the assembly of anterograde IFT trains, by connecting the IFT-A and IFT-B complexes at the base of cilia (Wei et al., 2012, Snow et al., 2004, Ou et al., 2005).

As observed for the other IFT proteins, the ciliary levels of BBS-1 were also increased in the absence of WDR-60 **(Figure 5C)**. When we analyzed the ciliary distribution of BBS-1

upon loss of WDR-60, we observed a strong accumulation along the whole length of cilia, but not particularly near the base **(Figure 5A and 5B)**. This result suggests that the BBSome becomes uncoupled from dynein-2 in the absence of WDR-60. Interestingly, removal of the NPHP module in this condition strongly reduced the levels of BBS-1 in the distal segment. However, a strong accumulation remained near the end of the middle segment. In turn, the sole removal of the NPHP module reduced the ciliary levels of BBS-1, similar to what occurred for IFT-A and IFT-B components **(Figure 5C)**.

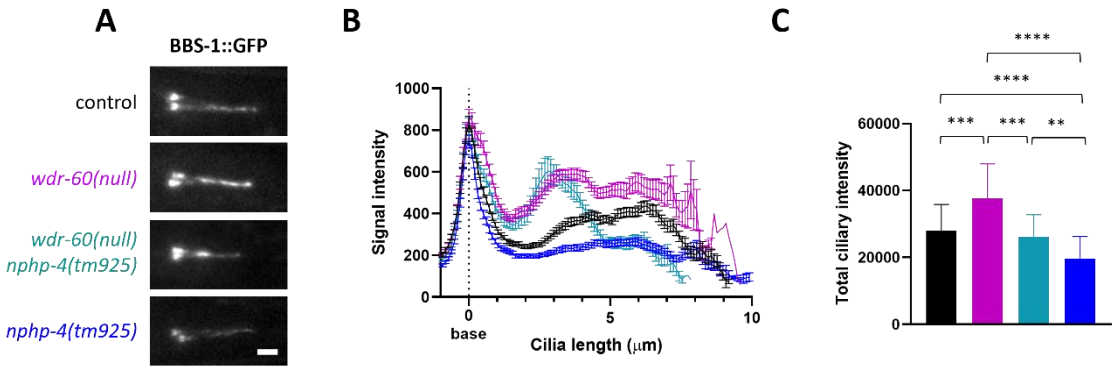

Figure 5 – BBS-1 accumulates inside cilia in the absence of WDR-60. (A) Representative examples of phasmid cilia expressing BBS-1::GFP (control), and in combination with the *wdr-60* and/or *nphp-4* mutant backgrounds. Scale bar: 2 μm. **(B)** Ciliary distribution of BBS-1 in these genetic conditions. For each condition, n ≥ 36 cilia. **(C)** Total intensity of BBS-1::GFP inside cilia of controls and *wdr-60*/*nphp-4* mutants. The Kruskal-Wallis test followed by Dunn's multiple comparisons were used to analyze the datasets. **, P ≤ 0.01; ***, P ≤ 0.001; ****, P ≤ 0.0001.

3.3. Discussion

3.3.1. Most of the IFT machinery remains coupled to dynein-2 in the absence of WDR-60

Here, we show that the total ciliary levels of the analyzed IFT components were increased in the absence of WDR-60, in contrast to dynein-2, whose levels were reduced. These observations indicate that the loss of WDR-60 does indeed impair retrograde IFT (De-

Castro et al., 2022), impeding the retrieval of IFT components back to the ciliary base, leading to their accumulation inside cilia.

We also observed that loss of WDR-60 led to the accumulation of most of the IFT machinery predominantly at the distal side of the TZ, as was observed for the dynein-2 motor. This indicates that, in the absence of WDR-60, most components of IFT remain coupled to dynein-2 during retrograde IFT. The few IFT components not found to accumulate mostly at the distal side of the TZ were IFT-121, IFT-74, and BBS-1. Loss of WDR-60 caused IFT-121 to also accumulate near the end of the middle segment, while IFT-74 and BBS-1 accumulated along the whole length of cilia.

When looking at IFT-121 and IFT-74, particularly, upon loss of WDR-60 **(Figures 2D, 2E, 3D, and 3E)**, a few images led us to consider the possibility that some cilia may be shorter (~4 µm) and accumulate material at the tip, hence the strong accumulations that we observe around 4 µm from the base. However, to be able to test such hypothetical scenario, we would have to co-image these IFT components with a ciliary membrane marker, or carry out extensive transmission electron microscopy analyses. Nevertheless, the observed accumulations indicate that, in the absence of WDR-60, these subunits may be at least partially uncoupled to dynein-2 during retrograde IFT. Accordingly, it has already been observed in human cells that loss of WDR60 leads to the accumulation of IFT88 and IFT54 at the base and at the tip of cilia, while IFT140 accumulates along the whole length of cilia (Hamada et al., 2018, Tsurumi et al., 2019, Vuolo et al., 2018), further indicating that loss of WDR60 may at least lead to partial uncoupling of specific IFT components from the retrograde train.

The N-terminus of the dynein-1 IC is known to interact with the regulatory proteins NudE/NudEL and dynactin (McKenney et al., 2011). Hence, it is possible that the ICs of dynein-2 may also share this regulatory function by binding components from the IFT-A/B complexes. Indeed, both IFT-121 and IFT-74 were enriched in immunoprecipitates from lysates of RPE1 cells expressing HA-tagged WDR60 (Hiyamizu et al., 2023). Therefore, it is plausible that loss of WDR-60 may hinder the interaction between IFT-121/IFT-74 and dynein-2 motors in retrograde IFT trains, leading to their uncoupling during IFT. We do note, however, that the loss of WDR-60 could lead to uncoupling of cargo due to structural alterations in the dynein-2 complex, and not only due to loss of direct protein interactions involving WDR-60.

Nonetheless, it is peculiar that only some subunits of the IFT-A and IFT-B complexes become uncoupled from dynein-2 upon loss of WDR-60, given the strong interactions established within these complexes (Lacey et al., 2023, Katoh et al., 2016, Hirano et al.,

2017). However, it is also worth noting that some of these strong interactions may occur specifically in the anterograde IFT trains, rather than in the retrograde IFT trains. Upon train remodeling at the ciliary tip, IFT-A/B complexes could possibly reorganize in a way that some IFT components are more prone to be uncoupled from retrograde trains upon loss of WDR-60. Unfortunately, the structure of the retrograde IFT trains has not yet been characterized, in contrast to that of the anterograde IFT trains. This could be in part because retrograde trains are smaller than anterograde trains, and harder to detect (De-Castro et al., 2022, Mijalkovic et al., 2017, Pigino et al., 2009, Stepanek and Pigino, 2016). It is also conceivable that, despite having a normal ciliary distribution in a wild type background, tagging some of these IFT components may also facilitate their uncoupling from WDR-60-deficient retrograde IFT trains.

Regarding the BBSome, since this complex is involved in the retrieval of activated GPCRs from cilia (Ye et al., 2018), we expect it to be bound to the periphery of the retrograde trains, close to the ciliary membrane. Hence, the uncoupling of BBS-1 could be a downstream effect of the uncoupling of components from the IFT-A/B complexes, or affecting the structure of dynein-2 and/or retrograde IFT trains.

In the future, we could perform single-molecule imaging of IFT components to further help elucidate the dynamics of the retrograde IFT machinery in the absence of WDR-60. It would be particularly interesting to analyze the IFT kinetics of IFT-121, IFT-74, and BBS-1, as these subunits seem to behave differently from dynein-2 in the absence of WDR-60.

Nevertheless, we showed in our previous publication that the chemotaxis index and osmotic avoidance of *wdr-60* KO worms were only mildly altered, relative to controls (De-Castro et al., 2022). This indicates that, despite the ciliary accumulations of IFT material that we observed, there must still occur partial retrieval of cargo back to the ciliary base upon loss of WDR-60, given that much of the ciliary function is still retained.

3.3.2. Heterotrimeric kinesin-2 motors return to the ciliary base by dynein-2-driven retrograde IFT

KLP-20 and KAP-1 also accumulated near the base in the absence of WDR-60, and this accumulation was almost completely prevented when we removed the NPHP module from the TZ, as was observed for the dynein-2 motor. This indicates that, upon loss of WDR-60 in *C. elegans*, the heterotrimeric kinesin-2 is still being transported back to the ciliary base as a cargo of dynein-2, in contrast to *Chlamydomonas*, where the heterotrimeric kinesin-2

is thought to return to the ciliary base by diffusion (Pedersen et al., 2006, Chien et al., 2017, Engel et al., 2009). This notion of dynein-2-dependant retrieval of kinesin-2 motors in *C. elegans* is in agreement with previous studies that show similar retrograde kinetics between dynein-2 and kinesin-2 subunits (Prevo et al., 2015, Mijalkovic et al., 2017, De-Castro et al., 2022, Yi et al., 2017).

3.3.3. Loss of NPHP-4 reduces the ciliary levels of IFT components, and facilitates the ciliary exit of retrograde trains

Interestingly, removal of the NPHP module from the TZ through the disruption of NPHP-4 also reduced the ciliary levels of many IFT components analyzed. Nonetheless, we do note that, apart from being a structural component of the TZ, NPHP-4 has been also observed at the transition fibers (Jensen et al., 2015), structures that have been reported to be involved in the recruitment of TZ and IFT components to the basal body (Garcia-Gonzalo and Reiter, 2017). As such, it is possible that the pool of NPHP-4 at the transition fibers may also have a small contribution for the recruitment of ciliary components.

However, we underline that the disruption of the NPHP module in the absence of WDR-60 prevented the accumulation of all analyzed IFT components at the distal side of the TZ, indicating that dynein-2 motors are able to exit cilia along with every IFT component that is coupled to it.

3.4. References

CHIEN, A., SHIH, S. M., BOWER, R., TRITSCHLER, D., PORTER, M. E. & YILDIZ, A. 2017. Dynamics of the IFT machinery at the ciliary tip. *Elife,* 6.

DE-CASTRO, A. R. G., RODRIGUES, D. R. M., DE-CASTRO, M. J. G., VIEIRA, N., VIEIRA, C., CARVALHO, A. X., GASSMANN, R., ABREU, C. M. C. & DANTAS, T. J. 2022. WDR60-mediated dynein-2 loading into cilia powers retrograde IFT and transition zone crossing. *J Cell Biol,* 221.

ENGEL, B. D., LUDINGTON, W. B. & MARSHALL, W. F. 2009. Intraflagellar transport particle size scales inversely with flagellar length: revisiting the balance-point length control model. *J Cell Biol,* 187**,** 81-9.

GARCIA-GONZALO, F. R. & REITER, J. F. 2017. Open Sesame: How Transition Fibers and the Transition Zone Control Ciliary Composition. *Cold Spring Harb Perspect Biol,* 9.

HAMADA, Y., TSURUMI, Y., NOZAKI, S., KATOH, Y. & NAKAYAMA, K. 2018. Interaction of WDR60 intermediate chain with TCTEX1D2 light chain of the dynein-2 complex is crucial for ciliary protein trafficking. *Mol Biol Cell,* 29**,** 1628-1639.

HESKETH, S. J., MUKHOPADHYAY, A. G., NAKAMURA, D., TOROPOVA, K. & ROBERTS, A. J. 2022. IFT-A structure reveals carriages for membrane protein transport into cilia. *Cell,* 185**,** 4971-4985 e16.

HIRANO, T., KATOH, Y. & NAKAYAMA, K. 2017. Intraflagellar transport-A complex mediates ciliary entry and retrograde trafficking of ciliary G protein-coupled receptors. *Mol Biol Cell,* 28**,** 429-439.

HIYAMIZU, S., QIU, H., VUOLO, L., STEVENSON, N. L., SHAK, C., HEESOM, K. J., HAMADA, Y., TSURUMI, Y., CHIBA, S., KATOH, Y., STEPHENS, D. J. & NAKAYAMA, K. 2023. Multiple interactions of the dynein-2 complex with the IFT-B complex are required for effective intraflagellar transport. *J Cell Sci,* 136.

JENSEN, V. L., LI, C., BOWIE, R. V., CLARKE, L., MOHAN, S., BLACQUE, O. E. & LEROUX, M. R. 2015. Formation of the transition zone by Mks5/Rpgrip1L establishes a ciliary zone of exclusion (CIZE) that compartmentalises ciliary signalling proteins and controls PIP2 ciliary abundance. *EMBO J,* 34**,** 2537-56.

JIANG, M., PALICHARLA, V. R., MILLER, D., HWANG, S. H., ZHU, H., HIXSON, P., MUKHOPADHYAY, S. & SUN, J. 2023. Human IFT-A complex structures provide molecular insights into ciliary transport. *Cell Res,* 33**,** 288-298.

KATOH, Y., TERADA, M., NISHIJIMA, Y., TAKEI, R., NOZAKI, S., HAMADA, H. & NAKAYAMA, K. 2016. Overall Architecture of the Intraflagellar Transport (IFT)-B Complex Containing Cluap1/IFT38 as an Essential Component of the IFT-B Peripheral Subcomplex. *J Biol Chem,* 291**,** 10962-75.

LACEY, S. E., FOSTER, H. E. & PIGINO, G. 2023. The molecular structure of IFT-A and IFT-B in anterograde intraflagellar transport trains. *Nat Struct Mol Biol,* 30**,** 584-593.

MA, Y., HE, J., LI, S., YAO, D., HUANG, C., WU, J. & LEI, M. 2023. Structural insight into the intraflagellar transport complex IFT-A and its assembly in the anterograde IFT train. *Nat Commun,* 14**,** 1506.

MCCAFFERTY, C. L., PAPOULAS, O., JORDAN, M. A., HOOGERBRUGGE, G., NICHOLS, C., PIGINO, G., TAYLOR, D. W., WALLINGFORD, J. B. & MARCOTTE, E. M. 2022.

Integrative modeling reveals the molecular architecture of the intraflagellar transport A (IFT-A) complex. *Elife,* 11.

MCKENNEY, R. J., WEIL, S. J., SCHERER, J. & VALLEE, R. B. 2011. Mutually exclusive cytoplasmic dynein regulation by NudE-Lis1 and dynactin. *J Biol Chem,* 286**,** 39615-22.

MELEPPATTU, S., ZHOU, H., DAI, J., GUI, M. & BROWN, A. 2022. Mechanism of IFT-A polymerization into trains for ciliary transport. *Cell,* 185**,** 4986-4998 e12.

MIJALKOVIC, J., PREVO, B., OSWALD, F., MANGEOL, P. & PETERMAN, E. J. 2017. Ensemble and single-molecule dynamics of IFT dynein in Caenorhabditis elegans cilia. *Nat Commun,* 8**,** 14591.

NAKAYAMA, K. & KATOH, Y. 2020. Architecture of the IFT ciliary trafficking machinery and interplay between its components. *Crit Rev Biochem Mol Biol,* 55**,** 179-196.

OU, G., BLACQUE, O. E., SNOW, J. J., LEROUX, M. R. & SCHOLEY, J. M. 2005. Functional coordination of intraflagellar transport motors. *Nature,* 436**,** 583-7.

PEDERSEN, L. B., GEIMER, S. & ROSENBAUM, J. L. 2006. Dissecting the molecular mechanisms of intraflagellar transport in chlamydomonas. *Curr Biol,* 16**,** 450-9.

PETRIMAN, N. A., LOUREIRO-LOPEZ, M., TASCHNER, M., ZACHARIA, N. K., GEORGIEVA, M. M., BOEGHOLM, N., WANG, J., MOURAO, A., RUSSELL, R. B., ANDERSEN, J. S. & LORENTZEN, E. 2022. Biochemically validated structural model of the 15-subunit intraflagellar transport complex IFT-B. *EMBO J,* 41**,** e112440.

PIGINO, G., GEIMER, S., LANZAVECCHIA, S., PACCAGNINI, E., CANTELE, F., DIENER, D. R., ROSENBAUM, J. L. & LUPETTI, P. 2009. Electron-tomographic analysis of intraflagellar transport particle trains in situ. *J Cell Biol,* 187**,** 135-48.

PREVO, B., MANGEOL, P., OSWALD, F., SCHOLEY, J. M. & PETERMAN, E. J. 2015. Functional differentiation of cooperating kinesin-2 motors orchestrates cargo import and transport in C. elegans cilia. *Nat Cell Biol,* 17**,** 1536-45.

SNOW, J. J., OU, G., GUNNARSON, A. L., WALKER, M. R., ZHOU, H. M., BRUST-MASCHER, I. & SCHOLEY, J. M. 2004. Two anterograde intraflagellar transport motors cooperate to build sensory cilia on C. elegans neurons. *Nat Cell Biol,* 6**,** 1109-13.

STEPANEK, L. & PIGINO, G. 2016. Microtubule doublets are double-track railways for intraflagellar transport trains. *Science,* 352**,** 721-4.

TSURUMI, Y., HAMADA, Y., KATOH, Y. & NAKAYAMA, K. 2019. Interactions of the dynein-2 intermediate chain WDR34 with the light chains are required for ciliary retrograde protein trafficking. *Mol Biol Cell,* 30**,** 658-670.

VUOLO, L., STEVENSON, N. L., HEESOM, K. J. & STEPHENS, D. J. 2018. Dynein-2 intermediate chains play crucial but distinct roles in primary cilia formation and function. *Elife,* 7.

WEI, Q., ZHANG, Y., LI, Y., ZHANG, Q., LING, K. & HU, J. 2012. The BBSome controls IFT assembly and turnaround in cilia. *Nat Cell Biol,* 14**,** 950-7.

YE, F., NAGER, A. R. & NACHURY, M. V. 2018. BBSome trains remove activated GPCRs from cilia by enabling passage through the transition zone. *J Cell Biol,* 217**,** 1847-1868.

YI, P., LI, W. J., DONG, M. Q. & OU, G. 2017. Dynein-Driven Retrograde Intraflagellar Transport Is Triphasic in C. elegans Sensory Cilia. *Curr Biol,* 27**,** 1448-1461 e7.

CHAPTER IV – Generation of WDR-60 N-terminal deletion mutants for separation of function analyses

4.1. Introduction

We previously uncovered several IFT defects that arise in the absence of WDR-60. Namely, less dynein-2 is loaded onto anterograde IFT trains, and retrograde IFT trains become underpowered and are unable to efficiently cross the transition zone to exit cilia (De-Castro et al., 2022). Moreover, our data suggest that some of the IFT machinery/cargo may become at least partially uncoupled from dynein-2 motors during retrograde IFT. The fact that we observed these various and apparently distinct phenotypes raised the question of whether the reduced incorporation of dynein-2 into cilia led to a detrimental chain of events, or if WDR-60 itself has several functions during IFT. To answer this question, we designed strategies to generate deletion mutants of WDR-60, aiming to probe for possible separation of functions. We previously generated a WDR-60 mutant lacking the C-terminal β-propeller, and observed that, while the dynein-2 behavior resembles the full loss of WDR-60, there was less IFT machinery accumulation inside cilia (De-Castro et al., 2022). This observation hints at a role of WDR-60 N-terminus in retrograde IFT train integrity.

Our analyses here unveil that a very conserved region in the N-terminus of WDR-60 is required to bind the anterograde IFT train. However, deletion of this conserved region did not significantly reduce dynein-2 loading into cilia, further corroborating that other important contacts occur between the dynein-2 complex and the anterograde IFT train. Also, we gather additional evidence that an upstream region of the *wdr-60* locus comprising the third exon is required for the correct transcription of the *wdr-60* gene.

4.2. Results

4.2.1. Generation of WDR-60 N-terminal deletion mutants

The *C. elegans* full-length WDR-60 is a 668 amino acid protein consisting of a mostly disordered N-terminus, and a C-terminal β-propeller **(Figure 1)**. The most upstream functional domain of WDR-60 is a very conserved region in the N-terminus (amino acids 55-73 in *C. elegans*/ 374-392 in humans) that has also been recently shown by the Stephens and the Nakayama labs to bind IFT54 in HEK293T cells (Hiyamizu et al., 2023b),

although the authors were not able to determine whether this interaction occurs in the context of anterograde or retrograde trains. The light chains binding sites have also been mapped. The TCTEX1D2 binding site is a conserved region (amino acids 140-187 in *C. elegans*/ 473-522 in humans) that has been identified by the Nakayama lab (Hamada et al., 2018). Three LC8 binding sites were mapped by the Roberts lab (Toropova et al., 2019), by solving the human dynein-2 complex ultrastructure in vitro (530-535, 541-546, and 553-558 in humans). These conserved sites also contain the consensus sequence for LC8 recognition (Rapali et al., 2011) in *C. elegans*, corresponding to amino acids 195-200, 206-211, and 218-223. The Roadblock binding site, also identified by the Roberts lab (586-606 in humans) (Toropova et al., 2019), corresponds to amino acids 245-266 in *C. elegans*. Lastly, the WD40 domains which form a 7-bladed β-propeller that binds the dynein-2 heavy chain span amino acids 282-647, according to the AlphaFold 3D structure prediction of the *C. elegans* WDR-60 **(Figure 1B)**.

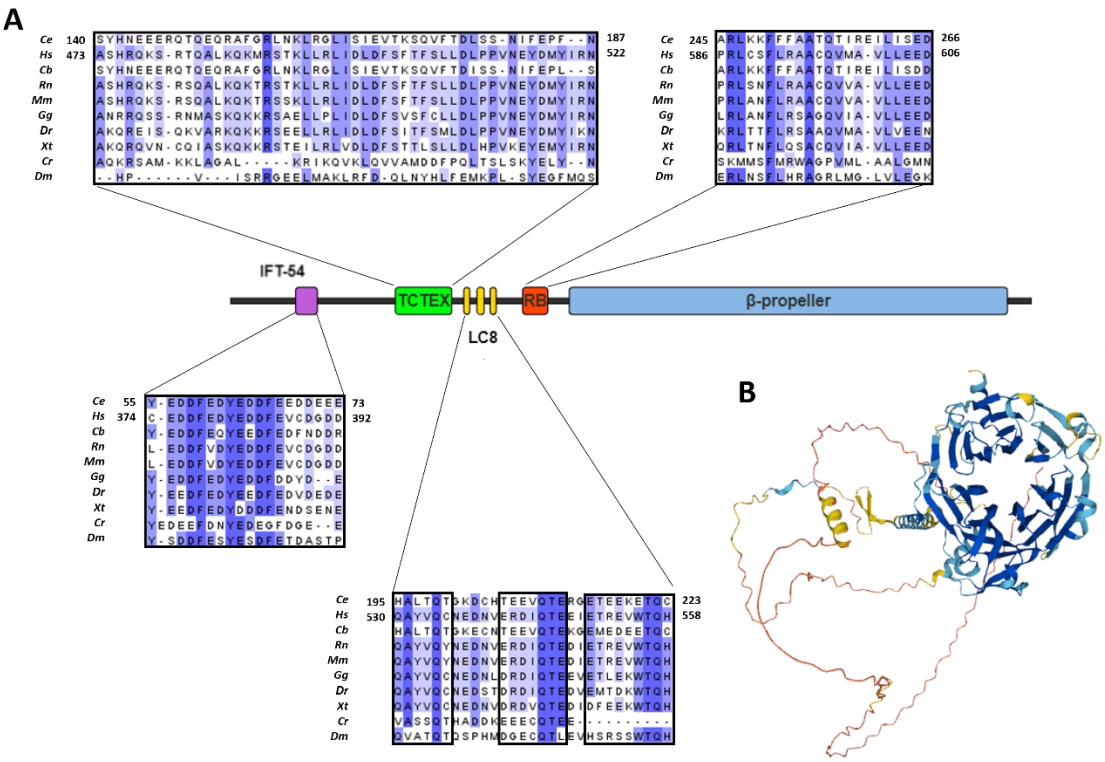

Figure 1 – Functional domains of *C. elegans* WDR-60. (A) Full length WDR-60 and known functional domains: IFT-54 binding site (purple); TCTEX1D2 binding site (green); LC8 binding sites (yellow); Roadblock binding site (red); WD40 domains that fold into a β-propeller (blue). **(B)** 3D structure of the *C. elegans* WDR-60 predicted by AlphaFold (identifier: AF-Q18263-F1).

To probe for WDR-60 separation of function we aimed to generate three N-terminal deletion mutants **(Figure 2)**. The WDR-60(288-668) mutant was intended to consist solely in the β-propeller that binds the dynein-2 heavy chain. However, at the time this mutant was planned there was still no 3D structure available for the *C. elegans* WDR-60, and, based on amino acid sequence alignment with the human WDR60, we reasoned that proline 288 could possibly be the starting point of the β-propeller, given that proline has a high tendency to generate turns. We also aimed to generate the WDR-60(140-668) mutant comprising the regions that bind the light chains, and the β-propeller. Despite missing the upstream N-terminal region, we reason that such mutant should still allow for the assembly of the dynein-2 complex. Lastly, the WDR-60(Δ55-73) mutant lacking only the IFT-54 binding domain.

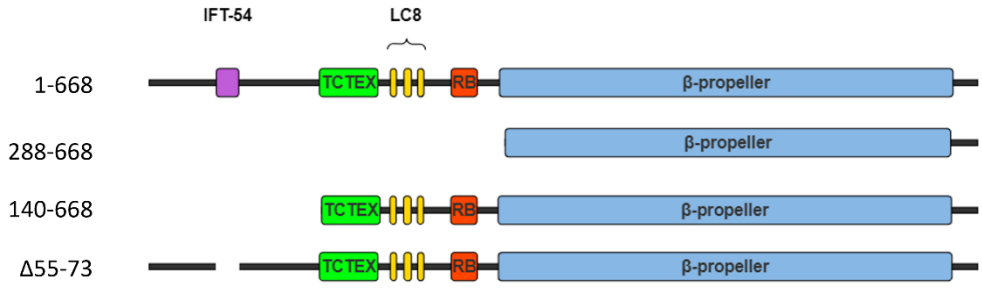

Figure 2 – WDR-60 N-terminal deletion mutants designed for separation of function analyses.

4.2.2. A highly conserved WDR-60 motif in its N-terminus binds anterograde IFT trains

Through the alignment of WDR60 amino acid sequences in a wide range of species, we identified a very conserved region of 19 amino acids (aa 55-74 in *C. elegans*) **(Figure 1A)**. The Stephens and Nakayama labs have recently shown that this conserved domain in the N-terminus of WDR60 is required to bind IFT54 (Hiyamizu et al., 2023b). However, their IP-based experiments with HEK293T lysates did not allow to discriminate whether this interaction occurs in anterograde or retrograde IFT trains. To answer this question, we took advantage of the fact that, in *C. elegans*, loss of the LIC XBX-1 abolishes the ciliary recruitment of the HC CHE-3 (resulting in short, stumpy cilia), but not of WDR-60, which is still targeted to cilia in the absence of CHE-3 and XBX-1 (Yi et al., 2017, De-Castro et al., 2022). This observation implies that WDR-60 alone can establish connections with the anterograde IFT trains to be incorporated into cilia. Strikingly, we found that deleting the 55-

74 amino acids in the *xbx-1* null background abolished the incorporation of WDR-60 into cilia **(Figure 3)**. Together, these observations allow us to conclude that the binding of the conserved WDR-60 motif to IFT trains occurs during anterograde IFT.

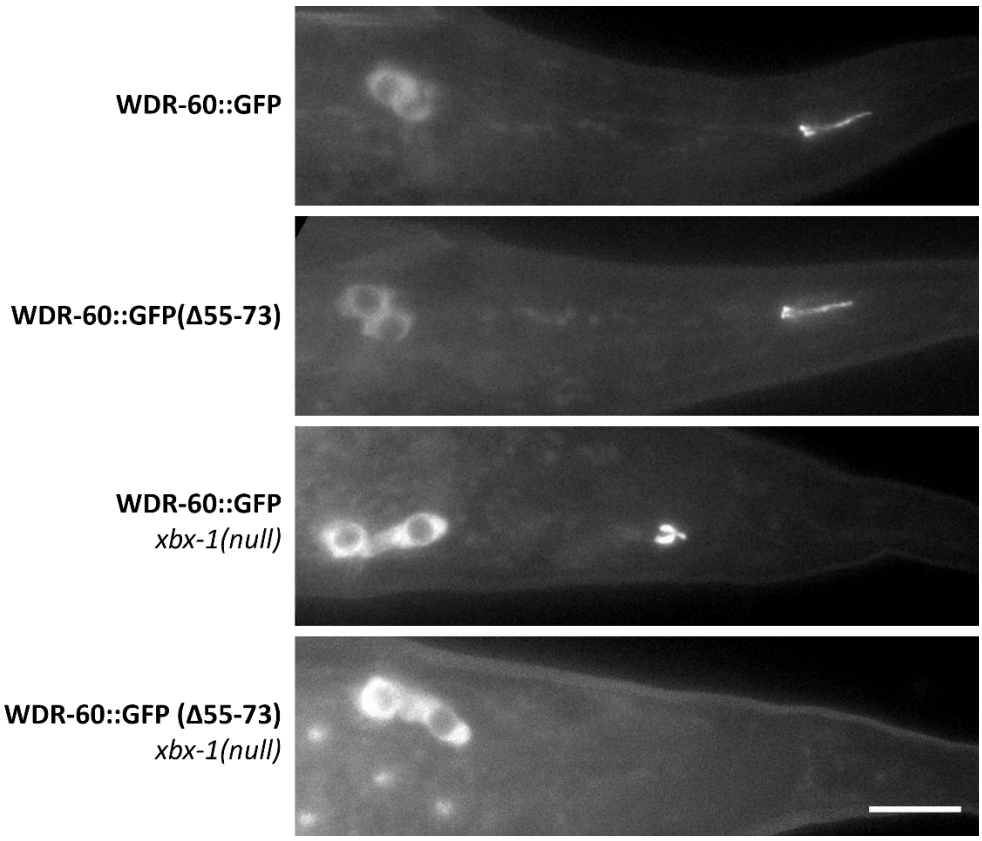

Figure 3 – Amino acids 55-74 of WDR-60 are required to bind IFT trains during anterograde IFT. The images show the distribution of WDR-60 in the phasmid neurons in the various mutants depicted. Scale bar: 10 μm.

We then sought to investigate how the loss of interaction between WDR-60 and IFT-54 in anterograde trains would impact cilia and IFT. An initial analysis of the ciliary distribution of WDR-60::GFP and GFP::CHE-3 did not reveal any striking alteration arising from the loss of amino acids 55-74 of WDR-60 **(Figure 4B, and 4E)**. Also, cilia length was similar to controls **(Figure 4C, and 4F)**. The most noticeable phenotype observed in WDR-60(Δ55-74) mutants was an increased release of ectosomes from the tip of cilia **(Figure 4A, and 4D)**. This higher release of IFT material through the ciliary tip may justify the slight decrease of WDR-60::GFP and GFP::CHE-3 levels at the base of cilia **(Figure 4B, and 4E)**, as less IFT material is being retrieved back to the ciliary base. However, additional experiments

need to be carried out in the future to be able to carefully quantify the release of ectosomes in this WDR-60 mutant strain.

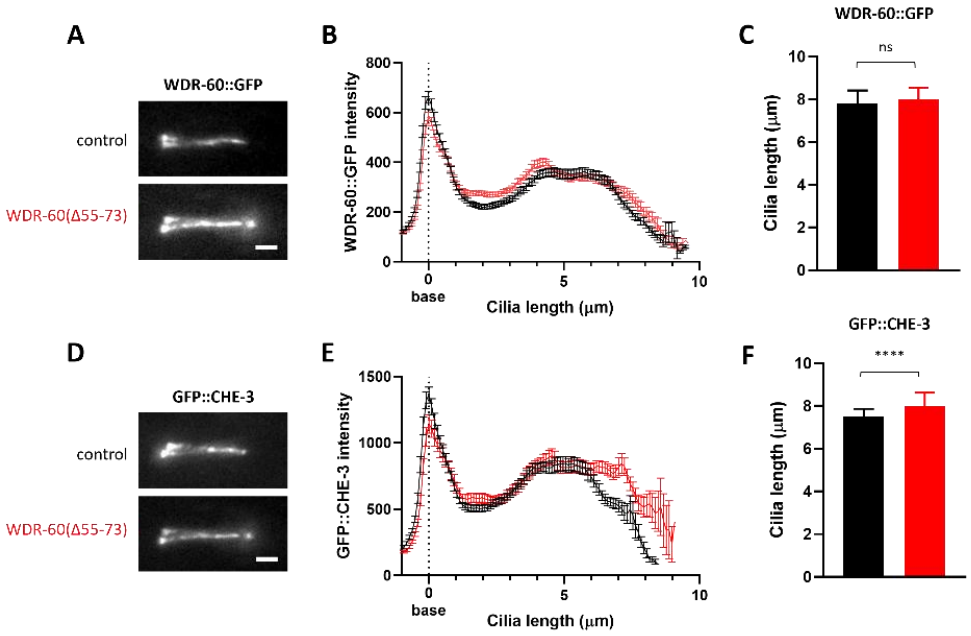

Figure 4 – Deletion of amino acids 55-74 of WDR-60 does not cause severe ciliary defects. (A and D) Representative examples of phasmid cilia expressing WDR-60::GFP or GFP::CHE-3, respectively, in control and WDR-60(Δ55-74) mutants. Scale bars: 2 μm. **(B and E)** Ciliary distribution of WDR-60::GFP and GFP::CHE-3, respectively, in the aforementioned genetic conditions. **(C and F)** Ciliary length of wild-type and WDR-60(Δ55-74) mutant worms measured by fluorescence of WDR-60::GFP and GFP::CHE-3, respectively. The Mann-Whitney test was used to analyze the datasets in **C**, and the Student's t-test was used to analyze the datasets in **F**. Ns, non-significant; ****, P ≤ 0.0001. For WDR-60::GFP analyses in **B** and **C**, n ≥ 66 cilia. For GFP::CHE-3 analyses in **E**, and **F**, n ≥ 38 cilia.

When analyzing the IFT kinetics of the dynein-2 heavy chain in the WDR-60(Δ55-74) mutant, we observed a small increase in both anterograde and retrograde velocities **(Figure 5A, and 5B)**. Also, there was a very small decrease in the levels of dynein-2 heavy chain being loaded onto anterograde IFT trains in the WDR-60(Δ55-74) mutant, when compared to controls **(Figure 5A, and 5C)**, which may result from the loss of interaction between WDR-60 and IFT-54 during anterograde transport. This conclusion could be further validated in the future by mutating the corresponding WDR-60 binding region in IFT-54.

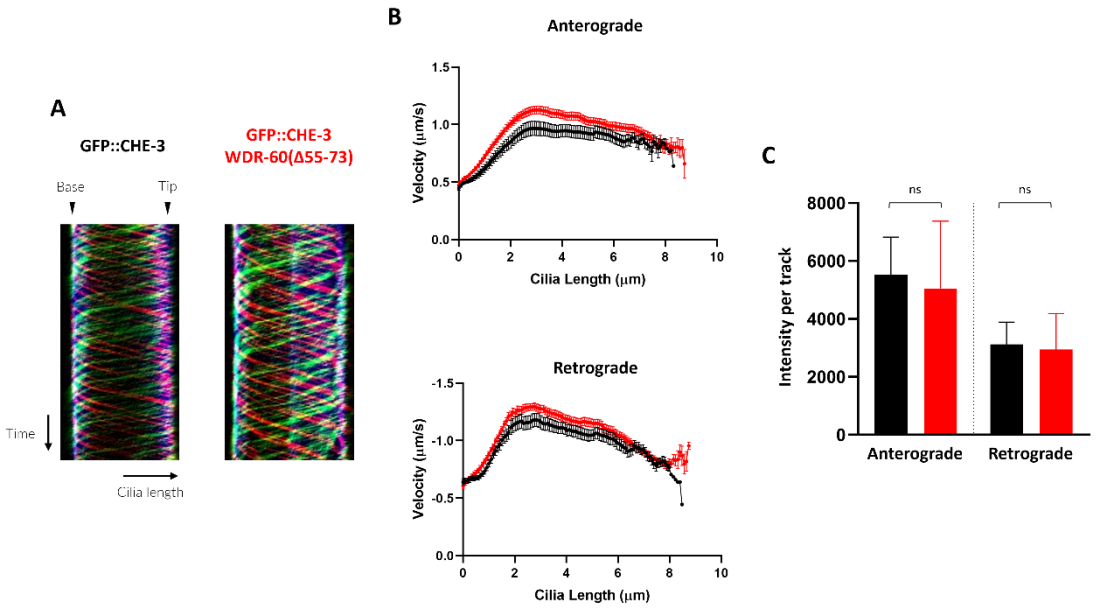

Figure 5 – Deletion of amino acids 55-74 of WDR-60 only mildly impacts IFT kinetics. (A) Representative kymographs of GFP::CHE-3 in wild-type and WDR-60(Δ55-74) mutant worms. **(B)** Anterograde and retrograde IFT velocities of GFP::CHE-3 in wild-type and WDR-60(Δ55-74) mutant worms. **(C)** Average intensity of GFP::CHE-3 in anterograde and retrograde IFT tracks of wild-type and WDR-60(Δ55-74) mutant worms. The Mann-Whitney test was used to analyze the datasets. n ≥ 16 cilia, obtained in a single experiment. Ns, non-significant.

4.2.3. A small DNA segment at the upstream region of *wdr-60* is required for gene expression

The WDR-60::GFP(288-668) mutant, which we had expected to contain only the β-propeller of WDR-60 tagged with GFP, did not produce any detectable fluorescence signal in any subcellular compartment of sensory neurons, namely somas, dendrites, or cilia **(Figure 6)**. Initially, this observation led us to believe that the β-propeller of WDR-60 alone could be destabilized in the absence of the N-terminus, and targeted for degradation. However, we then found out that deleting just the first 138 aa (excluding the initial methionine) to generate the WDR-60::GFP(140-668) mutant also resulted in the complete loss of GFP fluorescence. Unfortunately, we were unable to sequence the region flanking the deletion to validate this mutant, which rendered it unusable.

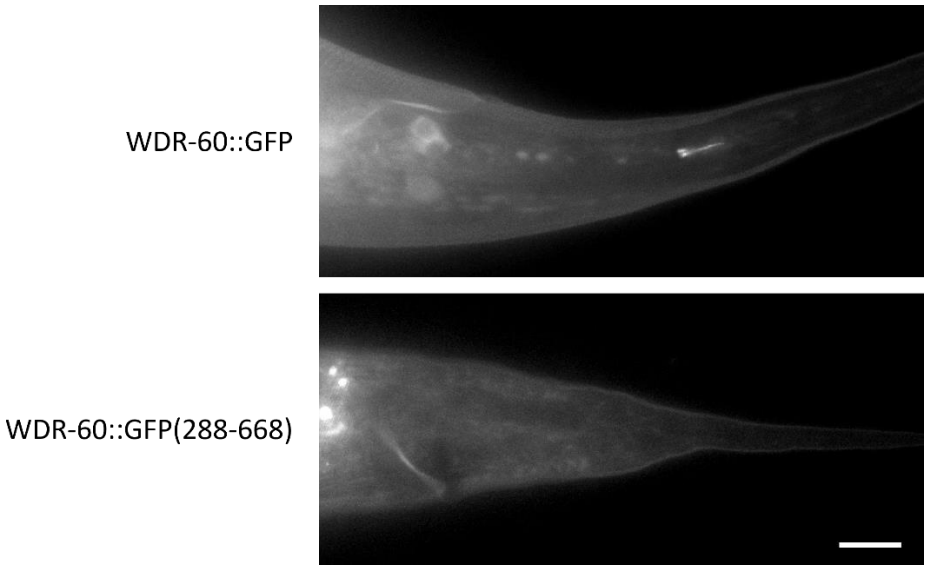

Figure 6 – Loss of the WDR-60 N-terminus abolishes protein expression. Tail region of *C. elegans* mutants expressing WDR-60::GFP, or WDR-60::GFP(288-668). No GFP signal is detected in the sensory neurons of WDR-60::GFP(288-668) mutants. Scale bar: 10 μm.

Having gathered evidence that these *wdr-60* mutants were not expressed, we sought to investigate whether any gene expression regulatory elements could be present in the exonic/intronic sequences deleted in these mutants. Indeed, taking advantage of the online ChIP-seq data compiled in the Wormbase database, we found a small DNA segment within the *wdr-60* locus that binds the transcription factors LSY-2, EFL-1, W03F9.2, and DPL-1 (Boyle et al., 2014, Zhong et al., 2010, Niu et al., 2011) **(Figure 7A)**. This DNA segment comprises the third exon that codes for amino acids 98-138 of WDR-60, and is lost when we generate the WDR-60::GFP(288-668) and WDR-60::GFP(140-668) mutants **(Figure 7B)**. Therefore, it is conceivable that we do not detect GFP signal in sensory neurons of the abovementioned *wdr-60* mutants, because we may be disrupting *wdr-60* gene expression when these are generated.

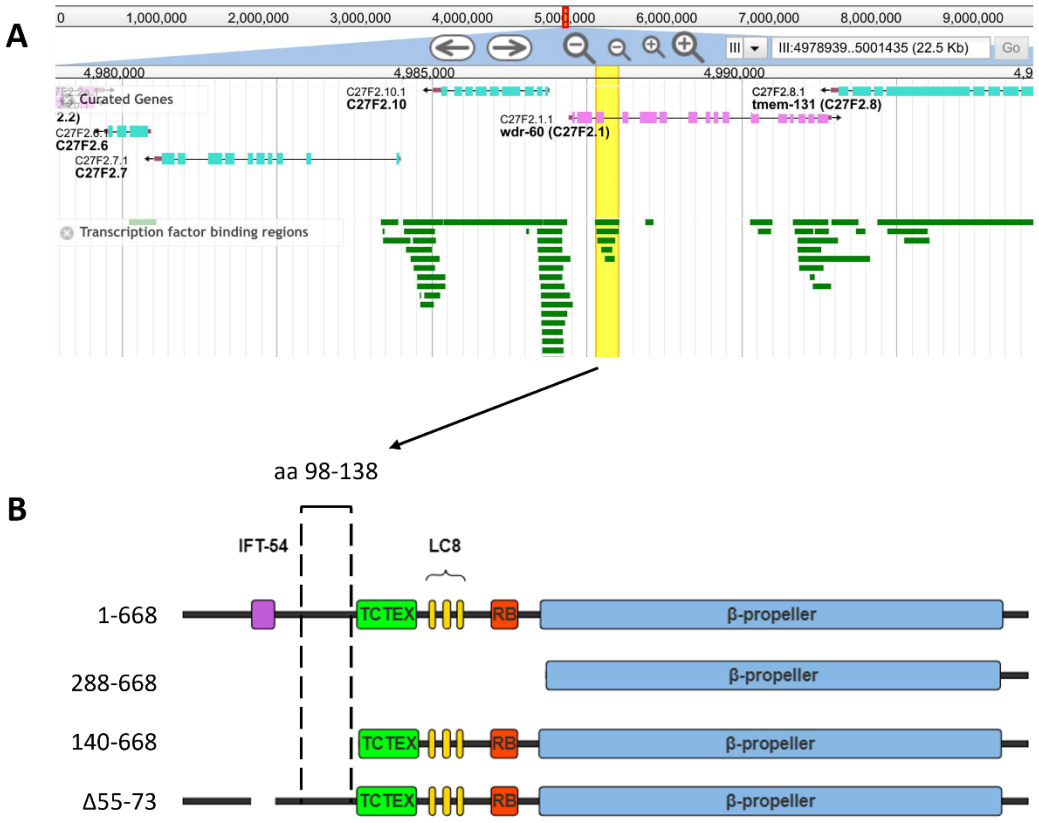

Figure 7 – A region of the *wdr-60* gene, near its third exon, has been implicated in the binding of transcription factors. (A) Wormbase genome browser (JBrowse 2) showing the *wdr-60* gene (pink) and transcription factor binding sites (dark green). Highlighted in yellow is the transcription factor binding site that comprises the third exon of *wdr-60*. **(B)** Amino acids 98-138 of WDR-60, coded in the intragenic transcription factor binding site of *wdr-60* are absent in the WDR-60::GFP(288-668) and WDR-60::GFP(140-668) mutants.

4.3. Discussion

4.3.1. The N-terminus of WDR-60 binds anterograde IFT trains through a very conserved motif

Together with the recent biochemical study (Hiyamizu et al., 2023b), our results strongly suggest that the very conserved patch (amino acids 55-74) in the N-terminus of WDR-60 binds to anterograde IFT trains via IFT-54. However, we found that the deletion of this conserved region only slightly reduced the loading of dynein-2 motors onto anterograde

trains. This observation led us to wonder about the significance of this highly conserved WDR-60 motif across evolution, given that it appears to have a very minor impact on IFT. Nevertheless, our results align with the results of previous studies that deleted this WDR60 motif in human cells (Hiyamizu et al., 2023a, Hiyamizu et al., 2023b). Importantly, our data strengthen the notion that the loading of dynein-2 motors onto anterograde IFT trains involves many other contacts between the dynein-2 complex and IFT-B, as proposed by recent structural studies (Lacey et al., 2023, Toropova et al., 2019, Hiyamizu et al., 2023b, Zhu et al., 2021).

Interestingly, we did observe a significant increase in the release of ectosomes from the ciliary tip of WDR-60(Δ55-74) mutants. A recent study has shown that the release of ectosomes from the tip or the PCMC of *C. elegans* sensory cilia can also serve to release deleterious excess IFT material, thus helping to avoid traffic jams and maintain IFT (Razzauti and Laurent, 2021). Hence, the higher amount of ectosomes detected in the WDR-60(Δ55-74) mutants may be indicative of excess IFT material accumulating at the ciliary tip. However, validating this possibility will require further testing with other IFT markers in the future.

4.3.2. Generation of WDR-60 N-terminal deletion mutants

In this chapter we gathered evidence that it may not be possible to generate some of the intended WDR-60 N-terminal mutants by truncation of the endogenous *locus*, due to the deletion of potential transcription factor binding sequences. One of those transcription factors, LSY-2, has already been shown to be involved in the differentiation of amphid neurons (Johnston and Hobert, 2005), but is not essential for worm survival. On that regard, we intend to generate a strain that combines the endogenous GFP-tagged *wdr-60* with an *lsy-2 null*, and assess the expression of WDR-60::GFP, to further validate our premise.

However, it would still be of high interest to analyze IFT in a WDR-60 mutant containing only the β-propeller, and in WDR-60(140-668). Given that the WDR-60(140-668) mutant still contains the HC-binding β-propeller and the LC binding sites, it should be compatible with normal dynein-2 complex assembly. Therefore, such mutant could allow us to determine if deleting the remaining N-terminal region would mimic the stronger reduction in dynein-2 loading and/or its reduced retrograde velocity observed in the *wdr-60* KO mutant (De-Castro et al., 2022). To circumvent the current problem with expressing these mutants, we can engineer Mos-1-mediated genomic insertions of constructs that express the coding sequence of mutant WDR-60 under the control of *Pift-139*, that has already been shown to

be functional in driving the expression of other coding sequences (Yi et al., 2017, Scheidel and Blacque, 2018). However, one of the drawbacks of this tool is that WDR-60 expression may differ from endogenous levels.

4.4. References

BOYLE, A. P., ARAYA, C. L., BRDLIK, C., CAYTING, P., CHENG, C., CHENG, Y., GARDNER, K., HILLIER, L. W., JANETTE, J., JIANG, L., KASPER, D., KAWLI, T., KHERADPOUR, P., KUNDAJE, A., LI, J. J., MA, L., NIU, W., REHM, E. J., ROZOWSKY, J., SLATTERY, M., SPOKONY, R., TERRELL, R., VAFEADOS, D., WANG, D., WEISDEPP, P., WU, Y. C., XIE, D., YAN, K. K., FEINGOLD, E. A., GOOD, P. J., PAZIN, M. J., HUANG, H., BICKEL, P. J., BRENNER, S. E., REINKE, V., WATERSTON, R. H., GERSTEIN, M., WHITE, K. P., KELLIS, M. & SNYDER, M. 2014. Comparative analysis of regulatory information and circuits across distant species. *Nature,* 512**,** 453-6.

DE-CASTRO, A. R. G., RODRIGUES, D. R. M., DE-CASTRO, M. J. G., VIEIRA, N., VIEIRA, C., CARVALHO, A. X., GASSMANN, R., ABREU, C. M. C. & DANTAS, T. J. 2022. WDR60-mediated dynein-2 loading into cilia powers retrograde IFT and transition zone crossing. *J Cell Biol,* 221.

HAMADA, Y., TSURUMI, Y., NOZAKI, S., KATOH, Y. & NAKAYAMA, K. 2018. Interaction of WDR60 intermediate chain with TCTEX1D2 light chain of the dynein-2 complex is crucial for ciliary protein trafficking. *Mol Biol Cell,* 29**,** 1628-1639.

HIYAMIZU, S., QIU, H., TSURUMI, Y., HAMADA, Y., KATOH, Y. & NAKAYAMA, K. 2023a. Dynein-2-driven intraciliary retrograde trafficking indirectly requires multiple interactions of IFT54 in the IFT-B complex with the dynein-2 complex. *Biol Open,* 12.

HIYAMIZU, S., QIU, H., VUOLO, L., STEVENSON, N. L., SHAK, C., HEESOM, K. J., HAMADA, Y., TSURUMI, Y., CHIBA, S., KATOH, Y., STEPHENS, D. J. & NAKAYAMA, K. 2023b. Multiple interactions of the dynein-2 complex with the IFT-B complex are required for effective intraflagellar transport. *J Cell Sci,* 136.

JOHNSTON, R. J., JR. & HOBERT, O. 2005. A novel C. elegans zinc finger transcription factor, lsy-2, required for the cell type-specific expression of the lsy-6 microRNA. *Development,* 132**,** 5451-60.

LACEY, S. E., FOSTER, H. E. & PIGINO, G. 2023. The molecular structure of IFT-A and IFT-B in anterograde intraflagellar transport trains. *Nat Struct Mol Biol,* 30**,** 584-593.

NIU, W., LU, Z. J., ZHONG, M., SAROV, M., MURRAY, J. I., BRDLIK, C. M., JANETTE, J., CHEN, C., ALVES, P., PRESTON, E., SLIGHTHAM, C., JIANG, L., HYMAN, A. A., KIM, S. K., WATERSTON, R. H., GERSTEIN, M., SNYDER, M. & REINKE, V. 2011. Diverse transcription factor binding features revealed by genome-wide ChIP-seq in C. elegans. *Genome Res,* 21**,** 245-54.

RAPALI, P., SZENES, A., RADNAI, L., BAKOS, A., PAL, G. & NYITRAY, L. 2011. DYNLL/LC8: a light chain subunit of the dynein motor complex and beyond. *FEBS J,* 278**,** 2980-96.

RAZZAUTI, A. & LAURENT, P. 2021. Ectocytosis prevents accumulation of ciliary cargo in C. elegans sensory neurons. *Elife,* 10.

SCHEIDEL, N. & BLACQUE, O. E. 2018. Intraflagellar Transport Complex A Genes Differentially Regulate Cilium Formation and Transition Zone Gating. *Curr Biol,* 28**,** 3279-3287 e2.

TOROPOVA, K., ZALYTE, R., MUKHOPADHYAY, A. G., MLADENOV, M., CARTER, A. P. & ROBERTS, A. J. 2019. Structure of the dynein-2 complex and its assembly with intraflagellar transport trains. *Nat Struct Mol Biol,* 26**,** 823-829.

YI, P., LI, W. J., DONG, M. Q. & OU, G. 2017. Dynein-Driven Retrograde Intraflagellar Transport Is Triphasic in C. elegans Sensory Cilia. *Curr Biol,* 27**,** 1448-1461 e7.

ZHONG, M., NIU, W., LU, Z. J., SAROV, M., MURRAY, J. I., JANETTE, J., RAHA, D., SHEAFFER, K. L., LAM, H. Y., PRESTON, E., SLIGHTHAM, C., HILLIER, L. W., BROCK, T., AGARWAL, A., AUERBACH, R., HYMAN, A. A., GERSTEIN, M., MANGO, S. E., KIM, S. K., WATERSTON, R. H., REINKE, V. & SNYDER, M. 2010. Genome-wide identification of binding sites defines distinct functions for Caenorhabditis elegans PHA-4/FOXA in development and environmental response. *PLoS Genet,* 6**,** e1000848.

ZHU, X., WANG, J., LI, S., LECHTRECK, K. & PAN, J. 2021. IFT54 directly interacts with kinesin-II and IFT dynein to regulate anterograde intraflagellar transport. *EMBO J,* 40**,** e105781.

CHAPTER V – DYCI-1 is unlikely to be an intermediate chain of the dynein-2 complex

5.1. Introduction

The dynein-2 complex comprises a heterodimer of the intermediate chains (ICs) WDR60 and WDR34 (Toropova et al., 2019, Asante et al., 2014, Patel-King et al., 2013, Rompolas et al., 2007). These, along with an array of light chains, bring together two copies of heavy and light-intermediate chains, to dimerize the dynein-2 complex (Toropova et al., 2019).

Our lab recently identified the WDR60 homolog in *C. elegans* (De-Castro et al., 2022). However, it is still elusive whether the *C. elegans* WDR-60 homodimerizes, or forms a heterodimer with another IC within the dynein-2 complex. Given that CHE-3 is still able to partially power retrograde IFT in the absence of WDR-60 (De-Castro et al., 2022), we hypothesized that another IC could be compensating for the loss of WDR-60. Taking this into consideration, we sought to investigate whether there is a homolog of the human WDR34 in *C. elegans*.

Through protein sequence alignments, we found that DYCI-1, the intermediate chain of the dynein-1 complex (Le Bot et al., 2003), was the protein with the highest homology to the human WDR34. In fact, DYCI-1 has been already observed inside cilia of a transgenic *C. elegans* strain expressing GFP::DYCI-1 under the control of the *dyf-1* promoter (Li et al., 2015). This observation raised the question whether, in *C. elegans*, DYCI-1, could be incorporated into both dynein-1 and dynein-2 complexes.

In contrast to most ciliary proteins, DYCI-1 is indispensable for worm development, which is not surprising given that this dynein-1 subunit participates in basic cellular processes such as mitosis or vesicle transport (O'Rourke et al., 2007). To be able to study the potential involvement of DYCI-1 in IFT, we constructed a *C. elegans* strain that combines the split GFP (Hefel and Smolikove, 2019) and the Auxin-Inducible Degradation (AID) (Zhang et al., 2015) systems. The aim of such strategy was to be able to simultaneously visualize and deplete DYCI-1 specifically in ciliated neurons, without compromising worm viability.

When probing for DYCI-1 in sensory neurons, we were able to detect its signal in the nerve ring, and phasmid neuron somas. However, DYCI-1 signal was never observed inside amphid or phasmid cilia. Nevertheless, we were also able to successfully implement the degron system to deplete DYCI-1 in ciliated neurons. To our surprise, we observed a phenotype compatible with loss of sensing of environmental cues, without ever observing significant ciliary defects.

5.2. Results

5.2.1. Designing the strategy for the functional analyses of DYCI-1 in sensory neurons

We used the BlastP tool to search for WDR34 orthologs in *C. elegans*, using the Uniprot Q96EX3 protein sequence (human WDR34) as a reference. The proteins with highest sequence homology, and most likely candidates, were DYCI-1, the already known dynein-1 intermediate chain (Le Bot et al., 2003), and WDR-60. To be able to assess DYCI-1 presence inside cilia, we used CRISPR-Cas9 to tag the C-terminal end of this IC with a 2xFLAG::AID::3xsGFP11 sequence **(Figure 1A)**. This tag contains three different functional elements: the FLAG sequences that allowed for biochemical detection of DYCI-1, and measurement of protein levels by western blot **(Figure 1B)**; the β-strands 11 of GFP reconstitute a fluorescent GFP in the presence of β-strands 1-10 (Cabantous et al., 2005) **(Figure 1C)**; and the AID sequence which, in the presence of auxin, is recognized for TIR1-mediated DYCI-1 poly-ubiquitination and degradation by the proteasome (Nishimura et al., 2009) **(Figure 1D)**.

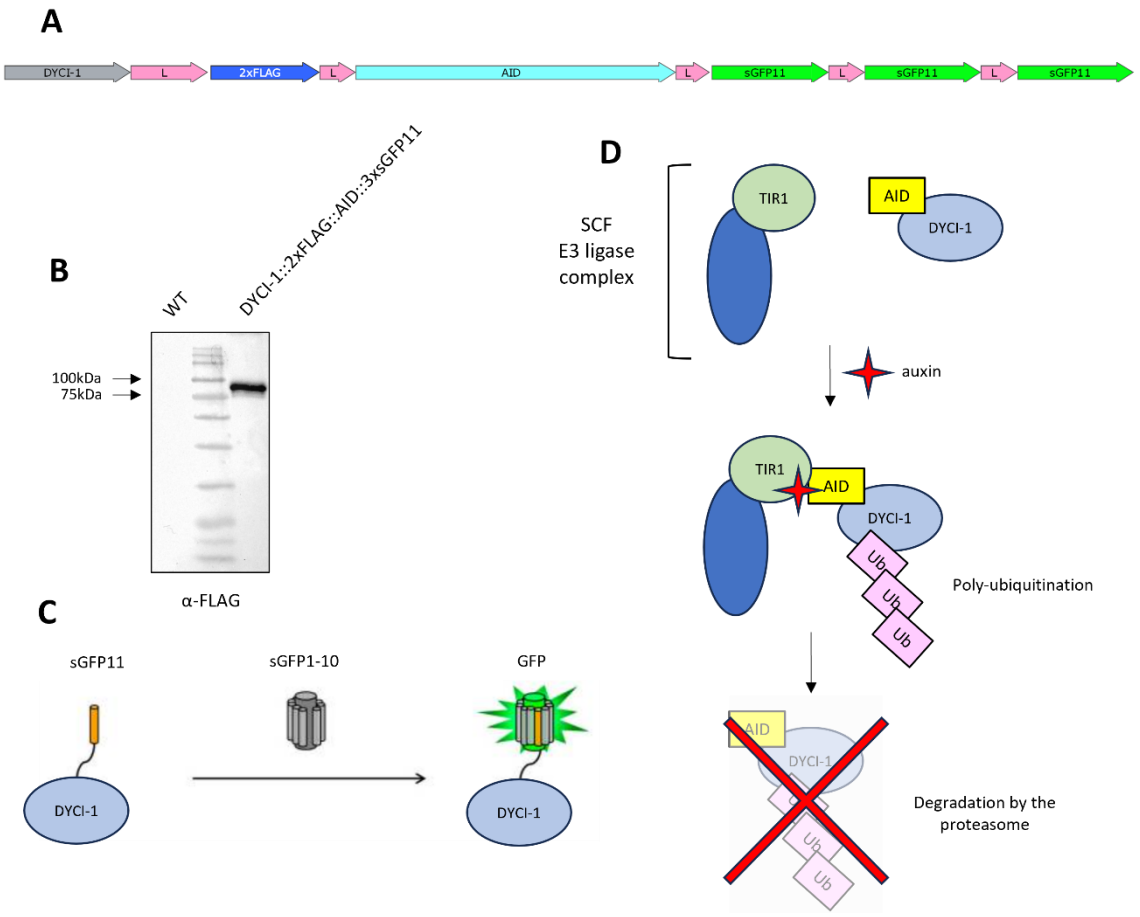

Figure 1 – Employing the split GFP (sGFP) and the auxin-inducible degradation (AID) systems to study a potential role of DYCI-1 in IFT. (A) The DNA sequence coding for 2xFLAG::AID::3xsGFP11 (annotated in annex IX) was inserted at the 3' end of the endogenous *dyci-1* locus; for simplicity, only the last exon of *dyci-1* is shown (gray box). **(B)** α-FLAG blot containing protein extracts of WT (N2, negative control) and DYCI-1::2xFLAG::AID::3xsGFP11 expressing worms. The tagged DYCI-1 protein was visible in the gel close to its predicted molecular weight, which is 86 kDa according to the ExPASy Mw tool. **(C)** Three copies of the β-sheets 11 of GFP (sGFP11) were present in the tagged DYCI-1. If β-sheets 1-10 of GFP are expressed in the same cells and establish contact with sGFP11, GFP fluorescence is restored (image adapted from (Pedelacq and Cabantous, 2019). **(D)** TIR1 is a substrate recognition subunit that forms an SCF E3 ubiquitin ligase complex. In the presence of the phytohormone auxin, AID-tagged DYCI-1 is poly-ubiquitinated by the SCF complex and targeted for degradation by the proteasome.

To first test if this tag was functional, we took advantage of an existing strain in the co-supervisor's lab (GCP794) that expresses sGFP1-10 in the germline and early embryo, under the control of the *mex-5* promoter. Upon crossing the two strains, we observed DYCI-1 signal in the gonad and embryos, predominantly at the nuclear envelope of germ cells, and in the mitotic spindle of blastomeres **(Figure 2)**, showing that our split GFP system was

functional. Also, these are the same subcellular structures that have been shown to recruit dynein-1 heavy chain in these tissues (Barbosa et al., 2021), indicating that tagged DYCI-1 behaved normally.

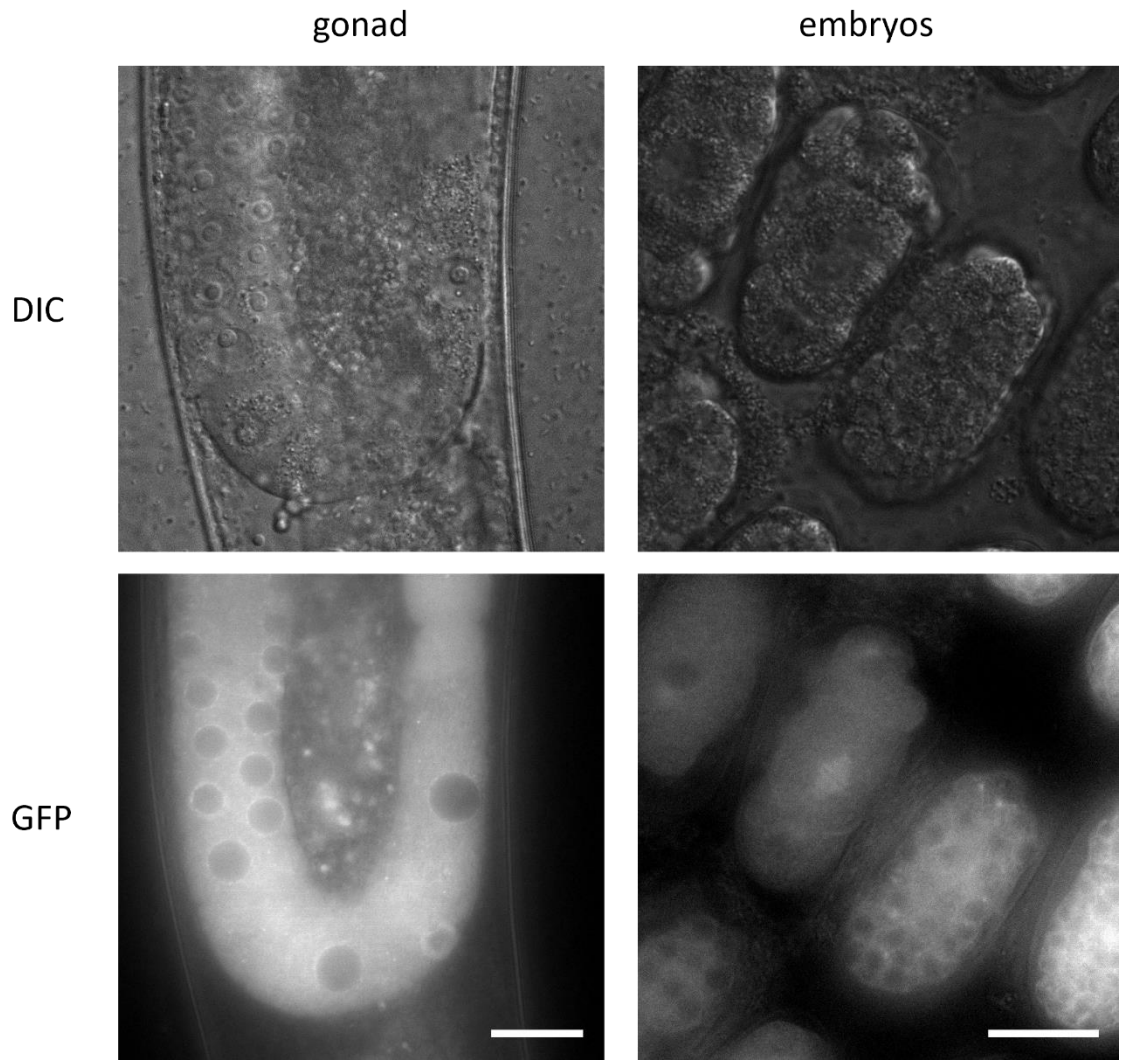

Figure 2 – DYCI-1::2xFLAG::AID::3xsGFP11 sub-cellular distribution in *C. elegans* gonad and embryos. DYCI-1 is visible at the nuclear envelope of germ cells, and in the mitotic spindle of blastomeres. Scale bars: 20 μm. Images from gonad and embryos were not scaled to the same brightness and contrast levels.

After validating the DYCI-1 tag, we set to generate a construct that induces the transgenic expression of sGFP1-10 and TIR1::mRuby specifically in the ciliated sensory neurons. For that, we amplified 780bp from the *ift-139* promoter, as previously described by the Ou lab (Yi et al., 2017), and subcloned it in an expression vector with TIR1 **(Figure 3)**. This

approach allowed us to visualize and deplete DYCI-1 in these neurons, without having background GFP signal, or compromising the function of dynein-1 in other tissues. The simultaneous expression of sGFP1-10 and TIR1::mRuby was achieved through the use of the *gpd-2*/*gpd-3* operon linker, which allows a single polycistronic pre-mRNA to be processed into two functional mRNAs (Sobral et al., 2021) **(Figure 3)**.

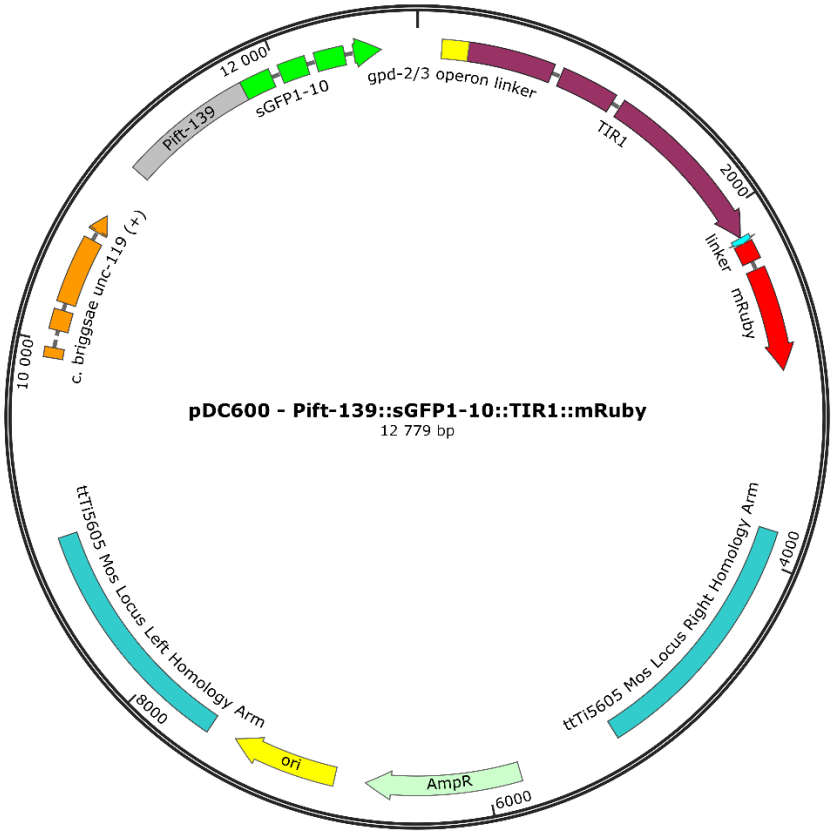

Figure 3 – Construct for the Mos1-mediated Single Copy Insertion (MosSCI) in chromosome II of *C. elegans*. The pDC600 plasmid available at the co-supervisor lab was used as a backbone for the insertion of the following sequence in the ttTi5605 locus of chromosome II: *Pift-139::sGFP1-10::gpd-2/3::TIR1::mRuby*. The plasmid DNA sequence was annotated in SnapGene Viewer (v5.0.8).

5.2.2. Sensory neuronal distribution of DYCI-1

Upon generating the strain that combines the ubiquitous expression of DYCI-1::2xFLAG::AID::3xsGFP11 with the sensory neuron-specific expression of sGFP1-10 and TIR1::mRuby, our first main objective was to assess the cellular distribution of DYCI-1 in sensory neurons. We were able to observe DYCI-1 in several neuronal structures such as the nerve ring (which contains the somas of many amphid neurons (White et al., 1986)),

phasmid neuron somas, and in some phasmid neuron dendrites **(Figure 4)**. However, no DYCI-1 signal was ever detectable in either amphid or phasmid cilia.

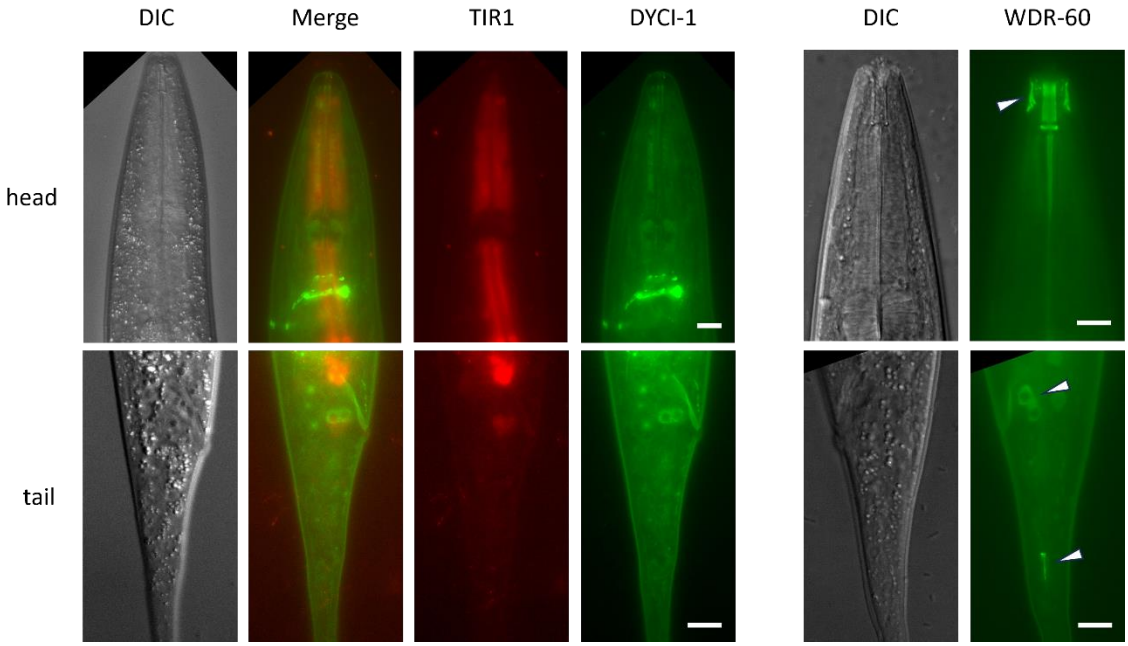

Figure 4 – DYCI-1 in sensory neurons. DYCI-1 signal was detected in the nerve ring, and in the somas of phasmid neurons, but never in cilia. TIR1 was observed at the somas of phasmid neurons, but not in the nerve ring. The WDR-60::GFP strain is shown as a marker for cilia/ dynein-2. White arrowheads point to amphid cilia in the head, and phasmid somas and cilia in the tail. Scale bars: 10 µm. The signal intensity between DYCI-1 and WDR-60 was not scaled to the same brightness and contrast levels in head and tail images.

Faced with these results, we considered the possibility that the expression of sGFP1-10 in sensory neurons attained using *Pift-139* might not be strong enough to allow the visualization of DYCI-1 inside cilia. To address this potential issue, we generated another MosSCI construct, as the one in **Figure 2**, but driving the pan-neuronal expression of sGFP1-10 under the control of the *rgef-1* promoter (Chen et al., 2011). Although this alternative construct also allowed us to we observe a strong sGFP signal in many neuronal structures, no sGFP-tagged DYCI-1 signal was ever detectable inside cilia of amphid or phasmid neurons **(Figure 5)**. Altogether, these results suggest that this intermediate chain does not enter cilia and thus, it does not integrate the ciliary dynein-2 complex.

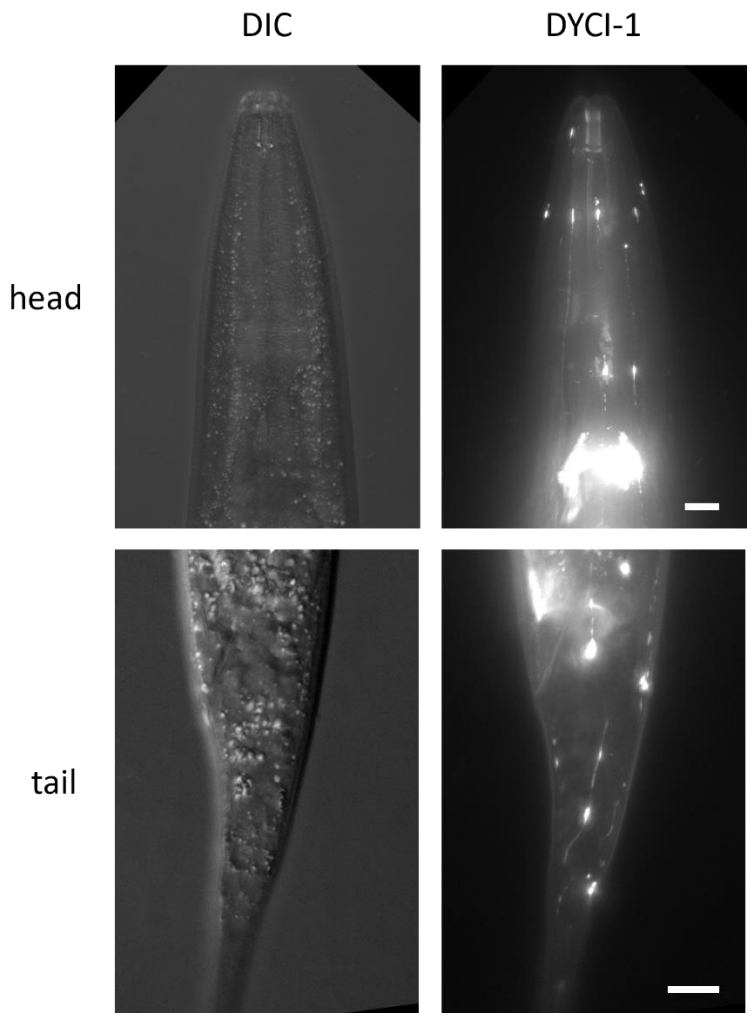

Figure 5 – Pan-neuronal localization of DYCI-1. Strong GFP signal was detected in several neuronal structures, but not inside cilia. Scale bars: 10 µm.

5.2.3. Auxin-induced degradation of DYCI-1 in sensory neurons

Despite not being able to observe DYCI-1 inside cilia, we still carried out the auxin-mediated degradation of DYCI-1 in sensory neurons to probe for possible ciliary defects. To initially test this system, we placed L3 worms in NGM plates with 100 µM auxin for 24 hours. The degron system proved to be highly functional as we could no longer detect any GFP signal in neuronal structures **(Figure 6A)**, indicating that DYCI-1 was mostly, if not completely, depleted in sensory neurons. Although we had not observed TIR1 in the nerve ring **(Figure 6A)**, it was most likely expressed in amphid neurons as DYCI-1 was also very efficiently degraded in these cells **(Figure 6A)**.

We then performed the dye filling assay as in chapter II, and observed that even worms that had been hatched and grown to adulthood in auxin-treated plates were still able to uptake the DiI dye into sensory neurons, akin to the non-treated worms **(Figure 6B)**. This observation suggests that depletion of DYCI-1 does not significantly compromise axoneme extension in developing worms.

To study the impact of loss of DYCI-1 on cilia morphology and dynein-2, we also measured cilia length and WDR-60 ciliary distribution. We initially hypothesized that, if WDR-60 could dimerize within the dynein-2 complex to compensate for the loss of DYCI-1, the ciliary levels of WDR-60 could potentially be increased. However, we observed that WDR-60 levels were increased only at the ciliary base, and reduced in the distal segment **(Figure 6C and 6D)**. Regarding cilia length, no significant alteration was observed upon depletion of DYCI-1 **(Figure 6E)**.

Altogether, the lack of a severe ciliary phenotype observed upon depletion of DYCI-1 in sensory neurons also suggests that this intermediate chain is not a subunit of Dynein-2.

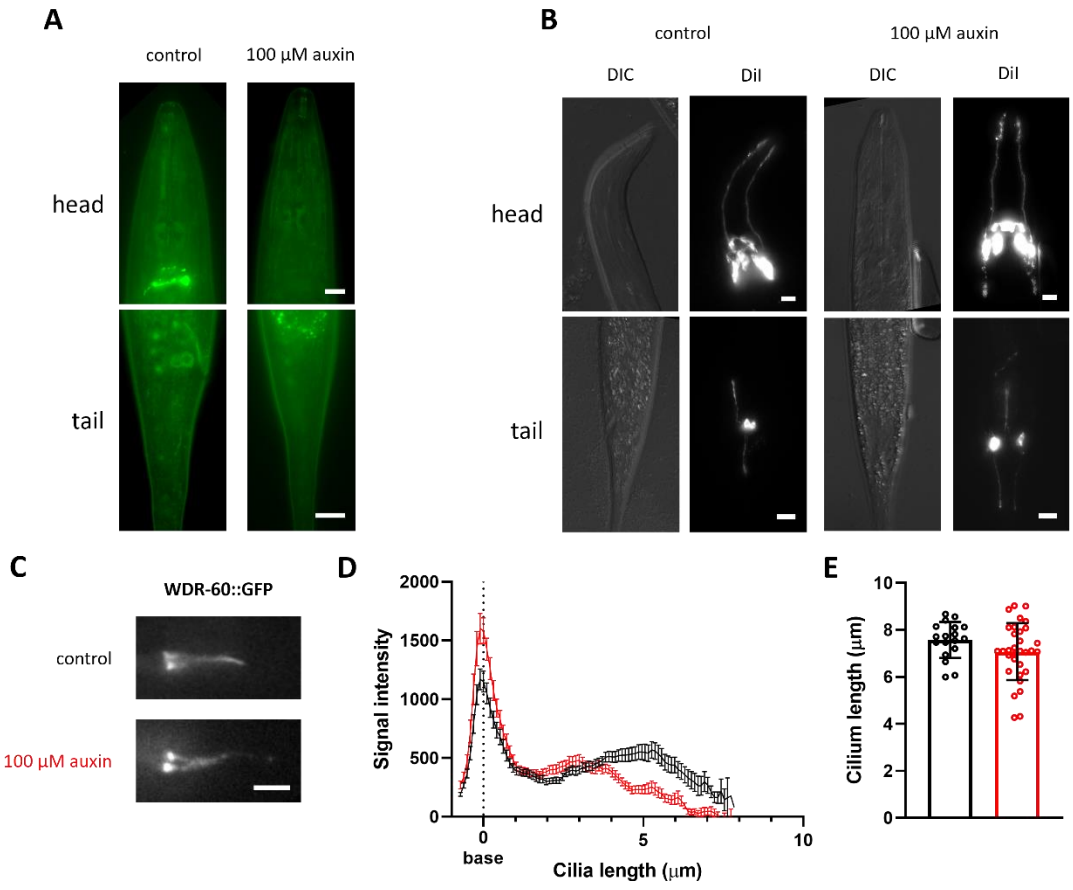

Figure 6 – Degradation of DYCI-1 in sensory neurons does not compromise cilia assembly. **(A)** Worms treated with 100 µM auxin no longer have detectable DYCI-1 signal in the nerve ring, or

in phasmid somas. **(B)** The dye filling assay shows that auxin-treated worms can still uptake the DiI dye into sensory neurons, akin to controls. **(C)** Representative examples of phasmid cilia expressing WDR-60::GFP in controls and in 100 µM auxin-treated worms. **(D)** Ciliary distribution of WDR-60 in controls and 100 µM auxin-treated worms. **(E)** Cilia length in controls and 100 µM auxin-treated worms. For each condition, n≥ 24 cilia in **D** and **E**, obtained in a single experiment. Scale bar in **C**: 2 µm. Scale bars in **A** and **B**: 10 µm. The signal intensity from DYCI-1 (A) and the DiI dye (B) was not scaled to the same brightness and contrast levels between images of the same panel.

Interestingly, when performing the auxin-mediated degradation of DYCI-1 in sensory neurons, we noticed that worms were smaller than wild types and non-treated worms. Unexpectedly, we also found that worms were evenly dispersed throughout the NGM plates, instead of being mostly found in the bacterial lawn **(Figure 7)**. These observations were not quantified properly as they were outside of the scope of the main project, however, they may indicate that the disruption of dynein-1 subunits, and consequent reduction of retrograde transport in dendrites, can lead to loss of sensory neuron function, as worms seemed to no longer be sensing food correctly.

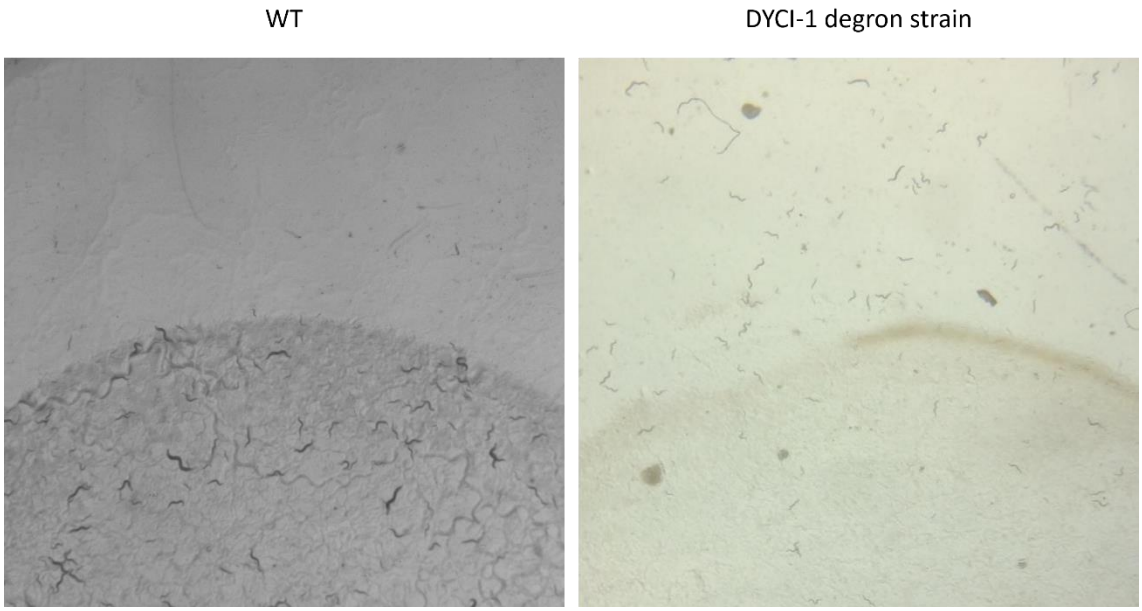

Figure 7 – Sensory neuron-specific degradation of DYCI-1 seems to lead to problems in sensing food. DYCI-1 degron worms that were hatched and grown to adulthood in auxin plates were smaller than wild types, and were evenly spread throughout the plates, rather than being mostly found in the bacterial lawn.

5.3. Discussion

5.3.1. DYCI-1 is unlikely to be an intermediate chain of the dynein-2 complex

The results obtained in this chapter indicate that DYCI-1 is not present inside cilia, and, accordingly, it is not a key intermediate chain of the dynein-2 motor complex. While we could observe the endogenous DYCI-1 signal in several neuronal structures, no signal was ever detected inside cilia. Also, the sensory neuron-specific degradation of DYCI-1 led to a much less severe ciliary phenotype than the ones already reported for other dynein-2 subunits (De-Castro et al., 2022, Schafer et al., 2003, Yi et al., 2017), which is more likely due to dynein-1 disfunction. In fact, a study was recently published claiming that DYCI-1 does not localize to cilia, and is not required for IFT or ciliary assembly (Higashida and Niwa, 2023). It is, therefore, possible that the observation of DYCI-1 inside cilia by the Ou lab could result from small amounts of the protein leaking into the cilium as a consequence of overexpression (Li et al., 2015).

DYCI-1 was the strongest candidate for a WDR34 homolog in *C. elegans*, and its absence from cilia raised the question whether WDR-60 is the only dynein-2 intermediate chain present in worms. In fact, while WDR60 and WDR34 homologs have been found to be part of the dynein-2 complex in vertebrates, only one intermediate chain has been found in *Tetrahymena* (Rajagopalan et al., 2009), so this could also be the case in *C. elegans*. However, we intend to immunoprecipitate WDR-60::GFP in worms and search for novel dynein-2 interactors by Mass Spectrometry. If WDR-60 heterodimerizes with another intermediate chain, it should come up as one of the strongest interactors, given their proximity in the complex. As a control for this experiment, we will make worm extracts of the LE309 strain provided by CGC, which expresses a soluble GFP specifically in sensory neurons, under the control of the ciliary *osm-6* promoter.

5.3.2 Retrograde IFT in the absence of WDR-60

If, indeed, the dynein-2 complex in *C. elegans* is dimerized by a homodimer of WDR-60, it might be surprising how retrograde IFT is still detected in a *wdr-60* KO strain (De-Castro et al., 2022). In fact, Aakash Mukhopadhyay from the Roberts lab has already shown that, while the single KO of *wdr60* or *wdr34* in IMCD3 cells is not enough to impair ciliogenesis,

the double KO of *wdr*60 and *wdr*34 resembles the phenotype of a *dync2h1* KO mutant (data presented at the Dynein 2021 online meeting, not yet subjected to peer-review), suggesting that dynein-2 activity in mammalian cells is only completely lost in the absence of both intermediate chains. On the other hand, the Roberts lab also showed that, without the IC-LC subcomplex, non-dimerized HC-LIC monomers alone are capable of driving rapid microtubule gliding (~530nm/s) *in vitro* (Toropova et al., 2019). Therefore, we can not exclude the possibility that, in *C. elegans*, the CHE-3-XBX-1 subcomplex alone is capable of driving the events of retrograde IFT that we observed in *wdr-60* KO worms (De-Castro et al., 2022). One possible approach to test this hypothesis in the future would be to tag the dynein-specific light chain roadblock with a fluorescence marker, and assess whether it is still present inside cilia of *wdr-60* KO worms. Given that the light chains bind the N-terminal of the intermediate chains (Toropova et al., 2019), if the latters are absent, roadblock should, in theory, not be able to integrate dynein-2 nor enter cilia.

Taking this into consideration, it would be interesting to measure the retrograde IFT kinetics of a dynein-2 (ΔIC-LC) mutant, and compare with the *wdr-60* KO mutant. However, we can not knock-out the light chains, as LC8 has already been shown to dimerize the disordered regions of many other binding proteins, apart from Dyneins (Barbar, 2008, Rapali et al., 2011), being essential for many cellular processes. Instead, one possible approach to generate a non-dimerized dynein-2 would be to mutate the LC binding sites within the WDR-60 N-terminus.

5.3.3. DYCI-1 degradation as a tool to study neurodegeneration

Given that DYCI-1 is essential for dynein-1 activity, its degradation in sensory neurons was expected to lead to detrimental effects in retrograde transport, and overall neuronal function. Indeed, the evenly distributed worms throughout the NGM plates and reduced size observed in **Figure 7** suggest loss of food sensing. This preliminary result needs to be confirmed in the future and perhaps chemosensory and osmotic avoidance assays can be carried out to study DYCI-1 function (direct or indirect) in the context of ciliary sensing functions. In such endeavor, the already characterized DHC-1 degron strain (Zhang et al., 2015) can be used as a control, to account for the collateral effects of disrupting dynein-1. Furthermore, these strains could be useful to study any potential sensory neuron degeneration phenotypes in the future.

5.4. References

ASANTE, D., STEVENSON, N. L. & STEPHENS, D. J. 2014. Subunit composition of the human cytoplasmic dynein-2 complex. *J Cell Sci,* 127**,** 4774-87.

BARBAR, E. 2008. Dynein light chain LC8 is a dimerization hub essential in diverse protein networks. *Biochemistry,* 47**,** 503-8.

BARBOSA, D. J., TEIXEIRA, V., DURO, J., CARVALHO, A. X. & GASSMANN, R. 2021. Dynein-dynactin segregate meiotic chromosomes in C. elegans spermatocytes. *Development,* 148.

CABANTOUS, S., TERWILLIGER, T. C. & WALDO, G. S. 2005. Protein tagging and detection with engineered self-assembling fragments of green fluorescent protein. *Nat Biotechnol,* 23**,** 102-7.

CHEN, L., FU, Y., REN, M., XIAO, B. & RUBIN, C. S. 2011. A RasGRP, C. elegans RGEF-1b, couples external stimuli to behavior by activating LET-60 (Ras) in sensory neurons. *Neuron,* 70**,** 51-65.

DE-CASTRO, A. R. G., RODRIGUES, D. R. M., DE-CASTRO, M. J. G., VIEIRA, N., VIEIRA, C., CARVALHO, A. X., GASSMANN, R., ABREU, C. M. C. & DANTAS, T. J. 2022. WDR60-mediated dynein-2 loading into cilia powers retrograde IFT and transition zone crossing. *J Cell Biol,* 221.

HEFEL, A. & SMOLIKOVE, S. 2019. Tissue-Specific Split sfGFP System for Streamlined Expression of GFP Tagged Proteins in the Caenorhabditis elegans Germline. *G3 (Bethesda),* 9**,** 1933-1943.

HIGASHIDA, M. & NIWA, S. 2023. Dynein intermediate chains DYCI-1 and WDR-60 have specific functions in Caenorhabditis elegans. *Genes Cells,* 28**,** 97-110.

LE BOT, N., TSAI, M. C., ANDREWS, R. K. & AHRINGER, J. 2003. TAC-1, a regulator of microtubule length in the C. elegans embryo. *Curr Biol,* 13**,** 1499-505.

LI, W., YI, P. & OU, G. 2015. Somatic CRISPR-Cas9-induced mutations reveal roles of embryonically essential dynein chains in Caenorhabditis elegans cilia. *J Cell Biol,* 208**,** 683-92.

NISHIMURA, K., FUKAGAWA, T., TAKISAWA, H., KAKIMOTO, T. & KANEMAKI, M. 2009. An auxin-based degron system for the rapid depletion of proteins in nonplant cells. *Nat Methods,* 6**,** 917-22.

O'ROURKE, S. M., DORFMAN, M. D., CARTER, J. C. & BOWERMAN, B. 2007. Dynein modifiers in C. elegans: light chains suppress conditional heavy chain mutants. *PLoS Genet,* 3**,** e128.

PATEL-KING, R. S., GILBERTI, R. M., HOM, E. F. & KING, S. M. 2013. WD60/FAP163 is a dynein intermediate chain required for retrograde intraflagellar transport in cilia. *Mol Biol Cell,* 24**,** 2668-77.

PEDELACQ, J. D. & CABANTOUS, S. 2019. Development and Applications of Superfolder and Split Fluorescent Protein Detection Systems in Biology. *Int J Mol Sci,* 20.

RAJAGOPALAN, V., SUBRAMANIAN, A., WILKES, D. E., PENNOCK, D. G. & ASAI, D. J. 2009. Dynein-2 affects the regulation of ciliary length but is not required for ciliogenesis in Tetrahymena thermophila. *Mol Biol Cell,* 20**,** 708-20.

RAPALI, P., SZENES, A., RADNAI, L., BAKOS, A., PAL, G. & NYITRAY, L. 2011. DYNLL/LC8: a light chain subunit of the dynein motor complex and beyond. *FEBS J,* 278**,** 2980-96.

ROMPOLAS, P., PEDERSEN, L. B., PATEL-KING, R. S. & KING, S. M. 2007. Chlamydomonas FAP133 is a dynein intermediate chain associated with the retrograde intraflagellar transport motor. *J Cell Sci,* 120**,** 3653-65.

SCHAFER, J. C., HAYCRAFT, C. J., THOMAS, J. H., YODER, B. K. & SWOBODA, P. 2003. XBX-1 encodes a dynein light intermediate chain required for retrograde intraflagellar transport and cilia assembly in Caenorhabditis elegans. *Mol Biol Cell,* 14**,** 2057-70.

SOBRAL, A. F., CHAN, F. Y., NORMAN, M. J., OSORIO, D. S., DIAS, A. B., FERREIRA, V., BARBOSA, D. J., CHEERAMBATHUR, D., GASSMANN, R., BELMONTE, J. M. & CARVALHO, A. X. 2021. Plastin and spectrin cooperate to stabilize the actomyosin cortex during cytokinesis. *Curr Biol,* 31**,** 5415-5428 e10.

TOROPOVA, K., ZALYTE, R., MUKHOPADHYAY, A. G., MLADENOV, M., CARTER, A. P. & ROBERTS, A. J. 2019. Structure of the dynein-2 complex and its assembly with intraflagellar transport trains. *Nat Struct Mol Biol,* 26**,** 823-829.

WHITE, J. G., SOUTHGATE, E., THOMSON, J. N. & BRENNER, S. 1986. The structure of the nervous system of the nematode Caenorhabditis elegans. *Philos Trans R Soc Lond B Biol Sci,* 314**,** 1-340.

YI, P., LI, W. J., DONG, M. Q. & OU, G. 2017. Dynein-Driven Retrograde Intraflagellar Transport Is Triphasic in C. elegans Sensory Cilia. *Curr Biol,* 27**,** 1448-1461 e7.

ZHANG, L., WARD, J. D., CHENG, Z. & DERNBURG, A. F. 2015. The auxin-inducible degradation (AID) system enables versatile conditional protein depletion in C. elegans. *Development,* 142**,** 4374-84.

CHAPTER VI – Materials and methods

6.1. *C. elegans* maintenance and strain generation

C. elegans strains were maintained at 20°C on standard nematode growth medium (NGM) plates seeded with Escherichia coli OP50 bacteria, and crossed using standard procedures (Brenner, 1974). Hermaphrodite worms were used in all assays. Mutant genotyping was performed by standard PCR.

Mutations at the endogenous *loci* were engineered by CRISPR-Cas9 using germline microinjection of Cas9, specific gRNAs (listed in Annex V), the *rol-6* co-injection marker, and homology repair templates consisting of either DNA oligonucleotides (for deletion mutations) or large partially single-stranded DNA fragments (for knock-ins) (Dokshin et al., 2018). Homology repair template oligos, and primers used to generate partially single stranded homology repair templates are listed in Annex VI and Annex VII, respectively. The "roller" and "dumpy" progeny of the injected worms was screened for the desired mutation by PCR. New strains generated by CRISPR-Cas9 were outcrossed four to six times to promote the removal of the *rol-6* mutation, and other potential mutations induced by Cas9 off-targeting.

Mos1-mediated Single Copy Insertions (MosSCI) were achieved by the germline microinjection of the desired construct, the Mos1 transposase, and co-injection markers driving the expression of mCherry under the *myo-2*, *myo-3*, and *rab-3* promoters. This mixture was injected on the EG6699 strain that possesses the ttTi5605 locus on chromosome II, and the *unc-119(ed3)* mutation. Injected worms were kept at 25°C until the plates reached confluence, to allow the genomic integration of the construct. Then, "mover" worms lacking mCherry signal were selected for screening of the insertion.

We used the Gibson Assembly cloning method (Gibson et al., 2009), as described by the authors, to generate plasmids containing the homology repair templates for the CRISPR-Cas9-mediated insertions of DNA sequences coding for "3xFLAG::GFP" at the 3' of the endogenous *wdr-60* gene, and "AID::GFP" at the 3' of the endogenous *bbs-1* gene. We also used the Gibson Assembly method to generate the mosSCI constructs that induced the neuronal specific expression of sGFP1-10 and TIR1::mRuby. The primers and cloning strategies used to generate these constructs are listed in Annex VIII.

The DNA sequences of the new tags generated here are listed in Annex IX. *C. elegans* strains and screening primers used in this study are listed in Annex III, and Annex IV, respectively.

6.2. Auxin plate preparation

The 98+% indole-3-acetic acid (IAA) (Alfa Aesar) was diluted in pure ethanol to make a 400 mM auxin stock solution. This stock solution was diluted into the NGM agar mixture to the final concentration specified in each experiment, right before pouring plates. Following agar polymerization, plates were seeded following standard procedures.

6.3. Fluorescence imaging

All imaging was performed using young adult hermaphrodite worms, with the exception of the aging experiments, in which animals at the larval stage 2, and 7 and 18 days after adulthood were also imaged for comparison. All animals used for imaging were immobilized using 5–10 mM levamisole, and were placed on a 5% agarose pad mounted on a microscope slide.

Acquisition of z-planes was carried out using an epifluorescence Axio Observer microscope (Zeiss), equipped with a Plan-Apochromat 63x/1.46 NA oil objective lens, an Orca Flash 4.0 camera (Hamamatsu), and controlled by ZEN software (Zeiss). Alternatively, for markers with small fluorescence intensity, z-plane acquisition was carried out on an Olympus IX81 (Olympus, UK) inverted microscope equipped with an UPLSAPO 100x/1.40 NA oil objective lens, and an Andor Revolution XD spinning disk confocal system composed of a solid-state laser combiner (ALC-UVP 350i, Andor Technology, UK), a CSU-X1 confocal scanner (Yokogawa Electric Corporation), and an iXonEM+ DU-897 with 2x port coupler camera (Andor Technology), controlled by Andor IQ3 software (Andor Technology). Z-stacks were acquired with 0.4 µm spacing between each z-plane.

Time-lapse imaging of IFT was performed using the same Andor Revolution XD spinning disk confocal system described above. Only phasmid cilia fully in focus in a single z-plane were selected for live imaging. 200 frames of each phasmid cilium were recorded at a rate of 3 frames/s (333 ms per frame). All imaging was performed in temperature-controlled rooms kept at 20°C.

6.4. Image processing and analyses of live IFT

Z-stack and time-lapse series were processed and analyzed with Fiji software (ImageJ). Fluorescence signal of ciliary components was used to measure the length of cilia in wild type and mutant strains from the center of the base to the ciliary tip. The distribution profiles of IFT components inside cilia were determined by drawing a segmented line along the length of each cilium, from the base to the tip, and measuring the fluorescence intensity of the pixels along that line. Background signal was measured at the farmost region of the tail and subtracted to the raw intensities obtained in the prior step. The resulting intensities determined along different cilia were averaged and plotted relative to the distance from the center of the ciliary base. When indicated, signal intensity values of each profile were normalized to their point of maximum intensity to facilitate comparison between profiles from different mutant combinations, and in these instances the total signal from base to tip was also determined and plotted separately.

Kymographs were generated in ImageJ (National Institutes of Health) using the KymographClear toolset plugin (v2.0) (Mangeol et al., 2016). To ensure the quality of the data used to analyze IFT dynamics, only cilia without severe malformations were used to generate kymographs. KymographDirect software (v2.1) (Mangeol et al., 2016) was used to analyze IFT dynamics, which takes into account background and bleaching automatically and is able to distinguish and separate anterograde from retrograde IFT. Anterograde tracks of individual IFT particles along the whole cilium length were automatically detected by the program as done in (Mijalkovic et al., 2017), and validated. Given the severity of the retrograde IFT phenotypes in *wdr-60* mutants, the program was unable to robustly detect the retrograde tracks of IFT particles. To account for that, all retrograde tracks (both in mutants and in controls) had to be drawn manually. Continuous IFT tracks drawn in the prior step were then used to automatically determine IFT velocities at different positions along cilia with KymographDirect. When average velocities were calculated for subregions of the

axoneme, they were subgrouped as follows: TZ (0–1 μm), middle segment (1–4.5 μm), and distal segment (4.5 μm to ciliary tip).

To determine the frequency of anterograde and retrograde IFT events, we employed the approach used in (Mijalkovic et al., 2017). As such, vertical straight line was drawn to cross the same position at the ciliary distal segment of each anterograde or retrograde kymograph. The line drawn on each kymograph was then used to generate an intensity profile plot, which allowed to score the number of IFT events in either direction by counting the number of intensity spikes. This quantification reflects the number of distinguishable particles that move in either direction over time.

The average signal intensities of anterogradely or retrogradely moving particles were determined using KymographDirect as in (Mijalkovic et al., 2017). The software automatically measured the intensity of all pixels composing the track of each IFT particle. Each point intensity plotted in the graphs corresponds to the average of all tracks (a minimum of 15), for either anterograde or retrograde IFT, from a particular cilium. At least 15 cilia were used per strain to determine the average intensity of particles moving in either direction.

Images of representative examples of phasmid cilia and kymographs within the same figure panel were always scaled to the same brightness and contrast levels. Instances where images were not equally scaled are discriminated in the figure legends.

6.5. Dye filling

A stock solution containing 8 mg/mL of DiI (1,1'-dioctadecyl- 3,3,3',3'-tetramethylindocarbocyanine perchlorate) in dimethyl formamide was prepared in advance and stored at −20°C. One confluent but not starved plate of worms from the strain to be tested was grown for each experiment, and a fresh dilution of DiI solution at 2.5 μg/mL was prepared in M9 (86 mM NaCl, 42 mM Na_2HPO_4, 22 mM KH_2PO_4, and 1 mM $MgSO_4$) and kept in the dark covered with aluminum foil. Worms were collected, washed in M9, and incubated in 500 μL of working DiI solution for 1 h at room temperature in the dark, with occasional flipping of the tubes. After washing in M9, worms were placed on an NGM seeded plate for 3 h at 20°C to further reduce the background of ingested dye. The neuronal uptake of dye was then examined using the Axio Observer microscope as described above.

At least 20 adult hermaphrodite worms were examined for each strain in ≥ 2 independent experiments.

6.6. Chemosensing assays

Chemotaxis to IA, an attractant compound, was assessed using 150–200 well-fed synchronized adult worms grown at 20°C per assay, following the guidelines of (Bargmann et al., 1993). Briefly, worms were washed three times in CTX buffer (1 mM $CaCl_2$, 1 mM $MgSO_4$, and 5 mM KH_2PO_4, pH 6.0) and placed on a 10 cm CTX plate without bacteria, at the starting/origin point. This origin point was set to be at the edge of the plate, equidistant to 10% IA attractant (in absolute ethanol) and vehicle (absolute ethanol) regions, which were drawn at opposite ends of the plate. Before adding 10 µl of 10% IA to the attractant site and 10 µl of 100% ethanol (solvent) to the control site, a solution of 1 M sodium azide (NaN_3) was added to these two points. Sodium azide immobilizes any worms that reach the attractant or vehicle (control) regions, preventing them from moving away. After being placed at the origin point, worms were allowed to freely explore the plate for 1 h at 20°C, after which their localization and chemotaxis index was determined. The chemotaxis index can vary from 1.0 to −1.0 and was calculated as follows: Chemotaxis index = (number of worms at the attractant site − number of worms at the control site) / total number of worms.

6.7. Osmotic avoidance assay

Osmotic avoidance assays were performed on NGM nonseeded plates at room temperature (~20°C), following the guidelines of (Sanders et al., 2015). Each repeat was performed using five young adult hermaphrodite worms of each strain isolated before the experiment. Worms were placed inside a glycerol ring with a diameter of ~1 cm, freshly prepared with a tube dipped in a 59% glycerol solution. Worm behavior was immediately monitored for 10 min to determine whether they avoided crossing the glycerol ring. Worms that left the ring

or stayed in contact with its glycerol border for >20 s were classified as escapers. Wild type and *xbx-1(null)* worms were used as controls.

6.8. Immunoblotting

For immunoblots of *C. elegans* extracts, four plates of hermaphrodites reaching confluence were collected and washed three times in M9, and the worm pellet was resuspended in an equal volume of 4× SDS-PAGE sample buffer (250 mM Tris-HCl, pH 6.8, 30% [vol/vol] glycerol, 8% [wt/vol] SDS, 200 mM DTT, and 0.04% [wt/vol] bromophenol blue). The worm suspension in sample buffer was supplemented with ~20 µL of glass beads, incubated for 5 min at 95°C, and vortexed for an additional 5 min. After boiling and vortexing twice, samples were centrifuged at 20,000 g for 1 min at room temperature, and supernatants were collected. 20% of each sample was loaded and resolved on a 10% SDS-PAGE gel and transferred to 0.2-µm nitrocellulose membranes (GE Healthcare). Membranes were rinsed in PBS (137 mM NaCl, 2.7 mM KCl, 8.1 mM Na_2HPO_4, and 1.47 mM KH_2PO_4) supplemented with 0.1% Tween-20 (PBS-T, pH 7.4), and then blocked with 5% (wt/vol) nonfat dry milk in PBS-T for 1 h. Subsequently, membranes were incubated with mouse anti-FLAG M2 antibody (Sigma-Aldrich; 1:500 for WDR-60::3xFLAG::GFP or 1:1000 for DYCI-1::2xFLAG::AID::GFP) or mouse anti-α-tubulin B512 antibody (1:5000; Sigma-Aldrich) overnight at 4°C. On the following day, membranes were washed three times in PBS-T for 10 min each. Membranes were then incubated with secondary antibodies coupled to HRP (1:10000; Jackson ImmunoResearch) for 1 h at room temperature and washed three times in PBS-T for 5 min each. Pierce ECL Western Blotting Substrate (Thermo Fisher Scientific) was added to membranes to visualize proteins by chemiluminescence using x-ray film or a Chemidoc station (Bio-Rad).

6.9. Amino acid sequence alignments

The WDR60 amino acid sequences were aligned in Jalview (version 2.11.2.6) using the GLprobsWS algorithm. These sequences were retrieved from Uniprot and have the following accession numbers: Q8WVS4 (*H. sapiens*), Q18263 (*C. elegans*), A8XPF3 (*C. briggsae*), A0A0G2K1X3 (*R. norvegicus*), Q8C761 (*M. musculus*), F1NVZ6 (*G. gallus*), A0A1D5NS24 (*D. rerio*), A0A6I8PTC1 (*X. tropicalis*), and Q7JR82 (*D. melanogaster*). Darker blue amino acid coloring represents higher percentage identity between species.

6.10. Data analyses and statistics

Statistical analyses of datasets were performed using GraphPad Prism software (v8). Unless otherwise mentioned, the total n analyzed in each assay was obtained from at least three different experiments. Shapiro–Wilk and Kolmogorov–Smirnov normality tests were performed to determine whether sample groups followed Gaussian distributions, which dictated the choice between the use of parametric or nonparametric statistical tests. One-way ANOVA followed by comparison of the mean of each experimental group with the mean of the control group was used to analyze parametric datasets; otherwise, we used the nonparametric Kruskal–Wallis test. Follow-up multiple comparison tests were selected according to GraphPad Prism software suggestions. For single-comparison statistical analyses of parametric datasets, the two-tailed Student's t test was used, while the two-tailed Mann–Whitney U test was used for nonparametric data. Differences were considered significant at P values <5% (*, $P \leq 0.05$; **, $P \leq 0.01$; ***, $P \leq 0.001$; and ****, $P \leq 0.0001$). XY velocity and intensity distribution graphs are shown as mean ± SEM. Graphs in columns are shown as mean ± SD.

6.11. References

BARGMANN, C. I., HARTWIEG, E. & HORVITZ, H. R. 1993. Odorant-selective genes and neurons mediate olfaction in C. elegans. *Cell,* 74**,** 515-27.

BRENNER, S. 1974. The genetics of Caenorhabditis elegans. *Genetics,* 77**,** 71-94.

DOKSHIN, G. A., GHANTA, K. S., PISCOPO, K. M. & MELLO, C. C. 2018. Robust Genome Editing with Short Single-Stranded and Long, Partially Single-Stranded DNA Donors in Caenorhabditis elegans. *Genetics,* 210**,** 781-787.

GIBSON, D. G., YOUNG, L., CHUANG, R. Y., VENTER, J. C., HUTCHISON, C. A., 3RD & SMITH, H. O. 2009. Enzymatic assembly of DNA molecules up to several hundred kilobases. *Nat Methods,* 6**,** 343-5.

MANGEOL, P., PREVO, B. & PETERMAN, E. J. 2016. KymographClear and KymographDirect: two tools for the automated quantitative analysis of molecular and cellular dynamics using kymographs. *Mol Biol Cell,* 27**,** 1948-57.

MIJALKOVIC, J., PREVO, B., OSWALD, F., MANGEOL, P. & PETERMAN, E. J. 2017. Ensemble and single-molecule dynamics of IFT dynein in Caenorhabditis elegans cilia. *Nat Commun,* 8**,** 14591.

SANDERS, A. A., KENNEDY, J. & BLACQUE, O. E. 2015. Image analysis of Caenorhabditis elegans ciliary transition zone structure, ultrastructure, molecular composition, and function. *Methods Cell Biol,* 127**,** 323-47.

Conclusions and future perspectives

The dynein-2 complex is pivotal for cilia function by powering the retrograde transport of multiple important cargo to the cytoplasm. In humans, mutations in dynein-2 subunits cause rare but very severe diseases that integrate the category of ciliopathies. However, little is known so far about the mechanisms by which defective dynein-2 function leads to disease.

Here, we identified the ortholog of the dynein-2 intermediate chain WDR60 in *C. elegans*. WDR-60 was not required for axoneme extension, but was essential for the robust loading of dynein-2 motors onto anterograde IFT trains, and to reach efficient retrograde kinetics for trains to effectively cross the transition zone and exit cilia.

To dissect the mechanisms by which WDR-60 regulates dynein-2 dynamics, we attempted to generate several WDR-60 N-terminal deletion mutants. This approach could allow us to determine whether WDR-60 functions are interconnected during IFT, and potentially isolate the observed phenotypes. We found a highly conserved domain in the N-terminus of WDR-60 that binds the anterograde IFT train. However, the removal of this domain did not severely impact dynein-2 ciliary kinetics. We also uncovered a transcription regulatory sequence in the upstream region of the *wdr-60* that precluded the generation of other WDR-60 mutants by manipulation of the endogenous locus. As such, in the future, other genetic tools will have to be employed to express those WDR-60 mutants in *C. elegans* sensory neurons.

We also uncovered that the NPHP module is the main transition zone component offering resistance to the passage of IFT trains, and that removal of the NPHP module from the transition zone was enough to restore retrograde train ciliary exit in the absence of WDR-60. These observations reinforce the notion of the transition zone acting as a dense physical barrier that IFT trains need to overcome to shuttle ciliary components between the cilium and the cytoplasm.

Yet, it is worth noting that the structure of the retrograde IFT train is still unknown, which sometimes complicates the analyses of the results. Having insights into the structure of the retrograde IFT trains could help explain why only some IFT subunits tend to detach from retrograde trains in the absence of WDR-60, or which IFT subunits could be involved in the activation of the dynein-2 motor.

Lastly, it remains unclear whether there is a homolog of WDR34 in *C. elegans*, or if WDR-60 homodimerizes within the dynein-2 complex. DYCI-1 was the *C. elegans* protein with the highest sequence homology to the human WDR34, however, we never detected this intermediate chain inside cilia. In the future, employing other genetic approaches or mass spectrometry of dynein-2 immunoprecipitates will be key to further characterize the subunit

composition of the *C. elegans* dynein-2 complex, and help us understand what happens to the dynein-2 complex in the absence of WDR-60.

Altogether, this work provides novel insights into the molecular mechanisms underlying WDR60-associated ciliopathies, and further enlightens the dynamics between the transition zone and the passage of IFT trains.

ANNEXES

ANNEX I - Article 1. “WDR60-mediated dynein-2 loading into cilia powers retrograde IFT and transition zone crossing”

JCB Journal of Cell Biology

ARTICLE

WDR60-mediated dynein-2 loading into cilia powers retrograde IFT and transition zone crossing

Ana R.G. De-Castro[1,2*], Diogo R.M. Rodrigues[1,2,3*], Maria J.G. De-Castro[1,2], Neide Vieira[4,5], Cármen Vieira[1,2], Ana X. Carvalho[1,2], Reto Gassmann[1,2], Carla M.C. Abreu[1,2], and Tiago J. Dantas[1,2]

The dynein-2 motor complex drives retrograde intraflagellar transport (IFT), playing a pivotal role in the assembly and functions of cilia. However, the mechanisms that regulate dynein-2 motility remain poorly understood. Here, we identify the *Caenorhabditis elegans* WDR60 homologue, WDR-60, and dissect the roles of this intermediate chain using genome editing and live imaging of endogenous dynein-2/IFT components. We find that loss of WDR-60 impairs dynein-2 recruitment to cilia and its incorporation onto anterograde IFT trains, reducing retrograde motor availability at the ciliary tip. Consistent with this, we show that fewer dynein-2 motors power WDR-60–deficient retrograde IFT trains, which move at reduced velocities and fail to exit cilia, accumulating on the distal side of the transition zone. Remarkably, disrupting the transition zone's NPHP module almost fully restores ciliary exit of underpowered retrograde trains in *wdr-60* mutants. This work establishes WDR-60 as a major contributor to IFT, and the NPHP module as a roadblock to dynein-2 passage through the transition zone.

Introduction

Cilia are microtubule-based structures that project outward from the surface of most mammalian cell types. These antenna-like structures can produce mechanical force for locomotion or fluid flow (such as in the multiciliated airway epithelia) or sense extracellular signals that modulate developmental pathways, ultimately regulating cell proliferation and differentiation (Drummond, 2012). Regardless of their type, the assembly and functions of cilia depend on a bidirectional transport system known as intraflagellar transport (IFT; Kozminski et al., 1993; Prevo et al., 2017; Webb et al., 2020). IFT is driven by two classes of molecular motors that travel on the ciliary microtubules that compose the axoneme. Kinesin-2 motors cooperate with both IFT-B and IFT-A complexes to power the transport of cargos in the anterograde direction from the base to the tip of cilia (Kozminski et al., 1995; Prevo et al., 2017). In the opposite direction, cytoplasmic dynein-2 motors (hereafter referred to as dynein-2) associate with the IFT-A complex to drive retrograde transport (Pazour et al., 1999; Porter et al., 1999; Wicks et al., 2000), which is critical for the retrieval of signaling molecules and the recycling of ciliary proteins (Prevo et al., 2017; Webb et al., 2020).

Between the base and the axoneme of cilia, a specialized ciliary gate known as the transition zone (TZ) controls which proteins and membrane components enter and exit the cilium, thus isolating the ciliary environment from the cytoplasm (Garcia-Gonzalo and Reiter, 2017). The assembly and gating function of the TZ is a complex process that involves many soluble and membrane-bound components organized into the MKS (Meckel–Gruber syndrome) and NPHP (nephronophthisis) modules (Garcia-Gonzalo and Reiter, 2017). These two modules cooperate for the building of Y-shaped structures (Y-links) that connect the proximal end of the axonemal doublets to the ciliary membrane at the region of the ciliary necklace (Blacque and Sanders, 2014). At the center of the TZ lies an apical ring (or central cylinder) that also contributes to the integrity and gating of the TZ (Li et al., 2016; Schouteden et al., 2015). Interestingly, dynein-2 has been recently shown to be required for the stability of the TZ (Jensen et al., 2018; Vuolo et al., 2018).

Problems in IFT or in the integrity of the TZ result in defects in cilia assembly/functions that can lead to congenital developmental diseases, collectively known as ciliopathies (Drummond, 2012; Garcia-Gonzalo and Reiter, 2017). Mutations in genes coding for dynein-2 subunits are associated with severe skeletal dysplasias such as Jeune syndrome (asphyxiating thoracic dystrophy), Ellis–van Creveld syndrome, and short-rib polydactyly syndrome (SRPS), which in many cases are incompatible with

[1]i3S - Instituto de Investigação e Inovação em Saúde, Universidade do Porto, Porto, Portugal; [2]IBMC - Instituto de Biologia Molecular e Celular, Universidade do Porto, Porto, Portugal; [3]Instituto de Ciências Biomédicas Abel Salazar (ICBAS), Universidade do Porto, Porto, Portugal; [4]Life and Health Sciences Research Institute (ICVS), School of Medicine, University of Minho, Campus Gualtar, Braga, Portugal; [5]ICVS/3B's - PT Government Associate Laboratory, Braga/Guimarães, Portugal.

*A.R.G. De-Castro and D.R.M. Rodrigues contributed equally to this paper; Correspondence to Carla M.C. Abreu: carla.abreu@ibmc.up.pt; Tiago J. Dantas: tiago.dantas@i3s.up.pt.

fetal survival (Cossu et al., 2016; Dagoneau et al., 2009; Huber et al., 2013; McInerney-Leo et al., 2013; Merrill et al., 2009; Niceta et al., 2018; Schmidts et al., 2015; Schmidts et al., 2013; Taylor et al., 2015). How mutations in dynein-2 subunits lead to these disorders remains poorly understood.

Dynein-2 is a giant (>1 MDa) motor protein complex composed of heavy chains (HCs), intermediate chains (ICs), light intermediate chains (LICs), and light chains (Toropova et al., 2019). A homodimer of two HCs (DHC2 encoded by *DYNC2H1*) makes up the core of the motor complex. Each DHC2 has an N-terminal tail that serves as a platform for the binding of other subunits, and a C-terminus (CT) comprising six AAA ATPase domains and a microtubule-binding domain that enable dynein-2 movement on microtubules. Two copies of the dynein-2–specific LIC3 (encoded by *DYNC2LI1*) bind and serve to stabilize the DHC2s (Mikami et al., 2002; Taylor et al., 2015; Toropova et al., 2019). The DHC2-LIC3 subcomplex binds a heterodimer of ICs, composed of WDR60 and WDR34 (encoded by *DYNC2I1* and *DYNC2I2*, respectively), through their CT β-propeller domains (Asante et al., 2014; Patel-King et al., 2013; Rompolas et al., 2007; Toropova et al., 2019). In turn, the WDR60-WDR34 heterodimer is stabilized through the binding of multiple light chains at their N-terminus (NT; Hamada et al., 2018; Schmidts et al., 2015; Toropova et al., 2019; Tsurumi et al., 2019).

Recent work analyzing the effects of depleting or disrupting the WDR60/WDR34 ICs in human cells has yielded inconsistent results, particularly regarding the requirement of WDR60 for ciliogenesis and cilia axoneme length control (Asante et al., 2014; Hamada et al., 2018; McInerney-Leo et al., 2013; Vuolo et al., 2018). Importantly, the impact of WDR60 loss on dynein-2 activity and dynamics during IFT has not been determined. This in part is due to the difficulty in visualizing and quantifying IFT kinetics of dynein-2 subunits (especially of DHC2) inside cilia of cultured cells (Hamada et al., 2018; Taylor et al., 2015; Vuolo et al., 2018).

In *Caenorhabditis elegans*, GFP/RFP-tagged dynein-2 HC and LIC subunits (see Table S1 for nomenclature) are readily detectable inside cilia and easy to track during IFT (Mijalkovic et al., 2017; Schafer et al., 2003; Yi et al., 2017). Another advantage of this model is that mutations in dynein-2 subunits that are lethal in mice (Huangfu and Anderson, 2005; May et al., 2005; Rana et al., 2004; Wu et al., 2017) do not compromise viability in *C. elegans* (Schafer et al., 2003; Wicks et al., 2000; Yi et al., 2017). Cilia are only present in a subset of *C. elegans* sensory neurons, which are analogous to human sensory cilia, such as those present in olfactory neurons. Despite being dispensable for survival, *C. elegans* cilia have key sensory functions that modulate easily quantifiable animal behaviors in response to environmental cues (Bae and Barr, 2008). These features make *C. elegans* a powerful model to dissect the roles of dynein-2 subunits during IFT.

Although most dynein-2 core subunits have been identified in *C. elegans*, clear homologues of WDR34 and WDR60 have remained unknown (Vuolo et al., 2020). Here, we identify the *C. elegans* WDR60 homologue, WDR-60, and dissect its contribution to ciliary recruitment of dynein-2 subunits, retrograde IFT, and cilia-mediated behavior. Using CRISPR/Cas9-mediated genome editing, we tagged endogenous WDR-60 with GFP and tracked its dynamics during IFT in cilia of sensory neurons. In addition, we generated a strain expressing an SRPS patient-equivalent WDR-60 truncation (McInerney-Leo et al., 2013) that lacks the DHC2-binding β-propeller domain (Toropova et al., 2019), and compared this mutant with a *wdr-60(null)* mutant. We show that WDR-60 is mostly dispensable for axoneme extension but is required for efficient loading of dynein-2 onto anterograde IFT trains, for reaching maximum retrograde IFT velocity, and for dynein-2 crossing of the TZ to exit cilia. By targeting specific TZ components, we were able to facilitate dynein-2 exit from WDR-60–deficient cilia, showing that dynein-2 is unable to overcome the resistance offered by the TZ barrier in the absence of WDR-60.

Results

WDR-60 is recruited to cilia in *C. elegans* sensory neurons and undergoes IFT with kinetics similar to those of dynein-2 HC

We set out to identify the gene encoding the so-far uncharacterized homologue of WDR60 in *C. elegans* (Hou and Witman, 2015; Vuolo et al., 2020). Through protein sequence alignments, we found that the *C27F2.1* gene in *C. elegans* encodes the protein with the highest sequence homology to human WDR60. Interestingly, *C27F2.1* (hereafter referred to as *wdr-60*) was one of the early candidate genes identified in a screen for transcripts specific for ciliated sensory neurons (Blacque et al., 2005). Like genes encoding for other dynein-2 subunits (Swoboda et al., 2000), *wdr-60* contains a predicted X-box sequence (Fig. S1 A), which is a target of the regulatory factor X (RFX)-like transcription factor DAF-19 (Blacque et al., 2005).

To directly visualize and analyze the dynamics of the protein encoded by *wdr-60*, we used genome editing to introduce the coding sequence for a 3xFLAG::GFP tag at the endogenous *wdr-60* locus (Fig. S1 A). Similar to what has been described for dynein-2 LIC and HC (Schafer et al., 2003; Wicks et al., 2000), we found that WDR-60 expression is restricted to ciliated sensory neurons. To better define the tissue-specific expression of WDR-60, we performed the classic dye filling assay that takes advantage of a lipophilic fluorescent dye (DiI) that is specifically incorporated into ciliated sensory neurons that have their cilia in contact with the environment. As a control, we used a GFP knock-in strain of dynein-2 HC, GFP::CHE-3 (Yi et al., 2017). We found that the expression pattern of WDR-60::3xFLAG::GFP is identical to that of GFP::CHE-3 and perfectly matches the neurons that take up dye (Fig. 1 A). While a large part of the signal is detected in the soma and dendrites of these neurons, WDR-60 is also found inside cilia, similar to what has been observed for GFP::CHE-3 (Yi et al., 2017).

When analyzing WDR-60::GFP ciliary distribution in more detail, we found that WDR-60 is particularly enriched at the ciliary base, as is the case for GFP::CHE-3 (Fig. 1, B–E). Furthermore, both subunits colocalize with dynein-2 LIC, XBX-1::RFP (Yi et al., 2017). Next, we performed time-lapse imaging to gain insight into WDR-60 dynamics (Video 1). We found that both anterograde and retrograde frequencies (Fig. 1, F and G) and velocities (Fig. 1, H–K) of WDR-60::GFP particles match

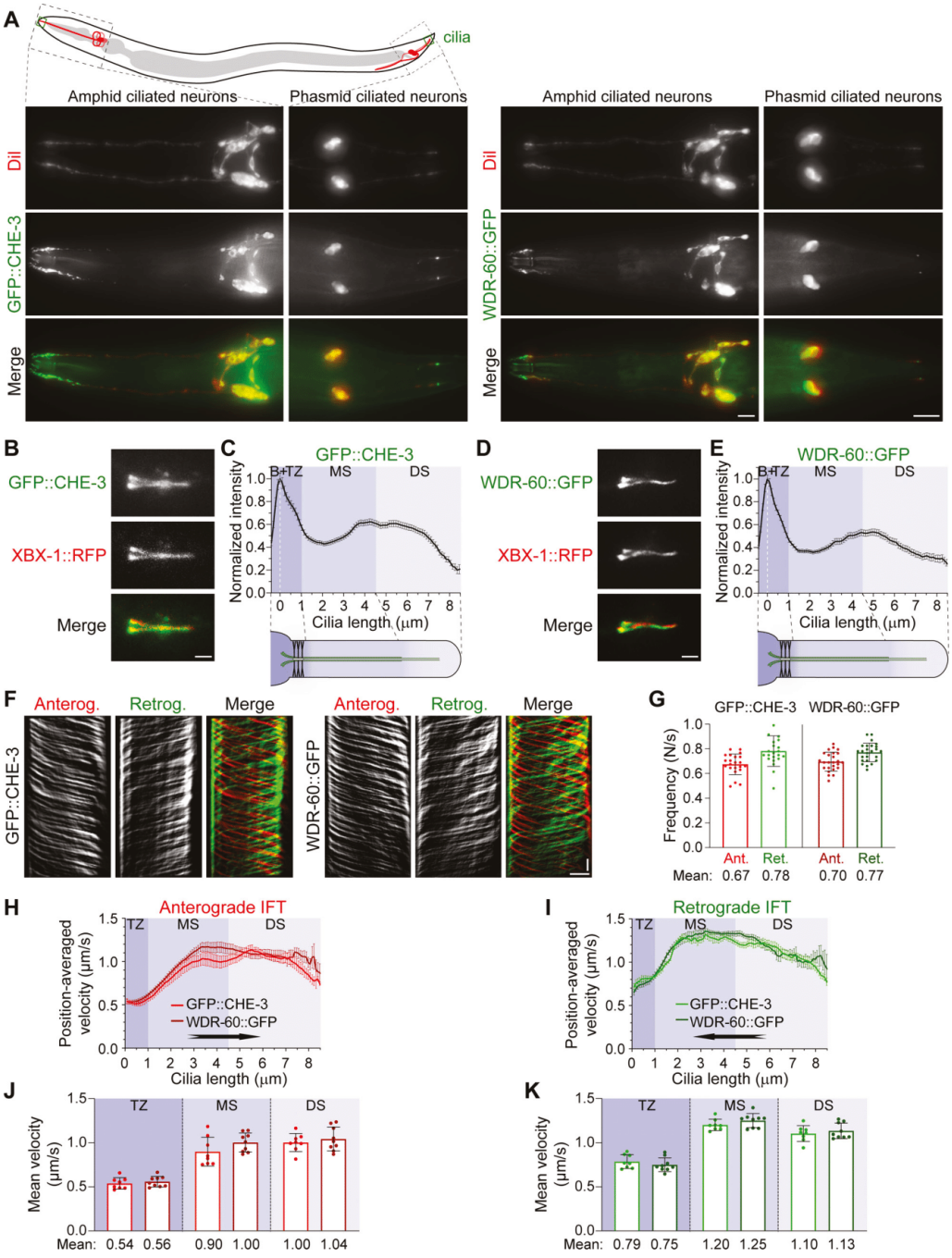

Figure 1. **WDR-60 expression is restricted to ciliated sensory neurons, where it has distribution and IFT kinetics similar to those of dynein-2 HC.** **(A)** Endogenously tagged WDR-60::3xFLAG::GFP is expressed in the same ciliated neurons that express dynein-2 HC (GFP::CHE-3). These are the same neurons that incorporate the DiI lipophilic dye. The top illustration shows the relative localization of amphid and phasmid ciliated neurons in *C. elegans*. **(B)** Phasmid cilia

coexpressing GFP::CHE-3 and XBX-1::RFP. **(C)** Quantification of GFP::CHE-3 signal intensity along cilia (n = 109 cilia). **(D)** Phasmid cilia coexpressing WDR-60::3xFLAG::GFP and XBX-1::RFP. **(E)** Quantification of WDR-60::3xFLAG::GFP signal intensity along cilia (n = 101 cilia). **(F)** Cilium kymographs of GFP::CHE-3 and WDR-60::3xFLAG::GFP. Single and merge channels for particles moving anterogradely and retrogradely are shown. **(G)** Mean IFT frequency of anterogradely and retrogradely moving GFP::CHE-3 and WDR-60::3xFLAG::GFP particles per second ($n \geq 22$ cilia). **(H and I)** Anterograde and retrograde velocities of GFP::CHE-3 and WDR-60::3xFLAG::GFP particles along cilia. **(J and K)** Mean velocities for each cilium subcompartment ($n \geq 430$ particle traces were analyzed in ≥ 8 cilia). B, cilium base; TZ, transition zone; MS, middle segment; DS, distal segment. XY velocity and intensity distribution graphs are shown as mean ± SEM, and graphs in columns are shown as mean ± SD. Student' t test was used to analyze the datasets in G, J, and K. Scale bars: 10 µm (A); 2 µm (B and D); vertical 5 s, horizontal 2 µm (F).

those of GFP::CHE-3. Furthermore, retrograde WDR-60::GFP motility follows a triphasic model, as previously reported for GFP::CHE-3 (Yi et al., 2017; Fig. 1, I and K). Together, these data strongly support that *C27F2.1/wdr-60* encodes for the *C. elegans* WDR60 homologue, which undergoes IFT with kinetics that resemble those of dynein-2 HC.

The β-propeller domain is important but not essential for WDR-60 incorporation into cilia

To determine the importance of WDR-60 for dynein-2–mediated IFT and cilia assembly, we first characterized WDR-60 levels and distribution in two distinct *wdr-60* mutants. We took advantage of the available *wdr-60* deletion allele *tm6453* (Fig. S1 B), a null mutation, and we engineered a *wdr-60* allele that produces a truncated form of WDR-60 specifically lacking the CT β-propeller domain (ΔCT; Figs. S1 C and 2 A), required for dynein-2 HC binding (Toropova et al., 2019). The *wdr-60(ΔCT)* mutant mimics a truncating mutation found in an SRPS patient (*WDR60*: c.1891C>T; p.Q631*; McInerney-Leo et al., 2013).

As endogenous labeling of WDR-60 did not alter IFT kinetics (Fig. 1, G–K), we inserted the same 3xFLAG::GFP tag sequence in-frame with the 3′ end of both *wdr-60* mutants (Figs. S1 A and 2 A). Together with the dye-filling assay, this allowed us to analyze the overall integrity of cilia while comparing the neuronal localization and relative levels of WDR-60 in wild-type and in each mutant (Fig. S2, A and B). Interestingly, and in contrast to the null *xbx-1(ok279)* LIC mutant, both *wdr-60* mutants had all ciliated sensory neurons stained with DiI, suggesting that sensory cilia can form and take up dye. No GFP signal was detectable in sensory neurons or in cilia of the *wdr-60(tm6453)* mutant, indicating that no WDR-60 is produced in this strain. In contrast, the GFP signal in neurons of the *wdr-60(ΔCT)* mutant was readily visible and overlapped with the neuronal pattern of the dye (Fig. S2, A and B; and Fig. 2 B). Interestingly, the ciliary signal of WDR-60(ΔCT)::GFP was overall weaker than in controls (approximately threefold reduction; Fig. 2 C) but showed a similar distribution profile along the axoneme, suggesting that a fraction of WDR-60(ΔCT) is able to enter cilia and undergo IFT. Strikingly, although dynein-2 LIC stabilizes the HC (Blisnick et al., 2014; Hou et al., 2004; Reck et al., 2016; Taylor et al., 2015) and contributes to ciliary entry of dynein-2 by directly interacting with IFT-B (Zhu et al., 2021), XBX-1 loss did not significantly affect the ciliary recruitment of WDR-60::GFP or WDR-60(ΔCT)::GFP (Fig. 2, B and C). However, it did lead to the accumulation of both forms of WDR-60 inside cilia, likely due to the complete block of retrograde IFT that occurs in the *xbx-1(null)* mutant (Schafer et al., 2003; Yi et al., 2017). We conclude that WDR-60 can be recruited to cilia independently of dynein-2 LIC and HC subunits.

Taking advantage of the 3xFLAG epitope in our tag, we performed immunoblotting to determine whether the reduction in ciliary levels of mutant WDR-60 reflected differences in overall protein levels (Fig. 2 D). Given that no protein bands were detectable in *wdr-60(tm6453)* worm extracts, we conclude that this mutant strain is indeed a *wdr-60* null. In contrast, the levels of WDR-60(ΔCT)::GFP were comparable to those of full-length WDR-60::GFP, indicating that the reduced ciliary recruitment of WDR-60(ΔCT)::GFP is due to loss of the β-propeller rather than a down-regulation of protein levels.

Disruption of WDR-60 reduces dynein-2 loading into cilia and the kinetics of retrograde IFT

Loss of the dynein-2 LIC XBX-1 destabilizes the dynein-2 HC CHE-3, completely abolishing its recruitment to cilia, blocking retrograde IFT and, consequently, axoneme extension. The resulting cilia are severely truncated and bulged (Schafer et al., 2003; Yi et al., 2017). To directly assess the impact of WDR-60 disruption on cilia and other dynein-2 subunits, we crossed the *wdr-60* mutants with knock-in strains of GFP::CHE-3/XBX-1::RFP (Yi et al., 2017) and analyzed their ciliary recruitment and distribution. While both *wdr-60* mutants were capable of assembling seemingly normal cilia (with only a minor reduction in length in the *wdr-60(null)* mutant), we observed a strong reduction in the total levels of ciliary GFP::CHE-3 (~40%; Fig. 3, A–C). Interestingly, we also found that the remaining pool of WDR-60–deficient dynein-2 accumulated particularly near the ciliary base (Fig. 3 D). Considering that GFP::CHE-3 levels were not greatly altered in the soma of the ciliated phasmid neurons of *wdr-60* mutants (Fig. S2 C), these observations suggest that WDR-60 contributes to both recruitment and ciliary distribution of dynein-2.

To determine when these WDR-60–associated phenotypes start manifesting and whether they vary with aging, we repeated our analysis of GFP::CHE-3 recruitment and distribution in developing and post-adulthood animals. We found that, as early as larval stage 2 in the *wdr-60(null)* mutant, ciliary levels of GFP::CHE-3 were already reduced and its distribution altered, albeit to a lesser degree than in young adults. This suggests that WDR-60–associated dynein-2 phenotypes arise early on and become progressively worse as the mutant animals develop (Fig. S3). In addition, we found that the abnormal distribution of GFP::CHE-3 does not significantly change with age in *wdr-60(null)* animals (7 and 18 days after adulthood; Fig. S3, C–H), suggesting that there is no age-dependent suppression of these WDR-60–associated phenotypes, in contrast to what has been observed for some IFT mutants (Cornils et al., 2016).

To gain further insight into the importance of WDR-60 for dynein-2 loading and dynamics inside cilia, we analyzed the IFT kinetics of GFP::CHE-3 by time-lapse imaging (Fig. 3, E–H; and

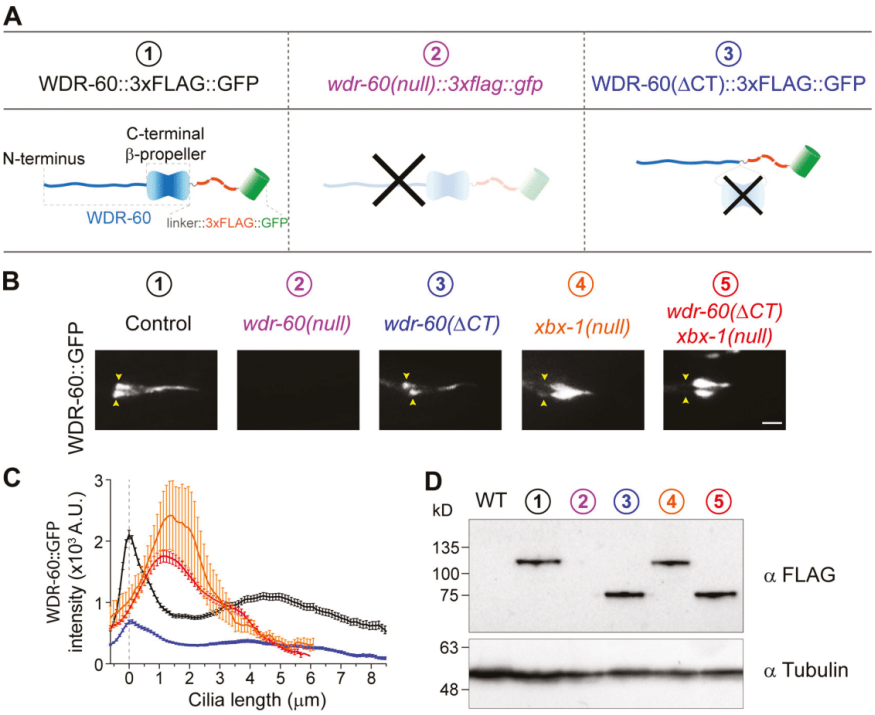

Figure 2. **Truncation of the β-propeller domain reduces, but does not abolish, entry of WDR-60 into cilia. (A)** Schematic representation of WDR-60 tagging with 3xFLAG::GFP in control, *wdr-60(tm6453)* null, and truncated *wdr-60* knock-in strains: (1) full-length WDR-60, composed of an NT disordered region and a CT β-propeller domain; (2) *wdr-60(tm6453)*, predicted to be a null mutant; (3) *wdr-60(ΔCT)*, expected to produce a protein composed of the WDR-60 NT fused to the 3xFLAG::GFP tag (lacking the β-propeller). **(B)** Phasmid cilia of each *wdr-60* knock-in strain as indicated. Yellow arrowheads indicate the ciliary base. Note that no GFP signal is detected in the *wdr-60(tm6453)::3xflag::gfp* strain. Scale bar, 2 µm. **(C)** Quantification of GFP signal intensity distribution along the cilium in *wdr-60* mutants shown in B ($n \geq 55$ cilia). Graph is shown as mean ± SEM. **(D)** Western blot of extracts from wild-type and *wdr-60* knock-in strains using an anti-FLAG antibody. The predicted sizes are 105.6 kD for WDR-60::3xFLAG::GFP and 63.2 kD for WDR-60(ΔCT)::3xFLAG::GFP truncation. No signal is detected in *wdr-60(tm6453)::3xflag::gfp* extracts, demonstrating that this is indeed a null strain. α-Tubulin was used as a loading control. Source data are available for this figure: SourceData F2.

Video 2). While we found a small increase in the frequency of GFP::CHE-3 particles moving in the anterograde direction in the *wdr-60(null)* mutant, the number of particles in the retrograde direction was significantly reduced in both mutants (~15%; Fig. 3 F). Importantly, we found that both the loss of WDR-60 and the truncation of its β-propeller led to a strong reduction in the average amount of GFP::CHE-3 transported on anterograde tracks (~67%; Fig. 3 G). This establishes a role for WDR-60 in the loading of dynein-2 onto anterograde IFT trains. Consistent with this, we found that the intensity of GFP::CHE-3 moving on retrograde tracks was significantly reduced in both *wdr-60* mutants, suggesting that each retrograde IFT train is being powered by fewer dynein-2 motors. In addition, while the velocity of anterograde trains carrying GFP::CHE-3 remained similar to that of controls, we observed a strong reduction in the velocity of GFP::CHE-3-driven retrograde trains in both *wdr-60* mutants (three- to fourfold; Fig. 3 H).

Taken together, these results show that loss of WDR-60 or truncation of its β-propeller reduces the loading of dynein-2 HC onto anterograde IFT trains, and consequently the pool of dynein-2 available at the tip of cilia to power retrograde IFT. In agreement, fewer dynein-2 motors were present in particles moving retrogradely, which may explain the reduced kinetics of retrograde IFT in *wdr-60* mutants and the inability of dynein-2 to fully return to the ciliary base.

WDR-60 is required for efficient recycling of IFT components and contributes to cilia-mediated behavior

To better understand the importance of WDR-60 in IFT, we analyzed fluorescently labeled subunits of the IFT-A/B complexes (Fig. 4, A–F) and anterograde kinesins (Fig. S4, B and C). Measurements of cilia expressing CHE-11::mCherry (IFT140) or IFT-74::GFP confirmed the small but significant decrease in cilium length in the *wdr-60(null)* mutant (Fig. 4, A, B, D, and E). We note, however, that this minor defect in axoneme extension is distinct from the severely shortened and bulged cilia phenotype caused by XBX-1 loss (Fig. 4, A and D).

When analyzing the ciliary distribution of CHE-11::mCherry, we found that this IFT-A component accumulated predominantly near the ciliary base in both *wdr-60* mutants (Fig. 4, A and C),

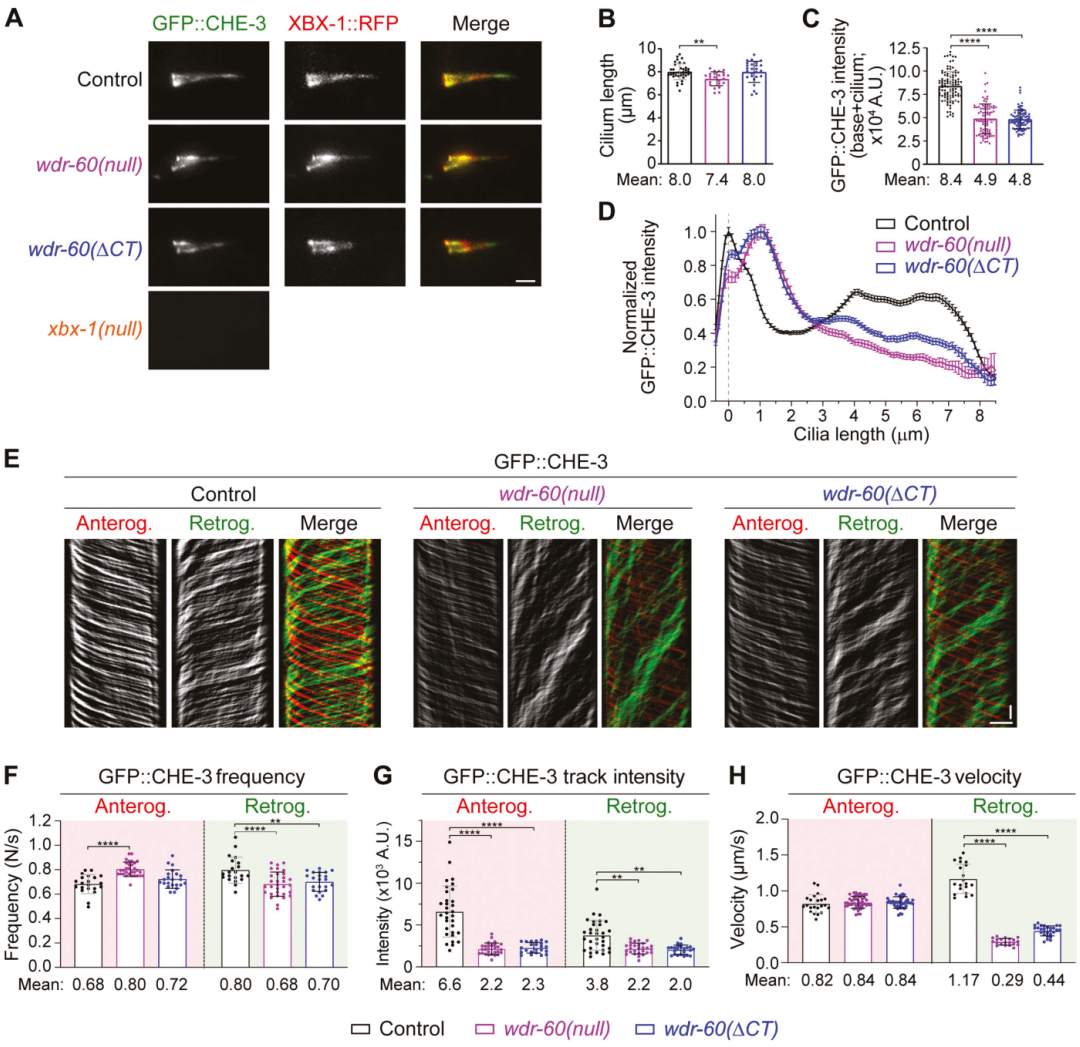

Figure 3. ***wdr-60* mutants have reduced dynein-2 recruitment and incorporation into cilia, accompanied by impaired retrograde IFT. (A)** Phasmid cilia coexpressing GFP::CHE-3 and XBX-1::RFP. **(B)** Cilia length in *wdr-60* mutants ($n \geq 24$ cilia). **(C and D)** Total signal intensity of GFP::CHE-3 from the base to the tip of cilia (C) and relative distribution of GFP::CHE-3 along cilia (D; $n \geq 88$ cilia). **(E)** GFP::CHE-3 kymographs of phasmid cilia of the indicated strains. Single and merge channels for particles moving anterogradely and retrogradely are shown. **(F)** Frequency of IFT particles detected at the distal segment of cilia ($n \geq 20$ cilia). **(G)** Quantification of the average intensity of GFP::CHE-3 particles moving on anterograde and retrograde tracks ($n \geq 345$ particle traces were analyzed in ≥23 cilia). **(H)** Velocity of anterograde and retrograde GFP::CHE-3 particles in control and *wdr-60* mutants ($n \geq 300$ particle traces were analyzed in ≥20 cilia). XY intensity distribution graph is shown as mean ± SEM, and graphs in columns are shown as mean ± SD. One-way ANOVA followed by Dunnett's, Holm–Sidak, and Games–Howell multiple comparison were used to analyze the datasets in B, F, and G, respectively. Kruskal–Wallis test followed by Dunn's multiple comparison were used to analyze the datasets in C and H. **, $P \leq 0.01$; ****, $P \leq 0.0001$. Scale bars: 2 μm (A); vertical 5 s, horizontal 2 μm (E).

similar to our observations with GFP::CHE-3. Interestingly, the total levels of CHE-11::mCherry retained inside cilia were substantially higher in the *wdr-60(null)* mutant when compared with the *wdr-60(ΔCT)* mutant.

Consistent with defects in dynein-2 function, we found that the retrograde velocity of CHE-11::mCherry was strongly reduced in both *wdr-60* mutants (approximately threefold; Fig. 4, G and H; and Video 3). In addition, the frequency of CHE-11::mCherry tracks was also significantly reduced in the retrograde direction (~16% lower in *wdr-60* null cilia; Fig. 4 I).

The IFT-B subunit IFT-74::GFP accumulated at multiple places along cilia in both *wdr-60* mutants (Fig. 4, D and F; Fig. S4 A;

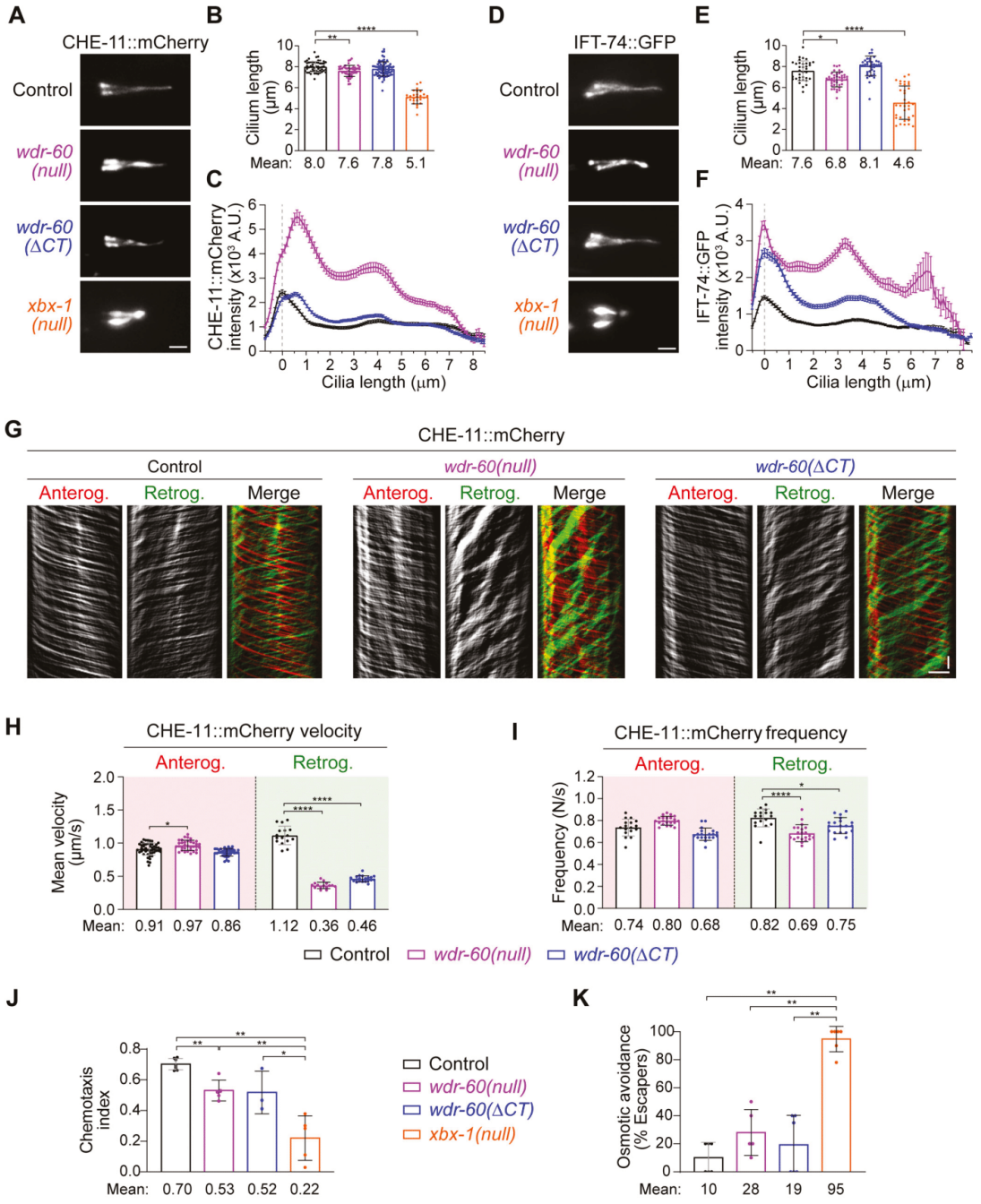

Figure 4. ***wdr-60* mutants have reduced retrograde transport of IFT-A and IFT-B complexes and lower efficiency of cilia-mediated signaling. (A and D)** Phasmid cilia from control, *wdr-60(null)*, *wdr-60(ΔCT)*, and *xbx-1(null)* animals expressing CHE-11::mCherry (A) or IFT-74::GFP (D). **(B and E)** Cilia length measured with CHE-11::mCherry (B) or IFT-74::GFP (E; $n \geq 26$ and $n \geq 34$ cilia, respectively). **(C and F)** Quantification of the average intensity of CHE-11::mCherry (C) and IFT-74::GFP (F) along cilia ($n \geq 42$ and $n \geq 66$ cilia, respectively). **(G)** CHE-11::mCherry kymographs of phasmid cilia from the indicated strains.

(H) Mean velocity of CHE-11::mCherry particles moving on anterograde and retrograde tracks ($n \geq 225$ particle traces were analyzed in ≥15 cilia). **(I)** Frequency of IFT particles detected at the distal segment of cilia ($n \geq 17$ cilia). **(J and K)** WDR-60 is required for efficient sensory cilia functions. **(J)** Chemotaxis index for the attractant IA ($n \geq 450$ animals tracked over ≥3 assays). **(K)** Osmotic avoidance assay to test whether sensory cilia detect a hypertonic glycerol barrier ($n \geq 20$ animals tracked over ≥4 assays). The dynein-2 LIC *xbx-1(null)* strain was used for comparison. XY intensity distribution graph is shown as mean ± SEM, and graphs in columns are shown as mean ± SD. One-way ANOVA followed by Tukey's multiple comparison were used to analyze the datasets in B, H, and I. Kruskal–Wallis test followed by Dunn's multiple comparison were used to analyze the datasets in E. *, $P \leq 0.05$; **, $P \leq 0.01$; ****, $P \leq 0.0001$. Scale bars: 2 µm (A and D); vertical 5 s, horizontal 2 µm (G).

and Video 4), underscoring the importance of WDR-60 in dynein-2–mediated transport of the IFT-B machinery to the ciliary base. When analyzing the distribution of kinesins, we also observed ciliary accumulations for the kinesin-2-associated protein KAP-1 (KIFAP3) and, to a lesser extent, for the distal segment kinesin OSM-3 (KIF17) (Fig. S4, B and C). Altogether, these results show that loss of WDR-60 greatly impairs removal of IFT components from cilia.

To determine the impact of *wdr-60*–associated IFT defects on ciliary functions, we analyzed cilia-dependent behavior in our mutant strains. We tested chemotaxis attraction to isoamyl alcohol (AI) and osmotic tolerance to high concentrations of glycerol (Fig. 4, J and K). Both *wdr-60* mutants showed modest defects in these assays, contrasting with the *xbx-1(null)* mutant, in which chemotaxis attraction and osmotic tolerance is severely compromised. These results suggest that although WDR-60 plays critical roles in dynein-2–mediated IFT, WDR-60–deficient sensory cilia remain partially functional.

TZ integrity and gating function are maintained in *wdr-60* mutants but not in the *xbx-1* mutant

Given that dynein-2 and IFT-A components were recently shown to be required for maintaining the TZ barrier (Jensen et al., 2018; Scheidel and Blacque, 2018; Vuolo et al., 2018), we investigated whether the integrity and gating capacity of the TZ are affected in *wdr-60* and *xbx-1* mutants. We analyzed the localization of four TZ components: TMEM-107, NPHP-4, MKS-6, and MKSR-1 (Jensen et al., 2018; Lambacher et al., 2016; Prevo et al., 2015; Schouteden et al., 2015; Williams et al., 2011). In agreement with what has been reported for CHE-3 and IFT-A mutants (Jensen et al., 2018; Scheidel and Blacque, 2018), we found that loss of XBX-1 results in ectopic localization of these TZ components along the ciliary axoneme (Fig. 5). In contrast, the localization of TZ components in *wdr-60* mutants was indistinguishable from controls (Fig. 5), suggesting that loss of WDR-60 does not affect the integrity of the TZ. To directly test the integrity and gating capacity of the TZ in *wdr-60* mutants, we analyzed its ability to block the entry of RPI-2::GFP (RP2), a component of the periciliary membrane compartment restricted to the base of cilia (Jensen et al., 2018). While loss of XBX-1 resulted in abnormal entry of RPI-2::GFP into cilia, no RPI-2::GFP signal was detectable inside cilia in *wdr-60* mutants (Fig. 5, C and D). These results show that the loss of WDR-60 does not compromise TZ integrity or its gating function in *C. elegans*. In addition, our results uncover an important role for the dynein-2 LIC XBX-1 in maintaining the TZ barrier, likely by stabilizing CHE-3.

WDR-60 is required for dynein-2 passage through the TZ to exit cilia

To more precisely determine where the ciliary pool of dynein-2 accumulates in *wdr-60* mutants, we colabeled GFP::CHE-3 with markers specific for the ciliary base (mCherry::HYLS-1; Schouteden et al., 2015) and for the TZ (MKS-6::mCherry; Williams et al., 2011). In controls, GFP::CHE-3 mainly accumulates at the ciliary base (Fig. 6 A) before entering cilia through the TZ. In contrast, we found that GFP::CHE-3 accumulates mostly at the distal side of the TZ in both *wdr-60* mutants (Fig. 6, B and C).

Recent studies have shown that retrograde trains slow down as they cross the TZ, suggesting that this ciliary gate offers resistance to the passage of retrograde IFT trains (Jensen et al., 2015; Oswald et al., 2018; Prevo et al., 2015). Given that loss of WDR-60 reduces the amount of dynein-2 driving retrograde trains and impairs retrograde IFT velocity (Fig. 3), we hypothesized that WDR-60–deficient retrograde trains may not be able to generate enough force to push through the TZ barrier, and are consequently unable to exit cilia. As removal of MKS-5 (RPGRIP1L), a key component for the assembly of all TZ structures, significantly increases the velocity of IFT trains moving in the TZ region (Jensen et al., 2015), we reasoned that the exit of WDR-60–deficient dynein-2 from cilia might be facilitated by disrupting MKS-5. In agreement, we found that GFP::CHE-3 no longer accumulated on the distal side of the TZ in the *mks-5(tm3100);wdr-60(null)* double mutant (Fig. 7, A–D). Instead, the GFP::CHE-3 distribution profile in this mutant was similar to that observed in controls. This result further supports that retrograde trains driven by dynein-2 are unable to efficiently cross the TZ in *wdr-60* mutants.

To better dissect which TZ modules restrict dynein-2 passage, we next examined GFP::CHE-3 distribution in *wdr-60(null)* cilia after disrupting key components required for the assembly of each TZ module. Removal of the MKS module by inhibiting MKSR-2 (B9D2) or CEP-290 with the *mksr-2(tm2452)* or *cep-290(tm4927)* mutations did not prevent the accumulation of GFP::CHE-3 near the TZ region of *wdr-60(null)* cilia (Fig. 7, E and F; and Fig. S5, A and B). In contrast, disrupting the NPHP module with the *nphp-4(tm925)* mutation in the *wdr-60(null)* background almost completely rescued GFP::CHE-3 accumulation at the distal side of the TZ (Fig. 7, G and H). Joint disruption of NPHP-4 and MKSR-2 further enhanced this rescue effect (Fig. 7, I and J), although we note that both cilia size and GFP::CHE-3 levels along cilia were strongly reduced in the *mksr-2(tm2452);nphp-4(tm925)* double mutant (Fig. 7 K; and Fig. S5, C and D). We conclude that NPHP is the main module restricting the passage of underpowered retrograde trains through the TZ in *wdr-60(null)* cilia.

Next, we tested whether disrupting the TZ could compensate for more severe retrograde IFT defects, such as those caused by a mutation in the microtubule-binding domain of CHE-3 (K2935Q), which completely blocks dynein-2 motility and leads to severely truncated cilia (Yi et al., 2017). In contrast to the

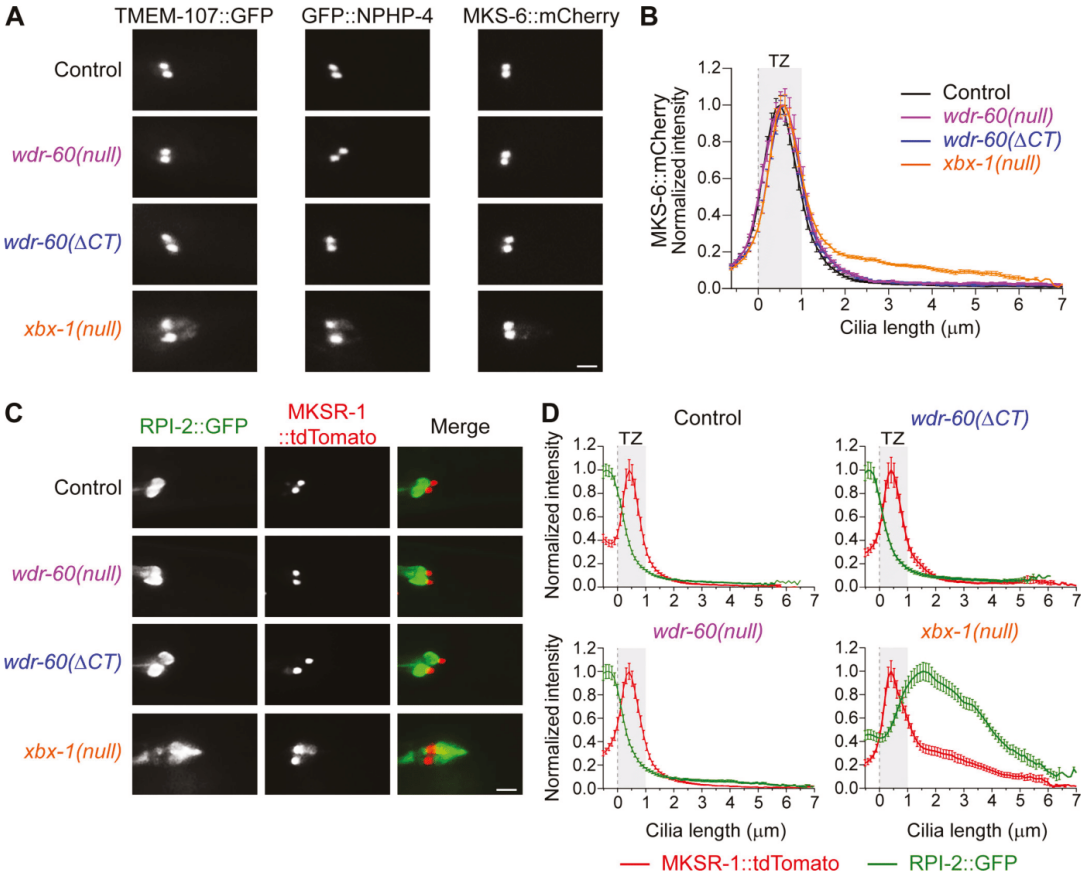

Figure 5. **The integrity and gating function of the TZ are maintained in *wdr-60* mutants but compromised in the *xbx-1* mutant. (A)** Analysis of the localization of several components of the MKS (TMEM-107::GFP and MKS-6::mCherry) and NPHP (GFP::NPHP-4) modules of the TZ in phasmid cilia of the indicated strains. **(B)** Quantification of MKS-6::mCherry signal intensity confined at the TZ and dispersed along cilia ($n \geq 38$ cilia). **(C)** Relative localization of the nonciliary membrane protein RPI-2::GFP to the TZ (labeled with MKSR-1::tdTomato) in phasmid cilia of the indicated strains. **(D)** Signal overlap between these components and quantification of the amount of RPI-2::GFP leaking into cilia ($n \geq 33$ cilia). Gray rectangles highlight the TZ region, defined by MKS-6 and MKSR-1 localization. XY intensity distribution graphs are shown as mean ± SEM. Scale bars: 2 µm.

rescue that we observed earlier in the *wdr-60(null)* mutant background, disrupting MKS-5, NPHP-4, or both MKSR-2/NPHP-4, failed to prevent GFP::CHE-3(K2935Q) accumulation inside cilia (Fig. 8, A–H). These results show that even the complete removal of the TZ barrier is not sufficient to rescue the accumulation of nonmotile dynein-2 inside cilia. Although cilia size slightly increased in the absence of MKS-5 or NPHP-4 (Fig. 8 I), none of the TZ mutants were able to restore anterograde IFT in animals expressing GFP::CHE-3(K2935Q) (Fig. 8 J and Video 5). Thus, IFT requires a minimum amount of functional dynein-2 regardless of the state of the TZ barrier.

The NPHP module restricts dynein-2 movement through the TZ

Next, we investigated whether the kinetics of WDR-60–deficient dynein-2 were altered by the complete removal of the TZ barrier or by the loss of the NPHP module. Consistent with a previous study (Jensen et al., 2015), we observed that loss of MKS-5 increases both the anterograde and retrograde velocities of GFP::CHE-3 particles in the TZ region (Fig. 9, A, C, and D; and Video 6). We also observed a similar, albeit more modest, increase in IFT velocities at the TZ region in the *nphp-4* mutant background. Importantly, we found that loss of either MKS-5 or NPHP-4 increased the retrograde velocity of GFP::CHE-3 in the TZ region of WDR-60–deficient cilia (Fig. 9, A, C, and D; and Video 7). Interestingly, retrograde IFT velocity in the middle segment of *wdr-60(null)* cilia also increased upon the removal of MKS-5 or NPHP-4 (Fig. 9 C), suggesting that clearing the accumulated IFT trains near the TZ allows for more steady buildup of retrograde IFT velocities in these mutants. We note that IFT frequency was not greatly affected by disruption of MKS-5 or NPHP-4 (Fig. 9 B), suggesting that loss of the TZ barrier does not compromise the

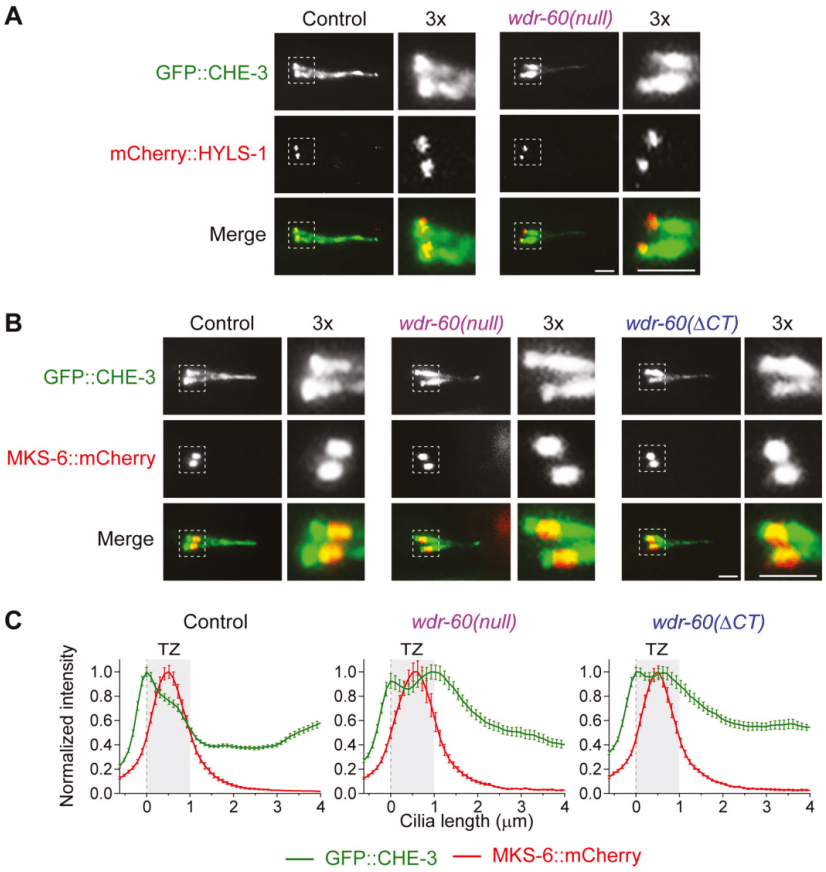

Figure 6. **Dynein-2 accumulates on the distal side of the TZ, unable to complete retrograde IFT in *wdr-60* mutants. (A)** GFP::CHE-3 localization relative to the centriolar wall component mCherry::HYLS-1 at the base of phasmid cilia of the indicated strains. **(B)** GFP::CHE-3 localization relative to the MKS-6::mCherry TZ component in phasmid cilia of the indicated strains. **(C)** Quantification GFP::CHE-3 signal distribution in relation to the TZ, as determined by MKS-6 localization ($n \geq 38$ cilia). Gray rectangles define the TZ region. 3× magnifications of the square section in each micrograph were included to better visualize the distribution of the dynein-2 HC relative to the base and TZ of *wdr-60* mutant cilia. Graphs are shown as mean ± SEM. Scale bars: 2 µm.

poorly understood mechanisms regulating the rate of IFT injection into cilia. Altogether, these results further support that WDR-60 loss impairs dynein-2 passage through the TZ, and that the NPHP module restricts dynein-2 exit from WDR-60–deficient cilia.

Discussion

WDR-60 is incorporated into cilia even in the absence of dynein-2

Our data reveal that WDR-60 is specifically expressed in ciliated sensory neurons in *C. elegans* and undergoes IFT with kinetics similar to those reported for the dynein-2 HC (GFP::CHE-3; Yi et al., 2017). Moreover, our findings indicate that WDR-60(ΔCT) is robustly expressed, showing that the β-propeller is not required for WDR-60 stability. Interestingly, we find that the WDR-60 NT on its own can be recruited to the ciliary base and incorporated into IFT trains, albeit less efficiently than full-length WDR-60. Furthermore, dynein-2 HC destabilization through XBX-1 loss resulted in WDR-60 and WDR-60(ΔCT) sequestration inside cilia, indicating that WDR-60 can enter cilia without dynein-2 but requires its activity in retrograde IFT to exit. Thus, we conclude that the NT of WDR-60 can establish links with other components of the IFT machinery to be incorporated into cilia in the absence of dynein-2. This is in agreement with the weaker but persistent interaction between IFT-B components and the human WDR60[Q631*] truncation lacking the DHC2-binding β-propeller domain (Vuolo et al., 2018).

WDR-60 is required for efficient IFT recycling and contributes to cilia-mediated behavior

Two recent studies in human cells showed that WDR60 loss leads to the misplacement of IFT and signaling particles in cilia

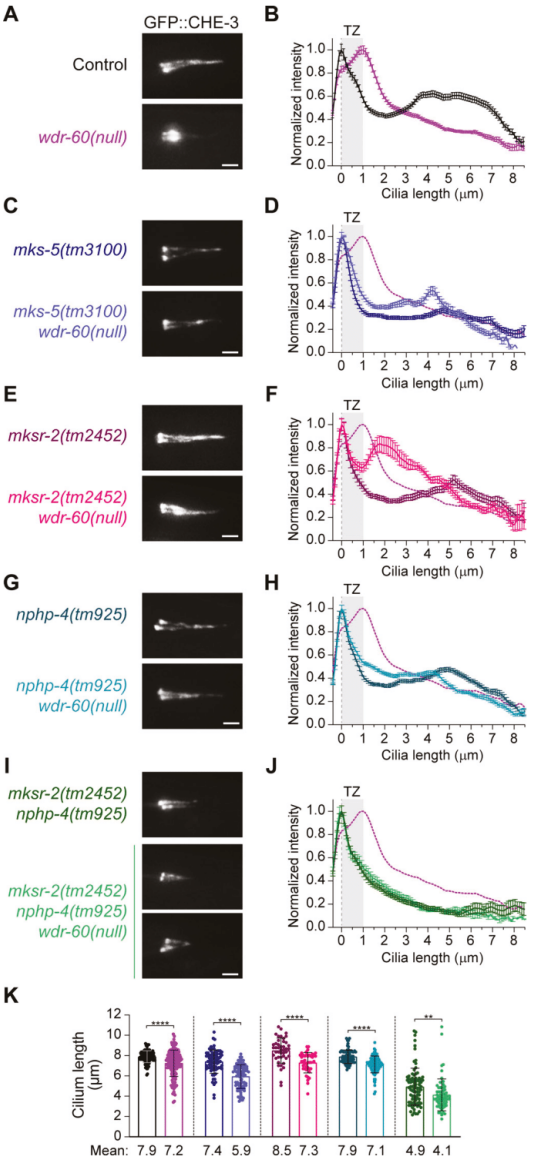

Figure 7. **Disruption of specific TZ components rescues dynein-2 accumulation inside cilia of *wdr-60* mutants. (A, C, E, G, and I)** Representative examples of phasmid cilia of the indicated *wdr-60* and TZ mutant genotypes, expressing GFP::CHE-3. **(B, D, F, H, and J)** Relative distribution of GFP::CHE-3 signal intensity along cilia. The purple dashed line represents the data from the *wdr-60(null)* in B. Gray rectangles highlight the TZ, as previously defined. $n \geq 108$ cilia for B, $n \geq 74$ cilia for D, $n \geq 42$ cilia for F, $n \geq 80$ cilia for H, and $n \geq 64$ cilia for J. XY intensity distribution graphs are shown as mean ± SEM. **(K)** Length of the cilia analyzed in B, D, F, H, and J from the same color-coded genotypes indicated in A, C, E, G, and I. Loss of WDR-60 combined with TZ mutations always resulted in a slight decrease of cilia length relative to the respective TZ mutant control. Graph is shown as mean ± SD. Mann–Whitney *U* test was used to analyze each pair of datasets. **, $P \leq 0.01$; ****, $P \leq 0.0001$. Scale bars: 2 µm.

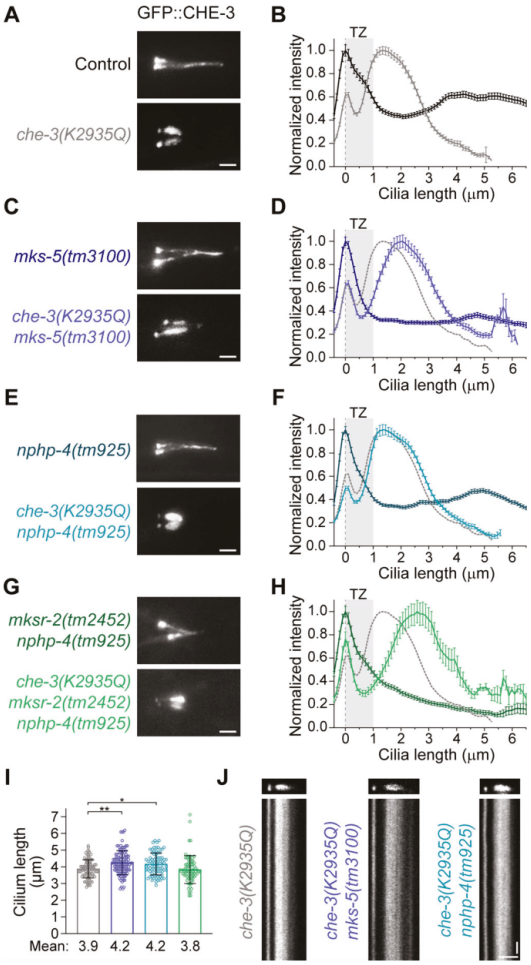

Figure 8. **Complete loss of dynein-2 motility results in ciliary accumulations even when the TZ barrier is completely disrupted. (A, C, E, and G)** Representative examples of phasmid cilia of the indicated TZ mutant genotypes, expressing wild-type GFP::CHE-3 or the nonmotile GFP::CHE-3(K2935Q). **(B, D, F, and H)** Relative distribution of GFP::CHE-3(K2935Q) signal intensity along cilia, in control and TZ mutant backgrounds. The gray dashed line represents the data from the GFP::CHE-3(K2935Q) mutant in B. Gray rectangles highlight the TZ, as previously defined. $n \geq 105$ cilia for B, $n \geq 104$ cilia for D, $n \geq 80$ cilia for F, and $n \geq 86$ cilia for H. XY intensity distribution graphs are shown as mean ± SEM. **(I)** Length of GFP::CHE-3(K2935Q) mutant cilia analyzed in B, D, F, and H, with the same color-coded genotypes as indicated. Graph is shown as mean ± SD. Kruskal–Wallis test followed by Dunn's multiple comparison were used to analyze these datasets. *, $P \leq 0.05$; **, $P \leq 0.01$. **(J)** Cilia and the respective kymographs from the specified strain genotypes. No anterograde or retrograde IFT was detectable in the GFP::CHE-3(K2935Q) mutant, not even in combination with the disruption of MKS-5 or NPHP-4. Scale bars: 2 µm (A, C, E, and G); vertical 5 s, horizontal 2 µm (J).

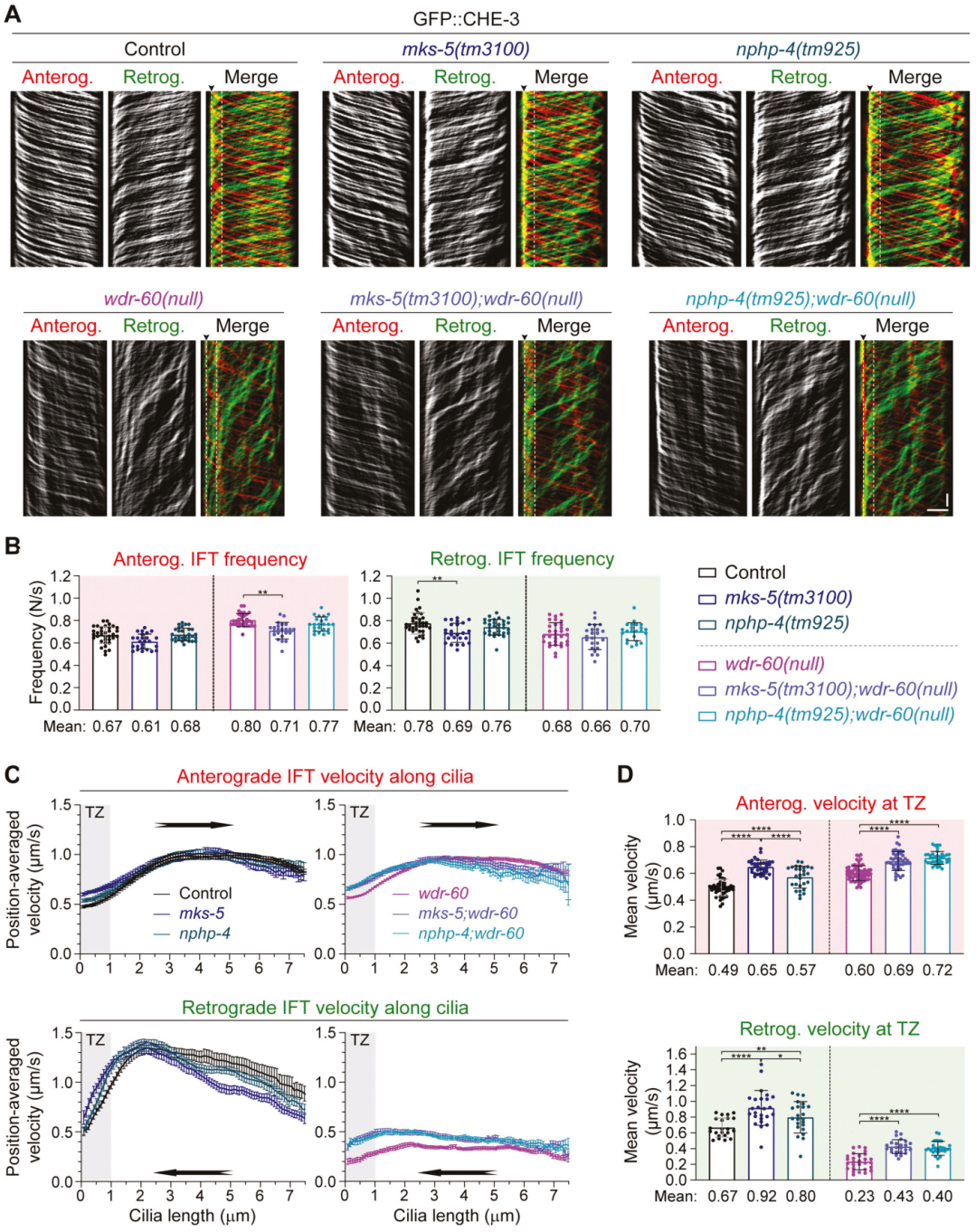

Figure 9. **Disruption of NPHP-4 is sufficient to increase the velocity of WDR-60–deficient dynein-2 through the TZ region. (A)** GFP::CHE-3 kymographs of phasmid cilia from the indicated strains. Single and merge channels for particles moving anterogradely and retrogradely are shown. Arrowhead labels the base, and white dashed line marks the limit of the TZ region (1 µm). Scale bars: vertical 5 s, horizontal 2 µm. **(B)** Frequency of IFT particles detected at the

distal segment of cilia for each represented strain ($n \geq 23$ cilia). **(C)** GFP::CHE-3 velocity moving in the anterograde and retrograde direction along the cilia of the indicated genotypes ($n \geq 345$ particle traces were analyzed in ≥23 cilia for each strain). Gray rectangles highlight the TZ, as previously defined. **(D)** Average velocity of GFP::CHE-3 crossing the TZ region of the same cilia analyzed in C, for each indicated genotype. XY velocity graphs are shown as mean ± SEM, and graphs in columns are shown as mean ± SD. One-way ANOVA followed by Sidak and the Holm–Sidak multiple comparisons were used to analyze the datasets in B and D, respectively. *, $P \leq 0.05$; **, $P \leq 0.01$; ****, $P \leq 0.0001$.

without greatly affecting axoneme extension (Hamada et al., 2018; Vuolo et al., 2018). Remarkably, in spite of the strong defect in retrograde IFT, we show that the *wdr-60(null)* mutant is still capable of building nearly full-length cilia in *C. elegans*, similar to what was observed in WDR60 knockout (KO) human cells (Vuolo et al., 2018). We also show that WDR-60–deficient cilia are at least partially functional in chemotaxis and osmotic tolerance assays, contrasting with the strong behavioral defects exhibited by the *xbx-1(null)* mutant, which assembles severely shortened cilia. The mild chemotaxis and osmotic defects that we observe in *wdr-60* mutants likely mirror the signaling defects underlying *WDR60*-associated SRPS (Cossu et al., 2016; Kakar et al., 2018; McInerney-Leo et al., 2013).

We find that WDR-60 disruption results in accumulation of IFT-74, CHE-11 (IFT140), and the kinesin-2 subunit KAP-1 inside cilia. However, we also show that WDR-60 disruption has different effects on the distribution profile of these IFT components along cilia: IFT-74 (IFT-B) levels peak at the tip and in the middle-to-distal-segment transition (both regions containing microtubule plus ends), while CHE-11 (IFT-A) and KAP-1 levels peak closer to the ciliary base and the TZ region, which is similar to the distribution profile of the dynein-2 motor itself. This suggests that some IFT subunits might be less efficiently incorporated into retrograde IFT trains in WDR-60–deficient cilia. In agreement with this, similar differences in IFT component distribution can be discerned in prior studies using WDR60 KO human cells: IFT88 (IFT-B) accumulates inside their cilia, peaking mostly at the tip, while the peak levels of accumulated IFT140 and IFT43 (both IFT-A) are found closer to the ciliary base (Hamada et al., 2018; Tsurumi et al., 2019; Vuolo et al., 2018).

Interestingly, our results suggest that the WDR-60 NT retains residual activity in IFT, as the accumulation of IFT-A/B particles inside cilia is less pronounced for the *wdr-60(ΔCT)* mutant than for the *wdr-60(null)* mutant. This is consistent with what was observed in WDR60 KO rescue experiments with an equivalent WDR60 β-propeller truncation construct (WDR60 [Q631*]; Vuolo et al., 2018). Apart from the less pronounced IFT accumulations, the loss of the WDR-60 β-propeller leads to defects in dynein-2 incorporation, retrograde IFT kinetics, and cilia-mediated behavior that are similar to those observed upon the complete loss of WDR-60. Thus, our results show that the WDR-60 β-propeller is critical for dynein-2 function.

Normal TZ integrity and gating function in the absence of WDR-60

A recent study uncovered that the dynein-2 HC CHE-3 is necessary for the stability and gating functions of the TZ (Jensen et al., 2018). Consistent with this, we show that loss of the dynein-2 LIC XBX-1 also impairs the integrity and gating functions of the TZ barrier. In a recent study, Vuolo et al. (2018) observed mislocalization of the TZ components TMEM67 and RPGRIP1L (MKS-5 orthologue) in a subset of human RPE1 WDR60 KO cells. In contrast, we do not observe any defects in TZ integrity and gating function in *wdr-60* mutants, as judged by the correct localization of multiple TZ components and the complete RPI-2 exclusion from their sensory cilia. We therefore conclude that the integrity and function of the TZ barrier are maintained in the absence of WDR-60 in *C. elegans*. The difference in TZ susceptibility to WDR60 loss may arise from the variations in TZ structure observed between different types of cilia (Akella et al., 2019; Jana et al., 2018) or from potential differences in the minimal threshold of dynein-2 function required for maintaining TZ integrity in each model system.

Disruption of WDR-60 reduces dynein-2 loading into cilia and the kinetics of retrograde IFT

Prior studies reported that WDR60 loss resulted in the complete disappearance of dynein-2 LIC from the base and axoneme of cilia (Hamada et al., 2018; Vuolo et al., 2018), but no detectable difference was observed in the recruitment of the dynein-2 HC to the ciliary base (Vuolo et al., 2018). Our analyses of endogenously labeled dynein-2 HC and LIC in *C. elegans* reveals that both subunits still colocalize inside WDR-60–deficient cilia. Importantly, the efficiency of dynein-2 HC recruitment to cilia is substantially decreased in the absence of WDR-60 or its dynein-2–binding β-propeller domain. Given that dynein-2 HC levels in the soma of ciliated sensory neurons are not greatly altered by the loss of WDR-60, our results argue that WDR-60 directly contributes to dynein-2 recruitment to cilia rather than having a significant role in dynein-2 HC stabilization, as is the case for dynein-2 LIC (Taylor et al., 2015; Toropova et al., 2019).

A recent structural study revealed that binding of the WDR60-WDR34 heterodimer contributes to the asymmetric conformation of the autoinhibited dynein-2 complex, and this was proposed to facilitate dynein-2 incorporation onto anterograde IFT trains (Toropova et al., 2017; Toropova et al., 2019). Our quantifications of dynein-2 HC (GFP::CHE-3) signal on anterograde tracks inside *wdr-60* mutant cilia provide the first direct evidence for this model in vivo. This conclusion is supported by the observation that the reduction in dynein-2 loading onto anterograde trains (approximately threefold) is even greater than the reduction in dynein-2 recruitment to cilia (approximately twofold) in *wdr-60* mutants.

Intriguingly, the observation that a fraction of dynein-2 motors still become incorporated onto anterograde IFT trains indicates that WDR-60 is not the only link that dynein-2 can establish with anterograde trains. This conclusion is further supported by the recent report of a direct interaction between dynein-2 LIC and IFT54 of the IFT-B complex (Zhu et al., 2021)

and by cryo-EM data suggesting that the main contacts between anterograde IFT trains and dynein-2 motors may also involve the HC (Toropova et al., 2019).

Although less dynein-2 reaches the cilium tip to then power retrograde IFT, we find that the frequency of retrograde IFT is only mildly affected in the absence of WDR-60. Taken together with the observation that dynein-2 does not accumulate at the ciliary tip, this result argues that WDR-60 is dispensable for dynein-2 activation and the start of retrograde IFT.

Underpowered retrograde IFT trains fail to push through the TZ barrier to exit cilia in *wdr-60* mutants

Emerging evidence points to an important interplay between IFT-A and the BBSome in regulating the traffic of G protein–coupled receptors in and out of cilia across the TZ, in part by coupling the receptors to IFT trains (reviewed in Nachury and Mick, 2019). As a dense gating structure, the TZ has been shown to slow down the passage of motor-powered IFT trains, supporting the notion that this physical barrier offers substantial resistance to the passage of IFT trains (Jensen et al., 2015; Oswald et al., 2018; Prevo et al., 2015). However, little is known about the mechanisms that enable the IFT machinery to pass through the TZ barrier.

Our live imaging analysis shows that WDR-60–deficient retrograde IFT trains are driven by fewer dynein-2 motors, at severely reduced velocity, and accumulate at the distal side of the TZ. We propose that the accumulation of these underpowered IFT trains reflects their inability to push through the TZ barrier (Fig. 10). Additional lines of evidence support a model in which a force production threshold needs to be met for retrograde IFT to cross the TZ barrier: (a) in experiments using purified "untrapped" dimers of GST-dynein-2 motor domains, maximum microtubule gliding velocity can be achieved only after a certain dynein-2 concentration is reached (Toropova et al., 2017); (b) the same study showed that DNA origamis mimicking IFT trains were transported less efficiently (less processive runs) when attached to three untrapped dynein-2 motor dimers than when attached to seven dimers (Toropova et al., 2017); (c) the cooperative action of multiple dynein-2 motors in retrograde IFT has been shown to be capable of generating considerable forces (≥25 pN) to move against resisting loads (Roberts, 2018; Shih et al., 2013); and (d) we show in this study that removing the resistance offered by the TZ rescues the exit of the underpowered retrograde IFT trains driven by fewer dynein-2 motors in *wdr-60* mutants.

Our findings are also consistent with the "motorized plough" model, which posits that dynein-2 motors remove IFT trains and their cargoes out of the cilium by dragging them while pushing through the TZ barrier (Nachury and Mick, 2019). We note, nonetheless, that we cannot fully exclude the possibility that WDR-60 might also contribute in other ways to retrograde IFT or ciliary exit.

The NPHP module offers resistance to dynein-2 passage through the TZ

Our results reveal that disrupting MKS-5, the most upstream TZ assembly factor, can rescue the exit of underpowered retrograde IFT trains from *wdr-60(null)* cilia. We then dissected which TZ modules offer resistance to dynein-2 exit by targeting their respective upstream components. We find that removal of the NPHP module by disrupting NPHP-4 almost completely rescues the exit of WDR-60–deficient dynein-2 from cilia, while the loss of the MKS module by disrupting MKSR-2 or CEP-290 did not. Given that previous studies showed that the recruitment of NPHP-4 and the assembly of the NPHP module are unaffected by the loss of either CEP-290 or MKSR-2 (Blacque and Sanders, 2014; Li et al., 2016; Schouteden et al., 2015), our findings support a pivotal role for the NPHP module in restricting dynein-2 passage through the TZ. Interestingly, in addition to disrupting the assembly of the NPHP module, NPHP-4 loss has also been shown to reduce the number of Y-links and their densities (Jensen et al., 2015; Lambacher et al., 2016). However, additional experimental work will be required to directly determine whether Y-links themselves influence the passage of IFT trains through the TZ.

Consistent with an important role for NPHP-4 and the NPHP module in restricting dynein-2 crossing of the TZ, studies in *C. elegans* and *Chlamydomonas* have shown that NPHP4 loss weakens and permeabilizes the TZ barrier, allowing entry of normally excluded cytoplasmic proteins and reducing the retention of ciliary proteins (Awata et al., 2014; Jauregui et al., 2008; Williams et al., 2011). In agreement with this, we find that removal of NPHP-4 increases the velocity of both anterograde and retrograde IFT trains crossing the TZ roadblock, particularly improving the retrograde velocity of underpowered WDR-60–deficient trains exiting cilia. This effect was even comparable with the increased IFT velocity in the TZ region that results from the disruption of MKS-5 in *wdr-60(null)* cilia. This supports the idea that even though NPHP-4 loss does not impair the TZ to the same extent as MKS-5 inhibition, it considerably reduces the resistance offered to IFT trains crossing the TZ barrier.

Interestingly, our results also indicate that even the complete removal of the TZ barrier is not sufficient for clearing out nonmotile CHE-3(K2935Q) dynein-2 from cilia. This finding implies that, although reduced, dynein-2 motors powering WDR-60–deficient retrograde IFT trains make an important contribution to the rescue observed upon disruption of the TZ barrier.

Taken together, our results provide direct evidence that the NPHP module of the TZ offers resistance to the passage of dynein-2–driven IFT trains and strongly support that dynein-2 motors need to reach a minimal force-generating threshold to power passage of retrograde trains through the TZ barrier to exit cilia.

Materials and methods

C. elegans maintenance and strain generation

C. elegans strains were maintained at 20°C on standard nematode growth medium (NGM) plates seeded with *Escherichia coli* OP50 bacteria and crossed using standard procedures (Brenner, 1974). Hermaphrodite worms were used in all assays. Mutant genotyping was performed by standard PCR. The *wdr-60* locus was

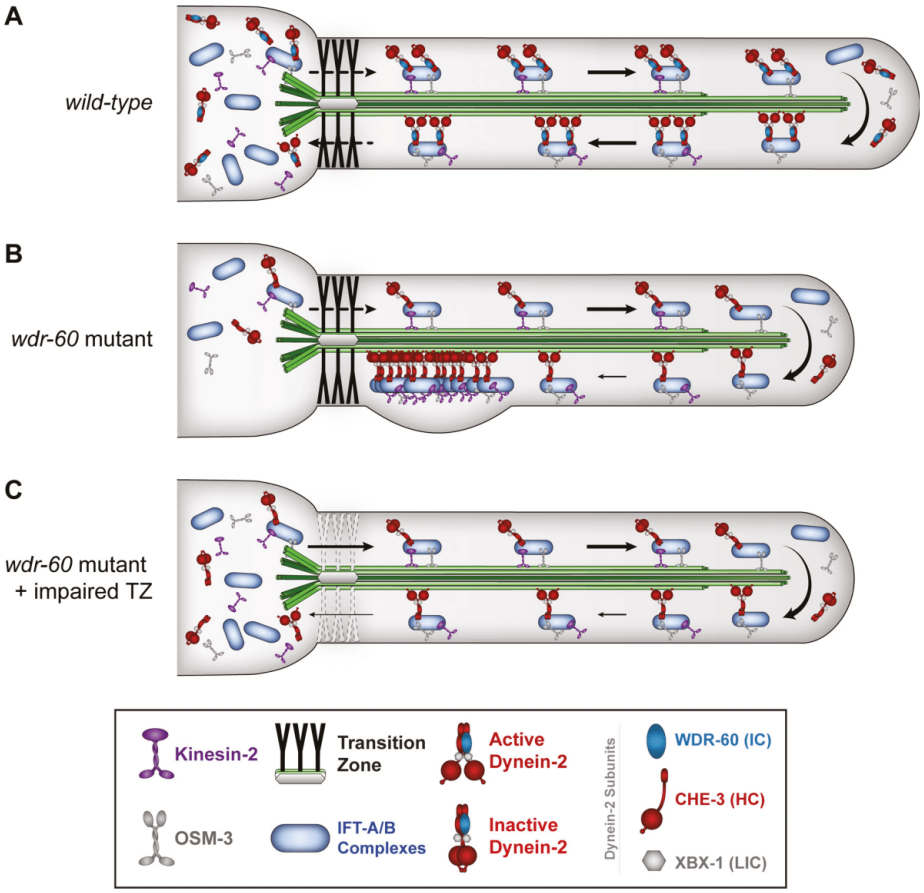

Figure 10. **Model for how WDR-60 contributes to efficient dynein-2–mediated retrograde IFT, and the crossing of the TZ to recycle the IFT machinery. (A)** In wild-type *C. elegans* cilia, kinesin motors carry dynein-2 as a cargo on anterograde IFT trains across the TZ to enter the cilium compartment and reach the ciliary tip. After rearrangement, dynein-2 transports trains in the retrograde direction, crossing the TZ barrier to return them to the base of the cilium, so they can be recycled. **(B)** In the absence of WDR-60, less dynein-2 is recruited and loaded onto anterograde IFT trains to be incorporated into cilia. Consequently, fewer dynein-2 motors are available at the ciliary tip to power the newly rearranged retrograde trains. These underpowered dynein-2–driven trains move at slower velocities and tend to accumulate at the distal side of the TZ, unable to generate enough force to cross this barrier. **(C)** Disrupting the NPHP module reduces the resistance offered by the TZ to the passage of IFT trains, facilitating the exit of retrograde IFT to the cilium base and compensating for the less efficient WDR-60–deficient dynein-2 trains.

engineered by CRISPR-Cas9 using germline microinjection of Cas9 and specific gRNA-expressing (5′-GACAAACGCAATTCGCAGA-3′ and 5′-TGTTCTAGAAGATCCCGCG-3′) constructs, supplemented with homology templates consisting in DNA oligonucleotides or large DNA fragments partially single stranded (Dokshin et al., 2018). The presence of the desired alleles was confirmed by PCR-based genotyping. New strains were outcrossed four to six times to ensure the absence of potential CRISPR-Cas9 off-target mutations. *C. elegans* strains and primers used in this study are listed in Table S2 and Table S3, respectively.

Fluorescence imaging

All imaging was performed using young adult hermaphrodite worms, with the exception of the aging experiments, in which animals at larval stage 2 and 7/18 days after adulthood were also imaged for comparison. All animals used for imaging were immobilized using 5–10 mM levamisole and were placed on a 5% agarose pad mounted on a microscope slide.

Cilia imaging to generate signal-intensity distribution profiles was performed using an Axio Observer microscope (Zeiss) equipped with a Plan-Apochromat 63×/1.46 NA oil objective lens and an Orca Flash 4.0 camera (Hamamatsu) and controlled by Zen software (Zeiss). Z-stacks were acquired with 0.4 µm between each z-section.

Time-lapse imaging of IFT was performed using an Olympus IX81 inverted microscope coupled to an Andor Revolution XD spinning disk confocal system composed of an iXon^{EM}+ DU-897 with 2× port coupler camera (Andor Technology), a solid-state

laser combiner (ALC-UVP 350i; Andor Technology), and a CSU-X1 confocal scanner (Yokogawa Electric Corp.), controlled by Andor IQ3 software (Andor Technology). 200 frames were recorded for each phasmid cilium at 3 frames/s (333 ms per frame) using an UPLSAPO 100×/1.40 NA oil objective lens. All imaging was performed in temperature-controlled rooms kept at 20°C.

Image processing and analyses of live IFT

Z-stack and time-lapse series were processed and analyzed with Fiji software (ImageJ v2.0.0-rc-56/1.52 p). Fluorescence signal of ciliary components (such as IFT-74::GFP, CHE-11::mCherry, and GFP::CHE-3) were used to measure the length of cilia in wild-type and mutant strains from the center of the base to the ciliary tip. The profile of IFT particle distribution was determined along cilia using fluorescently labeled IFT markers. The signal intensity of each pixel was measured from the base to the tip of each cilium, and the relative signal distribution of particles was determined. When indicated, signal intensity values of each profile were normalized to their point of maximum intensity to facilitate comparison between profiles from different mutant combinations, and in these instances the total signal from base to tip was also determined and plotted separately.

Kymographs were generated in ImageJ (National Institutes of Health) using the KymographClear toolset plugin (v2.0; Mangeol et al., 2016). To ensure the quality of the data used to analyze IFT dynamics, only cilia without severe malformations and completely visible in single stable focal planes were used to generate kymographs. KymographDirect software (v2.1; Mangeol et al., 2016) was used to analyze IFT dynamics, which takes into account background and bleaching automatically and is able to distinguish and separate anterograde from retrograde IFT. Anterograde tracks of individual IFT particles along the whole cilium length were automatically detected by the program as done in Mijalkovic et al. (2017) and validated. Given the severity of the retrograde IFT phenotypes in *wdr-60* mutants, the program was unable to robustly detect the retrograde tracks of IFT particles. To account for that, all retrograde tracks (both in mutants and in controls) had to be drawn manually. Continuous IFT tracks drawn in the prior step were then used to automatically determine IFT velocities at different positions along cilia with KymographDirect. When average velocities were calculated for particular subregions of the axoneme, they were subgrouped as follows: TZ (0–1 µm), middle segment (1–4.5 µm), and distal segment (4.5 µm to ciliary tip).

To determine the frequency of anterograde and retrograde IFT events (data in Figs. 1 G, 3 F, 4 I, and 9 B), we employed the approach used in Mijalkovic et al. (2017). A vertical straight line was drawn to cross the same position at the ciliary distal segment of each anterograde or retrograde kymograph. The line drawn on each kymograph was then used to generate an intensity profile plot, which allowed to score the number of IFT events in either direction by counting the number of intensity spikes. This quantification reflects the number of distinguishable GFP::CHE-3 particles that move in either direction over time.

The average signal intensities of anterogradely or retrogradely moving GFP::CHE-3 particles were determined using KymographDirect as in Mijalkovic et al. (2017). The software automatically measured the intensity of all pixels composing each IFT track, including the retrograde tracks that had to be drawn manually, as mentioned above. The pixel values were then averaged to provide a single intensity value, representative of each individual track. Each point of GFP::CHE-3 intensity plotted in Fig. 3 G corresponds to the average of all of the tracks (a minimum of 15) from a single cilium, for either anterograde or retrograde IFT. At least 15 cilia were used per strain to determine the average GFP::CHE-3 intensity particles moving in either direction.

Dye filling

A stock solution containing 8 mg/ml of DiI (1,1′-dioctadecyl-3,3,3′,3′-tetramethylindocarbocyanine perchlorate) in dimethyl formamide was prepared in advance and stored at −20°C. One confluent but not starved plate of worms from the strain to be tested was grown for each experiment, and a fresh dilution of DiI solution at 2.5 µg/ml was prepared in M9 (86 mM NaCl, 42 mM Na_2HPO_4, 22 mM KH_2PO_4, and 1 mM $MgSO_4$) and kept in the dark covered with aluminum foil. Worms were collected and washed in M9 and incubated in 500 µl of working DiI solution for 1 h at room temperature in the dark, with occasional flipping of the tubes. After washing in M9, worms were placed on an NGM seeded plate for 3 h at 20°C to further reduce the background of ingested dye. The neuronal uptake of dye was then examined using the Axio Observer microscope as described above. At least 20 adult hermaphrodite worms were examined for each strain in ≥2 independent experiments.

Chemosensing assays

Chemotaxis to IA, an attractant compound, was assessed using 150–200 well-fed synchronized adult worms grown at 20°C per assay, following the guidelines of Bargmann et al. (1993). Briefly, worms were washed three times in CTX buffer (1 mM $CaCl_2$, 1 mM $MgSO_4$, and 5 mM KH_2PO_4, pH 6.0) and placed on a 10-cm CTX plate without bacteria, at the starting/origin point. This origin point was set to be at the edge of the plate, equidistant to 10% IA attractant (in absolute ethanol) and vehicle (absolute ethanol) regions, which were drawn at opposite ends of the plate. Before adding 10 µl of 10% IA to the attractant site and 10 µl of 100% ethanol (solvent) to the control site, a solution of 1 M sodium azide (NaN_3) was added to these two points. The sodium azide serves to immobilize any worms that reach the attractant or vehicle (control) regions, preventing them from moving away. After being placed at the origin point, worms were allowed to freely explore the plate for 1 h at 20°C, after which their localization and chemotaxis index was determined. The chemotaxis index can vary from 1.0 to −1.0 and was calculated as follows: Chemotaxis index = (number of worms at the attractant site − number of worms at the control site) / total number of worms.

Osmotic avoidance assay

Osmotic avoidance assays were performed on NGM nonseeded plates at room temperature (~20°C), following the guidelines of Sanders et al. (2015). Each repeat was performed using five

young adult hermaphrodite worms of each strain isolated before the experiment. Worms were placed inside a glycerol ring with a diameter of ∼1 cm, freshly prepared with a tube dipped in a 59% glycerol solution. Worm behavior was immediately monitored for 10 min to determine whether they avoided crossing the glycerol ring. Worms that left the ring or stayed in contact with its glycerol border for >20 s were classified as escapers. Wild-type and *xbx-1(null)* worms were used as controls.

Immunoblotting

For immunoblots of *C. elegans* extracts, four plates of hermaphrodites reaching confluence were collected and washed three times in M9, and the worm pellet was resuspended in an equal volume of 4× SDS-PAGE sample buffer (250 mM Tris-HCl, pH 6.8, 30% [vol/vol] glycerol, 8% [wt/vol] SDS, 200 mM DTT, and 0.04% [wt/vol] bromophenol blue). The worm suspension in sample buffer was supplemented with ∼20 µl of glass beads, incubated for 5 min at 95°C, and vortexed for an additional 5 min. After boiling and vortexing twice, samples were centrifuged at 20,000 *g* for 1 min at room temperature, and supernatants were collected. 20% of each sample was loaded and resolved on a 10% SDS-PAGE gel and transferred to 0.2-µm nitrocellulose membranes (GE Healthcare). Membranes were rinsed in PBS (137 mM NaCl, 2.7 mM KCl, 8.1 mM Na_2HPO_4, and 1.47 mM KH_2PO_4) supplemented with 0.1% Tween-20 (PBS-T, pH 7.4), and then blocked with 5% (wt/vol) nonfat dry milk in PBS-T for 1 h. Subsequently, membranes were incubated with mouse anti-FLAG M2 antibody (1:500; Sigma-Aldrich) or mouse anti-α-tubulin B512 antibody (1: 5,000; Sigma-Aldrich) overnight at 4°C. On the following day, membranes were washed three times in PBS-T for 10 min each. Membranes were then incubated with secondary antibodies coupled to HRP (1:10,000; Jackson ImmunoResearch) for 1 h at room temperature and washed three times in PBS-T for 5 min each. Pierce ECL Western Blotting Substrate (Thermo Fisher Scientific) was added to membranes to visualize proteins by chemiluminescence using x-ray film or a Chemidoc station (Bio-Rad). Each immunoblot was repeated several times using samples from independent experiments. The predicted protein sizes were based on the NCBI WDR-60 sequence (NP_001367569.1).

Data analyses and statistics

Statistical analyses of datasets were performed using GraphPad Prism software (v8). For the majority of the experiments, ≥20 worms from different plates were examined for each strain, in at least three independent experiments. Shapiro–Wilk and Kolmogorov–Smirnov normality tests were performed to determine whether sample groups followed Gaussian distributions, which dictated the choice between the use of parametric or nonparametric statistical tests. One-way ANOVA, followed by comparison of the mean of each experimental group with the mean of the control group, was used to analyze parametric datasets; otherwise, we used the nonparametric Kruskal–Wallis test. Follow-up multiple comparison tests were selected according to GraphPad Prism software suggestions. For single-comparison statistical analyses of parametric datasets, the two-tailed Student's *t* test was used, while the two-tailed Mann–Whitney *U* test was used for nonparametric data. Differences were considered significant at P values <5% (*, P ≤ 0.05; **, P ≤ 0.01; ***, P ≤ 0.001; and ****, P ≤ 0.0001). XY velocity and intensity distribution graphs are shown as mean ± SEM. Graphs in columns are shown as mean ± SD.

Online supplemental material

Fig. S1 shows a schematic of the *C27F2.1* locus organization in the *C. elegans* genome and the strategies used to generate *wdr-60* mutants and the 3xFLAG::GFP knock-in. Fig. S2 shows that WDR-60::3xFLAG::GFP expression is restricted to ciliated sensory neurons; it also shows the average GFP::CHE-3 intensity in soma of phasmid sensory neurons of control and *wdr-60* mutants. Fig. S3 shows the analyses of WDR-60–associated phenotypes at different stages of development and aging. Fig. S4 shows kymographs illustrating IFT-74::GFP kinetics in *wdr-60* mutants and the ciliary distribution profile for KAP-1 and OSM-3. Fig. S5 shows the levels of ciliary GFP::CHE-3 in the mutant backgrounds of *wdr-60* and disrupted TZ components, and that the GFP::CHE-3 accumulation at the distal side of the TZ associated with WDR-60 loss is not ameliorated in the *cep-290(tm4927)* mutant background. Table S1 contains the nomenclature of *C. elegans* proteins that are mentioned in the text, and their corresponding homologues or orthologues in humans. Table S2 contains the list of strains used in this study. Table S3 contains the list of primers used in this study. Video 1 shows GFP::CHE-3 and WDR-60::GFP undergoing IFT in *C. elegans* phasmid cilia. Video 2 shows the dynamics of GFP::CHE-3 in *C. elegans* phasmid cilia from control and *wdr-60* mutants. Video 3 shows the dynamics of CHE-11::mCherry in *C. elegans* phasmid cilia from control and *wdr-60* mutants. Video 4 shows the dynamics of IFT-74::GFP in *C. elegans* phasmid cilia from control and *wdr-60* mutants. Video 5 shows the dynamics of GFP::CHE-3(K2935Q) in *C. elegans* phasmid cilia from control, *mks-5(tm3100)*, and *nphp-4(tm925)* strains. Video 6 shows the dynamics of GFP::CHE-3 in *C. elegans* phasmid cilia from control, *mks-5(tm3100)*, and *nphp-4(tm925)* strains. Video 7 shows the dynamics of GFP::CHE-3 in *C. elegans* phasmid cilia from *wdr-60(null)*, *wdr-60(null);mks-5(tm3100)*, and *wdr-60(null);nphp-4(tm925)* mutants.

Acknowledgments

We thank Dr. Alexander Dammermann (University of Vienna, Vienna, Austria) for discussions and members of the Dantas lab for critical reading of the manuscript. The authors also thank Drs. Alexander Dammermann (University of Vienna, Vienna, Austria), Erwin Peterman (Vrije Universiteit Amsterdam, Amsterdam, Netherlands), Guangshuo Ou (Tsinghua University, Beijing, China), Oliver Blacque (University College Dublin, Dublin, Ireland), Michel Leroux (Simon Fraser University, Burnaby, Canada), and Bram Prevo (University of Edinburgh, Edinburgh, Scotland) for providing *C. elegans* strains.

This work was financed by Fundo Europeu de Desenvolvimento Regional (FEDER) through the COMPETE 2020 Operacional Programme for Competitiveness and Internationalisation (POCI), Portugal 2020, and Portuguese funds through Fundação para a Ciência e a Tecnologia (FCT)/Ministério da Ciência, Tecnologia e Ensino Superior in the framework of the project POCI-01-0145-FEDER-029471 (PTDC/BIA-BID/29471/2017) to T.J. Dantas.

A.X. Carvalho, R. Gassmann, C.M.C. Abreu, and T.J. Dantas were supported by the FCT: CEECIND/01967/2017, CEECIND/00333/2017, CEECIND/01985/2018, and CEECIND/00771/2017, respectively. N. Vieira is a Junior Researcher under the scope of the FCT Transitional Rule DL57/2016, and her work was supported by a 2016 NARSAD Young Investigator Grant (#24929) from the Brain and Behavior Research Foundation. D.R.M. Rodrigues received a PhD fellowship from FCT (SFRH/BD/143985/2019) and support from the Biomedical Sciences PhD program at Instituto de Ciências Biomédicas Abel Salazar (ICBAS). Some strains were provided by the National Bioresource Project for *C. elegans* and by the Caenorhabditis Genetics Center (CGC), which is funded by the National Institutes of Health Office of Research Infrastructure Programs (P40 OD010440).

The authors declare no competing financial interests.

Author contributions: A.R.G. De-Castro and D.R.M. Rodrigues performed most of the experiments, actively contributed to the experimental design, analyzed data, and helped prepare figures and write the manuscript. M.J.G. De-Castro helped with several experiments, quantifications, and figure preparation. N. Vieira carried out the chemotaxis assay, and C. Vieira generated some strains. R. Gassmann and A.X. Carvalho provided strains, reagents, and equipment and helped with experimental design. T.J. Dantas and C.M.C. Abreu conceived the project, designed and helped with experiments, analyzed and interpreted data, prepared figures, wrote the manuscript, and supervised the project. All authors read the manuscript and provided input for the final version.

Submitted: 31 October 2020
Revised: 20 September 2021
Accepted: 13 October 2021

References

Akella, J.S., M. Silva, N.S. Morsci, K.C. Nguyen, W.J. Rice, D.H. Hall, and M.M. Barr. 2019. Cell type-specific structural plasticity of the ciliary transition zone in C. elegans. *Biol. Cell.* 111:95–107. https://doi.org/10.1111/boc.201800042

Asante, D., N.L. Stevenson, and D.J. Stephens. 2014. Subunit composition of the human cytoplasmic dynein-2 complex. *J. Cell Sci.* 127:4774–4787. https://doi.org/10.1242/jcs.159038

Awata, J., S. Takada, C. Standley, K.F. Lechtreck, K.D. Bellvé, G.J. Pazour, K.E. Fogarty, and G.B. Witman. 2014. NPHP4 controls ciliary trafficking of membrane proteins and large soluble proteins at the transition zone. *J. Cell Sci.* 127:4714–4727. https://doi.org/10.1242/jcs.155275

Bae, Y.K., and M.M. Barr. 2008. Sensory roles of neuronal cilia: cilia development, morphogenesis, and function in C. elegans. *Front. Biosci.* 13:5959–5974. https://doi.org/10.2741/3129

Bargmann, C.I., E. Hartwieg, and H.R. Horvitz. 1993. Odorant-selective genes and neurons mediate olfaction in C. elegans. *Cell.* 74:515–527. https://doi.org/10.1016/0092-8674(93)80053-H

Blacque, O.E., and A.A. Sanders. 2014. Compartments within a compartment: what C. elegans can tell us about ciliary subdomain composition, biogenesis, function, and disease. *Organogenesis.* 10:126–137. https://doi.org/10.4161/org.28830

Blacque, O.E., E.A. Perens, K.A. Boroevich, P.N. Inglis, C. Li, A. Warner, J. Khattra, R.A. Holt, G. Ou, A.K. Mah, et al. 2005. Functional genomics of the cilium, a sensory organelle. *Curr. Biol.* 15:935–941. https://doi.org/10.1016/j.cub.2005.04.059

Blisnick, T., J. Buisson, S. Absalon, A. Marie, N. Cayet, and P. Bastin. 2014. The intraflagellar transport dynein complex of trypanosomes is made of a heterodimer of dynein heavy chains and of light and intermediate chains of distinct functions. *Mol. Biol. Cell.* 25:2620–2633. https://doi.org/10.1091/mbc.e14-05-0961

Brenner, S. 1974. The genetics of Caenorhabditis elegans. *Genetics.* 77:71–94. https://doi.org/10.1093/genetics/77.1.71

Cornils, A., A.K. Maurya, L. Tereshko, J. Kennedy, A.G. Brear, V. Prahlad, O.E. Blacque, and P. Sengupta. 2016. Structural and Functional Recovery of Sensory Cilia in C. elegans IFT Mutants upon Aging. *PLoS Genet.* 12:e1006325. https://doi.org/10.1371/journal.pgen.1006325

Cossu, C., F. Incani, M.L. Serra, A. Coiana, G. Crisponi, L. Boccone, and M.C. Rosatelli. 2016. New mutations in DYNC2H1 and WDR60 genes revealed by whole-exome sequencing in two unrelated Sardinian families with Jeune asphyxiating thoracic dystrophy. *Clin. Chim. Acta.* 455:172–180. https://doi.org/10.1016/j.cca.2016.02.006

Dagoneau, N., M. Goulet, D. Geneviève, Y. Sznajer, J. Martinovic, S. Smithson, C. Huber, G. Baujat, E. Flori, L. Tecco, et al. 2009. DYNC2H1 mutations cause asphyxiating thoracic dystrophy and short rib-polydactyly syndrome, type III. *Am. J. Hum. Genet.* 84:706–711. https://doi.org/10.1016/j.ajhg.2009.04.016

Dokshin, G.A., K.S. Ghanta, K.M. Piscopo, and C.C. Mello. 2018. Robust Genome Editing with Short Single-Stranded and Long, Partially Single-Stranded DNA Donors in *Caenorhabditis elegans*. *Genetics.* 210:781–787. https://doi.org/10.1534/genetics.118.301532

Drummond, I.A. 2012. Cilia functions in development. *Curr. Opin. Cell Biol.* 24:24–30. https://doi.org/10.1016/j.ceb.2011.12.007

Garcia-Gonzalo, F.R., and J.F. Reiter. 2017. Open Sesame: How Transition Fibers and the Transition Zone Control Ciliary Composition. *Cold Spring Harb. Perspect. Biol.* 9:a028134. https://doi.org/10.1101/cshperspect.a028134

Hamada, Y., Y. Tsurumi, S. Nozaki, Y. Katoh, and K. Nakayama. 2018. Interaction of WDR60 intermediate chain with TCTEX1D2 light chain of the dynein-2 complex is crucial for ciliary protein trafficking. *Mol. Biol. Cell.* 29:1628–1639. https://doi.org/10.1091/mbc.E18-03-0173

Hou, Y., and G.B. Witman. 2015. Dynein and intraflagellar transport. *Exp. Cell Res.* 334:26–34. https://doi.org/10.1016/j.yexcr.2015.02.017

Hou, Y., G.J. Pazour, and G.B. Witman. 2004. A dynein light intermediate chain, D1bLIC, is required for retrograde intraflagellar transport. *Mol. Biol. Cell.* 15:4382–4394. https://doi.org/10.1091/mbc.e04-05-0377

Huangfu, D., and K.V. Anderson. 2005. Cilia and Hedgehog responsiveness in the mouse. *Proc. Natl. Acad. Sci. USA.* 102:11325–11330. https://doi.org/10.1073/pnas.0505328102

Huber, C., S. Wu, A.S. Kim, S. Sigaudy, A. Sarukhanov, V. Serre, G. Baujat, K.H. Le Quan Sang, D.L. Rimoin, D.H. Cohn, et al. 2013. WDR34 mutations that cause short-rib polydactyly syndrome type III/severe asphyxiating thoracic dysplasia reveal a role for the NF-κB pathway in cilia. *Am. J. Hum. Genet.* 93:926–931. https://doi.org/10.1016/j.ajhg.2013.10.007

Jana, S.C., S. Mendonça, P. Machado, S. Werner, J. Rocha, A. Pereira, H. Maiato, and M. Bettencourt-Dias. 2018. Differential regulation of transition zone and centriole proteins contributes to ciliary base diversity. *Nat. Cell Biol.* 20:928–941. https://doi.org/10.1038/s41556-018-0132-1

Jauregui, A.R., K.C. Nguyen, D.H. Hall, and M.M. Barr. 2008. The Caenorhabditis elegans nephrocystins act as global modifiers of cilium structure. *J. Cell Biol.* 180:973–988. https://doi.org/10.1083/jcb.200707090

Jensen, V.L., C. Li, R.V. Bowie, L. Clarke, S. Mohan, O.E. Blacque, and M.R. Leroux. 2015. Formation of the transition zone by Mks5/Rpgrip1L establishes a ciliary zone of exclusion (CIZE) that compartmentalises ciliary signalling proteins and controls PIP2 ciliary abundance. *EMBO J.* 34:2537–2556. https://doi.org/10.15252/embj.201488044

Jensen, V.L., N.J. Lambacher, C. Li, S. Mohan, C.L. Williams, P.N. Inglis, B.K. Yoder, O.E. Blacque, and M.R. Leroux. 2018. Role for intraflagellar transport in building a functional transition zone. *EMBO Rep.* 19:e45862. https://doi.org/10.15252/embr.201845862

Kakar, N., D. Horn, E. Decker, N. Sowada, C. Kubisch, J. Ahmad, G. Borck, and C. Bergmann. 2018. Expanding the phenotype associated with biallelic WDR60 mutations: Siblings with retinal degeneration and polydactyly lacking other features of short rib thoracic dystrophies. *Am. J. Med. Genet. A.* 176:438–442. https://doi.org/10.1002/ajmg.a.38562

Kozminski, K.G., K.A. Johnson, P. Forscher, and J.L. Rosenbaum. 1993. A motility in the eukaryotic flagellum unrelated to flagellar beating. *Proc. Natl. Acad. Sci. USA.* 90:5519–5523. https://doi.org/10.1073/pnas.90.12.5519

Kozminski, K.G., P.L. Beech, and J.L. Rosenbaum. 1995. The Chlamydomonas kinesin-like protein FLA10 is involved in motility associated with the flagellar membrane. *J. Cell Biol.* 131:1517–1527. https://doi.org/10.1083/jcb.131.6.1517

Lambacher, N.J., A.L. Bruel, T.J. van Dam, K. Szymańska, G.G. Slaats, S. Kuhns, G.J. McManus, J.E. Kennedy, K. Gaff, K.M. Wu, et al. 2016. TMEM107 recruits ciliopathy proteins to subdomains of the ciliary transition zone and causes Joubert syndrome. *Nat. Cell Biol.* 18:122–131. https://doi.org/10.1038/ncb3273

Li, C., V.L. Jensen, K. Park, J. Kennedy, F.R. Garcia-Gonzalo, M. Romani, R. De Mori, A.L. Bruel, D. Gaillard, B. Doray, et al. 2016. MKS5 and CEP290 Dependent Assembly Pathway of the Ciliary Transition Zone. *PLoS Biol.* 14:e1002416. https://doi.org/10.1371/journal.pbio.1002416

Mangeol, P., B. Prevo, and E.J. Peterman. 2016. KymographClear and KymographDirect: two tools for the automated quantitative analysis of molecular and cellular dynamics using kymographs. *Mol. Biol. Cell.* 27: 1948–1957. https://doi.org/10.1091/mbc.e15-06-0404

May, S.R., A.M. Ashique, M. Karlen, B. Wang, Y. Shen, K. Zarbalis, J. Reiter, J. Ericson, and A.S. Peterson. 2005. Loss of the retrograde motor for IFT disrupts localization of Smo to cilia and prevents the expression of both activator and repressor functions of Gli. *Dev. Biol.* 287:378–389. https://doi.org/10.1016/j.ydbio.2005.08.050

McInerney-Leo, A.M., M. Schmidts, C.R. Cortés, P.J. Leo, B. Gener, A.D. Courtney, B. Gardiner, J.A. Harris, Y. Lu, M. Marshall, et al. UK10K Consortium. 2013. Short-rib polydactyly and Jeune syndromes are caused by mutations in WDR60. *Am. J. Hum. Genet.* 93:515–523. https://doi.org/10.1016/j.ajhg.2013.06.022

Merrill, A.E., B. Merriman, C. Farrington-Rock, N. Camacho, E.T. Sebald, V.A. Funari, M.J. Schibler, M.H. Firestein, Z.A. Cohn, M.A. Priore, et al. 2009. Ciliary abnormalities due to defects in the retrograde transport protein DYNC2H1 in short-rib polydactyly syndrome. *Am. J. Hum. Genet.* 84:542–549. https://doi.org/10.1016/j.ajhg.2009.03.015

Mijalkovic, J., B. Prevo, F. Oswald, P. Mangeol, and E.J. Peterman. 2017. Ensemble and single-molecule dynamics of IFT dynein in Caenorhabditis elegans cilia. *Nat. Commun.* 8:14591. https://doi.org/10.1038/ncomms14591

Mikami, A., S.H. Tynan, T. Hama, K. Luby-Phelps, T. Saito, J.E. Crandall, J.C. Besharse, and R.B. Vallee. 2002. Molecular structure of cytoplasmic dynein 2 and its distribution in neuronal and ciliated cells. *J. Cell Sci.* 115: 4801–4808. https://doi.org/10.1242/jcs.00168

Nachury, M.V., and D.U. Mick. 2019. Establishing and regulating the composition of cilia for signal transduction. *Nat. Rev. Mol. Cell Biol.* 20: 389–405. https://doi.org/10.1038/s41580-019-0116-4

Niceta, M., K. Margiotti, M.C. Digilio, V. Guida, A. Bruselles, S. Pizzi, A. Ferraris, L. Memo, N. Laforgia, M.L. Dentici, et al. 2018. Biallelic mutations in DYNC2LI1 are a rare cause of Ellis-van Creveld syndrome. *Clin. Genet.* 93:632–639. https://doi.org/10.1111/cge.13128

Oswald, F., B. Prevo, S. Acar, and E.J.G. Peterman. 2018. Interplay between Ciliary Ultrastructure and IFT-Train Dynamics Revealed by Single-Molecule Super-resolution Imaging. *Cell Rep.* 25:224–235. https://doi.org/10.1016/j.celrep.2018.09.019

Patel-King, R.S., R.M. Gilberti, E.F. Hom, and S.M. King. 2013. WD60/FAP163 is a dynein intermediate chain required for retrograde intraflagellar transport in cilia. *Mol. Biol. Cell.* 24:2668–2677. https://doi.org/10.1091/mbc.e13-05-0266

Pazour, G.J., B.L. Dickert, and G.B. Witman. 1999. The DHC1b (DHC2) isoform of cytoplasmic dynein is required for flagellar assembly. *J. Cell Biol.* 144: 473–481. https://doi.org/10.1083/jcb.144.3.473

Porter, M.E., R. Bower, J.A. Knott, P. Byrd, and W. Dentler. 1999. Cytoplasmic dynein heavy chain 1b is required for flagellar assembly in Chlamydomonas. *Mol. Biol. Cell.* 10:693–712. https://doi.org/10.1091/mbc.10.3.693

Prevo, B., P. Mangeol, F. Oswald, J.M. Scholey, and E.J. Peterman. 2015. Functional differentiation of cooperating kinesin-2 motors orchestrates cargo import and transport in C. elegans cilia. *Nat. Cell Biol.* 17: 1536–1545. https://doi.org/10.1038/ncb3263

Prevo, B., J.M. Scholey, and E.J.G. Peterman. 2017. Intraflagellar transport: mechanisms of motor action, cooperation, and cargo delivery. *FEBS J.* 284:2905–2931. https://doi.org/10.1111/febs.14068

Rana, A.A., J.P. Barbera, T.A. Rodriguez, D. Lynch, E. Hirst, J.C. Smith, and R.S. Beddington. 2004. Targeted deletion of the novel cytoplasmic dynein mD2LIC disrupts the embryonic organiser, formation of the body axes and specification of ventral cell fates. *Development.* 131: 4999–5007. https://doi.org/10.1242/dev.01389

Reck, J., A.M. Schauer, K. VanderWaal Mills, R. Bower, D. Tritschler, C.A. Perrone, and M.E. Porter. 2016. The role of the dynein light intermediate chain in retrograde IFT and flagellar function in Chlamydomonas. *Mol. Biol. Cell.* 27:2404–2422. https://doi.org/10.1091/mbc.e16-03-0191

Roberts, A.J. 2018. Emerging mechanisms of dynein transport in the cytoplasm versus the cilium. *Biochem. Soc. Trans.* 46:967–982. https://doi.org/10.1042/BST20170568

Rompolas, P., L.B. Pedersen, R.S. Patel-King, and S.M. King. 2007. Chlamydomonas FAP133 is a dynein intermediate chain associated with the retrograde intraflagellar transport motor. *J. Cell Sci.* 120:3653–3665. https://doi.org/10.1242/jcs.012773

Sanders, A.A., J. Kennedy, and O.E. Blacque. 2015. Image analysis of Caenorhabditis elegans ciliary transition zone structure, ultrastructure, molecular composition, and function. *Methods Cell Biol.* 127:323–347. https://doi.org/10.1016/bs.mcb.2015.01.010

Schafer, J.C., C.J. Haycraft, J.H. Thomas, B.K. Yoder, and P. Swoboda. 2003. XBX-1 encodes a dynein light intermediate chain required for retrograde intraflagellar transport and cilia assembly in Caenorhabditis elegans. *Mol. Biol. Cell.* 14:2057–2070. https://doi.org/10.1091/mbc.e02-10-0677

Scheidel, N., and O.E. Blacque. 2018. Intraflagellar Transport Complex A Genes Differentially Regulate Cilium Formation and Transition Zone Gating. *Curr. Biol.* 28:3279–3287.e2. https://doi.org/10.1016/j.cub.2018.08.017

Schmidts, M., J. Vodopiutz, S. Christou-Savina, C.R. Cortés, A.M. McInerney-Leo, R.D. Emes, H.H. Arts, B. Tüysüz, J. D'Silva, P.J. Leo, et al. UK10K. 2013. Mutations in the gene encoding IFT dynein complex component WDR34 cause Jeune asphyxiating thoracic dystrophy. *Am. J. Hum. Genet.* 93:932–944. https://doi.org/10.1016/j.ajhg.2013.10.003

Schmidts, M., Y. Hou, C.R. Cortés, D.A. Mans, C. Huber, K. Boldt, M. Patel, J. van Reeuwijk, J.M. Plaza, S.E. van Beersum, et al. UK10K. 2015. TCTEX1D2 mutations underlie Jeune asphyxiating thoracic dystrophy with impaired retrograde intraflagellar transport. *Nat. Commun.* 6:7074. https://doi.org/10.1038/ncomms8074

Schouteden, C., D. Serwas, M. Palfy, and A. Dammermann. 2015. The ciliary transition zone functions in cell adhesion but is dispensable for axoneme assembly in C. elegans. *J. Cell Biol.* 210:35–44. https://doi.org/10.1083/jcb.201501013

Shih, S.M., B.D. Engel, F. Kocabas, T. Bilyard, A. Gennerich, W.F. Marshall, and A. Yildiz. 2013. Intraflagellar transport drives flagellar surface motility. *eLife.* 2:e00744. https://doi.org/10.7554/eLife.00744

Swoboda, P., H.T. Adler, and J.H. Thomas. 2000. The RFX-type transcription factor DAF-19 regulates sensory neuron cilium formation in C. elegans. *Mol. Cell.* 5:411–421. https://doi.org/10.1016/S1097-2765(00)80436-0

Taylor, S.P., T.J. Dantas, I. Duran, S. Wu, R.S. Lachman, S.F. Nelson, D.H. Cohn, R.B. Vallee, and D. Krakow. University of Washington Center for Mendelian Genomics Consortium. 2015. Mutations in DYNC2LI1 disrupt cilia function and cause short rib polydactyly syndrome. *Nat. Commun.* 6:7092. https://doi.org/10.1038/ncomms8092

Toropova, K., M. Mladenov, and A.J. Roberts. 2017. Intraflagellar transport dynein is autoinhibited by trapping of its mechanical and track-binding elements. *Nat. Struct. Mol. Biol.* 24:461–468. https://doi.org/10.1038/nsmb.3391

Toropova, K., R. Zalyte, A.G. Mukhopadhyay, M. Mladenov, A.P. Carter, and A.J. Roberts. 2019. Structure of the dynein-2 complex and its assembly with intraflagellar transport trains. *Nat. Struct. Mol. Biol.* 26:823–829. https://doi.org/10.1038/s41594-019-0286-y

Tsurumi, Y., Y. Hamada, Y. Katoh, and K. Nakayama. 2019. Interactions of the dynein-2 intermediate chain WDR34 with the light chains are required for ciliary retrograde protein trafficking. *Mol. Biol. Cell.* 30:658–670. https://doi.org/10.1091/mbc.E18-10-0678

Vuolo, L., N.L. Stevenson, K.J. Heesom, and D.J. Stephens. 2018. Dynein-2 intermediate chains play crucial but distinct roles in primary cilia formation and function. *eLife.* 7:e39655. https://doi.org/10.7554/eLife.39655

Vuolo, L., N.L. Stevenson, A.G. Mukhopadhyay, A.J. Roberts, and D.J. Stephens. 2020. Cytoplasmic dynein-2 at a glance. *J. Cell Sci.* 133:jcs240614. https://doi.org/10.1242/jcs.240614

Webb, S., A.G. Mukhopadhyay, and A.J. Roberts. 2020. Intraflagellar transport trains and motors: Insights from structure. *Semin. Cell Dev. Biol.* 107:82–90. https://doi.org/10.1016/j.semcdb.2020.05.021

Wicks, S.R., C.J. de Vries, H.G. van Luenen, and R.H. Plasterk. 2000. CHE-3, a cytosolic dynein heavy chain, is required for sensory cilia structure and function in Caenorhabditis elegans. *Dev. Biol.* 221:295–307. https://doi.org/10.1006/dbio.2000.9686

Williams, C.L., C. Li, K. Kida, P.N. Inglis, S. Mohan, L. Semenec, N.J. Bialas, R.M. Stupay, N. Chen, O.E. Blacque, et al. 2011. MKS and NPHP modules cooperate to establish basal body/transition zone membrane associations

and ciliary gate function during ciliogenesis. *J. Cell Biol.* 192:1023–1041. https://doi.org/10.1083/jcb.201012116

Wu, C., J. Li, A. Peterson, K. Tao, and B. Wang. 2017. Loss of dynein-2 intermediate chain Wdr34 results in defects in retrograde ciliary protein trafficking and Hedgehog signaling in the mouse. *Hum. Mol. Genet.* 26: 2386–2397. https://doi.org/10.1093/hmg/ddx127

Yi, P., W.J. Li, M.Q. Dong, and G. Ou. 2017. Dynein-Driven Retrograde Intraflagellar Transport Is Triphasic in C. elegans Sensory Cilia. *Curr. Biol.* 27:1448–1461.e7. https://doi.org/10.1016/j.cub.2017.04.015

Zhu, X., J. Wang, S. Li, K. Lechtreck, and J. Pan. 2021. IFT54 directly interacts with kinesin-II and IFT dynein to regulate anterograde intraflagellar transport. *EMBO J.* 40:e105781. https://doi.org/10.15252/embj.2020105781

Supplemental material

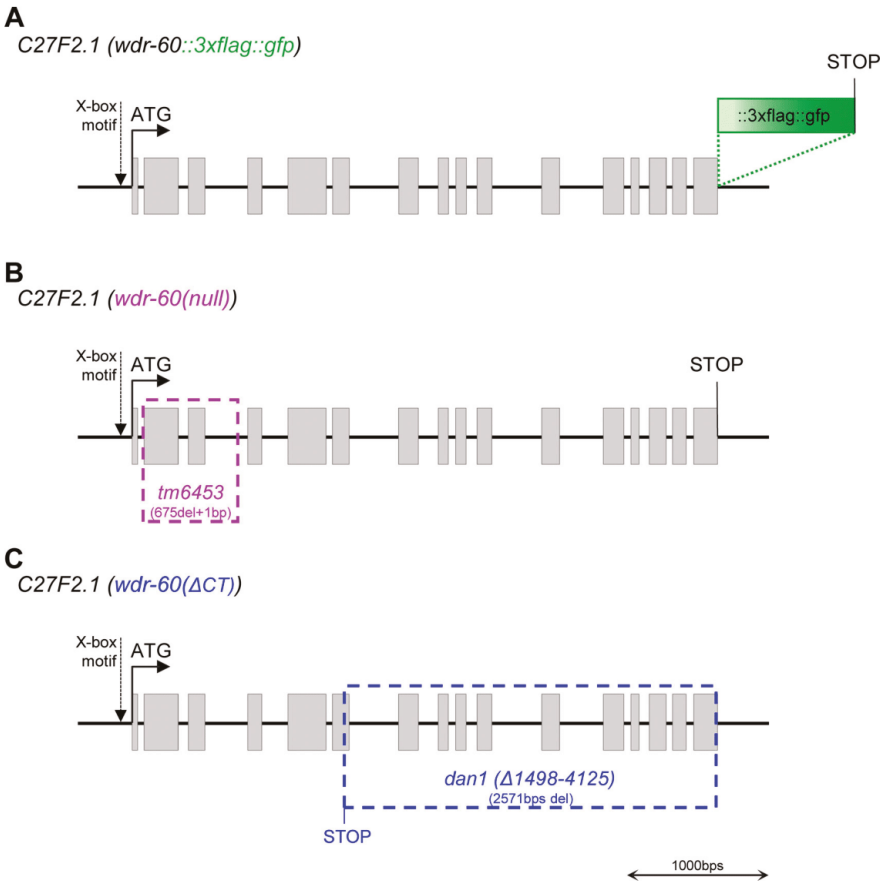

Figure S1. **Schematic of the *C27F2.1* locus organization in the *C. elegans* genome**. Related to Figs. 1 and 2. Predicted *wdr-60* exons (in gray boxes), including the start and stop codons, and the X-box motif according to Blacque et al. (2005). **(A)** Knock-in insertion of the *::3xflag::gfp* sequence at the 3′ end of the *wdr-60* genomic sequence (in-frame with the WDR-60 coding sequence). **(B)** Representation of the *wdr-60(tm6453)* null allele. **(C)** Representation of the *wdr-60(ΔCT)* allele (also named *dan1(Δ1498-4125 bps)*) corresponding to a WDR-60 truncation of the C-terminal β-propeller domain (Δ288–668 aa).

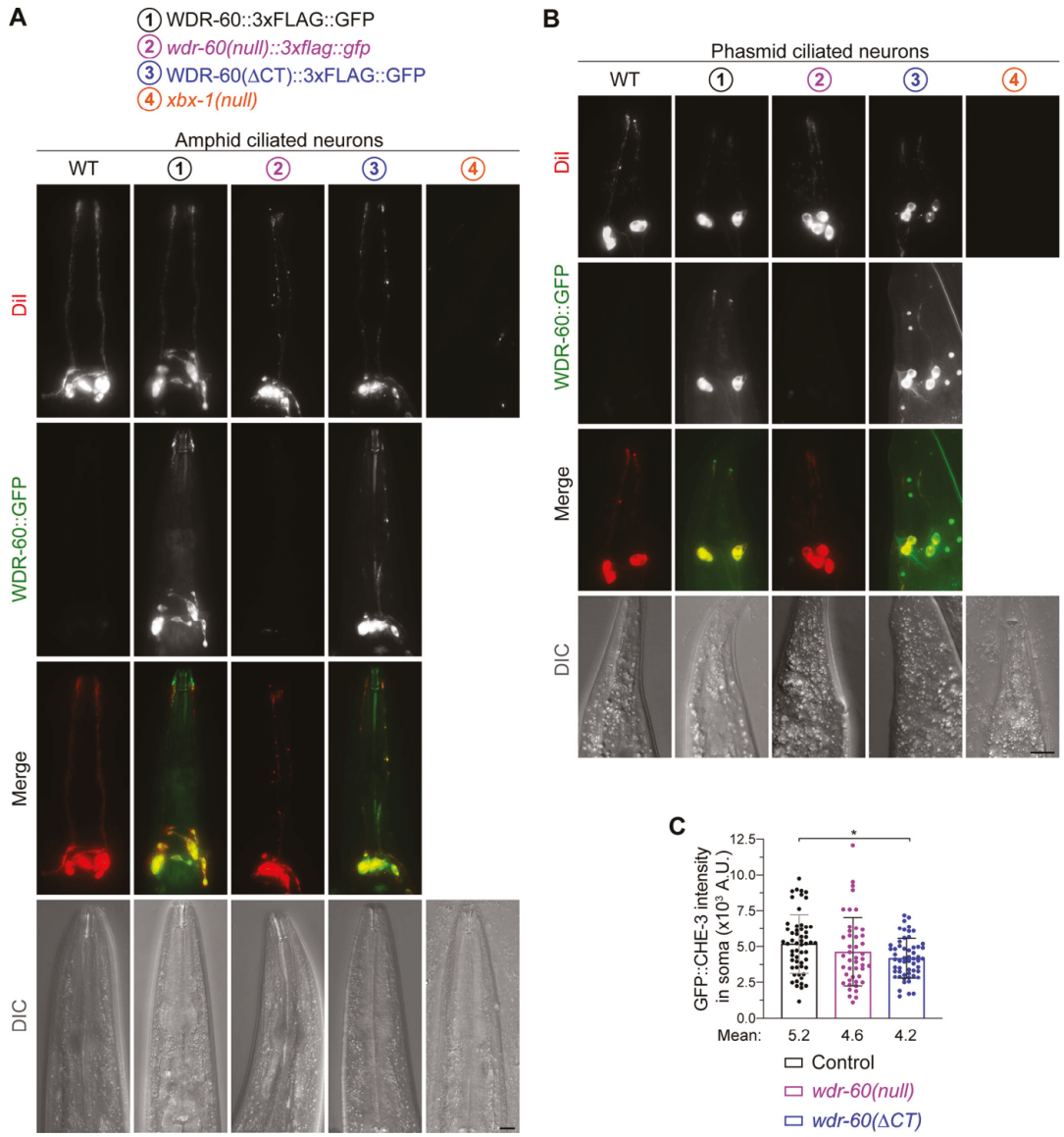

Figure S2. **WDR-60::3xFLAG::GFP expression is restricted to ciliated sensory neurons.** Related to Figs. 2 and 3. **(A and B)** Endogenously tagged WDR-60::3xFLAG::GFP and WDR-60(ΔCT)::3xFLAG::GFP are expressed in the same amphid (A) and phasmid (B) ciliated neurons that incorporate the DiI lipophilic dye (in red). The *wdr-60(null)::3xflag::gfp* strain has no detectable GFP signal in its neurons; however, they are still able to take up the DiI dye. Scale bars: 10 µm. DIC, differential interference contrast. **(C)** GFP::CHE-3 intensity in soma of phasmid sensory neurons of untagged *wdr-60* mutants ($n \geq 45$ somas). Graph is shown as mean ± SD. Kruskal–Wallis test followed by the Dunn's multiple comparison were used to analyze these datasets. *, $P \leq 0.05$.

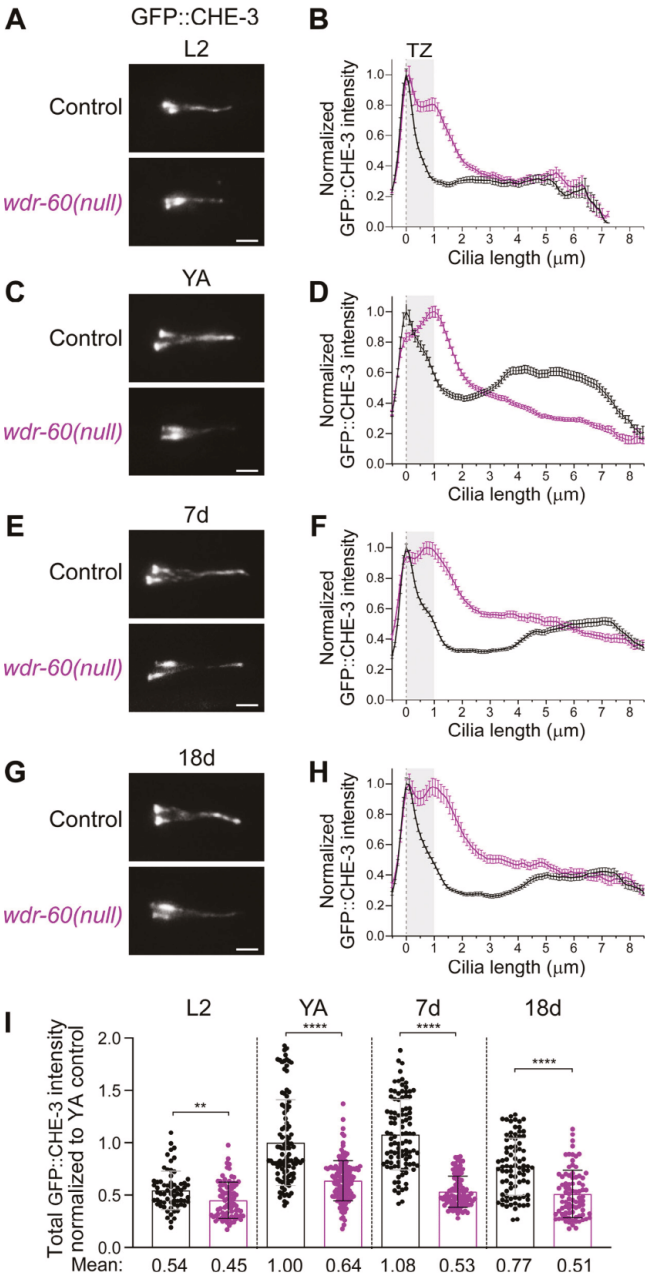

Figure S3. **WDR-60–associated phenotypes become worse as the animals develop to adulthood and do not improve with aging.** Related to Fig. 3. **(A, C, E, and G)** GFP::CHE-3-expressing phasmid cilia of wild-type and *wdr-60(null)* mutants at several stages of development and aging. L2, larval stage 2 worms; YA:,young adult worms; 7d, worms 7 days after reaching adulthood; 18d, worms 18 days after reaching adulthood. Scale bars: 2 μm. **(B, D, F, and H)** Corresponding distribution of GFP::CHE-3 signal intensity along cilia. Gray rectangles highlight the TZ, as previously defined. $n = 77$ cilia for B, $n \geq 95$ cilia for D, $n \geq 113$ cilia for F, and $n \geq 110$ cilia for H. XY intensity distribution graphs are shown as mean ± SEM. **(I)** Column graph showing GFP::CHE-3 total intensity from the base to the tip of cilia from wild-type and *wdr-60(null)* mutants analyzed in B, C, F, and H. Graph is shown as mean ± SD. Mann–Whitney *U* test was used to analyze these datasets. **, $P \leq 0.01$; ****, $P \leq 0.0001$.

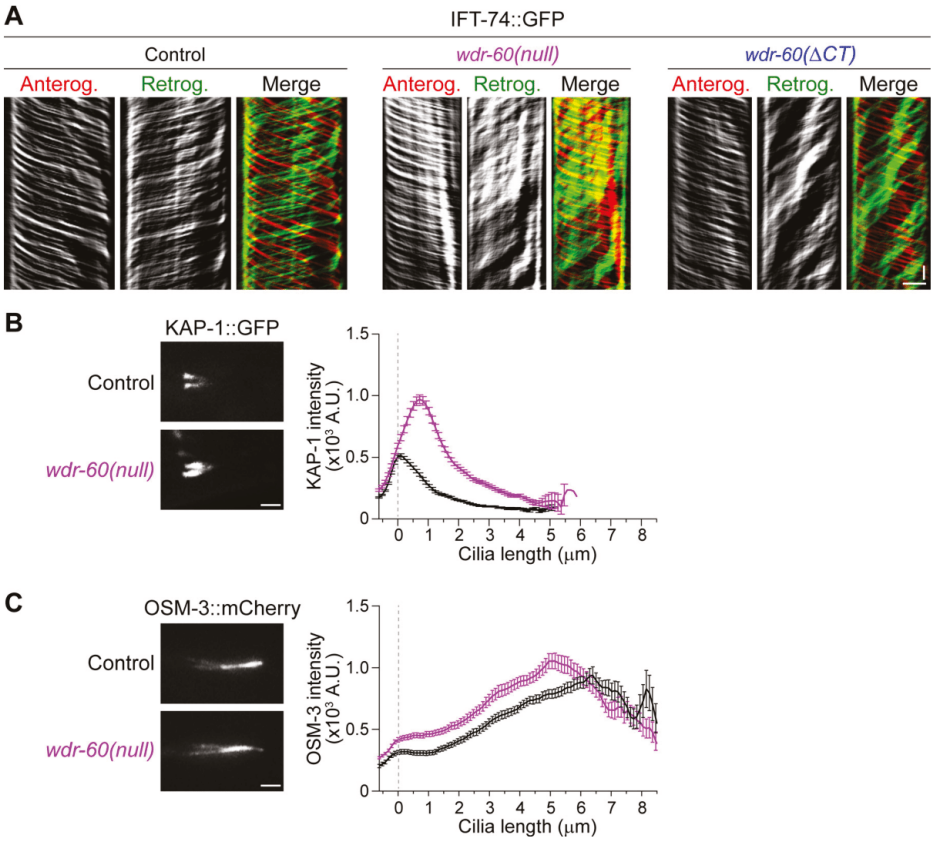

Figure S4. **Loss of WDR-60 results in a severe accumulation of KAP-1 near the base of cilia but only has a modest effect on the distribution of OSM-3.** Related to Fig. 4. **(A)** IFT-74::GFP kymographs of a phasmid cilia from control and *wdr-60(null)* worms. Single channels of particles moving anterogradely and retrogradely are shown, together with their respective merge. **(B)** Examples of phasmid cilia from control and *wdr-60(null)* worms expressing KAP-1::GFP and quantification of the signal intensity along cilia ($n \geq 60$ cilia for each strain). The intensity of KAP-1::GFP in cilia is significantly increased in the *wdr-60(null)* mutant with particles accumulating near the TZ. **(C)** Examples of phasmid cilia from control and *wdr-60(null)* worms expressing OSM-3::mCherry and quantification of the signal intensity along cilia ($n \geq 88$ cilia for each strain). OSM-3::mCherry distribution and intensity along the cilium is only slightly altered in the *wdr-60(null)* mutant. XY intensity distribution graphs are shown as mean ± SEM. Scale bars: vertical 5 s, horizontal 2 µm (A); 2 µm (B and C).

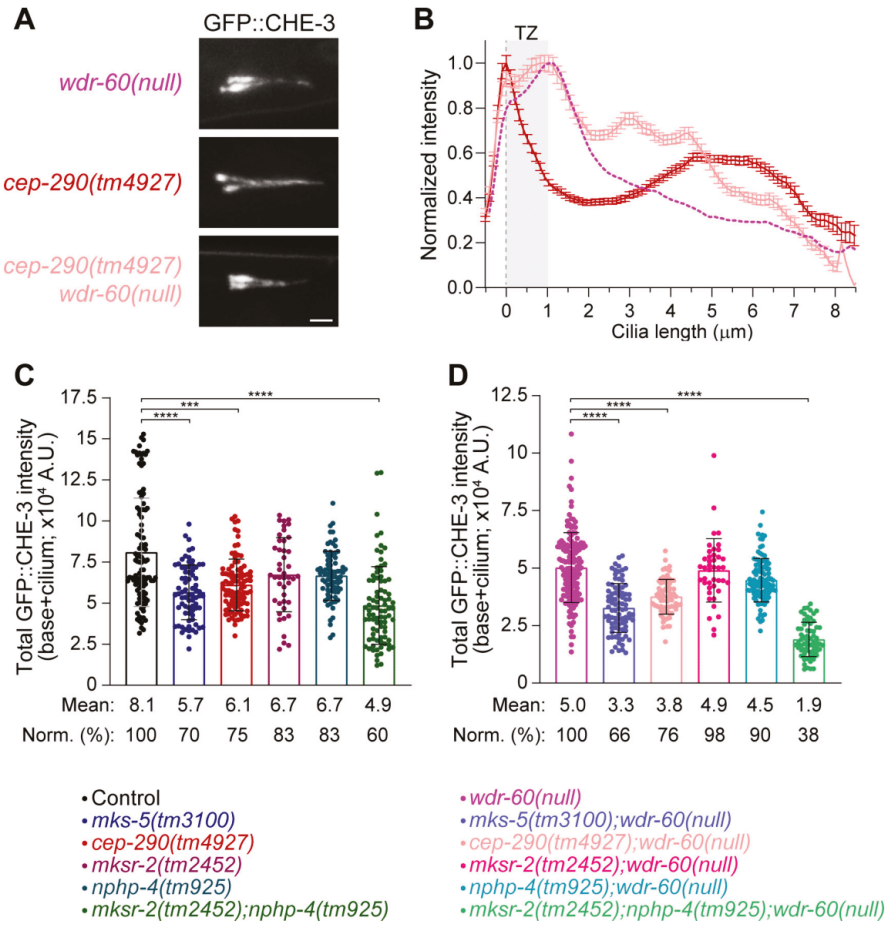

Figure S5. **Disruption of some TZ components changes the average levels of ciliary dynein-2.** Related to Fig. 7. **(A)** Phasmid cilia of the indicated *wdr-60* and *cep-290* mutant genotypes, expressing GFP::CHE-3. Scale bar: 2 μm. **(B)** Distribution of GFP::CHE-3 signal intensity along cilia from the strains in A ($n \geq 74$ cilia). The gray rectangle highlights the TZ, as previously defined. XY intensity distribution graph is shown as mean ± SEM. **(C and D)** Total GFP::CHE-3 intensity from the base to the tip of cilia from TZ mutants of the indicated genotypes, in wild-type *wdr-60* (C) and *wdr-60(null)* mutant (D) backgrounds. The cilia quantified here correspond to the same that were used to quantify the GFP::CHE-3 distribution profiles depicted in Fig. 7. Column graphs are shown as mean ± SD. Kruskal–Wallis test followed by Dunn's multiple comparison were used to analyze these datasets. ***, $P \leq 0.001$; ****, $P \leq 0.0001$.

Video 1. **Live imaging of GFP::CHE-3 (top) and WDR-60::GFP (bottom) undergoing IFT in *C. elegans* phasmid cilia.** Related to Fig. 1. Images were acquired at 3 fps, and playback is set at 15 fps (5× speed). Scale bar: 2 µm. The timer counts min:s.

Video 2. **Live imaging of GFP::CHE-3 in *C. elegans* phasmid cilia from control (top), *wdr-60(null)* (center), and *wdr-60(ΔCT)* (bottom) strains.** Related to Fig. 3. Images were acquired at 3 fps, and playback is set at 15 fps (5× speed). Scale bar: 2 µm. The timer counts min:s.

Video 3. **Live imaging of CHE-11::mCherry in *C. elegans* phasmid cilia from control (top), *wdr-60(null)* (center), and *wdr-60(ΔCT)* (bottom) strains.** Related to Fig. 4. Scale bar, 2 µm. Images were acquired at 3 fps, and playback is set at 15 fps (5× speed). Scale bar: 2 µm. The timer counts min:s.

Video 4. **Live imaging of IFT-74::GFP in *C. elegans* phasmid cilia from control (top), *wdr-60(null)* (center), and *wdr-60(ΔCT)* (bottom) strains.** Related to Figs. 4 and S4. Images were acquired at 3 fps, and playback is set at 15 fps (5× speed). Scale bar: 2 µm. The timer counts min:s.

Video 5. **Live imaging of GFP::CHE-3(K2935Q) in *C. elegans* phasmid cilia from control (top); *mks-5(tm3100)* (center), and *nphp-4(tm925)* (bottom) strains.** Related to Fig. 8. Images were acquired at 3 fps, and playback is set at 15 fps (5× speed). Scale bar: 2 µm. The timer counts min:s.

Video 6. **Live imaging of GFP::CHE-3 in *C. elegans* phasmid cilia from control (top), *mks-5(tm3100)* (center), and *nphp-4(tm925)* (bottom) strains.** Related to Fig. 9. Images were acquired at 3 fps, and playback is set at 15 fps (5× speed). Scale bar: 2 µm. The timer counts min:s.

Video 7. **Live imaging of GFP::CHE-3 in *C. elegans* phasmid cilia from *wdr-60(null)* (top), *wdr-60(null);mks-5(tm3100)* (center), and *wdr-60(null);nphp-4(tm925)* (bottom) strains.** Related to Fig. 9. Images were acquired at 3 fps, and playback is set at 15 fps (5× speed). Scale bar: 2 µm. The timer counts min:s.

Provided online are three tables. Table S1 shows the nomenclature of *C. elegans* proteins mentioned in the text and their corresponding homologues or orthologues in humans. Table S2 lists the strains used in this study. Table S3 lists the primers used in this study.

ANNEX II - Article 2. “The IFT20 homolog in *Caenorhabditis elegans* is required for ciliogenesis and cilia-mediated behavior”

microPublication BIOLOGY

5/4/2021 - *Open Access*

The IFT20 homolog in *Caenorhabditis elegans* is required for ciliogenesis and cilia-mediated behavior

Ana R. G. De-Castro[1,2*], Joana Quintas-Gonçalves[1,2*], Tiago Silva-Ribeiro[1,2], Diogo R. M. Rodrigues[1,2], Maria J. G. De-Castro[1,2], Carla M. Abreu[1,2§], Tiago J. Dantas[1,2§]

[1]i3S - Instituto de Investigação e Inovação em Saúde, Universidade do Porto, Porto, Portugal

[2]IBMC - Instituto de Biologia Molecular e Celular, Universidade do Porto, Porto, Portugal

[§]To whom correspondence should be addressed: carla.abreu@ibmc.up.pt; tiago.dantas@i3s.up.pt

[*]These authors contributed equally.

Abstract

Cilia are microtubule-based organelles that carry out a wide range of critical functions throughout the development of higher animals. Regardless of their type, all cilia rely on a motor-driven, bidirectional transport system known as intraflagellar transport (IFT). Of the many components of the IFT machinery, IFT20 is one of the smallest subunits. Nevertheless, IFT20 has been shown to play critical roles in the assembly of several types of mammalian cilia. Here we show that the IFT20 homolog in *Caenorhabditis elegans*, IFT-20, is also important for correct cilium assembly in sensory neurons. Strikingly, however, we find that IFT-20-deficient animals are able to assemble short, vestigial cilia. Despite of this, we show that practically all IFT-20-deficient animals fail to respond to environmental cues that are normally detected by cilia to modulate their behavior. Altogether, our results indicate that IFT-20 is critical for both the correct assembly and function of cilia in *C. elegans*.

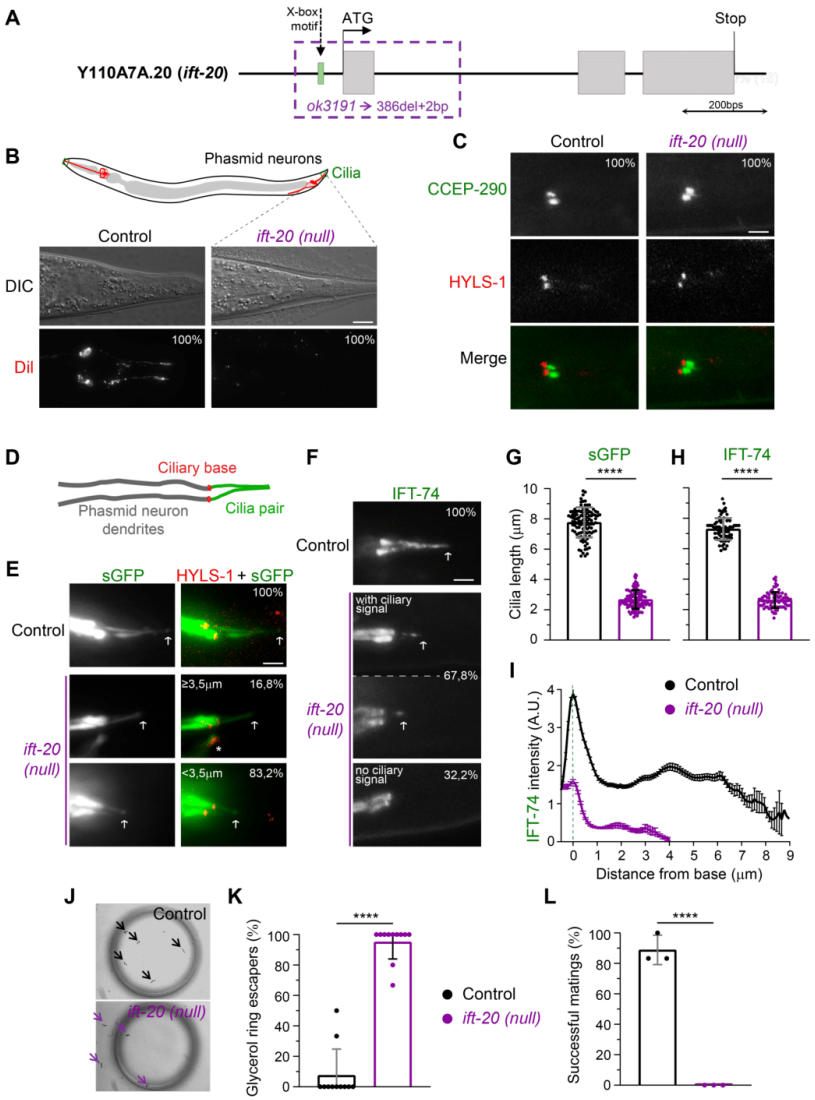

Figure 1.

Disruption of *ift-20* results in defective cilium assembly and function in *C. elegans*

(A) Schematic of the Y110A7A.20 locus, showing the predicted *ift-20* exons (in grey boxes) and the relative position of the X-box motif according to (Blacque *et al.* 2005; Efimenko *et al.* 2005). The *ok3191* deletion/substitution allele (-386bp, +2bp=C+T) was mapped and is represented in purple. **(B)** Examples of the Dil lipophilic dye-filling test in sensory phasmid neurons of wild-type and *ift-20* mutant worms. 100% of the *ift-20* mutant worms fail to incorporate dye (N≥15 worms per strain). Scale bar, 10 µm. **(C)** Examples of the dendritic ends of phasmid neurons from wild-type and *ift-20* mutants expressing CCEP-290::GFP and HYLS-1::mCherry, labeling the transition zone and the base of cilia, respectively (N≥18 cilia per strain). Scale bar, 2 µm. **(D)** Illustration of the ciliated dendritic ends of phasmid neurons. **(E)** Examples of cilia of phasmid neurons of wild-type and *ift-20* mutants, labeled with soluble GFP (sGFP; able to enter cilia) and HYLS-1::mCherry (ciliary base). *refers to a dendrite from a different type of neuron (PQR) also present in the figure. **(F)** Examples of the distribution of endogenously labeled IFT-74::GFP and its incorporation into cilia of phasmid neurons. White arrows point at the tips of cilia. Scale bars, 2 µm. **(G, H)** IFT-20-deficient worms have defects in ciliogenesis but manage to assemble severely shortened cilia as shown in the quantifications (N≥107 sGFP labeled cilia were analyzed per strain; N≥80 cilia with detectable IFT-74::GFP were analyzed per strain). Bars in graphs show the average cilia length (± SD). **(I)** IFT-74::GFP signal distribution and intensity (± SEM) along cilia are altered in *ift-20* mutant worms, revealing

that they incorporate less IFT-74 (N≥80 cilia for each strain; worms with no ciliary IFT-74 signal were not included). **(J)** Osmotic avoidance assay shows that sensory cilia of *ift-20* mutant worms fail to sense the high glycerol concentrations of the ring surrounding them, and cross it to escape. **(K)** Graph shows mean percentage of worms (± SD) that cannot sense a hypertonic glycerol barrier (N=28 worms in controls; N=35 *ift-20* mutant worms; analyzed over 11 independent experiments). **(L)** Mating assay was also used to test the proficiency of sensory cilia functions in *ift-20* mutant worms. The graph shows the mating success score (± SD) of each experimental repeat: considering 0% (no mating) or 100% (mating) for each hermaphrodite singled-out from a plate containing males of the strain being tested (a total of N=18 male worms from each strain were analyzed, over 3 independent experiments). 100% of the *ift-20* mutant males fail to mate with wild-type control hermaphrodites. ****P≤0,0001.

Description

A high diversity of cilium types have evolved to carry out a multitude of sensorial and motility functions in animal organisms. It is therefore not surprising that defects in cilia structure and function have been associated with various severe multi-organ disorders, commonly known as ciliopathies (Sreekumar and Norris 2019). Regardless of their type, cilium assembly relies on a bidirectional motor-driven transport known as intraflagellar transport (IFT; Prevo *et al.* 2017). Anterograde IFT driven by kinesin-2 transports different cargos in IFT trains along axonemal microtubules from the ciliary base to the tip of the cilium. Upon reaching the tip, these IFT trains are dismounted, rearranged and prepared for transport in the opposite direction back to the ciliary base by the dynein-2 motor complex. IFT trains are composed of at least 16 IFT-B subunits and 6 IFT-A subunits (Prevo *et al.* 2017). IFT20 is part of the IFT-B complex and has been shown to be of critical importance for ciliogenesis in human and mouse models (Follit *et al.* 2006; Jonassen *et al.* 2008; Katoh *et al.* 2017; Lim *et al.* 2020).

In *C. elegans*, IFT-20 is encoded by the Y110A7A.20 locus in chromosome I. Y110A7A.20 was identified in 2004 as a locus containing a X-box sequence (Fan *et al.* 2004; Blacque *et al.* 2005; Efimenko *et al.* 2005) under the control of DAF-19, a RFX-type transcription factor that regulates ciliary gene expression in ciliated sensory neurons (Swoboda *et al.* 2000) (the only ciliated cells in *C. elegans*). Expression of a GFP reporter under the control of the *ift-20* promoter revealed that IFT-20 expression is restricted to sensory neurons, similarly to other IFT components (Blacque *et al.* 2005). In fact, disruption of *daf-19* resulted in the almost complete loss of expression of this GFP reporter (Blacque *et al.* 2005), confirming that DAF-19 drives IFT-20 expression most likely by recognizing the X-box at position -59 of the *ift-20* promoter (Blacque *et al.* 2005; Efimenko *et al.*2005). Later, Ou and colleagues constructed a vector for IFT-20::GFP expression, and found that the *C. elegans* IFT20 homolog is also recruited to cilia where it undergoes IFT with similar kinetics to other IFT subunits (Ou *et al.* 2007). However, in contrast to its homolog in mammalian cells, IFT-20 was not detectable at the Golgi and does not seem to interact with the *C. elegans* homolog of GMAP210 (Broekhuis *et al.* 2013), which anchors IFT20 to the Golgi in mammalian cells (Follit *et al.* 2008).

Despite of these early analyses of IFT-20 expression and localization, the extent to which IFT-20 contributes to ciliogenesis in *C. elegans* has remained unknown. To dissect the importance of the homolog of IFT20 in *C. elegans*, we obtained and mapped a null deletion allele (*ok3191*) of the *ift-20* locus (Figure 1A). This allele carries a deletion of 386bps that includes part of the 5' UTR, the X-box motif that controls *ift-20* expression, the start codon, and all of the 1st exon (sequencing data was submitted to WormBase). Because the expression of *ift-20* was previously shown to be under the control of the DAF-19 transcription factor, and since it lacks the complete first exon, we expect that this allele results in the complete loss of IFT-20. Thus, we refer to the *ift-20* (*ok3191*) allele as an *ift-20 (null)*.

We started our analysis of *ift-20* mutant worms by performing the classic dye-filling assay to test whether cilia are able to form normally in the absence of IFT-20. This assay takes advantage that the lipophilic, fluorescent Dil dye is specifically incorporated into a subset of ciliated sensory neurons through their cilia if these are present and in contact with the environment outside of the worm (Supplementary Figure 1A). In contrast to the wild-type controls that incorporated the dye, none of the *ift-20* mutant worms had Dil signal in their neurons (Figure 1B; Supplementary Figure 1B). To confirm that this dye-filling phenotype results from ciliary defects rather than abnormal dendritic morphology/extension, we expressed cytoplasmic GFP in sensory neurons (driven by the *osm-6/ift-52* promoter) to analyze their morphology. We found no significant differences in the length and morphology of sensory neurons (Supplementary Figure 1C), which, together with our dye-filling results, suggest that IFT-20 loss leads to defects in sensory cilia.

Using established markers for the cilium base (HYLS-1) and the ciliary transition zone (CCEP-290) (Schouteden *et al.* 2015), we found that *ift-20* mutant worms still positioned their basal body normally at the extremity of the dendrite in phasmid neurons and are able to form at least the CCEP-290 module of the ciliary transition zone (Figure 1C). We then took advantage of the incorporation of the soluble/cytoplasmic GFP into cilia of phasmid sensory neurons to visualize cilia and measure their length in *ift-20* mutant worms. Strikingly, we found that severely shortened/vestigial cilia were still able to form in phasmid neurons of *ift-20* null animals (Figure 1D,E,G). This suggests that IFT-20 loss leads to a severe defect in ciliary axoneme assembly but does not completely block ciliogenesis in C. elegans.

In order to directly visualize IFT particles in cilia of *ift-20* mutant animals, we analyzed the distribution of IFT-74::GFP (Yi *et al*. 2017), another subunit of the IFT-B complex. IFT-74::GFP was readily detectable in dendrites of amphid and phasmid neurons, which allowed us to further confirm the normal development and morphology of these neurons in *ift-20* null worms (Supplementary Figure 1D). In controls, IFT-74::GFP was strongly recruited and entered cilia, labeling the complete axoneme (Figure 1F,H). In contrast, IFT-74-labeled cilia were severely shortened in the majority of *ift-20* null phasmid neurons (67,8%; Figure 1F,H), consistent with our observations using soluble GFP-labeled cilia. Interestingly, however, no IFT-74-labeled cilia were detectable in the remaining fraction of phasmid neurons (32,2%; Figure 1F), suggesting that IFT-20 is also required for IFT-74 incorporation into cilia. To further confirm this possibility, we quantified the distribution of any detectable IFT-74 signal in phasmid cilia of *ift-20* mutant worms. We found that the signal intensity of IFT-74 recruited to the ciliary base and inside cilia of phasmid sensory neurons was indeed strongly reduced in *ift-20* mutant worms (Figure 1I). These results reveal that, in addition to being important for cilia assembly in *C. elegans*, IFT-20 plays a role in the ciliary recruitment and entry of IFT subunits.

The fact that short cilia could still form in phasmid sensory neurons of *ift-20* null worms was somewhat unexpected given the critical role of IFT20 for the initiation of ciliogenesis in most mammalian models (Follit *et al.* 2006; Jonassen *et al.* 2008; Katoh *et al.* 2017). Interestingly, however, we note that very short flagella with abnormal axonemes (but still motile) can form in sperm of mice with male germline-specific disruption of IFT20 (Zhang *et al.* 2016).

To assess the degree of functionality of the IFT-20-deficient vestigial cilia, we performed osmotic and mating assays. In contrast to controls and consistent with ciliary defects, *ift-20*-deficient worms were unable to sense the normally repulsive high concentrations of glycerol as virtually all of them readily crossed the glycerol rings that wild-type worms avoided (Figure 1J,K). In agreement with defective ciliary sensory functions, all *ift-20* mutant male worms failed to mate with wild-type hermaphrodites, suggesting that their cilia were unable to detect the latter for mating to take place (Figure 1L). These results strongly suggest that IFT-20 loss completely impairs cilia-dependent functions in *C. elegans*. Although we did not analyze the morphology and IFT of all types of sensory cilia in the *ift-20* mutant, our cilia-dependent behavior analyses are consistent with the cilia assembly defects that we observed in *ift-20 null* phasmid sensory neurons.

Altogether, our results show that IFT-20 is required for ciliogenesis and cilia sensory functions in *C. elegans*. Our data also suggest that IFT-20 is important for the robust recruitment and entry of IFT subunits into vestigial cilia that assemble in *ift-20* null animals.

Methods

Caenorhabditis elegans maintenance and strain generation

C. elegans strains were maintained on standard nematode growth medium (NGM) plates seeded with *Escherichia coli* OP50 bacteria at 20°C, and crossed using standard procedures. Mutant genotyping was performed by standard PCR. *C. elegans* strains used in this study are listed in Table 1.

Fluorescence imaging

Young adult hermaphrodite worms were immobilized for imaging using 10mM Levamisol and were placed on a microscope slide with a 5% agarose pad. Imaging of worms and their cilia was carried out over at least 3 independent experiments using an Axio Observer microscope (Zeiss) controlled by ZEN software (Zeiss), equipped with a 63x 1.46 NA objective lens and an Orca Flash 4.0 camera (Hamamatsu). Z-stacks were acquired with 0.4 µm between each z-section for imaging cilia. Z-stack images were processed and analyzed with Fiji software (Image J version 2.0.0-rc-56/1.52 p). Fluorescence signals of cilium-incorporated soluble GFP/Hyls-1::mCherry and IFT-74::GFP were used to measure the length of cilia in phasmid neurons (starting at the maximum signal at the base). The IFT-74::GFP signal intensity of each pixel was measured from the base to the tip of each cilium to generate an averaged profile of IFT-74 distribution along cilia.

Dye-Filling

Worms from each strain were collected from a confluent but not starved plate and washed in M9. They were then incubated in 500µL of Dil (1,1'-Dioctadecyl-3,3,3',3'-Tetramethylindocarbocyanine Perchlorate) solution at 0,625µg/ml for 1 h at room temperature in the dark, with occasional flipping of the tubes. After washing worms in M9, these were placed on a NGM seeded plate for 1-3 h at 20°C, to reduce the background of ingested dye. The neuronal uptake of dye was then examined using the Axio Observer microscope as described above.

Mating Assay

Male mating efficiency is known to rely on sensory signals given by the hermaphrodite that are sensed by the cilia of the male tail for mating. Mating assays were performed as described in (Hodgkin 1983) for quantitative mating efficiency tests. Briefly, six L4 wild-type hermaphrodites and six young males of the strain to be tested were placed together on a mating plate (i.e. a 5 cm NGM agar plate with an ~1 cm spot of OP50 seeded at the center of the plate). Note that males were separated 24 hours prior to the experiment and placed on a 5 cm NGM seeded plate at 20°C. The worms were then

allowed to mate for 24 hours at 20°C, after which the hermaphrodites were isolated onto a new 5 cm NGM seeded plate and kept at 20°C for 24 hours to lay eggs. After this period, hermaphrodites were removed and plates with eggs were kept at 25°C. Two days after, the number of total progeny and the number of male progeny on the plate were counted. In order to obtain enough males to be used in these assays, both strains used for mating contained a *him-8* mutation, which leads to an increase in mis-segregation of the X chromosome during meiosis I (Phillips *et al.* 2005).

Osmotic Avoidance Assay

Osmotic avoidance assays were performed on NGM non-seeded plates at 20°C, following the guidelines of (Sanders *et al.* 2015). Each repeat was carried out using five young adult hermaphrodite worms of each strain isolated before the experiment. Worms were placed inside of a glycerol ring, with a diameter of approximately 1 cm, freshly prepared with a tube dipped in a 59% glycerol solution. Worm behavior was immediately monitored for 5 minutes using a camera (controlled by the Micro-Manager 1.4 software) to determine whether worms avoided crossing the glycerol ring or not. Worms that left the ring or stayed in contact with its glycerol border for more than 20 seconds were classified as escapers. Worms that failed to explore the area within the timeframe of the experiment were excluded.

Data analysis and statistics

Statistical analyses of datasets were performed using GraphPad Prism software. Two-tailed student T test was used to analyze the data in the graphs of Figure 1. Differences were considered significant at P values below 5% (*P≤0,05; **P≤0,01; ***P≤0,001; ****P≤0,0001).

Reagents

Table 1: List of *C. elegans* strains used in this work.

Strain	Genotype	Short description	Source/Ref.
N2	wild-type	ancestral N2 Bristol	CGC
RB2353	*ift-20(ok3191)I*	*ift-20(null)*	OMRF Knockout Project/ CGC
GOU2362	*ift-74(cas499[ift-74::gfp])II*	IFT-74::GFP knock-in	Dr. Guangshuo Ou/CGC (Yi *et al.* 2017)
DAM456	*vieSi12[pAD373; Pccep-290::gfp::ccep-290cDNA; cb unc-119(+)]II; vieSi16[pAD390; Phyls-1::mCherry::hyls-1; cb unc-119(+)]IV*	CCEP-290::GFP (*Mos* transposase-mediated single-copy insertion (MosSCI)) + HYLS-1::mCherry (MosSCI)	Dr. Alexander Dammermann (Schouteden *et al.*2015)
AND16	*ift-20(ok3191)I*	*ift-20(null)* outcrossed 6x	This study, made from RB2353
AND56	*him-8(e1489)IV*	*him-8* mutant for matting assay	This study, made from OE3002
AND67	*ift-20(ok3191)I; him-8(e1489)IV*	*ift-20(null)* + *him-8* mutant for matting assay	This study
AND185	*ift-20(ok3191)I; ift-74(cas499[ift-74::gfp])II*	*ift-20(null)* + IFT-74::GFP	This study
AND196	*ift-20(ok3191)I; vieSi12[pAD373; Pccep-290::gfp::ccep-290cDNA; cb unc-119(+)]II; vieSi16[pAD390; Phyls-1::mCherry::hyls-1; cb unc-119(+)]IV*	*ift-20(null)* + CCEP-290::GFP (MosSCI) + HYLS-1::mCherry (MosSCI)	This study
AND226	*vieSi16[pAD390; Phyls-1::mCherry::hyls-1; cb unc-119(+)]IV; lqIs2[Posm-6::GFP; lin-15(+)]X*	HYLS-1::mCherry (MosSCI) + *Posm-6::GFP*	This study, made from LE309
AND227	*ift-20(ok3191)I; vieSi16[pAD390; Phyls-1::mCherry::hyls-1; cb unc-119(+)]IV; lqIs2[Posm-6::GFP; lin-15(+)]X*	*ift-20(null)* + HYLS-1::mCherry (MosSCI) + *Posm-6::GFP*	This study, made from LE309

Acknowledgments: We thank Dr. Alexander Dammermann and Dr. Guangshuo Ou for providing strains. We also thank the C. elegans Gene Knockout Project at the Oklahoma Medical Research Foundation for generating the original ift-20 mutant strain. Some strains were obtained from the Caenorhabditis Genetics Center (CGC), which is funded by the NIH Office of Research Infrastructure Programs (P40 OD010440). We are also very grateful to the Gassmann and the Carvalho labs at i3S for technical help with experiments.

Extended Data

Supplementary Figure 1. Image. Supplementary Figure 1.pdf.

References

Blacque OE, Perens EA, Boroevich KA, Inglis PN, Li C, Warner A, Khattra J, Holt RA, Ou G, Mah AK, McKay SJ, Huang P, Swoboda P, Jones SJ, Marra MA, Baillie DL, Moerman DG, Shaham S, Leroux MR. 2005. Functional genomics of the cilium, a sensory organelle. Curr Biol 15: 935-41. PubMed

Broekhuis JR, Rademakers S, Burghoorn J, Jansen G. 2013. SQL-1, homologue of the Golgi protein GMAP210, modulates intraflagellar transport in C. elegans. J Cell Sci 126: 1785-95.
PubMed

Efimenko E, Bubb K, Mak HY, Holzman T, Leroux MR, Ruvkun G, Thomas JH, Swoboda P. 2005. Analysis of xbx genes in C. elegans. Development 132: 1923-34. PubMed

Follit JA, Tuft RA, Fogarty KE, Pazour GJ. 2006. The intraflagellar transport protein IFT20 is associated with the Golgi complex and is required for cilia assembly. Mol Biol Cell 17: 3781-92.
PubMed

Follit JA, San Agustin JT, Xu F, Jonassen JA, Samtani R, Lo CW, Pazour GJ. 2008. The Golgin GMAP210/TRIP11 anchors IFT20 to the Golgi complex. PLoS Genet 4: e1000315.
PubMed

Hodgkin J. 1983. Male Phenotypes and Mating Efficiency in CAENORHABDITIS ELEGANS. Genetics 103: 43-64.
PubMed

Jonassen JA, San Agustin J, Follit JA, Pazour GJ. 2008. Deletion of IFT20 in the mouse kidney causes misorientation of the mitotic spindle and cystic kidney disease. J Cell Biol 183: 377-84. PubMed

Katoh Y, Michisaka S, Nozaki S, Funabashi T, Hirano T, Takei R, Nakayama K. 2017. Practical method for targeted disruption of cilia-related genes by using CRISPR/Cas9-mediated, homology-independent knock-in system. Mol Biol Cell 28: 898-906. PubMed

Lim J, Li X, Yuan X, Yang S, Han L, Yang S. 2020. Primary cilia control cell alignment and patterning in bone development via ceramide-PKCζ-β-catenin signaling. Commun Biol 3: 45. PubMed

Ou G, Koga M, Blacque OE, Murayama T, Ohshima Y, Schafer JC, Li C, Yoder BK, Leroux MR, Scholey JM. 2007. Sensory ciliogenesis in Caenorhabditis elegans: assignment of IFT components into distinct modules based on transport and phenotypic profiles. Mol Biol Cell 18: 1554-69. PubMed

Phillips CM, Wong C, Bhalla N, Carlton PM, Weiser P, Meneely PM, Dernburg AF. 2005. HIM-8 binds to the X chromosome pairing center and mediates chromosome-specific meiotic synapsis. Cell 123: 1051-63. PubMed

Sreekumar V, Norris DP. 2019. Cilia and development. Curr Opin Genet Dev 56: 15-21. PubMed

Prevo B, Scholey JM, Peterman EJG. 2017. Intraflagellar transport: mechanisms of motor action, cooperation, and cargo delivery. FEBS J 284: 2905-2931. PubMed

Sanders AA, Kennedy J, Blacque OE. 2015. Image analysis of Caenorhabditis elegans ciliary transition zone structure, ultrastructure, molecular composition, and function. Methods Cell Biol 127: 323-47. PubMed

Schouteden C, Serwas D, Palfy M, Dammermann A. 2015. The ciliary transition zone functions in cell adhesion but is dispensable for axoneme assembly in C. elegans. J Cell Biol 210: 35-44. PubMed

Sreekumar V, Norris DP. 2019. Cilia and development. Curr Opin Genet Dev 56: 15-21. PubMed

Swoboda P, Adler HT, Thomas JH. 2000. The RFX-type transcription factor DAF-19 regulates sensory neuron cilium formation in C. elegans. Mol Cell 5: 411-21. PubMed

Yi P, Li WJ, Dong MQ, Ou G. 2017. Dynein-Driven Retrograde Intraflagellar Transport Is Triphasic in C. elegans Sensory Cilia. Curr Biol 27: 1448-1461.e7. PubMed

Zhang Z, Li W, Zhang Y, Zhang L, Teves ME, Liu H, Strauss JF 3rd, Pazour GJ, Foster JA, Hess RA, Zhang Z. 2016. Intraflagellar transport protein IFT20 is essential for male fertility and spermiogenesis in mice. Mol Biol Cell 27:3705-3716.
PubMed

Funding: This work was financed by FEDER - Fundo Europeu de Desenvolvimento Regional funds through the COMPETE 2020 - Operacional Programme for Competitiveness and Internationalisation (POCI), Portugal 2020, and by Portuguese funds through the Fundação para a Ciência e a Tecnologia (FCT) / Ministério da Ciência, Tecnologia e Ensino Superior in the framework of the project POCI-01-0145-FEDER-029471 (PTDC/BIA-BID/29471/2017) to TJD. DRMR received a predoctoral fellowship from FCT (SFRH/BD/143985/2019). CMA and TJD salaries were also supported by the FCT: CEECIND/01985/2018 and CEECIND/00771/2017, respectively.

5/4/2021 - *Open Access*

Author Contributions: Ana R. G. De-Castro: investigation, methodology, visualization, formal analysis, validation, writing - review editing. Joana Quintas-Gonçalves: investigation, methodology, visualization, formal analysis, writing - review editing. Tiago Silva-Ribeiro: investigation, methodology, visualization, validation, writing - review editing. Diogo R. M. Rodrigues: investigation, methodology, writing - review editing, visualization. Maria J. G. De-Castro: investigation, methodology, writing - review editing, visualization. Carla M. Abreu: conceptualization, methodology, formal analysis, funding acquisition, project, supervision, writing - original draft, writing - review editing. Tiago J. Dantas: conceptualization, methodology, formal analysis, funding acquisition, project, supervision, writing - original draft, writing - review editing.

Citation: De-Castro, AR.; Quintas-Gonçalves, J; Silva-Ribeiro, T; Rodrigues, DR.; De-Castro, MJ.; Abreu, CM.; Dantas, TJ. (2021), The IFT20 homolog in *Caenorhabditis elegans* is required for ciliogenesis and cilia-mediated behavior. microPublication Biology.

ANNEX III – List of *C. elegans* strains used in this study

Table 1 - List of *C. elegans* strains used in this study.

Strains	Genotype	Short annotation	Reference
N2		wild-type	
GOU2162	*che-3 (cas443[gfp::che-3]) I; xbx-1 (cas502[xbx-1::tagrfp::3xflag]) V*	GFP::CHE-3 + XBX-1::RFP::3xFLAG	Yi et al., 2017
GOU2362	*ift-74 (cas499[ift-74::gfp]) II*	IFT-74::GFP	Yi et al., 2017
GOU2366	*che-3(cas511[gfp::che-3(K2935Q)]) I*	GFP::CHE-3(K2935Q)	Yi et al., 2017
JT11069	*xbx-1 (ok279) V*	*xbx-1* null	Schafer et al., 2003
DAM459	*ttTi4391-vieSi23[pAD402; Pnphp-4::gfp::nphp-4cDNA; cb unc-119(+)] I; cxTi10882-vieSi16[pAD390; Phyls-1::mcherry::hyls-1; cb unc-119(+)] IV*	GFP::NPHP-4 + mCherry::HYLS-1	Schouteden et al., 2015
DAM543	*cep-290(tm4927) I; mksr-2(tm2452) IV; nphp-4(tm925) V*	*cep-290* null + *mksr-2* null + *nphp-4* null	Schouteden et al., 2015
DAM954	*vuaSi21 [pBP39; Pmks-6::mks-6::mcherry; cb-unc-119(+)] II*	MKS-6::mCherry	Schouteden et al., 2015
OEB730	*oqEx500 [tmem-107::gfp + unc-122p::dsred]*	TMEM-107::GFP	Lambacher et al., 2016
EJP13	*kap-1(ok676) III; vuaSi1 [pBP20; Pkap-1::kap-1::egfp; cb-unc-119(+)] IV*	KAP-1::eGFP	Prevo et al., 2015
EJP16	*vuaSi2 [pBP22; Posm-3::osm-3::mcherry; cb-unc-119(+)] II; unc-119(ed3) III; osm-3(p802) IV*	OSM-3::mCherry	Prevo et al., 2015
EJP81	*vuaSi24 [pBP43; Pche-11::che-11::mcherry; cb-unc-119(+)] II; unc-119(ed3) III; che-11(tm3433) V*	CHE-11::mCherry	Prevo et al., 2015
MX1932	*nxEx250[rpi-2::gfp; mksr-1::tdtomato; rol-6(su1006)]*	RPI-2::GFP + MKSR-1::tdTomato	Li et al., 2016
AND10	*che-3 (cas443[gfp::che-3]) I*	GFP::CHE-3	this study
AND22	*ift-74 (cas499[ift-74::gfp]) II; xbx-1 (ok279) V*	IFT-47::GFP + *xbx-1* null	this study
AND24	*che-3 (cas443[gfp::che-3]) I; xbx-1 (ok279) V*	GFP::CHE-3 + *xbx-1* null	this study

AND37	*wdr-60 (tm6453) III*	*wdr-60* null	this study
AND38	*ift-74 (cas499[ift-74::gfp]) II; wdr-60 (tm6453) III*	IFT-47::GFP + *wdr-60* null	this study
AND40	*wdr-60 (tm6453) III; che-3 (cas443[gfp::che-3]) I; xbx-1 (cas502[xbx-1::tagrfp::3xflag]) V*	GFP::CHE-3 + XBX-1::RFP::3xFLAG + *wdr-60* null	this study
AND45	*wdr-60 (dan1[wdr-60Δ1498_4125]) III*	WDR-60(ΔCT)	this study
AND46	*wdr-60 (dan1[wdr-60Δ1498_4125]) III; ift-74 (cas499[ift-74::gfp]) II*	IFT-47::GFP + WDR-60(ΔCT)	this study
AND47	*wdr-60 (dan3[wdr-60::3xflag::gfp]) III*	WDR-60::3xFLAG::GFP	this study
AND48	*wdr-60 (dan1[wdr-60Δ1498_4125]) III; che-3 (cas443[gfp::che-3]) I*	GFP::CHE-3 + WDR-60(ΔCT)	this study
AND49	*wdr-60 (dan1[wdr-60Δ1498_4125]) III; che-3 (cas443[gfp::che-3]) I; xbx-1 (cas502[xbx-1::tagrfp::3xFlag]) V*	GFP::CHE-3 + XBX-1::RFP::3xFLAG + WDR-60(ΔCT)	this study
AND50	*wdr-60 (dan3[wdr-60::3xflag::gfp]) III; xbx-1 (cas502[xbx-1::tagrfp::3xflag]) V*	WDR-60::3xFlag::GFP + XBX-1::RFP	this study
AND59	*wdr-60 (dan3[wdr-60::3xFlag::gfp]) III; xbx-1 (ok279) V*	WDR-60::3xFlag::GFP+ *xbx-1* null	this study
AND60	*wdr-60 (dan1[wdr-60Δ1498_4125]) III; oqEx500 [tmem-107::gfp + unc-122p::dsred]*	TMEM-107::GFP + WDR-60(ΔCT)	this study
AND66	*che-3(cas443[gfp::che-3]) I; him-8 (e1489) IV*	GFP::CHE-3 + *him-8* (e1489)	this study
AND73	*wdr-60 (dan4[wdr-60(Δ1498_4125)::3xflag::gfp]) III*	WDR-60(ΔCT)::3xFlag::GFP	this study
AND79	*oqEx500 [tmem-107::gfp + unc-122p::dsred]; xbx-1 (ok279) V*	TMEM-107::GFP + *xbx-1* null	this study
AND80	*wdr-60 (tm6453) III; oqEx500 [tmem-107::gfp + unc-122p::DsRed]; him-8 (e1489) IV*	TMEM-107::GFP + *wdr-60* null	this study
AND81	*wdr-60 (dan5[wdr-60(tm6453)::linker::3xflag::gfp]) III*	*wdr-60*(null)::3xFlag::GFP	this study
AND83	*xbx-1 (ok279) V; wdr-60 (dan4[wdr-60(Δ1498_4125)::linker::3xFlag::gfp]) III*	*wdr-60*(ΔCT)::linker::3xFlag::gfp+ *xbx-1* null	this study
AND86	*che-3 (cas443[gfp::che-3]) I; wdr-60 (tm6453) III*	GFP::CHE-3 + *wdr-60* null	this study
AND90	*wdr-60 (tm6453) III; che-11 (tm3433) V; vuaSi24 [pBP43; Pche-11::che-11::mcherry; cb-unc-119(+)] II*	CHE-11::mCherry + *wdr-60* null	this study

AND92	*wdr-60 (tm6453) III; vuaSi2 [pBP22; Posm-3::osm-3::mcherry; cb-unc-119(+)] II; osm-3(p802) IV*	OSM-3::mCherry + *wdr-60* null	this study
AND96	*che-3 (cas443[gfp::che-3])I; vuaSi21 [pBP39; Pmks-6::mks-6::mcherry; cb-unc-119(+)] II*	GFP::CHE-3 + MKS-6::mCherry	this study
AND97	*che-3 (cas443[gfp::che-3])I; mksr-2 (tm2452) IV; nphp-4 (tm925) V*	GFP::CHE-3 + *mksr-2*(tm2452) + *nphp-4*(tm925)	this study
AND99	*che-3 (cas443[gfp::che-3]) I; wdr-60 (tm6453) III; mksr-2 (tm2452) IV; nphp-4 (tm925) V*	GFP::CHE-3 + *wdr-60* null + *mksr-2*(tm2452) + *nphp-4*(tm925)	this study
AND100	*che-3 (cas443[gfp::che-3]) I; wdr-60 (tm6453) III; mksr-2 (tm2452) IV*	GFP::CHE-3 + *wdr-60* null + *mksr-2*(tm2452)	this study
AND103	*vuaSi21 [pBP39; Pmks-6::mks-6::mcherry; cb-unc-119(+)] II; xbx-1 (ok279) V*	MKS-6::mCherry + *xbx-1* null	this study
AND104	*che-3 (cas443[gfp::che-3]) I; vuaSi21 [pBP39; Pmks-6::mks-6::mcherry; cb-unc-119(+)] II; wdr-60 (tm6453) III*	GFP::CHE-3 + MKS-6::mCherry + *wdr-60* null	this study
AND110	*wdr-60 (tm6453) III; vuaSi1 [pBP20; Pkap-1::kap-1::egfp; cb-unc-119(+)] IV*	KAP-1::GFP + *wdr-60* null	this study
AND112	*che-3(cas511[gfp::che-3(K2935Q)]) I; nphp-4 (tm925) V*	GFP::CHE-3(K2935Q) + *nphp-4*(tm925)	this study
AND113	*che-3(cas511[gfp::che-3(K2935Q)]) I; mksr-2 (tm2452) IV ; nphp-4 (tm925) V*	GFP::CHE-3(K2935Q) + *nphp-4*(tm925) + *mksr-2*(tm2452)	this study
AND114	*che-3(cas511[gfp::che-3(K2935Q)]) I; mksr-2 (tm2452) IV*	GFP::CHE-3(K2935Q) + *mksr-2*(tm2452)	this study
AND119	*vuaSi24 [pBP43; Pche-11::che-11::mCherry; cb-unc-119(+)] II; wdr-60 (dan1[wdr-60Δ1498_4125]) III ; che-11 (tm3433) V*	CHE-11::mCherry + WDR-60(ΔCT)	this study
AND122	*che-3 (cas443[gfp::che-3]) I ; vuaSi21 [pBP39; Pmks-6::mks-6::mCherry; cb-unc-119(+)] II; wdr-60 (dan1[wdr-60Δ1498_4125]) III*	GFP::CHE-3 + MKS-6::mCherry + WDR-60(ΔCT)	this study
AND127	*vuaSi1 [pBP20; Pkap-1::kap-1::egfp; cb-unc-119(+)] IV*	KAP-1::GFP	this study
AND129	*che-3 (cas443[gfp::che-3]) I; mksr-2 (tm2452) IV*	GFP::CHE-3 + *mksr-2*(tm2452)	this study

AND143	*ltSi1188[pDC600; Pmex-5::sgfp1-10::gpd-2/3::mcherry::his-15; cb-unc-119(+)] II; unc-119(ed3) III; dyci-1(dan7[dyci-1::2xflag::aid::3xsgfp11]) IV*	gonad (sGFP1-10 + mCherry::HIS-15) + DYCI-1::2xFLAG::AID::3xsGFP	this study
AND153	*ttTi5605 [Pift-139::sgfp1-10::gpd-2/3::tir1mruby; unc-119(+)] II; unc-119(ed3) III; dyci-1(dan7[dyci-1::2xflag::aid::3xsgfp11]) IV*	sensory neuron (sGFP1-10 + TIR1mRuby) + DYCI-1::2xFLAG::AID::3xsGFP	this study
AND158	*ttTi5605 [Pift-139::sgfp1-10::gpd-2/3::tir1mruby; unc-119(+)] II; wdr-60 (dan3[wdr-60::3xflag::gfp]) III; dyci-1(dan7[dyci-1::2xflag::aid::3xsgfp11]) IV*	sensory neuron (sGFP1-10 + TIR1mRuby) + DYCI-1::2xFLAG::AID::3xsGFP + WDR-60::3xFLAG::GFP	this study
AND173	*che-3(cas443[gfp::che-3])I; nphp-4 (tm925)V*	GFP::CHE-3 + *nphp-4*(tm925)	this study
AND174	*che-3(cas443[gfp::che-3]) I; wdr-60 (tm6453) III; nphp-4 (tm925)V*	GFP::CHE-3 + *wdr-60* null + *nphp-4*(tm925)	this study
AND184	*che-3(cas511[gfp::che-3(K2935Q)]) I; mks-5 (tm3100) II*	GFP::CHE-3(K2935Q) + *mks-5*(tm3100)	this study
AND190	*che-3(cas443[gfp::che-3]) I; mks-5 (tm3100) II; wdr-60 (tm6453) III*	GFP::CHE-3 + *wdr-60* null + *mks-5*(tm3100)	this study
AND194	*che-3(cas443[gfp::che-3]) I; mks-5 (tm3100) II*	GFP::CHE-3 + *mks-5*(tm3100)	this study
AND198	*ttTi4391-vieSi23[pAD402; Pnphp-4::gfp::nphp-4cDNA; cb-unc-119(+)] I; wdr-60 (tm6453) III; cxTi10882-vieSi16[pAD390; Phyls-1::mcherry::hyls-1; cb unc-119(+)] IV*	GFP::NPHP-4 + mCherry::HYLS-1 + *wdr-60* null	this study
AND200	*che-3(cas443[gfp::che-3]) I; wdr-60 (tm6453) III; cxTi10882-vieSi16[pAD390; Phyls-1::mcherry::hyls-1; cb unc-119(+)] IV*	GFP::CHE-3 + mCherry::HYLS-1 + *wdr-60* null	this study
AND201	*che-3(cas443[gfp::che-3]) I; cxTi10882-vieSi16[pAD390; Phyls-1::mcherry::hyls-1; cb unc-119(+)] IV*	GFP::CHE-3 + mCherry::HYLS-1	this study
AND203	*vuaSi24 [pBP43; Pche-11::che-11::mCherry; cb-unc-119(+)] II; xbx-1(ok279) V*	CHE-11::mCherry + *xbx-1* null	this study
AND204	*nxEx250[rpi-2::gfp; mksr-1::tdtomato; rol-6(su1006)]; wdr-60 (dan1[wdr-60Δ1498_4125]) III*	RPI-2::GFP + MKSR-1::tdTomato + *wdr-60*(ΔCT)	this study
AND207	*che-3(cas443[gfp::che-3]) I; cep-290 (tm4927) I*	GFP::CHE-3 + *cep-290*(tm4927)	this study
AND208	*cep-290 (tm4927) I; che-3(cas443[gfp::che-3]) I; wdr-60 (tm6453) III*	GFP::CHE-3 + *cep-290*(tm4927) + *wdr-60* null	this study

AND215	*ttTi4391-vieSi23[pAD402; Pnphp-4::gfp::nphp-4cDNA; cb-unc-119(+)] I; cxTi10882-vieSi16[pAD390; Phyls-1::mcherry::hyls-1; cb-unc-119(+)] IV; xbx-1 (ok279) V*	GFP::NPHP-4 + mCherry::HYLS-1 + *xbx-1* null	this study
AND216	*ttTi4391-vieSi23[pAD402; Pnphp-4::gfp::nphp-4cDNA; cb-unc-119(+)] I; wdr-60 (dan1[wdr-60Δ1498_4125]) III; cxTi10882-vieSi16[pAD390; Phyls-1::mcherry::hyls-1; cb-unc-119(+)] IV*	GFP::NPHP-4 + mCherry::HYLS-1 + *wdr-60*(ΔCT)	this study
AND219	*nxEx250[rpi-2::gfp; mksr-1::tdtomato; rol-6(su1006)]; wdr-60 (tm6453) III*	RPI-2::GFP + MKSR-1::tdTomato + *wdr-60* null	this study
AND222	*nxEx250[rpi-2::gfp; mksr-1::tdtomato; rol-6(su1006)]; xbx-1(ok279) V*	RPI-2::GFP + MKSR-1::tdTomato + *xbx-1* null	this study
AND266	*ttTi5605 [Pift-139::tir1mruby::Prgef-1::sgfp1-10; unc-119(+)] II; unc-119(ed3) III; dyci-1 (dan7[dyci-1::2xflag::aid::3xsgfp11]) IV*	sensory neuron TIR1mRuby + pan-neuronal sGFP1-10 + DYCI-1::2xFLAG::AID::3xsGFP	this study
AND337	*klp-20(cas447[klp-20::gfp]) III*	KLP-20::GFP	this study
AND338	*klp-20(cas447[klp-20::gfp]) III ; wdr-60(tm6453) III*	KLP-20::GFP + *wdr-60* null	this study
AND384	*ifta-1(dan21[ifta-1::aid::gfp]) X*	IFT-121::GFP	AND lab
AND393	*ift-74(cas499[ift-74::gfp]) II ; wdr-60(tm6453) III ; nphp-4(tm925) V*	IFT-74::GFP + *wdr-60* null + *nphp-4* null	this study
AND394	*klp-20(cas447[klp-20::gfp]) III ; wdr-60(tm6453) III; nphp-4(tm925) V*	KLP-20::GFP + *wdr-60* null + *nphp-4* null	this study
AND397	*klp-20(cas447[klp-20::gfp]) III ; nphp-4(tm925) V*	KLP-20::GFP + *nphp-4* null	this study
AND399	*ift-74(cas499[ift-74::gfp]) II ; nphp-4(tm925) V*	IFT-74::GFP + *nphp-4* null	this study
AND420	*dyf-2(dan19[dyf-2::aid::gfp]) III*	IFT-144::GFP	AND lab
AND424	*vuaSi1[pBP20 ; Pkap-1::kap-1::egfp ; cb-unc-119(+)] IV ; wdr-60(tm6453) III ; nphp-4(tm925) V*	KAP-1::GFP + *wdr-60* null + *nphp-4* null	this study
AND425	*vuaSi1[pBP20 ; Pkap-1::kap-1::egfp ; cb-unc-119(+)] IV ; nphp-4(tm925) V*	KAP-1::GFP + *nphp-4* null	this study
AND433	*dyf-2(dan19[dyf-2::aid::gfp]) III ; wdr-60(tm6453) III ; nphp-4(tm925) V*	IFT-144::GFP + *wdr-60* null + *nphp-4* null	this study
AND434	*dyf-2(dan19[dyf-2::aid::gfp]) III ; nphp-4(tm925) V*	IFT-144::GFP + *nphp-4* null	this study
AND435	*dyf-2(dan19[dyf-2::aid::gfp]) III ; wdr-60(tm6453) III*	IFT-144::GFP + *wdr-60* null	this study

AND459	*wdr-60(dan20[wdr-60(Δ4_1497)::3xflag::gfp]) III*	WDR-60(Δ2-287)::3xFLAG::GFP	this study
AND470	*dyf-11(dan26[dyf-11::aid::gfp]) X*	IFT-54::GFP	AND lab
AND472	*wdr-60(dan24[wdr-60(Δ204_260)::3xflag::gfp]) III*	WDR-60(Δ55-74)::3xFLAG::GFP	this study
AND473	*che-3(cas443[gfp::che-3]) I; wdr-60(dan23[wdr-60(Δ204_260)]) III*	WDR-60(Δ55-74) + GFP::CHE-3	this study
AND474	*wdr-60(tm6453) III; dyf-11(dan26[dyf-11::aid::gfp]) X*	IFT-54::GFP + *wdr-60* null	this study
AND475	*nphp-4(tm925) V; dyf-11(dan26[dyf-11::aid::gfp]) X*	IFT-54::GFP + *nphp-4* null	this study
AND476	*wdr-60(tm6453) III ; nphp-4(tm925) V; dyf-11(dan26[dyf-11::aid::gfp]) X*	IFT-54::GFP + *wdr-60* null + *nphp-4* null	this study
AND501	*wdr-60(tm6453) III; ifta-1(dan21[ifta-1::aid::gfp]) X*	IFT-121::GFP + *wdr-60* null	this study
AND502	*nphp-4(tm925) V; ifta-1(dan21[ifta-1::aid::gfp]) X*	IFT-121::GFP + *nphp-4* null	this study
AND503	*wdr-60(tm6453) III ; nphp-4(tm925) V; ifta-1(dan21[ifta-1::aid::gfp]) X*	IFT-121::GFP + *wdr-60* null + *nphp-4* null	this study
AND522	*bbs-1(dan27[bbs-1::aid::gfp]) I*	BBS-1::GFP	this study
AND532	*vuaSi15[pBP36 ; Posm-6::osm-6::egfp ; cb-unc119(+)] I ; wdr-60(tm6453) III*	OSM-6::GFP + *wdr-60* null	this study
AND533	*vuaSi15[pBP36 ; Posm-6::osm-6::egfp ; cb-unc119(+)] I ; nphp-4(tm925) V*	OSM-6::GFP + *nphp-4* null	this study
AND534	*vuaSi15[pBP36 ; Posm-6::osm-6::egfp ; cb-unc119(+)] I ; wdr-60(tm6453) III ; nphp-4(tm925) V*	OSM-6::GFP + *wdr-60* null + *nphp-4* null	this study
AND535	*vuaSi15[pBP36 ; Posm-6::osm-6::egfp ; cb-unc119(+)] I*	OSM-6::GFP	this study
AND550	*bbs-1(dan27[bbs-1::aid::gfp]) I ; wdr-60(tm6453) III*	BBS-1::GFP + *wdr-60* null	this study
AND551	*bbs-1(dan27[bbs-1::aid::gfp]) I ; nphp-4(tm925) V*	BBS-1::GFP + *nphp-4* null	this study
AND552	*bbs-1(dan27[bbs-1::aid::gfp]) I ; wdr-60(tm6453) III ; nphp-4(tm925) V*	BBS-1::GFP + *wdr-60* null + *nphp-4* null	this study
AND562	*wdr-60(dan24[wdr-60(Δ204_260)::3xflag::gfp]) III ; xbx-1(ok279) V*	WDR-60(Δ55-74)::3xFLAG::GFP + *xbx-1* null	this study
AND571	*mnEx171[dyf-6::GFP + rol-6(su1006)]*	IFT-46::GFP	this study

AND572	*mnEx171[dyf-6::GFP + rol-6(su1006)] ; wdr-60(tm6453) III*	IFT-46::GFP + *wdr-60* null	this study
AND573	*mnEx171[dyf-6::GFP + rol-6(su1006)] ; nphp-4(tm925) V*	IFT-46::GFP + *nphp-4* null	this study
AND574	*mnEx171[dyf-6::GFP + rol-6(su1006)] ; wdr-60(tm6453) III ; nphp-4(tm925) V*	IFT-46::GFP + *wdr-60* null + *nphp-4* null	this study

ANNEX IV – List of primers used for the screening of genetic mutations in *C. elegans*

Table 2 - List of primers used for the screening of genetic mutations in *C. elegans*.

	Screen		Primer ID	Sequence (5'-3')
Dynein components	**CHE-3**	**GFP tag knock-in**	oTD54 (FW)	ACAGGTGGAGTGTATTTAATGAG
			oTD2 (RV)	ACAACACGAAAGACGTTGGCTG
		CHE-3(K2935Q)	oTD7 (FW)	GGTGCTAGAATGGCTAAACAATG
			oTD8 (RV)	CACCGATATTGTTAGAGTATATCAC
	XBX-1	**RFP tag knock-in**	oTD3 (FW)	GTTCGACGCCTCGTTGAGAA
			oTD4 (RV)	CACCAATACAAGTCTAAGCTAG
		xbx-1(ok279)	oTD22 (FW)	AGTTCGTCGGAGACACGAATC
			oTD23 (RV)	CCACGAACGGCAATTGGTTAC
	WDR-60	**WDR-60(∆CT)**	oTD26 (FW)	GAGAGAGGAGAGACAGAAGAGAAAGAG
			oTD41 (RV)	CAAATGCCACAAGATACGGAC
		GFP tag knock-in	oTD42 (FW)	TCATAACATACTGGGATTTGGG
			oTD41 (RV)	CAAATGCCACAAGATACGGAC
		wdr-60(null)	oTD40 (FW)	AGTTGAGTTGATTTCCTTGGG
			oTD53 (RV)	GATATGAAACCTGTGTTGCAG
		WDR-60(∆55-74)	oTD25 (FW)	GCGTCTTCGAGCAAAGTTACG
			oTD600 (RV)	CTGAGCCTGAACCAGTGAAC
		WDR-60(∆NT)	oTD40 (FW)	AGTTGAGTTGATTTCCTTGGG
			oTD69 (RV)	CTGAAGTCGTCAAAGTTTGG
	DYCI-1	**split GFP knock-in**	oTD61 (FW)	GTTCGTTGGTGATGATGAGG
			oTD62 (RV)	CACAATTACACACACAAGAAGAG
IFT Kinesin subunits	**OSM-3**	**wild type**	oTD163 (FW)	GGATGCTCTTCTTCGAGAGTACC
			oTD164 (RV)	CGAGACGATCCAGTTCGAATTC
		osm-3(p802)	oTD165 (FW)	GGATGCTCTTCTTCGAGAGTACT
			oTD164 (RV)	CGAGACGATCCAGTTCGAATTC
	kap-1(ok676)		oTD157 (FW)	TTTCATTCCTGCCACGTCAC

		oTD158 (RV)	CTTTGATTGACCCAACTCACC
	KLP-20::GFP knock-in	oTD403 (FW)	CCAGAACAACAACCAAACGG
		oTD404 (RV)	CAATTACAGGCTTCGCCCTT
IFT-A/B Complexes	**IFT-74::GFP knock-in**	oTD5 (FW)	CACGAGTATGACTCACAAGGAG
		oTD6 (RV)	CGGAAAGGGTGCTTCATACTTG
	che-11 (tm3433)	oTD161 (FW)	TCTTCGTAGTATCTTGCAGCG
		oTD162 (RV)	TACAACTTCAAGGAATGCAGC
	IFT-144::AID::GFP knock-in	oTD604 (FW)	GTGCCGTACTGTATTCTTAC
		oTD605 (RV)	CATGTAAAGCGGAATGTAAG
	IFT-121::AID::GFP knock-in	oTD613 (FW)	TCCAAGATTTCTGTTTACCG
		oTD614 (RV)	GAAATTCGATTGTTTGAGCAC
	IFT-54::AID::GFP knock-in	oTD615 (FW)	AGATAGAGGAGCTTTGGTG
		oTD616 (RV)	TTAATCTGGGTTTTCCTGTG
BBS complex	**BBS-1::AID::GFP knock-in**	oTD638 (FW)	GGCTTAGGTTTAGGCTCAAC
		oTD639 (RV)	GAAGGGATATTGGTCCGATG
Transition Zone components	***mks-5 (tm3100)***	oTD393 (FW)	TTCAATAGCAGATTTCGCCG
		oTD394 (RV)	AATCACATTCCTCTTGCAGC
	nphp-4 (tm925)	oTD153 (FW)	GCCATTCTTGGATCCGCATA
		oTD154 (RV)	CCGGCCAGTTGAAATGAAAC
	mksr-2(tm2452)	oTD155 (FW)	TTGCTCATCTCCCTAATGGC
		oTD156 (RV)	TGGATTCGGTGATAATCGGC

	cep-290(tm4927)		oTD159 (FW)	AGCTTGTTCGTCATTTCGGT
			oTD160 (RV)	CTGTAGGCACAAGGCCATAA
MosSCI knock-in	**MosSCI Chr I (ttTi4391)**	**knock-in**	oTD436 (FW)	AGACTATCAGCTCAATGTGC
			oTD271 (RV)	TTTACAAGGACTTGGATAAATTGG
		wild type	oTD436 (FW)	AGACTATCAGCTCAATGTGC
			oTD437 (RV)	ACCGACTGCCATGATATAGC
	MosSCI Chr I (ttTi4348)	**knock-in**	oTD644 (FW)	CACTTGAGCTTACAATAACTTGC
			oTD271 (RV)	TTTACAAGGACTTGGATAAATTGG
		wild type	oTD642 (FW)	GAGAGCAACACTGACGAAGAA
			oTD643 (RV)	TGCAGTTCGAAATGGTGATTGA
	MosSCI Chr II (ttTi5605)	**knock-in**	oTD270 (FW)	GACATTTGAGAATGGCATTGA
			oTD271 (RV)	TTTACAAGGACTTGGATAAATTGG
		wild type	oTD272 (FW)	AGGCAGAATGTGAACAAGACTCG
			oTD273 (RV)	ATCGGGAGGCGAACCTAACTG
	MosSCI Chr IV (cxTi10882)	**knock-in**	oTD320 (FW)	CAGGAGAGCAAGGACCAAAG
			oTD271 (RV)	TTTACAAGGACTTGGATAAATTGG
		wild type	oTD320 (FW)	CAGGAGAGCAAGGACCAAAG
			oTD319 (RV)	GCCAAATGCCATAGTCAATGG

ANNEX V – List of sgRNAs used in this study

Table 3 - List of sgRNAs used in this study.

Target	sgRNA ID	Sequence (5'-3') (PAM)
wdr-60	pTD135 (plasmid)	CGGAATGGATTATATCCCC (TGG)
	pTD136 (plasmid)	TGTTCTAGAAGATCCCGCG (CGG)
	pTD133 (plasmid)	TCTTTCTTCGATTTTCGGG (TGG)
	sgRNA35	TTTCGAAGAAGATGATGAAG (AGG)
bbs-1	sgRNA49	CACAAATCGGAGCCAATAAG (GGG)
dyci-1	pRG371 (plasmid)	AAGCAATCGAATGAGGAAG (CGG)
	pRG393 (plasmid)	TAACATGTAGACGAATGCG (CGG)

ANNEX VI – Oligos used as homology repair templates for CRISPR-Cas9-mediated genomic editing

Table 4 - Oligos used as homology repair templates for CRISPR-Cas9-mediated genomic editing.

modification	oligo ID	Sequence (5'-3')
WDR-60(Δ288-668)	oTD18	GGATAAATCTGCCGAGGAAGATGAAACGAGGGAAAAGTCAATTTCTAAGTTTTCTAGGGGATATAATTGAGCGCGGAAGAATCAAAACGAAACCATTTTGGAGGTTTTGAGAAG
WDR-60(Δ2-287)	oTD68	CATAGCAACTAAAATGTGCAGCATTTGAACGACCCGAAAATCGAAGAAAGATTTCATTTTATTCCATTTTCTATGAAAAATGCCATTCCGACTTTGTCAAGTTGTCACTAGTGAGTTTTC
WDR-60(Δ55-73)	oTD628	TAAGCCTGAGCCTGAGCCTGAACCAGTGAACGAAAAAAAGGCTCCGAAAGTTGAAGAAAAGCCACAAAAAGAATCAAAAGTAGAAGCTGAGGTAGATAAC

ANNEX VII - Primers used to generate partially single stranded homology repair templates for CRISPR-Cas9-mediated genomic editing

Table 5 - Primers used to generate partially single stranded homology repair templates for CRISPR-Cas9-mediated genomic editing.

Endogenous knock-in	Primer ID	Sequence (5'-3')	Description
BBS-1::AID::GFP	oTD636 (FW)	AGGTTCCGTTTTAGGCTTAG	to amplify the larger fragment
	oTD637 (RV)	GTAGTGGTACTGTAGGGTAC	
	oRG2794 (FW)	GGAGGATCTGGAGGCGGTTC	to amplify the smaller fragment
	oTD583 (RV)	TTTGTAAAGTTCATCCATTCCAAGAGTTATTC	
DYCI-1::2xFLAG::AID::3xsGFP11	oTD151 (FW)	AAGTTTGTACGTGTTGAAGAGCGAAGAATGGAATCGATTT GCTAGGTAAGCAGCTACCCGTTCCTCTTTCTACATGAAAA ATGTGCAATTTTCAGAGTTTTATCTGATATGAAGCAATCG	to amplify the larger fragment
	oTD152 (RV)	GCCACGTTTCAATAAGAAAGCGTGGGAAAATATGCTTTGT AAGGGATTTAAAAAACAAGTACCTATGATTTAAATATGATA AATAGAAAATCTGATTAAAGTTAAGATTGGAAAGAACCG	
	oRG982 (FW)	GAGTTTTATCTGATATGAAGCAATCG	to amplify the smaller fragment
	oRD938 (RV)	AGTTAAGATTGGAAAGAACCGC	
WDR-60::3xFLAG::GFP	oTD63 (FW)	GAAAAGTATGGAGAGGTTACTG	to amplify the larger fragment
	oTD64 (RV)	GGAGACAATTCAAATTCGG	
	oTD56 (FW)	GGATCTGGTAGCGGAGAC	to amplify the smaller fragment
	oTD60 (RV)	TCATTTGTATAGTTCATCCATGCC	

ANNEX VIII – List of primers used to generate the constructs for the genomic editing of *C. elegans*

Table 6 - List of primers used to generate the constructs for the genomic editing of *C. elegans*.

Primer ID	Sequence (5'-3')	Description	Final construct
oRG510 (RV)	CATATGGTGCACTCTCAG	to make a linear fragment of pUC57 backbone (Gibson Assembly fragment 1)	**pUC57 - (wdr-60) 5'Harm::3xFLAG::GFP::3' Harm**
oRG509 (FW)	GGCGTAATCATGGTCATAG		
oTD43 (FW)	GATTGTACTGAGAGTGCACCATATGGAGCGGTTTTAGAAAAGTATGGAGAG	to amplify 625bp upstream of *wdr-60* stop codon and generate the 5' homology arm (Gibson Assembly fragment 2)	
oTD44 (RV)	CCCAAATTTTTAATTCTTCTCAAAACCTCCAAAATGGTTTCGTTTTGATTCTTGCGCGCGGGATCTTCTAGAAC		
oTD46 (RV)	CAATATCCAAAAAAGATCATTCATTTGTATAGTTCATCCATGCC	to amplify the 3xFLAG::GFP tag from pRG604 (provided by the co-supervisor) and add an upstream linker sequence (Gibson Assembly fragment 3)	
oTD45 (FW)	GGAGGTTTTGAGAAGAATTAAAAATTTGGGATCTGGTAGCGGAGACTACAAAGACCATGACGG		
oTD47 (FW)	CAAATGAATGATCTTTTTTGGATATTG	to amplify 508bp downstream of *wdr-60* stop codon and generate the 3' homology arm (Gibson Assembly fragment 4)	
oTD48 (RV)	AGGAAACAGCTATGACCATGATTACGCCGGAGACAATTCAAATTCGG		
oTD636 (FW)	AGGTTCCGTTTTAGGCTTAG	to amplify 1033bp homology arms of *bbs-1* (522bp upstream of stop codon + 511bp downstream of stop codon) to clone into pNZY28 and generate pNZY28 - bbs-1 Harms	**pNZY28 - (bbs-1) 5'Harm::AID::GFP::3'Harm**
oTD637 (RV)	GTAGTGGTACTGTAGGGTAC		
oRG2650 (FW)	GACTGGATGGAGGCGGATAAAG	to amplify the first half of the pNZY28 backbone and the 5' homology arm from pNZY28 - bbs-1 Harms (Gibson Assembly fragment 1)	
oTD635 (RV)	GAACCGCCTCCAGATCCTCCATCAAGTGGAAATTCGCTGAAG		
oRG2794 (FW)	GGAGGATCTGGAGGCGGTTC	to amplify the AID::GFP tag from the CA1207 strain (Zhang 2015) (Gibson Assembly fragment 2)	
oTD583 (RV)	TTTGTAAAGTTCATCCATTCCAAGAGTTATTC		
oTD636 (FW)	ACTCTTGGAATGGATGAACTTTACAAATAGTTCCAGTTTTCACCTTATTGG		

oRG2649 (RV)	CTTTATCCGCCTCCATCCAGTC	to amplify the second half of the pNZY28 backbone and the 3' homology arm from pNZY28 - bbs-1 Harms (Gibson Assembly fragment 3)	
oRG2650 (FW)	GACTGGATGGAGGCGGATAAAG	to amplify part of the pDC600 backbone cointaining the first half of AmpR, ttTi5605 5' homology arm, and unc-119(+) (Gibson Assembly fragment 1)	**pDC600 - (ttTi5605) Pift-139::sGFP::gpd-2/3::TIR1mRuby**
oAC654 (FW)	CCTAGTTCTAGACATTCTC		
oTD245 (FW)	CATTAGAGAATGTCTAGAACTAGGAATCGACTTAATTGGTACAG	to amplify Pift-139 (Gibson Assembly fragment 2)	
oTD246 (RV)	GAAAAGTTCTTCTCCTTTACTCATTTTTAAATTGAGATATCAGC		
oTD265 (FW)	ATGAGTAAAGGAGAAGAACTTTTC	to amplify sGFP1-10 and the gpd-2/3 operon linker from pDC600 (Gibson Assembly fragment 3)	
oTD264 (RV)	CGATTCTCTTTTGCATGATGCGTTGAAGCAGTTTCCCTG		
oTD267 (FW)	CTTCAACGCATCATGCAAAAGAGAATCGCCTTG	to amplify TIR1::mRuby from the GCP637 strain (Gibson Assembly fragment 4)	
oTD268 (RV)	GATGCGGAGCTCTTATCCTCCTCCAAGTCCAGC		
oTD266 (FW)	CTTGGAGGAGGATAAGAGCTCCGCATCGGC	to amplify part of the pDC600 backbone cointaining ttTi5605 3' homology arm, and the second half of AmpR (Gibson Assembly fragment 5)	
oRG2649 (RV)	CTTTATCCGCCTCCATCCAGTC		
oRG2650 (FW)	GACTGGATGGAGGCGGATAAAG	to amplify part of the pDC600 backbone cointaining the first half of AmpR, ttTi5605 5' homology arm, and unc-119(+) (Gibson Assembly fragment 1)	**pDC600 - (ttTi5605) Pift-139::TIR1mRuby::Prgef-1::sGFP1-10**
oAC654 (FW)	CCTAGTTCTAGACATTCTC		
oTD245 (FW)	CATTAGAGAATGTCTAGAACTAGGAATCGACTTAATTGGTACAG	to amplify Pift-139 (Gibson Assembly fragment 2)	
oTD345 (RV)	ACAAGGCGATTCTCTTTTGCATTTTTAAATTGAGATATCAGC		
oTD344 (FW)	AATGCAAAAGAGAATCGCCTTGTCGTTTCCAGAAGAAGTACTC	to amplify TIR1::mRuby from the GCP637 strain (Gibson Assembly fragment 3)	
oTD268 (RV)	GATGCGGAGCTCTTATCCTCCTCCAAGTCCAGC		

oTD266 (FW)	CTTGGAGGAGGATAAGAGCTCCGCATCGGC	to amplify Prgef-1 (Gibson Assembly fragment 4)	
oTD248 (RV)	GAAAAGTTCTTCTCCTTTACTCATCTTTACTGCT GATCGTCGTCGTC		
oTD265 (FW)	ATGAGTAAAGGAGAAGAACTTTTC	to amplify sGFP1-10 from pDC600 (Gibson Assembly fragment 5)	
oTD342 (RV)	ACGCGTCAATGAGACTTTTTTCTTG		
oTD341 (FW)	CAAGAAAAAAGTCTCATTGACGCGTTCGTGGAT CCAGATATCCT	to amplify part of the pDC600 backbone cointaining ttTi5605 3' homology arm, and the second half of AmpR (Gibson Assembly fragment 6)	
oRG2649 (RV)	CTTTATCCGCCTCCATCCAGTC		

ANNEX IX – DNA sequences coding for the new protein tags generated in this study

The DNA sequence coding for the “3xFLAG::GFP” tag inserted at 3’ of the endogenous *wdr-60* locus was amplified from pRG604 (provided by the co-supervisor), adding a 5’ linker sequence.

5’ to 3’ sequence:

GGATCTGGTAGCGGAGACTACAAAGACCATGACGGTGATTATAAAGATCATGATATCGATTACAAGG
ACGATGACGATAAGATGAGTAAAGGAGAAGAACTTTTCACTGGAGTTGTCCCAATTCTTGTTGAATT
AGATGGTGATGTTAATGGGCACAAATTTTCTGTCAGTGGAGAGGGTGAAGGTGATGCAACATACGG
AAAACTTACCCTTAAATTTATTTGCACTACTGGAAAACTACCTGTTCCATGGGTAAGTTTAAACATATA
TATACTAACTAACCCTGATTATTTAAATTTTCAGCCAACACTTGTCACTACTTTCTGTTATGGTGTTCAA
TGCTTCTCGAGATACCCAGATCATATGAAACGGCATGACTTTTTCAAGAGTGCCATGCCCGAAGGTT
ATGTACAGGAAAGAACTATATTTTTCAAAGATGACGGGAACTACAAGACACGTAAGTTTAAACAGTT
CGGTACTAACTAACCATACATATTTAAATTTTCAGGTGCTGAAGTCAAGTTTGAAGGTGATACCCTTG
TTAATAGAATCGAGTTAAAAGGTATTGATTTTAAAGAAGATGGAAACATTCTTGGACACAAATTGGA
ATACAACTATAACTCACACAATGTATACATCATGGCAGACAAACAAAAGAATGGAATCAAAGTTGTA
AGTTTAAACATGATTTTACTAACTAACTAATCTAATTTAAATTTTCAGAACTTCAAAATTAGACACAAC
ATTGAAGATGGAAGCGTTCAACTAGCAGACCATTATCAACAAAATACTCCAATTGGCGATGGCCCTG
TCCTTTTACCAGACAACCATTACCTGTCCACACAATCTGCCCTTTCGAAAGATCCCAACGAAAAGAG
AGACCACATGGTCCTTCTTGAGTTTGTAACAGCTGCTGGGATTACACATGGCATGGATGAACTATAC
AAA

DNA sequence annotated in SnapGene Viewer (v5.0.8):

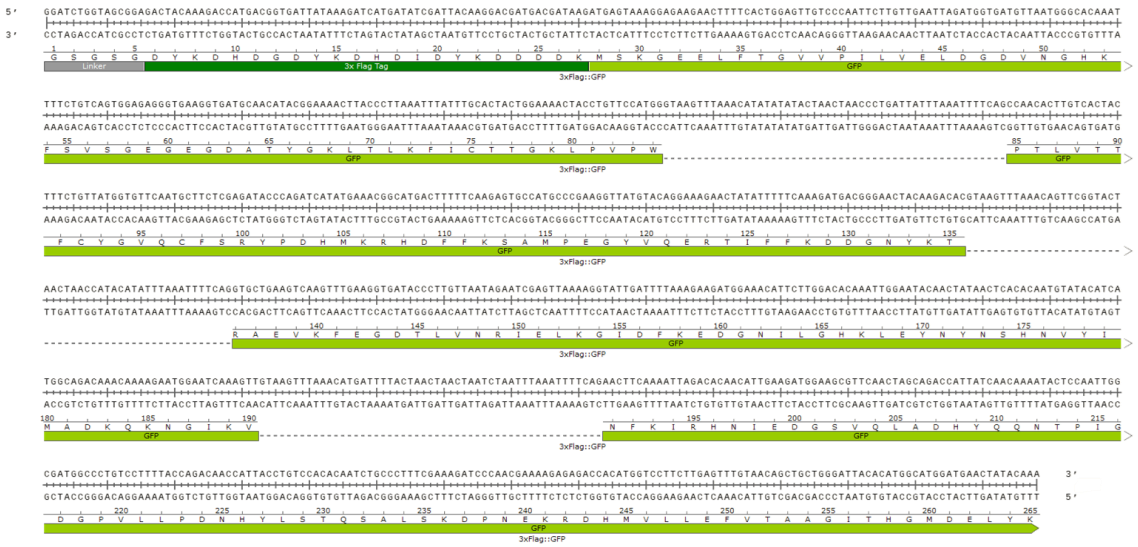

The DNA sequence coding for the “2xFLAG::AID::3xsGFP11” tag inserted at 3’ of the endogenous *dyci-1* locus was synthesized as a gBlock (IDT).

5’ to 3’ sequence:

GGAGGTGGATCTGGAGGCGGTTCCGGAGGTGGAGATTATAAAGATCATGATATCGATTACAAGGAT
GACGATGACAAGGGAGGTTCCGGAGGCCCAAAGGATCCAGCCAAGCCACCAGCCAAGGCTCAGG
TTGTCGGATGGCCACCAGTCAGATCTTACCGCAAGAACGTCATGGTTTCCTGCCAAAAGTCTTCCGG
TGGACCAGAGGCTGCCGCTTTCGTCAAGGGAGGATCTGGTGGAAGAGATCATATGGTCCTCCACG
AATACGTTAACGCTGCCGGTATCACTGGAGGATCTGGAGGACGTGACCATATGGTTCTCCACGAATA
CGTCAATGCCGCCGGAATCACCGGAGGTTCCGGAGGAAGAGACCATATGGTTCTTCACGAATACGT
CAACGCCGCTGGAATCACC

DNA sequence annotated in SnapGene Viewer (v5.0.8):